



HAL
open science

Zero-group-velocity Lamb modes in laser ultrasonics : fatigue monitoring and material characterization

Guqi Yan

► **To cite this version:**

Guqi Yan. Zero-group-velocity Lamb modes in laser ultrasonics: fatigue monitoring and material characterization. Mechanics of materials [physics.class-ph]. Le Mans Université, 2018. English. NNT : 2018LEMA1026 . tel-01954447

HAL Id: tel-01954447

<https://theses.hal.science/tel-01954447v1>

Submitted on 13 Dec 2018

HAL is a multi-disciplinary open access archive for the deposit and dissemination of scientific research documents, whether they are published or not. The documents may come from teaching and research institutions in France or abroad, or from public or private research centers.

L'archive ouverte pluridisciplinaire **HAL**, est destinée au dépôt et à la diffusion de documents scientifiques de niveau recherche, publiés ou non, émanant des établissements d'enseignement et de recherche français ou étrangers, des laboratoires publics ou privés.

THESE DE DOCTORAT DE

LE MANS UNIVERSITE
COMUE UNIVERSITE BRETAGNE LOIRE

ECOLE DOCTORALE N° 602
Sciences pour l'Ingénieur
Spécialité : *Acoustique*

Par

Guqi YAN

Zero-group-velocity Lamb modes in laser ultrasonics: fatigue monitoring and material characterization

Thèse présentée et soutenue à Le Mans, le 20 Novembre 2018
Unité de recherche : Laboratoire d'Acoustique de l'Université du Mans, UMR-CNRS 6613
Thèse N° : 2018LEMA1026

Rapporteurs avant soutenance :

David HURLEY Directeur de recherche, Idaho National Laboratory (USA)
Emmanuel MOULIN Professeur, IEMN - Université de Valenciennes et du Hainaut Cambrésis

Composition du Jury :

Présidente	: Claire PRADA	Directrice de recherche CNRS, Institut Langevin - ESPCI, PSL
Examineur	: Thomas DEHOUX	Chargé de recherche CNRS, ILM - Université Lyon 1
Examineur	: Nikolay CHIGAREV	Ingénieur de recherche, LAUM - Le Mans Université
Dir. de thèse	: Vincent TOURNAT	Directeur de recherche CNRS, LAUM - Le Mans Université
Co-dir. de thèse	: Vitalyi E. GUSEV	Professeur, LAUM - Le Mans Université
Co-encadrant	: Samuel RAETZ	Maître de conférence, LAUM - Le Mans Université

Académie de Nantes

Le Mans Université, Le Mans, France
École Doctorale Sciences pour l'Ingénieur

Doctoral Thesis

Speciality : Acoustics

Presented by

Guqi YAN

submitted for the Doctoral degree

ZERO-GROUP-VELOCITY LAMB MODES IN LASER ULTRASONICS: FATIGUE MONITORING AND MATERIAL CHARACTERIZATION

Defended on November 20th, 2018

Members of the committee:

D. HURLEY	Research Director, Idaho National Laboratory (USA)	<i>Reviewer</i>
E. MOULIN	Professeur, IEMN - Université de Valenciennes et du Hainaut Cambrésis	<i>Reviewer</i>
C. PRADA	Directrice de recherche CNRS, Institut Langevin - ESPCI, PSL	<i>Chair of committee</i>
T. DEHOUX	Chargé de recherche au CNRS, ILM - Université Lyon 1	<i>Examiner</i>
N. CHIGAREV	Ingénieur de recherche, LAUM - Le Mans University	<i>Examiner</i>
V. TOURNAT	Directeur de recherche CNRS, LAUM - Le Mans University	<i>Thesis supervisor</i>
V. GUSEV	Professeur, LAUM - Le Mans University	<i>Thesis co-supervisor</i>
S. RAETZ	Maître de Conférences, LAUM - Le Mans University	<i>Thesis co-adviser</i>

Académie de Nantes

Le Mans Université, Le Mans, France
École Doctorale Sciences pour l'Ingénieur

Thèse de Doctorat
Spécialité : Acoustique

Présentée par

Guqi YAN

pour obtenir le grade de Docteur d'Université

**MODES DE LAMB À VITESSE DE GROUPE
NULLE EN ULTRASONS LASER : SUIVI DE LA
FATIGUE ET CARACTÉRISATION DE MATÉRIAUX**

Soutenue prévue le 20 Novembre 2018
devant le jury composé de :

D. HURLEY	Directeur de recherche, Idaho National Laboratory (USA)	<i>Rapporteur</i>
E. MOULIN	Professeur, IEMN - Université de Valenciennes et du Hainaut Cambrésis	<i>Rapporteur</i>
C. PRADA	Directrice de recherche CNRS, Institut Langevin - ESPCI, PSL	<i>Présidente</i>
T. DEHOUX	Chargé de recherche au CNRS, ILM - Université Lyon 1	<i>Examineur</i>
N. CHIGAREV	Ingénieur de recherche, LAUM - Le Mans University	<i>Examineur</i>
V. TOURNAT	Directeur de recherche CNRS, LAUM - Le Mans University	<i>Directeur de thèse</i>
V. GUSEV	Professeur, LAUM - Le Mans University	<i>Co-directeur de thèse</i>
S. RAETZ	Maître de Conférences, LAUM - Le Mans University	<i>Co-encadrant de thèse</i>

To Xinxin

Acknowledgements

This doctoral dissertation is achieved in Laboratoire d'Acoustique de l'Université du Mans (LAUM) and financed by the Ministère de l'Éducation Nationale et de la Recherche Scientifique, in Le Mans, France, from October 2015 to October 2018. I would like to thank hereby both all the people who made helpful contribution to this PhD work and all the others who made this PhD life enjoyable during the past three years.

First of all, I would like to thank my thesis supervisors Dr. Vincent TOURNAT, Prof. Vitali E. GUSEV, Dr. Nikolay CHIGAREV and Dr. Samuel RAETZ for their proposition of this PhD subject to me and for giving me the opportunity to shape my own PhD research. I'm very grateful for their confidence in me, for their kind advises and encouragements, for their patient pedagogy and constant enthusiasm during the past three years along my PhD work. In a word, without their help, this work would not have been achieved. If possible, I hope that we can work together on other projects again in the future.

I would like to acknowledge Dr. David HURLEY and Prof. Emmanuel MOULIN for having agreed to be the reviewers of this thesis. I would also like to acknowledge Dr. Claire PRADA, Dr. Thomas DEHOUX for having agreed to be the members of my jury committee as well as for giving me very pertinent comments on my PhD work. I would like to thank Dr. Bertrand LIHOREAU and Prof. Pascal RUELLO for having taken part of my *Comité de suivi de thèse* and for the discussions with them. I would like to thank Dr. Claire PRADA again for her agreement to be the president of my PhD defense jury committee.

Considering that this PhD thesis is largely an experimental work, I would like to thank a second time Dr. Nikolay CHIGAREV for his help provided during the set-up of the experiments. I do not forget to thank James BLONDEAU for his help to my requests on softwares, especially his technical help on the experiments and the computer softwares to control the equipments in the second part of this work. I would like to thank also Hervé MÉZIERE and Jacky MAROUDAYE for their technical support of the experimental devices.

I would like to thank all the friendly collaborators and their contribution during my PhD work: thanks to Dr. Jean-Philippe GROBY, Dr. Alan GESLAIN and Dr. Aroune DUCLOS for their proposition of the *S*Lat*Cow* method; thanks to Dr. Hogeon SEO and Prof. Kyung-Young JHANG for providing their samples used in

the fifth chapter of my work; thanks to Dr. David HURLEY a second time for his fruitful discussions about metal fatigue as well as knowledge about material science. I would like also to thank Prof. Sohbi SAHRAOUI for discussions about *buckling*, and to thank Prof. Alain BULOUE for his preparation of sample pictures.

I do not forget to thank the colleagues with whom I worked in the preparation of teaching laboratory sessions and tutorials: Dr. Frédéric ABLITZER, Dr. Christophe AYRAULT, Dr. Wenping BI, Prof. Olivier RICHOUX, Dr. Rémi BUSSELEZ and Dr. Samuel RAETZ.

The scientific context of this work also played an important role. I want to thank the director and co-director of LAUM, Dr. Joël GILBERT and Prof. Laurent SIMON, respectively, and Dr. Pierrick LOTTON who succeed to Dr. GILBERT at the position of director of the laboratory. I want to thank them for their enthusiastic reception in the laboratory and their contribution to the life of Le Mans Université.

During the past three years, it was a real pleasure to work in a great environment and I would like to thank all the LAUM members for the convivial atmosphere of work with a special acknowledgement to the *Opto-acoustics & Laser ultrasonics* team and the colleagues in this group: Damien, Artem, Romain, Elton, and Haiyang for their good mood and discussions. I would also thank my (former and new) office mates: Alberto, Artem, Cédric and Sobin. I thank all the people who have walked alongside me through my thesis with interesting discussions during these three years, post-doc, PhD, master students as well as all the staff in LAUM ... and all the others I probably forgot to quote.

Thank again all my supervisors for all of their helps and guides in three years.

Before personal thanks, I want to sincerely thank once again Samuel RAETZ for all his helps in the past three years and his patience for his FIRST PhD student.

Finally, to my families, to my parents

Last but most important,

My wife,

Xinxin.

Die Liebe herrscht nicht, aber sie bildet; und das ist mehr!
Love doesn't rule, but it shapes; and that's more!
— Johann Wolfgang von Goethe

Written in front

The original idea of doing this doctoral project was very simple. After graduated from Le Mans University in 2013, me and Xinxin, we both decided to continue our Master study in France. Then, during the first three semesters, especially in the class of the following three courses: *Introduction à l'Acoustique Non-linéaire* given by V. Tournat, *Propagation dans les Solides* given by V. Gusev et *Optoacoustique & Applications au CND* given by V. Gusev and S. Raetz, the author was deeply attracted by all these professors. In the process of my internship (supervised by Prof. Sohbi Sahraoui) about acoustic foams, the author learned that there was going to exist a proposition of a PhD work which is supervised exactly by the above-mentioned three professors. At that moment, under the strongly initiated idea in the mind of the author, the decision to apply to this PhD position appears deep in the heart and the feeling of this mind became more and more clear, do not know whether it is right or wrong. With the endless confusion and doubts after graduation of Master degree, this is the beginning of the story ...

我成功的秘诀：知识、汗水、灵感、机遇。 — 袁隆平
The secret of my success: knowledge, sweat, inspiration, opportunity.
— Longping Yuan

Contents

Acknowledgements	i
Written in front	iii
List of Figures	xvi
List of Tables	xvii
General Introduction	1
I Knowledge background on laser ultrasonic nondestructive testing and on the use of the Lamb waves	5
1 Introduction	7
1.1 General background and motivation	8
1.2 Research objectives	10
1.3 Overview of the thesis	12
2 Fundamental background	15
2.1 Introduction	16
2.2 Laser ultrasonics and its applications	16
2.2.1 Brief history of optoacoustics	17
2.2.2 Laser generation and detection	18
2.2.3 Nondestructive testing and the use of laser ultrasonics for this purpose	19
2.3 Zero-Group-Velocity (ZGV) Lamb modes	21
2.3.1 A reminder on elastic theory for waveguides	21
2.3.2 Dispersion curves of Lamb waves and ZGV Lamb modes	27
2.3.3 Literature review about ZGV Lamb modes/resonances	37
2.4 Metal fatigue	49
2.4.1 About fatigue damage	49
2.4.2 Features of fatigue	51
2.4.3 Classification of fatigue	52
2.4.4 Factors affecting metal fatigue	52
2.5 Conclusion	54

II	Characterization of homogeneous isotropic solid thin plates by laser ultrasonic monitoring of zero-group-velocity Lamb modes: intact and damaged cases	55
3	Experimental study of ultrasonic attenuation in metallic thin plates with laser-based zero-group-velocity Lamb modes and its application for nondestructive evaluation	57
3.1	Introduction	58
3.2	ZGV Lamb modes in Aluminum and Copper	59
3.3	Experimental Setup and Measurements	61
3.4	Application of SLaTCoW: estimation of ultrasonic attenuations . . .	64
3.5	Conclusion	69
4	Laser ultrasonic evaluation of cumulative fatigue damage in thin films using zero-group-velocity Lamb modes	71
4.1	Introduction	72
4.2	Description of the fatigue test configuration	74
4.3	Experimental results and analysis	77
4.3.1	Experimental results	77
4.3.2	Analysis	81
4.3.3	Observation of a specimen during the fatigue test under microscope	82
4.4	Empirical model and numerical analyzes	83
4.4.1	Empirical model	83
4.4.2	Numerical model based on FEM	88
4.5	Conclusion	96
III	Extending application of laser-based zero-group-velocity Lamb modes: nonlinearity extraction and texture imaging	99
5	Evolution of a nonlinear parameter in heat-treated metallic plates evaluated with laser-based zero-group-velocity Lamb modes	101
5.1	Introduction	102
5.2	Experimental samples	103
5.3	Experimental setup and example of a detected signal	105
5.4	Pseudo-Phase-Plane (PPP) analysis	106
5.5	Signal processing model	109
5.6	Evolution of the nonlinear parameter with the thermal fatigue	111
5.7	Discussion on the influence on the ZGV resonance of the temperature rise caused by laser absorption	116
5.7.1	Temperature rise influence on ZGV resonance frequency in Aluminum alloys (AlAl-5083)	117
5.7.2	Influence of the temperature rise due to the pulsed laser . . .	118
5.8	Conclusions	119

6	Application of laser-based ZGV resonances to characterize the texture in rolled metallic plates	121
6.1	Introduction	122
6.2	Experimental setup	124
6.3	Effect of the anisotropy of the Copper sample on the ZGV frequency	125
6.4	Study of the texture of the anisotropic Copper plate by using laser-based ZGV resonance	126
6.4.1	Results of the 1D experimental scanning measurements	127
6.4.2	Results of the 2D experimental scanning measurements	127
6.5	Conclusions	129
	General conclusions	133
	Perspectives	135
	Bibliography	139
A	Synthesis of scientific publications, communications and activities during this thesis work	159
A.1	Articles	160
A.2	Conferences	160
A.3	Posters	160
A.4	Activities	161
A.5	Teaching	161
A.5.1	Tutorial and Practical courses	161
A.5.2	Supervisions	161
A.6	Formations	161
B	Additional details of the part of cumulative fatigue damage (CFD) in Chapter 4: published article	163
C	Examples of COMSOL code for explanation of the details of ZGV mode excitation & detection simulations by finite element method (FEM)	171
D	Matlab program for calculation of Lamb wave dispersion curves: frequency V.S. real wavenumber	175
E	Details about temperature rise influence caused on ZGV resonant frequency in Aluminium Alloys	181

List of Figures

1.1	The phononic spectrum with photos of corresponding phenomena over a wide frequency range.	9
2.1	Two categories of photo-thermal generation, (a) thermoelastic regime and (b) ablation regime.	19
2.2	Schematic illustration of plane wave interaction at solid surface and Lamb wave in homogeneous isotropic plate with thickness of $2h$ (above) showing deformations of the plate for a symmetrical mode (below left) and an anti-symmetrical mode (below right).	25
2.3	Normalized dispersion curves (product $f \cdot 2h$ vs. kh/π) of Lamb waves for both symmetric (red solid lines) and anti-symmetric (blue dashed lines) modes of an homogeneous isotropic Aluminum plate with thickness $2h$. The red arrow indicates the position of the first ZGV point.	28
2.4	Dispersion curves, (a) phase velocity (V_{ph}) and (b) group velocity (V_g) vs. $f \cdot 2h$, of symmetric (red solid lines) and anti-symmetric (blue dashed lines) Lamb modes for an homogeneous isotropic Aluminum plate.	29
2.5	(a) Three dimensional view (k_r, k_i, f) of complex dispersion curves of Lamb waves in a $75 \mu\text{m}$ -thick Aluminum plate for the first three symmetrical modes propagating in both $+x$ (solid lines) and $-x$ (dashed lines) direction, with subscript 'b' for backward mode; (b) Top view of the dispersion curves of Lamb modes in the complex wavenumber domain, i.e. k_r vs. k_i	32
2.5	(Continued) Dispersion curves of the first three symmetrical Lamb modes in a $75 \mu\text{m}$ -thick Aluminum plate: frequency as a function of (c) real part and (d) imaginary part of the wavenumber. Note that S_0/S_{-0} , S_1/S_{-1} and S_2/S_{-2} are in blue solid/dashed, yellow solid/-dashed and red solid/dashed lines, respectively. The two black solid circles plotted in each subfigure indicates the position of the ZGV point.	33

-
- 2.6 (a) Amplitude normalized to the maximal value of $u_x(0, z)$ of the axial u_x (solid line) and the normal (dashed line) displacement components of the S_1S_2 -ZGV mode at the position of excitation ($x = 0$) as a function of the thickness coordinate z ; (b) decrease of the lobe amplitude as a function of the lateral coordinate x , the line source is at $x = 0$ with length of $500 \mu\text{m}$; (c-1,2) axial and normal displacement components associated to the S_1S_2 -ZGV Lamb mode assuming infinite line source and without considering the material damping; (d-1,2) axial and normal displacement components associated to the S_1S_2 ZGV Lamb mode calculated by considering the spatial attenuation (decrease of amplitude along x -axis) due to the finite length of the line source (source length equal to $500 \mu\text{m}$) and still without considering the material damping. 36
- 2.7 Theoretical and experimental phase velocity dispersion curves in vicinity of the ZGV point for a tungsten plate with thickness of $50 \mu\text{m}$. . . 38
- 2.8 Spatial distribution of the displacement amplitude resulting from the interferences of the two Lamb modes S_1 and S_2 in a Duralumin plate with thickness of 0.49 mm 39
- 2.9 Dimensionless cutoff frequencies $2f_c h/V_T$ (horizontal lines) and $2f_c h/V_L$ (dash-dotted curves) and dimensionless minimum (ZGV) frequency $2f_0 h/V_T$ vs. Poisson's ratio in the range $0 \leq \nu \leq 0.5$. The ZGV branches (thick lines) appear about crossing points of cutoff frequency curves for modes belonging to the same family: symmetric or anti-symmetric. Vertical dashed lines correspond to the critical values $\nu = 0.1$ and $\nu = 1/3$ 40
- 2.10 Local vibration spectrum of a fused Silica plate of thickness $2h = 1.1 \text{ mm}$ on the left and of a Duralumin plate of thickness $2h = 1.0 \text{ mm}$ on the right. The vertical dotted lines in the central part correspond to the Poisson's ratio of fused Silica $\nu = 0.172$ and of Duralumin $\nu = 0.338$ 41
- 2.11 First order symmetric ZGV Lamb mode S_1S_2 . Variation of the resonance parameter β_1 vs. Poisson's ratio ν 42
- 2.12 Second order antisymmetric ZGV Lamb mode A_2A_3 . Variation of the resonance parameter β_2 vs. Poisson's ratio ν . Note that for $\nu > 0.31$, $\beta_2 = 1$ due to the disappearance of A_2A_3 ZGV mode (resonance is then the thickness resonance). 42
- 2.13 Variations of the resonance frequency ratio f_1/f_2 vs. Poisson's ratio ν . 43
- 2.14 (a) Waveform and spectrum of ultrasound transmitted through 5.46-mm Lucite. (b) Air-coupled C-scan image of Scotch-tape strips on Lucite, 218 kHz . (c) Air-coupled C-scan image of Teflon inserts buried within carbon fiber-epoxy, 186 kHz 43

2.15 (Color online) Results of the experimental investigations of the excitability of ZGV resonances with constant pulse energy: (a) Detected displacement signals for different excitation spot diameters. (b) Spectra for the presented excitation spot diameters in (a). (c) Variation of the spectra of the measured signals with increasing spot diameter. The vertical plane and the line within the plane mark the position of the S_1S_2 -ZGV resonance. (d) Variation of the amplitude of the S_1S_2 ZGV resonance normalized to constant energy density for each pulse diameter. The maximum at $D/h \approx 1.4$ is apparent.	44
2.16 In the case of a point laser source, (a) Signal generated by the pulsed laser on a thin silicon plate cut along the crystallographic plane (001) and detected at the same point by the optical probe and (b) expanded view of the S_1S_2 -ZGV resonances and thickness mode resonance. (c) In the case of a line laser source, the amplitude of the Fourier spectrum as a function of the frequency, from 7.7 to 8.1 MHz, and of the angle that the direction of the line source forms with the (100) direction. The thickness resonance frequency is constant while the ZGV resonance frequency oscillates with a 90° period.	46
2.17 (a) Experimental spectra for the three different bonding layers, compared with theoretical ZGV frequencies for (b) a single plate, (c) symmetrical modes, (d) anti-symmetrical modes.	47
2.18 Time domain B-scans of the composite plate when the scan line is: (a) line 1 across the impact location, (b) line 2 near the impact location, and (c) line 3 far from the impact location. The related frequency domain B-scans obtained with a Hann time window (respectively d, e and f). Dashed white lines: maximum dimension of the flaw observed optically.	48
2.19 Metal fatigue and caused accidents.	49
3.1 Real plane dispersion curves for (a) the Aluminum sample and (b) the Copper sample. The red arrows indicate the position of the S_1S_2 -ZGV mode in each case.	60
3.2 Experimental setup (a) and illustration of the two types of scanning: (b) the rotational mirror is fixed with $d = 20 \mu m$, and then translation plate is moved; (c) the translational plate is fixed, and the mirror rotates.	61
3.3 Example of measured signal [(a) in Al and (c) in Cu] and its Fourier transform [(b) in Al and (d) in Cu].	62
3.4 Experimental results on Aluminum (a) and Copper (d), their 2DFFT images (b) for Aluminum and (e) for Copper, and zoomed part around the S_1S_2 -ZGV mode for Aluminum (c) and for Copper (f).	63
3.5 Theoretical and experimental dispersion curves in (a-b) the real plane (k_r, f) and (c-d) the plane (k_i, f) for [(a) and (c)] a plate made of Aluminum and [(b) and (d)] a plate made of Copper.	66

3.6	Illustration of the minimization process: map in the plane (k_i, f) , for (a) Aluminum and (b) Copper, of the change in the position of the S_2 and S_1 theoretical branches with changing the ultrasonic attenuation α from 0 dB/cm/MHz (bright yellow) to 1 dB/cm/MHz (dark blue), the experimental results shown in Fig. 3.5(c)-(d) are also reported; curves showing the evolution of Δk_i vs. α for (c) Aluminum and (d) Copper, calculated with the S_2 mode (red circles), the S_1 mode (blue crosses), and both the S_2 and S_1 modes (black triangles).	67
4.1	Fatigue configuration : (a) Illustration of the plate specimen loaded (top) and unloaded (bottom); (b) side-view photo of the loaded specimen; (c) top-view photo of the unloaded specimen.	75
4.2	Buckling of a thin plate : (a) normal deflection of a plate with unloaded length of $2L = 25$ mm and shortening length of $2\Delta L = 5$ mm, (b) space distribution of the cross section stress σ_{xx} in (x, z) plane, and (c) surface stress distribution $\sigma_{xx}(x, h)$ (solid line) and specimen's tensile yield strength (dashed red line).	76
4.3	(a) Example of a received a received laser ultrasonic temporal signal on the intact specimen ($N = 0$) and (b) its fast Fourier transform (FFT) with a sharp peak corresponding to the S_1S_2 -ZGV resonance frequency	77
4.4	Several chosen experimental measurements : amplitude spectrum density as a function of frequency (f) and specimen position (x) for loading cycles (a) $N = 0$, (b) $N = 4000$, (c) $N = 6000$, (d) $N = 8000$, (e) $N = 9000$, and (f) $N = 11000$	79
4.4	(Color online) Continued.	80
4.5	(a) Experimental evolution of $\Delta f/f$ (with error bars) as a function of fatigue duration at the center ($x = 0.1$ mm) of specimen 1. (b) Comparison of the evolution of $\Delta f/f$ measured in specimens 1, 2, and 3 (failure at approximately 12500, 16000, and 14000 cycles) as a function of normalized fatigue lifetime.	80
4.6	Experimental measurements of the spatial distribution of the ZGV resonance frequency for different fatigue cycles ($N = 0, 1000, 2000, \dots 9000, 9500$) and their qualitative classification in three regions. . .	81
4.7	Top-view photos through optical microscope of the fatigue progression on a specimen at (a) 30000 cycles, (b) 32000 cycles, and (c) ~ 33000 cycles (specimen failure). (d) Side-view of the broken specimen after 33000 cycles under optical microscope showing symmetrical decrease of the thickness around the fracture.	82

4.8	Illustration of the change in the specimen profiles caused by the fatigue damage. The gray background represents the remaining section of the plate after N_f fatigue cycles and the different color shades stand for the evolutive profiles of the plate subjected to fatigue damage: from the intact situation (light yellow) to the failure (dark blue) as indicated by the color bar. Numerical values of the input parameters for the calculation are: $P_N = 50$, $\sigma = 1$ mm, $\Delta x = 0$ mm, $2L = 25$ mm, $\delta l = 0.1$ mm, $a_c = 0.98$, $a_b = a_t = 0.01$, and the ratio $N/N_f \in [0\%, 100\%]$	86
4.9	Comparison between theoretical model and experimental results: (a) distribution of theoretically calculated $\Delta f/f$ as a function of the number of loading cycles N and of the lateral position x ; (b) distribution of experimental $\Delta f/f$ as a function of the number of loading cycles N and of the lateral position x ; (c) comparison between experimental results and the theoretical fitting after 9500 fatigue cycles; (d) theoretical and experimental evolution of $\Delta f/f$ in the center of the fatigued region (at $x = \Delta x = 0.1$ mm) as a function of the number of the loading cycles N	87
4.10	Results of the numerical simulations for the intact specimen ($N = 0$): (a) first eleven temporal opto-acoustic signals (normal velocity of the front surface [$z = -h$] calculated by numerical simulations from the epicenter ($x = 0$ mm) to $x = 0.1$ mm with a step of $10 \mu\text{m}$ and (b) their Fourier spectrum; (c) zoom for $x \in [-0.20.2]$ mm of the spatial distribution of the normalized amplitude of the normal velocity in a $75 \mu\text{m}$ -thick Aluminum plate at 15 ns after the wave generation.	92
4.11	Numerical simulations of the normal velocity distribution at about 90 periods, i.e. $t \cong 90/f(N)$, for intact ($N = 0$) and damaged ($N = 4000, 9500$ and 10000) specimens, taking into account the reduction of thickness as illustrated in Fig. 4.8.	93
4.12	f-k diagram for the analyzes of the Lamb modes propagating in (a) an intact plate and (b-d) a damaged plate calculated from a set of 376 temporal signals with a spatial scanning step of $10 \mu\text{m}$ from $x = 0$ mm to $x = L_{\text{num}} = 3.75$ mm. Each temporal signal is calculated for a duration of $5 \mu\text{s}$ with a time step of 1 ns.	94
4.13	(a) Theoretical (solid line) and numerical evolution (solid circles) of the relative variation of the ZGV frequency at the center of the fatigued region as a function of the loading fatigue cycles N ; (b) Comparison of the experimental (triangles) and the numerical (solid circles) Q factors as a function pf N	96
5.1	Experimental specimens heat-treated for different durations numbered from 1 (0 min of heat-treatment) to 8 (1000 h of heat-treatment).	104
5.2	Schematic representation of the heat-treatment processes for Aluminum alloy blocks.	104

5.3	Dispersion curves of Lamb modes in the Aluminum alloy plate with thickness of 100 μm for both A (dashed blue lines) and S (solid red lines) modes. The red arrow denotes the position of the first ZGV mode.	105
5.4	Experimental setup.	106
5.5	One example of the temporal received signal on sample 1 before (a) and after (c) bandpass filtering, and its frequency spectrum before (b) and after (d) bandpass filtering. The sharp peak corresponds to the ZGV resonance peak.	107
5.6	(a) Phase Plane for the linear signal for different values of t_{ini} : (a-1) 0 μs , (a-2) 0.32 μs , (a-3) 0.64 μs , and (a-4) 0.96 μs ; (b) Pseudo-Phase Plane with $T = 12$ ns for the linear signal for different values of t_{ini} : (b-1) 0 μs , (b-2) 0.4 μs , (b-3) 0.8 μs , and (b-4) 1.2 μs ; (c) Phase Plane for the nonlinear signal for different values of t_{ini} : (c-1) 0 μs , (c-2) 0.32 μs , (c-3) 0.64 μs , and (c-4) 0.96 μs ; (d) Pseudo-Phase Plane with $T = 12$ ns for the nonlinear signal for different values of t_{ini} : (d-1) 0 μs , (d-2) 0.4 μs , (d-3) 0.8 μs , and (d-4) 1.2 μs ; (e) PPPs reconstructed using experimental result with $T = 12$ ns for different values of t_{ini} : (e-1) 0 μs , (e-2) 0.4 μs , (e-3) 0.8 μs , and (e-4) 1.2 μs	108
5.7	(Top) An example of the processing for a received signal using the <code>smooth</code> function: original data (black dotted line), smoothed signal (red dashed line), and filtered signal (blue solid line); (Bottom) Instantaneous SNR of the processed signal as a function of time. The red dashed horizontal line shows the threshold of 5 dB below which the signal is considered as noise.	112
5.8	Results in the eight samples of the signal filtering with the <code>smooth</code> function.	112
5.9	Representations of the cost function used in the minimization process as a function of the coefficients a_0 and b_1	114
5.10	Evolution of $\bar{\beta}'_1$ (blue dashed line with square symbols), of $\bar{\beta}'_2$ (red dash-dotted line with downward triangle symbols), and of the fractional change of b_1 (black solid line with disk symbols) according to the heat-treatment durations.	115
5.11	Laser-induced temperature rise and its influence on the shift of the ZGV frequency. (a) Temperature rise due to pulsed laser as a function of depth at different time; (b) ZGV resonance frequency variation as a function of time in the position of the exciting point.	118

6.1	(a) Top: Experimental setup. A pulsed Nd:YAG laser is used for ultrasonic generation and a photorefractive interferometer is used to detect out-of-plane surface motion. The inset in the bottom left shows the ultrasonic ring-down in the sample after laser excitation. Bottom: Details of microstructure evolution. A texture is imparted by rolling. A well defined cube texture is formed upon annealing. (b) Top left: generation and detection beams strike corner of sample. Top right: sample holder. Bottom pane: EBSD micrographs of ECAE and rolled samples.	123
6.2	Experimental setup.	125
6.3	(a) An example of the received opto-acoustic signal and (b) its frequency spectrum normalized in amplitude.	126
6.4	Distribution of the frequency in the frequency range of the ZGV resonance multiple peaks as a function of the scanning positions along (a) the x -axis and (b) the y -axis.	127
6.5	2D distribution of the frequency associated to the peak with the maximum amplitude within the ZGV resonance multiple peaks as a function of the position on the plate.	128
6.6	Comparison between (a) the photo under optical microscope and (b) the image obtained with the spatial distribution of f_{max} . The white square approximately corresponds to the measured area on the sample.	128
6.7	(a) 2D distribution example of the spectral density at $f = 7.0648$ MHz and (b) the frequency spectrum of one measured position (at $x = 0.5$ mm and $y = 2.5$ mm) showing at least three peaks of resonances.	129
6.8	2D distribution of the spectral density at (a) $f = 7.05$ MHz, (b) $f = 7.11$ MHz, (c) $f = 7.17$ MHz, (d) $f = 7.22$ MHz, (e) $f = 7.28$ MHz, (f) $f = 7.34$ MHz, (g) $f = 7.39$ MHz, (h) $f = 7.45$ MHz, and (i) $f = 7.51$ MHz.	130
P.1	Calculated variation of the ZGV resonant frequency V.S. variation of several considered elastic constants: (a) longitudinal and (b) shear acoustic velocity, (c) density, and (d) Poisson ratio.	137
C.1	Screen capture of FEM software COMSOL in case of intact sample with thickness of 75 micrometers, with illustration of the normal displacement distribution field around excitation point at time of 16 nanoseconds.	172
C.2	Screen capture of FEM software COMSOL in case of damaged sample (maximal decrease of thickness equals to 1% at $x = 0$ mm) with thickness of 75 micrometers, with illustration of the normal displacement distribution field around excitation point at time of 16 nanoseconds.	173
C.3	Screen capture of FEM software COMSOL in case of damaged sample (maximal decrease of thickness equals to 2% at $x = 0$ mm) with thickness of 75 micrometers, with illustration of the normal displacement distribution field around excitation point at time of 16 nanoseconds.	173

C.4	Screen capture of FEM software COMSOL in case of damaged sample (maximal decrease of thickness equals to 5% at $x = 0\text{mm}$) with thickness of 75 micrometers, with illustration of the normal displacement distribution field around excitation point at time of 16 nanoseconds. .	174
C.5	Screen capture of FEM software COMSOL in case of damaged sample (maximal decrease of thickness equals to 10% at $x = 0\text{mm}$) with thickness of 75 micrometers, with illustration of the normal displacement distribution field around excitation point at time of 16 nanoseconds. .	174
E.1	Dispersion relations of Aluminium Alloy 5083 with thickness $100\mu\text{m}$.	182
E.2	S_1 mode dispersion relation: calculation and 4th order polynomial fitting.	182
E.3	Considered thermal dependant material properties.	183
E.4	Considered thermal dependant material properties variations V.S. temperature rise.	183
E.5	S_1 mode dispersion curves for different temperature rise, above: complete dispersion curve for wavenumber until 120mm^{-1} ; below: zoomed part of subfigure at left (coloured hollow circles) and 4th order polynomial fitting (coloured solid lines).	184
E.6	Calculated ZGV frequency variation as a function of temperature rise ($\Delta f - \Delta T$) and the best fitting curve (4th order polynomial).	185

List of Tables

2.1	Relations between the different elastic constants of an isotropic solid material.	23
3.1	Elastic properties for Aluminum and Copper samples.	60
3.2	Estimated ultrasonic attenuations in Aluminum and Copper.	69
4.1	Mechanical, thermal and optical properties of Aluminum plate used in this work for both theoretical calculations and numerical simulations.	89
5.1	Longitudinal velocity V_L , shear velocity V_T , Young modulus E , Poisson's ratio ν of the used samples and nonlinear parameters measured by different approaches for different heat-treatment time (T_{heat}): PZT-PZT SAW contact method (β'_1), Laser-PZT SAW semi-contact method (β'_2) and Laser-Laser ZGV resonance contactless method (b_1).	116
5.2	Theoretical ZGV frequency variations and related temperature rise by considering thermal dependent E , G , h and Poisson ratio ν	117

General Introduction

Nowadays, developing noncontact and nondestructive technique to probe interface quality, adhesion, nonlinear phenomena, or local mechanical properties at the micrometric scale is of utmost importance in numerous applications, from advanced micro- and nano-technologies to fundamental research on material properties.

The plates are present in many industrial sectors, such as aeronautics, civil engineering, coatings, etc ... Different types of wave can spread there: besides the waves which propagate in the bulk of the material, there are modes guided by the walls of the structure, which acts as a waveguide.

In solid plate structure, ultrasonic guided waves can be easily excited and detected, since such a structure is one of the simplest acoustic waveguides in many practical issues. The main advantage of guided waves over bulk waves for layered structures is that these guided waves can propagate over large distance, and thus they enable long range inspection. It is important to note that guided waves are multi-mode, so a preferred mode can be selectively used, although it is sometimes more efficient to use multiple wave modes.

The most common methods of non-destructive testing are radiography, eddy currents, and ultrasound techniques. During the last decades, many ultrasonic methods of non-destructive testing have been developed, which will be of the main interest in this manuscript. Some methods are based on elastic volume waves, for example in pulse-echo techniques for which the measurement of times of flight makes possible to evaluate the velocity of the elastic waves or the thickness of the sample by simply considering a round trip of the wave. Similarly, to detect a crack or a delamination, it is common to generate bulk waves that will be reflected or diffracted due to the impedance discontinuity associated to the presence of the defect. The appearance of a characteristic reflected signal makes possible to conclude on the presence of the defect and under certain conditions to estimate its dimensions. In the control of thin films or localized defects in them, the waves used are rather elastic surface waves. These waves do not penetrate into the bulk of the material, but remain localized near the surface, allowing exploration of the specimen to a certain depth. To inspect cylindrical plates or shells, it is interesting to use guided waves such as Lamb waves.

Lamb waves allow to quickly explore large areas, to identify possible defects or to evaluate the mechanical characteristics or the thickness of the material. In this case, the estimated properties are not local; they are generally equal to the average value over the wave path. This effect is accentuated in the determination of the speeds: to reduce the error on the measurement of the time of flight between the emitter and the detector, it is necessary to increase the distance between them, but the measurement is in this case less and less local. For some values of the

frequency and of the wave number, there are some particular cases for which the group velocity ($V_g = \partial\omega/\partial k$) of a Lamb mode is zero while the phase velocity ($V_{ph} = \omega/k$) remains finite. This is why these modes are called “Zero-Group-Velocity” (ZGV) Lamb modes. These singular cases can give rise to narrow local resonances with very interesting properties: their frequency varies mainly according to the local thickness of the plate and its local mechanical properties, thus opening up interesting prospects in non-destructive testing. Since ZGV resonances are local resonances, the measurement of their frequency makes it possible to solve an inverse problem to get certain local physical parameters. Such resonances can be generated and detected using an appropriate device avoiding any mechanical contact with the tested sample: the LASER (for Light Amplification by Stimulated Emission of Radiation).

The generation and detection of ultrasounds by lasers is at the basis of the laser ultrasonic techniques, or opto-acoustic techniques, which present the advantage, among others, of allowing contactless analyzes of a sample. Such absence of contacts makes the laser ultrasonic techniques suitable for any pressure and temperature conditions and suitable for nondestructive testing from a distance. It avoids the use of contact transducers which are possible sources of nonlinearities. The opto-acoustic technique also provides a high spatial resolution because of the possibility to focus the beam down to micrometers. There are three main features of opto-acoustics compared to other acoustic techniques: (i) small size of acoustic sources and detectors (several micrometers); (ii) contactless operation achievable from a significant distance if necessary (generation and detection of sound in the sample can be carried out remotely); (iii) access to imaging of the samples with high sensitivity and high spatial resolution.

In recent years, zero-group-velocity (ZGV) Lamb modes have proven to be an efficient tool to probe locally and very accurately the thickness of a sample or the mechanical properties of either isotropic or anisotropic materials. This particular type of guided waves, corresponding to sharp local resonances of the inspected structure, results of the interference of two Lamb waves having opposite phase velocity and coexisting at a given couple of frequency and wavenumber. Laser ultrasonic technique has demonstrated its ability to efficiently generate and detect such local resonances at MHz frequencies. Indeed, the standard all-optical setup, consisting of a pulsed laser source to generate elastic waves and an interferometer to probe the associated normal displacement field, avoids any contact with the sample that could result in the broadening or suppression of the resonances. Despite their great ability and promises, the use of all-optically monitored ZGV modes at the micrometric scale in order to locally probe fatigued materials where the changes of the mechanical properties and/or of the thickness, or even where some nonlinear phenomena could develop, is still to be further explored and requires additional research.

The goals of the theoretical part of the PhD research are, first of all, to understand the ZGV Lamb modes through the dispersion relations and curves of the Lamb waves considering complex wavenumbers, and then, to propose an empirically-based model of the thickness variations in metal plates due to mechanical fatigue to be used in the developed numerical simulations of the Lamb modes in such fatigued plates. The goals of the experimental part of the PhD research are to achieve the generation and the detection of the ZGV Lamb modes at the micrometric scale by

lasers, to apply this technique for nondestructive characterization of thin films, and more specifically for the evaluation of multiple types of fatigue damage as well as of nonlinear responses due to related damage evolution.

Therefore, this PhD dissertation is written in three parts: the first part is the general introduction and fundamental background of this work; the second part presents the experimental study of ZGV Lamb modes in isotropic materials and its application for assessing the cumulative fatigue damage of metallic materials; the third part introduces the observation of nonlinear phenomena in thermal aged material by ZGV Lamb mode as well as its application for thermal fatigue evaluation, and the preliminary results of the characterization of texture in thermally-fatigued rolled high purity polycrystal copper using ZGV Lamb modes.

*If you want to find the secrets of the universe, think in terms of energy, frequency
and vibration. — Nikola Tesla*

Part I

Knowledge background on laser
ultrasonic nondestructive testing and
on the use of the Lamb waves

温故而知新，可以为师矣。 — 孔子 · 论语
Gaining new insights through reviewing. — Confucius · Analects.

Chapter 1

Introduction

Contents

1.1	General background and motivation	8
1.2	Research objectives	10
1.3	Overview of the thesis	12

Keywords: *LU, NDT&E, ZGV, Fatigue*

实践活动的目的无法完全独立于实践活动本身加以界定，在极端情况下，良好的
实践本身就是目的。 — 陈嘉映

*The aim of a practice can not be defined entirely independently of the practice itself,
and in extreme cases, good practice is itself a goal. — Jiaying Chen*

In this chapter, we introduce the conspectus of this doctoral dissertation. The purpose is to give the readers an overview as well as some general ideas of this work. We start by presenting the general background about laser ultrasonics (LU) and optoacoustics (OA) techniques and their applications in the field of nondestructive evaluation and testing (NDE and NDT) which lead to the motivation of this research study. The objectives of this research are then presented. Finally, this chapter ends with a more detailed presentation of the structure of this thesis. Some commonly used notions and abbreviations of terminologies are simultaneously given in the end of this chapter.

1.1 General background and motivation

The sound is one of the earliest physical phenomena studied by humanity and acoustics is an ancient and rapidly developing discipline. As a branch of physics, acoustics deals with the study of all mechanical waves in gases, liquids, and solids including topics such as vibration, sound, ultrasound, and infrasound. In addition to its sub-disciplines, acoustics is often combined with other disciplines to create interdisciplinary subjects. This relates to the interaction of sound with thermal waves in crystals (phonons), with light (photons), with electrons in metals and semiconductors (acousto-electric phenomena), with magnetic excitations in ferromagnetic crystals (magnons), etc. This also makes phonons become, besides electrons and photons, another everyday particles in our life [1]. Acoustic phenomena are widely found in our daily lives, in production practices, and in scientific research, and cover a very wide range of frequency domain as shown in Fig. 1.1: (above from left to right) sound barrier, music & instruments, medical ultrasound, and continuous wave laser¹; (below from left to right) volcanic eruption, Foehn wind, aircraft engine, and ultrasonic inspection for nondestructive testing and evaluation (NDT&E)².

The concerns of acoustics can be classified into two classes: (i) one deals with understanding how the physical properties of a medium (solid, liquid, or gas) influence the propagation of acoustic waves in this medium in order to use this knowledge for practical purposes, (ii) the other one is to obtain the relevant information about a medium under consideration by measuring the properties of acoustic waves propagating through this medium. With the exploration of these two points, the application of acoustics has penetrated into almost all important natural science and engineering technology fields [2]. One of its most important applications in industrial domain is the NDT&E³ by using ultrasound. The advantage of NDT&E method is that it enables the monitoring of the integrity of structures during their life, without having to destroy them.

The applications field of NDT&E is very broad [3]. The aeronautic industry needs to ensure the structural integrity of components used in the manufacturing

¹<https://pixabay.com/>; <http://art-wuchen.com/>; <https://www.romper.com/>; <http://russian-science.com/>, accessed 09/20/2018.

²<https://www.kannz.com/>; <https://skiclubgb.wordpress.com/>; <http://www.taopic.com/>; <https://www.oilandgasclub.com/>, accessed 09/20/2018.

³Numerous non-destructive evaluation (NDE) methods have emerged in recent years involving various domains of physics, such as X-rays, heat-transfer, or ultrasound.

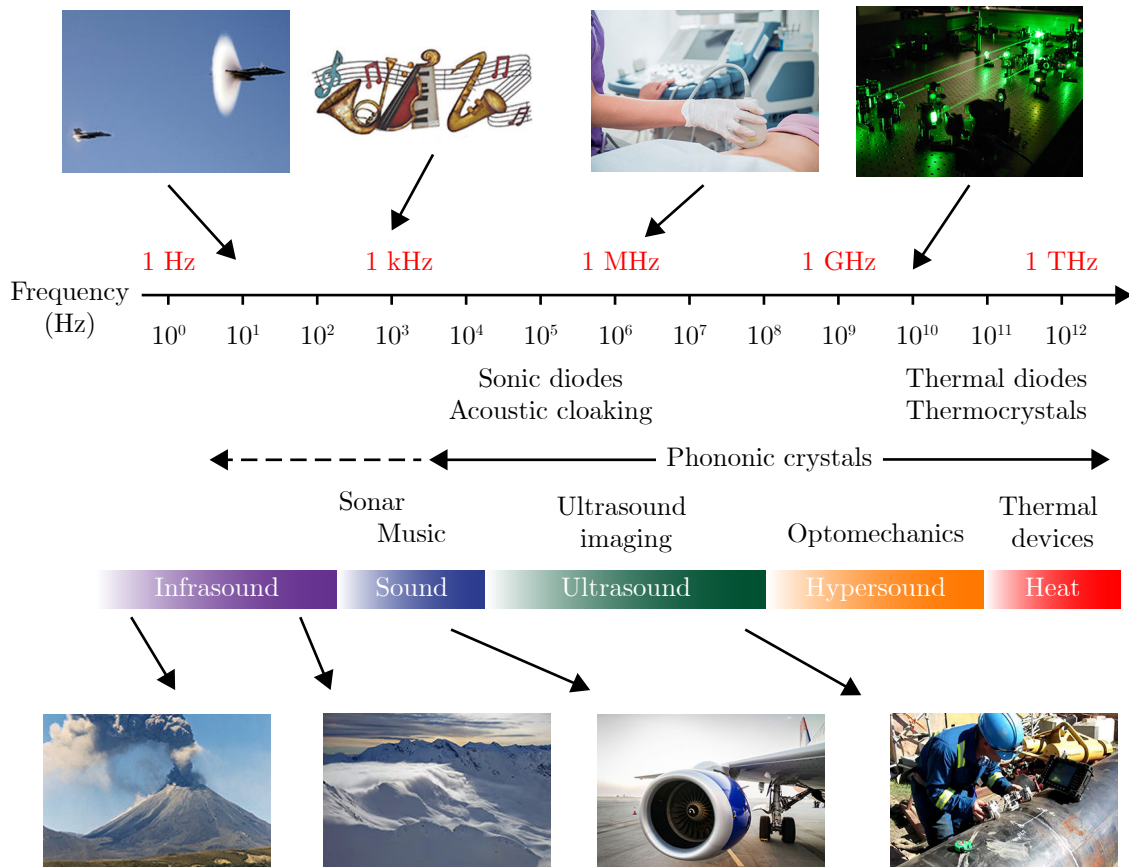


Figure 1.1: The phononic spectrum with photos of corresponding phenomena over a wide frequency range.

of aircraft. The need to detect defects or corrosion zones which may occur in toxic chemicals storage sites is also important. The preservation in ideal conditions of oil in cylindrical tanks, as well as of nuclear wastes in concrete containers or in granite caves, requires frequent inspection of the waterproofness of the structures containing these chemicals. The transport of material which may be dangerous, is also a topic for which the study of the integrity of pipes is required. For all these examples, defects such as cracks, voids, and delaminations can be prejudicial to safety.

Concerning ultrasound, the transmission and reflection testing methods have been studied extensively and have proved to be very effective. These conventional techniques enable the rendering of the shape and location of the defects, but are time-demanding, especially for large structures. Waves which are able to propagate over these large distances would facilitate faster inspection. Lamb waves⁴ are exactly such needed waves. They are guided by the geometry of the insonified structure in plates, cylindrical pipes or shells, propagate in structures for which the thickness is small compared to other dimensions and these waves can propagate in isotropic

⁴Lamb waves were discovered at the beginning of the XXth century by H. Lamb in 1917 [4] after the fundamental studies on bulk waves described by E.B. Christoffel in 1877 [5] and surface waves studied by Lord J.W.S. Rayleigh in 1888 [6]

or anisotropic media. As a new branch of acoustics and as an emerging multidisciplinary field, the optoacoustics is very suitable for the contactless generation and the detection of acoustic waves in plate structures or shells in order to achieve the goal of “nondestructive”. History of optoacoustics (OA) had started in the end of the XIXth century from the works of Alexander Graham Bell [7]. This domain of physics is studying the conversion by a medium of light energy (UV, visible and IR ranges) to mechanical energy (acoustic waves) [8].

More recently, laser-based zero-group-velocity Lamb modes (described in the next chapter) have proven to be very useful for the characterization of the mechanical properties of materials [9–18]. This combination of the laser ultrasonic technology and the specific Lamb modes brings both the advantages of the contactless laser-based technique and the efficiency of ZGV resonance which is very sensitive to material properties (thickness, elastic modulus, Poisson’s ratio ...). Therefore, researchers are truly encouraged to challenge this theme and motivated to try to extend this technique to different kinds of damage in the NDT&E fields. The original idea of this PhD work is mainly divided into the following steps: first step, to be familiar with LU technique (principles and experimental setup) and with ZGV Lamb modes (by calculating theoretically and by reconstructing experimentally Lamb wave dispersion curves); second step, to make use of the laser-based ZGV Lamb modes to assess mechanical fatigue damage; last step, to try to study the other types of damage (such as thermal fatigue damage, creeping, three or four points fatigue ...) as well as the nonlinear phenomena caused by damage influence, and the try to extend ZGV-Lamb-modes-based-NDE method to different fields.

Finally, for the details of the objectives/tasks of this project and the separation of each chapter of this work, readers are referred to Sec. 1.2 and Sec. 1.3, respectively.

1.2 Research objectives

As mentioned previously, the research goal of my PhD work presented in this dissertation is to develop, using laser generated and detected ZGV Lamb modes at micrometric scale, an accurate and efficient technique for nondestructive characterization of thin films. The scope of this work covers the theoretical background of elastic waves in solid, signal processing, finite element simulation, empirical modelling analysis, and experiments for nondestructive characterization. In summary, the objectives of this research are:

1. to be familiar with Lamb waves and ZGV Lamb modes through theoretical and experimental study of Lamb wave dispersion curves;
2. to achieve the laser-based generation and detection of ZGV Lamb modes in thin plates;
3. to develop a cumulative and local mechanical fatigue method for thin plates and to develop a ZGV-mode-based technique for evaluation of such damage in plates;

4. to develop a numerical simulation accompanied with empirically-based theoretical fatigue model using finite element method;
5. to apply the laser-based ZGV-Lamb-mode method to other kinds of fatigue damage: thermal fatigue damage as a first step in this case because it has a different nature from mechanical fatigue;
6. to extend application of ZGV Lamb modes to other research directions for the characterization/evaluation of materials, such as: anisotropy, texture, cracks, high-pressure, imaging ...

This research consists of several separate concepts or techniques: laser ultrasonics, ZGV Lamb modes, metal fatigue, finite element simulation. However, these concepts will all be used for the same purpose, namely non-destructive testing and evaluation of material damage. Therefore, the above several research objectives are classified into the following five tasks. Among them, each task may contain several objectives, and the same objective may exist in different tasks.

- **Task 1:** Study of the literature containing elastic theory for waveguides, optoacoustics, metal fatigue. A particular attention will be paid to the recent and current researches about ZGV Lamb modes, both theoretically and experimentally. The aim of this task was to have a basic process of sorting out existing knowledge.
- **Task 2:** To develop a Matlab code for the calculation of the Lamb wave dispersion curves of isotropic homogeneous solid plates with given thickness in both real and complex wavenumber domains. Then, to experimentally reconstruct the dispersion curves using spatio-temporal measurements, first in the frequency - real wavenumber domain using spatio-temporal Fourier transform and then in the frequency - complex wavenumber domain using spatial Laplace transform. The aim here was to be familiar with ZGV Lamb modes through Lamb dispersion curves. Another goal of this task was to estimate the ultrasonic attenuation from the complex dispersion curves thanks to the separation, caused by material dissipation, of the two branches in the vicinity of the ZGV mode.
- **Task 3:** Develop a local fatigue technique for thin plates at micro-metric scale and design a system of experiment for nondestructive characterization of the cumulative fatigue damage using laser ultrasonic monitoring of ZGV Lamb modes. The aim was to investigate the influence of mechanical fatigue on the variation of ZGV resonance frequency and the possibility of the use of ZGV Lamb mode for fatigue lifetime prediction.
- **Task 4:** Establish an empirically-based theoretical model using the variation of chosen material parameters for each stage of fatigue according to experimental variation of the ZGV resonance frequency. Develop a numerical modelling (finite element method) for the simulation of the cumulative fatigue progress using numerical parameters extracted from experiments. This task is closely

connected to the previous one, the completion of this task depended on the experimental progress of the previous task.

- **Task 5:** Realize the experiments for generation and detection of ZGV Lamb mode in nonlinear solid materials. Extract useful information about nonlinearity through ZGV resonance signals and discuss the influence of the temperature rise caused by pump and probe lasers. Try to analyze and understand the causes of nonlinearity. Apply the observed phenomenon for nondestructive evaluation of thermal aging.
- **Task 6:** Extend the use of the proposed method to the characterization of textured materials showing anisotropic elastic properties.

1.3 Overview of the thesis

This doctoral dissertation is divided into six chapters: the first chapter is the global background of this work; the second chapter is the fundamental background and the scientific introduction of the work; chapter 3 to chapter 5 are the main part of this PhD work, corresponding to the study of the complex dispersion curves of Lamb modes, to assess the cumulative and mechanical fatigue in metallic plates and the thermal damage in Aluminum alloys (the common feature of all these three chapter is the use of ZGV Lamb modes, particularly the first symmetric ZGV Lamb mode (S_1S_2)); chapter 6 is the extension of the previous work through the international collaboration with a visiting scientific researcher. At the end of each chapter, there will be an instant summary of the current chapter, and after all these six chapters, the entire PhD work is concluded in the part named general conclusion. The last chapter before the appendix deals with the perspectives of my work: some ongoing researches and future goals with practical details are mentioned as a part of continuing work and recommendations for the later PhD students, Post-Doctoral fellows, or researchers who will be willing to pursue this work in the future.

In the chapter 1, i.e. the current chapter, we introduce the general background and an overview of the presented thesis. The purpose is to give a concise scope of this study with overall ideas and rationales.

Chapter 2 introduces the fundamental background of the necessary knowledges in this work. We start with a basic background upon the laser ultrasonic technique and its fields of applications. A reminder on the elastic guided waves in solids is then proposed, after which the Rayleigh-Lamb equations are deduced and the dispersion curves of the Lamb modes are plotted and analyzed. A literature review of the ZGV Lamb modes is also presented hereat. Finally, a brief introduction to fatigue damage in metals is given.

Chapter 3 presents the experimental study of the complex dispersion relations of Lamb modes, especially around the ZGV point for extracting the information of the ultrasonic attenuation. The theoretical dispersion curves used for the inverse estimation of the ultrasonic attenuation from experimental results are already introduced in chapter 2. This chapter includes a little part of Task 1 and the whole Task 2.

The fourth chapter contains the main part of this doctoral work, i.e. the study of the cumulative fatigue damage by means of laser-based ZGV Lamb modes: fatigue test configuration, multi-dimensional measurements, analysis of the results, establishment of the empirical theory, numerical simulation based on FEM are all covered in this chapter. In the chapter 4, both Task 3 and Task 4 are carried out. The experimental results of this chapter will also become one of the focuses for publication of scientific papers.

The Task 5, is presented in chapter 5. In this chapter, we focus on the analysis of the ZGV mode in the case of thermal fatigue damage in Aluminum alloys. With a dedicated signal processing method based on an assumed signal model, information of hysteretic nonlinearity is extracted from ZGV resonance oscillations according to the relation between resonance frequency shift and amplitude measured under different powers of the excitation laser. Experimental results obtained by our non-contact method are compared with results measured by other contact or semi-contact methods.

In chapter 6, we present preliminary results of the imaging of the texture of a high purity copper sample corresponding to the Task 6.

Finally, the conclusions and perspectives are drawn and discussed. The details of the cumulative fatigue until the sample failure and of the numerical simulations are placed in the appendix.

Chapter 2

Fundamental background

Contents

2.1	Introduction	16
2.2	Laser ultrasonics and its applications	16
2.2.1	Brief history of optoacoustics	17
2.2.2	Laser generation and detection	18
2.2.3	Nondestructive testing and the use of laser ultrasonics for this purpose	19
2.3	Zero-Group-Velocity (ZGV) Lamb modes	21
2.3.1	A reminder on elastic theory for waveguides	21
2.3.2	Dispersion curves of Lamb waves and ZGV Lamb modes	27
2.3.3	Literature review about ZGV Lamb modes/resonances	37
2.4	Metal fatigue	49
2.4.1	About fatigue damage	49
2.4.2	Features of fatigue	51
2.4.3	Classification of fatigue	52
2.4.4	Factors affecting metal fatigue	52
2.5	Conclusion	54

Keywords: *Dispersion relations, ZGV Lamb modes, LU, NDT/E, Fatigue, NL*

Was vernünftig ist, das ist Wirklich; und was wirklich ist, das ist vernünftig.

What is reasonable is real; that which is real is reasonable.

— Georg Wilhelm Friedrich Hegel.

2.1 Introduction

As pointed in the chapter of **General Introduction**, the three main topics of this PhD work are: (i) laser ultrasonics, as the experimental technology and the observation tool; (ii) ZGV Lamb modes, as the studied phenomenon; and (iii) metal fatigue, as the assessed physical problem and the field of exploration. Therefore, the following part of this chapter is separated into three sections corresponding to these three topics:

1. In the second section, we talk about the laser-based ultrasonic technique which has been proven to be very useful for experimental study of the ZGV resonance in thin plates. Some basic knowledge of photoacoustic field for both optoacoustic generation of acoustic waves and the contactless detection using laser is introduced here in this section. The main domain of applications of laser-based techniques, i.e. the nondestructive testing or evaluation, is also presented in this section. Other application fields (far from the current PhD topic), like the biomedical applications and the characterization of material under extreme conditions (fundamental reaserches) are also briefly mentioned in the end of this section.
2. After the brief recall of laser ultrasonics, we focus on the introduction of the Lamb waves as well as the key point of this PhD thesis, i.e. ZGV Lamb modes, in the third section. Considering that the Lamb waves are dispersive and multimode by nature, we start by introducing the dispersion curves of Lamb waves. Then, the ZGV Lamb modes are also introduced thanks to the dispersion curves (in both real and complex wavenumbers spaces), some examples of current researches (a brief literature review) on ZGV resonances by means of laser ultrasonics method or other methods are also presented in the end of this section.
3. In the last section of this chapter before conclusion, we talk about the fatigue in metals with some examples of fatigue-damage-induced problem and some recent study of fatigue damage using ultrasound methods.

Reviewing the existing knowledge allows us to systematically summarize the past, to recognize the current development status of the research field and to find the potential research directions hereafter and the point of innovation that can be expanded in the future.

2.2 Laser ultrasonics and its applications

In order to excite and detect ZGV resonances, a non-contact technique with no required physical contact is preferred, for both generation and detection, so that it ensures not to modify the boundary conditions. There are several contactless techniques such as air-coupled ultrasonic transducer [19, 20], or electromagnetic acoustic transducers (EMATs) [21–23] which are quite useful for inspection of large area of metallic plates or rails tracks. In this PhD work, we use a photoacoustic technique

which has demonstrated its ability for generating and probing ZGV resonances in thin plates [9–12, 15, 17, 18, 24–26]. Hence, we introduce briefly in this section the history, basic idea, advantages and applications of laser ultrasonics. Please note that the majority part of this section is based on the summary of the introduction part of previous PhD works [8, 27–29] and the summary of the lessons *Optoacoustique & Applications au CND* taught by Prof. Vitaliy GUSEV and Assoc. Prof. Samuel RAETZ, who are the co-director and the co-advisor of this PhD work in Le Mans, respectively. In addition, the classic books of D. Royer [30–32] are also the important references. Note that the author was taught by Assoc. Prof. RAETZ in 2015 and the current version of the lecture notes ‘*Cours Optoacoustique - Master 2 recherche*’ should have been updated. Hence, for the people who are interested in some details of this theme, the author invites these readers to consult the personal website of Assoc. Prof. RAETZ¹ for an updated version of this lecture as well as for further understanding.

2.2.1 Brief history of optoacoustics

Generally, when we talk about laser ultrasonics (LU), it involves two processes: the generation of the ultrasonic wave by a laser and the detection of the ultrasonic wave by a laser. The first one is made possible thanks to the optoacoustic effect and the last one is by the acousto-optic effect. Both optoacoustic and acousto-optic effects refer to the interactions or energy transfers between electromagnetic waves and acoustical waves and the difference between the two lies on the type of such interaction. An optoacoustic effect involves the influence of an electromagnetic wave on an acoustic wave, and conversely, an acousto-optic phenomenon denotes the influence of the propagation of an acoustic wave on an optical wave. The first observation of such a conversion between these two different type of waves was obtained in the experiment of A.G. Bell in 1880 [7]. In his experiment, a closed gas volume was excited by a modulated light beam and then an acoustic wave could be heard. This discovery was shortly confirmed by Tyndall [33] and Röntgen [34]. This observed phenomenon was also proposed by Bell to be used in the form of the photophone (a means of wireless communication and similar to the telephone). However, due to the lack of sufficiently powerful light sources and reliable tools of measuring the acoustic signals, the applications of optoacoustic effect remained limited. With the inventions of maser in the late 50’s and then of laser in early 60’s of the last century, particularly the later, people once again raised a strong interest to optoacoustic effects. The appearance of laser provided a ideal light source for laboratory experiments. Almost at the same time, Askaryan and Prokhorov in the USSR and White in the USA performed and published their works in liquid medium and solid material using laser light as the source of the generation of elastic waves [35–37]. With the development of photoacoustics and the widespread use of laser instruments, a large number of classic books on laser, photoacoustics, laser ultrasound, etc. were written. Two seminal books are ‘*Laser Ultrasonics: Techniques and Applications*’ published in 1990 [38] and ‘*Laser Optoacoustics*’ published² in 1993 [39]. The first

¹http://perso.univ-lemans.fr/~sraetz/M2_optoac/, accessed 09/20/2018.

²The first version of this book was in Russian and published in 1991

book by C.B. Scruby and L. Drain provides a full description of the state of the art in several research fields involving laser ultrasonics as well as the possible applications of the optoacoustic techniques, and the other book by V.E. Gusev and A.A. Karabutov presents, amongst others, the basic theoretical/mathematical approaches for the analysis of optoacoustic phenomena and describes the general approach for the analysis of pulse-mode optical excitation of sound. After that, in the early 21st century, as laser ultrasound is widely used in the field of non-destructive testing, related books have also been published, such as ‘*Ultrasonic Nondestructive Evaluation: Engineering and Biological Material Characterization*’ [40].

Next, before we introduce the various advanced modern applications of laser ultrasound, let’s briefly review the knowledge about the laser generation and the laser detection of ultrasonic waves.

2.2.2 Laser generation and detection

As presented in Sec. 2.2.1, laser ultrasonics can be schematically separated into two families of processes: the optoacoustics concerning the effects, the conversion, the influence of an electromagnetic field on an acoustic field (leading for instance to the laser generation process) and the acousto-optics concerning the study of the acoustic phenomena influencing an electromagnetic field (e.g. involved in the laser detection process).

We firstly introduce the non-contact optical generation of an elastic wave in a solid. Ultrasonic laser generation depends on the parameters of the laser beam (wavelength, incident power, size, shape, duration) and the optical, thermal, elastic, and electronic properties of the material. In the nanosecond regime, the most used sources are the triggered (Q-switched, sometimes known as giant pulse formation) Nd:YAG pulsed laser consisting of a neodymium doped $Y_3Al_5O_{12}$ (Aluminum and Yttrium garnet) crystal and the CO_2 laser [30]. At the present time, the mechanical diagnosis of nanometric or submicron systems imposes laser sources of ultra-short duration (sub-nanosecond, picosecond or even femtosecond). Depending on the absorbed power density, the impact of a light pulse on the free surface of an opaque solid generates elastic waves according to different mechanisms. In the nanosecond regime, the most encountered mechanisms can be sorted out into two categories: the thermoelastic regime and the ablation regime. These two regimes of photo-thermal generation of acoustic waves in solid are illustrated in Fig. 2.1: in the thermoelastic regime [Fig. 2.1(a)], local expansion through heating leads to forces mostly parallel to the free surface; in the so-called *ablation* regime [Fig. 2.1(b)], the incident laser pulse vaporizes a small quantity of matter and then the generated momentum transfer (due to material ejection) produces forces more or less normal to the free surface.

The threshold between the two different regimes is normally defined by the absorbed light power density, for example, for Aluminum, this value is of the order of 15 MW/cm^2 [30, 32]. It means that when the absorbed light power density is less than 15 MW/cm^2 , the regime is thermoelastic and when the absorbed light power density is greater than 15 MW/cm^2 , the generation regime involves ablation. The expression of the ablation threshold as a function of the parameters of the material

and the laser beam was determined by Ready [41]. For the thermoelastic regime, the temperature rise due to the absorption of the laser radiation is sufficiently low for the state of the solid surface not to be modified. This thermoelastic source only creates longitudinal waves if it is located inside the solid. The presence of the surface is at the origin of a conversion into transverse waves: the combination of longitudinal and transverse displacements generates a Rayleigh wave that is guided by the free surface of a semi-infinite solid or Lamb waves that are guided by the free surfaces of a solid plate [32]. For the ablation regime, the vaporization of material caused by the incident light occurs (amplitude of the ultrasound can be proportional to the square of the light intensity [42]), which makes this regime unsuitable for NDT&E purposes, and therefore will be disregarded in this work.

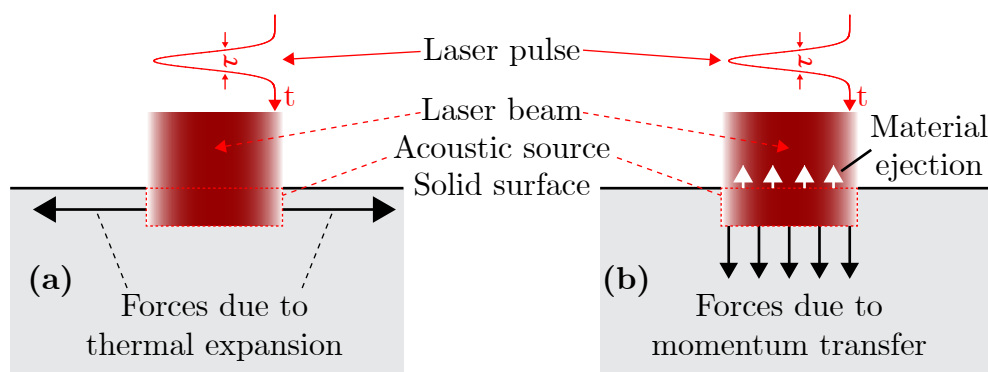


Figure 2.1: Two categories of photo-thermal generation, (a) thermoelastic regime and (b) ablation regime [32].

We now introduce the basic idea of contactless detection based on the acousto-optic phenomenon, i.e. the laser detection of acoustic (ultrasound) waves. Compared with *conventional* piezoelectric contact sensor measuring devices, the optical methods have the advantage of non-contact measurement with a wide bandwidth, although with less sensitivity. There are two categories of optical technique: non-interferometric probes that exploit the intensity modulation, the deflection or diffraction of the light beam, and interferometric probes that exploit the modulation of the phase or frequency of the light beam reflected on the vibrating surface [30]. The principle of interferometric methods is as follows: a continuous or pulsed laser emits a beam which is reflected (or scattered) by the surface to be probed and then combined with a reference beam. The optical phase shift is then converted into an amplitude modulation which is detectable by a photodiode.

For more details of the laser generation and detection as well as the opto-acoustic experimental setups, readers are suggested to see the Ref. [32]. In the next section, we introduce several applications of laser ultrasonics to non destructive testing.

2.2.3 Nondestructive testing and the use of laser ultrasonics for this purpose

In this paragraph, we briefly review one of the most important applications of optoacoustics: nondestructive testing and evaluation.

"Nondestructive testing (NDT) is a wide group of analysis techniques used in science and technology industry to evaluate the properties of a material, component or system without causing damage³. Because NDT does not permanently alter the specimen being inspected, it is a highly valuable technique that can save both money and time in product evaluation, troubleshooting, and research."

One of the six most widespread methods⁴ for nondestructive evaluation is the ultrasonic method. The ultrasonic diagnostics in most cases is based on investigation of the frequency dependence of the attenuation, scattering or velocity of ultrasonic waves upon their propagation through a specimen [43]. The frequency dependence of the attenuation coefficient of the ultrasound in a sufficiently wide spectral range can be used for estimating the characteristic sizes of inhomogeneities of a composite structure for instance [44]. The detection of scattered ultrasound is the most developed method of ultrasonic imaging. To avoid any destructive issues of the sample and any contact with the sample at the same time during its evaluation, the use of laser thermoelastic generation of sound is rather promising [38]. Upon thermoelastic generation of sound in a medium with known thermo-physical and acoustic parameters and at given parameters of the absorbed laser radiation (energy and pulse duration), it is possible to obtain high-power wide-band acoustic pulses with known characteristics—the amplitude and duration (or frequency spectrum)—and to use them for the acoustic spectroscopy and imaging of materials. Laser pulses of different durations can be used in laser opto-acoustic setups for non-destructive testing depending on the characteristic dimensions of the tested sample and on the targeted applications.

The solid plate-structure materials (metal sheets, composite plates, polymer films, glasses, etc ...) are quite widely used in many industrial sectors, such as aeronautics, civil engineering, coatings, etc ... The problem of nondestructive testing of such structure materials is rather urgent, since defects in structures arising during manufacture and operation of articles can reduce considerably the strength of materials. Therefore, the elaboration of methods for nondestructive evaluation and defectoscopy of solid plates which would make possible to carry out investigations either at a stage of manufacturing or during operation of the structures is of great importance. In the recent years, several laser-based NDT&E methods have been investigated for the study of the typical damages and defects of the structure of solid plates, such as: measurements of material nonlinearity in fatigued Aluminum alloys using nonlinear Lamb waves [45]; investigation of corrosion and adhesive disbond in plates via ZGV resonances [15]; evaluation of closed crack through non-contact ultrasonic propagation imaging [46]; all-optical monitoring of the nonlinear motion of a surface-breaking crack on the surface of glass [47]; detection of fatigue cracks [48] using laser nonlinear wave modulation spectroscopy (LNWMS); non-contact surface acoustic waves (SAWs) for assessing thermal aging of Aluminum Alloy [49]; flaw

³The terms nondestructive examination (NDE), nondestructive inspection (NDI), and nondestructive evaluation (NDE) are also commonly used to describe this technology. For details, see: https://en.wikipedia.org/wiki/Nondestructive_testing, accessed 09/20/2018.

⁴The six most frequently used NDT methods are eddy-current, magnetic-particle, liquid penetrant, radiographic, ultrasonic, and visual testing. See details on the webpage *Introduction to Non-destructive Testing*: <https://asnt.org/MinorSiteSections/AboutASNT/Intro-to-NDT.aspx>, accessed 09/20/2018.

detection in composites using laser generated ZGV resonance [50]; etc ...

Before finishing this subsection, we mentioned here that the application fields (out of the scope of this PhD work, but maybe interesting for readers) of optoacoustic techniques contains also the bio-medical fields (like photoacoustic microscopy for dynamic 3D imaging of microcirculation in vivo [51]; functional photoacoustic imaging of the ocular microvasculature in living animals [52]; small size photoacoustic mini-probe for inserting into a standard video endoscope instrument channel [53]; etc ...) and fundamental research, such as characterization of material parameters in extreme conditions (like the study of the relaxation of coherent acoustic phonon modes in ultrathin free-standing silicon membranes [54]; complete mechanical measurements of submicron films using picosecond ultrasonic technique [55]; determination of material properties under extreme pressure [8, 56–61] using diamond anvil cell [62, 63]; etc ...).

2.3 Zero-Group-Velocity (ZGV) Lamb modes

Now that a short overview on the experimental technique to be used in this work has been presented, it is proposed in this section to deal with the fundamental introduction of Lamb waves, as well as with the ZGV Lamb modes which is the key topic of this PhD work.

2.3.1 A reminder on elastic theory for waveguides

We start with the governing equations for a linear homogeneous orthotropic⁵ elastic solid, i.e. the three fundamental relations of linear elasticity where bold symbols (here and after) denote appropriately either a vector or a tensor:

1. the equations of motion in three dimensions (also called Cauchy momentum equation or Cauchy's first law of movement)

$$\nabla \cdot \boldsymbol{\sigma} + \rho \mathbf{f} = \rho \ddot{\mathbf{u}}, \quad (2.1)$$

2. the Cauchy's relations (relations between strain and displacement)

$$\boldsymbol{\varepsilon} = \frac{1}{2}(\nabla \mathbf{u} + \nabla^T \mathbf{u}), \quad (2.2)$$

3. and the stress-strain relations (constitutive equations, Hooke's law)

$$\boldsymbol{\sigma} = \mathbf{C} : \boldsymbol{\varepsilon}, \quad (2.3)$$

relations that could be rewritten by using the Einstein notation as follows:

$$\sigma_{ij,j} + \rho f_i = \rho \ddot{u}_i, \quad (2.4)$$

$$\varepsilon_{ij} = \frac{1}{2}(u_{i,j} + u_{j,i}), \quad (2.5)$$

$$\sigma_{ij} = C_{ijkl} \varepsilon_{kl}. \quad (2.6)$$

⁵The properties are said to be orthotropic if they relate to a crystal of the orthorhombic system characterized by the presence of three orthogonal direct or inverse binary axes (see Refs. [31, 64] or Wikipedia).

In the previous equations (2.1)-(2.6), ∇ is the differential operator that reads $\nabla = \mathbf{e}_1 \partial \cdot / \partial x_1 + \mathbf{e}_2 \partial \cdot / \partial x_2 + \mathbf{e}_3 \partial \cdot / \partial x_3$ in Cartesian coordinates, σ_{ij} denotes the components of the stress tensor $\boldsymbol{\sigma}$, ε_{ij} denotes the components of the strain tensor $\boldsymbol{\varepsilon}$, f_i is the components of the volume forces \mathbf{f} , the C_{ijkl} coefficients are the components of the 4th order stiffness (or elasticity) tensor \mathbf{C} , ρ is the density of the material, u_i stands for the components of the displacement field \mathbf{u} , the summation convention is taken for $i, j, k, l \in \{1, 2, 3\}$, and the comma stands for a comma derivative, which is just a convenient notation for a partial derivative with respect to one of the coordinates. For the orthotropic solid material, the strain and the stress tensors are respectively written

$$\boldsymbol{\varepsilon} = [\varepsilon_{11}, \varepsilon_{22}, \varepsilon_{33}, \varepsilon_{23}, \varepsilon_{31}, \varepsilon_{12}], \quad (2.7)$$

$$\boldsymbol{\sigma} = [\sigma_{11}, \sigma_{22}, \sigma_{33}, \sigma_{23}, \sigma_{31}, \sigma_{12}], \quad (2.8)$$

and the Hooke's law is therefore written

$$\sigma_\alpha = C_{\alpha\beta} \varepsilon_\beta, \text{ with } \alpha, \beta = 1, 2, \dots, 6, \quad (2.9)$$

using the Voigt notation where the following rule of change of the indices is applied [31, 64]:

$$\begin{aligned} (11) &\leftrightarrow (1), (22) \leftrightarrow (2), (33) \leftrightarrow (3), \\ (23) &= (32) \leftrightarrow (4), (13) = (31) \leftrightarrow (5), (12) = (21) \leftrightarrow (6). \end{aligned} \quad (2.10)$$

The stiffness matrix (or elasticity matrix) \mathbf{C} for the orthotropic material is written:

$$\mathbf{C} = \begin{bmatrix} C_{11} & C_{12} & C_{13} & 0 & 0 & 0 \\ C_{12} & C_{22} & C_{23} & 0 & 0 & 0 \\ C_{13} & C_{23} & C_{33} & 0 & 0 & 0 \\ 0 & 0 & 0 & C_{44} & 0 & 0 \\ 0 & 0 & 0 & 0 & C_{55} & 0 \\ 0 & 0 & 0 & 0 & 0 & C_{66} \end{bmatrix}. \quad (2.11)$$

In the case of isotropic⁶ material, the stiffness matrix \mathbf{C} is simplified as follows:

$$\mathbf{C} = \begin{bmatrix} C_{11} & C_{12} & C_{12} & 0 & 0 & 0 \\ C_{12} & C_{11} & C_{12} & 0 & 0 & 0 \\ C_{12} & C_{12} & C_{11} & 0 & 0 & 0 \\ 0 & 0 & 0 & (C_{11} - C_{12})/2 & 0 & 0 \\ 0 & 0 & 0 & 0 & (C_{11} - C_{12})/2 & 0 \\ 0 & 0 & 0 & 0 & 0 & (C_{11} - C_{12})/2 \end{bmatrix}. \quad (2.12)$$

In the case of an isotropic material, the number of independent components is reduced to two. Thus, the elastic behavior of the solid can be described either by the elastic constants C_{11} and C_{12} , or by the Lamé coefficients λ and μ (μ is also called shear modulus and sometimes denoted by the letter G) or the pair (E, ν) where ν is

⁶An isotropic solid is a solid material in which physical properties do not depend on its orientation (see Refs. [31, 64] or Wikipedia).

the Poisson's ratio and E the Young's modulus (often referred to modulus of tensile elasticity or simply as the elastic modulus). It is recalled that the Poisson's ratio characterizes the contraction of the material perpendicular to the direction of the applied force. The Young's modulus, index of rigidity of the material, characterizes the ratio of the applied tensile or compressive stress to the resulting deformation. The elastic constants described above are linked by simple relationships summarized in the Tab. 2.1. In this simple case of isotropy, Hooke's law is reduced to:

$$\sigma_{ij} = \lambda \varepsilon_{kk} \delta_{ij} + 2\mu \varepsilon_{ij}, \quad (2.13)$$

where ε_{kk} is the trace of the strain tensor and δ_{ij} is the Kronecker delta (equals to 1 if $i = j$, and 0 otherwise).

Table 2.1: Relations between the different elastic constants of an isotropic solid material.

	E	ν	λ	μ
(E, ν)	E	ν	$\frac{E\nu}{(1+\nu)(1-2\nu)}$	$\frac{E}{2(1+\nu)}$
(λ, μ)	$\frac{\mu(3\lambda+2\mu)}{\lambda+\mu}$	$\frac{\lambda}{2(\lambda+\mu)}$	λ	μ
(C_{11}, C_{12})	$\frac{(C_{11}-C_{12})(C_{11}+2C_{12})}{C_{11}+C_{12}}$	$\frac{C_{12}}{C_{11}+C_{12}}$	C_{12}	$\frac{C_{11}-C_{12}}{2}$

Introducing the strain-displacement relations [Eq. (2.5)] into the stress-strain relations [Eq. (2.6)], the stress tensor components can be expressed in terms of displacement vector components as following:

$$\sigma_{ij} = \lambda u_{i,i} \delta_{ij} + \mu [u_{i,j} + u_{j,i}]. \quad (2.14)$$

Substituting the stress-displacement relations [Eq. (2.14)] in the equation of motion [Eq. (2.4)] and simplifying, we get

$$(\lambda + \mu) u_{j,ji} + \mu u_{i,ij} + \rho f_i = \rho \ddot{u}_i, \quad (2.15)$$

or in vector form:

$$(\lambda + \mu) \nabla \nabla \cdot \mathbf{u} + \mu \Delta \mathbf{u} + \rho \mathbf{f} = \rho \ddot{\mathbf{u}}, \quad (2.16)$$

which is called the Navier's equation of motion. The symbol Δ is the laplacian operator and, in the system of rectangular Cartesian coordinates, i.e. $\mathcal{R}_0(\mathbf{e}_1, \mathbf{e}_2, \mathbf{e}_3) = \mathcal{R}_0(\mathbf{x}, \mathbf{y}, \mathbf{z})$ where the vectors are unit vectors directed along the corresponding axes, it can be written as

$$\Delta = \nabla^2 = \frac{\partial^2}{\partial x^2} + \frac{\partial^2}{\partial y^2} + \frac{\partial^2}{\partial z^2}. \quad (2.17)$$

In the absence of body forces the equation of motion in vector form reduces to

$$(\lambda + \mu) \nabla \nabla \cdot \mathbf{u} + \mu \Delta \mathbf{u} = \rho \ddot{\mathbf{u}}. \quad (2.18)$$

The system of equations (2.18) is coupled in the three displacement components u_x , u_y , and u_z . These equations can be uncoupled by expressing the components of the displacement vector in terms of derivatives of scalar and vector potentials (represented by ϕ and $\boldsymbol{\psi}$, respectively) in the form [31, 65, 66] of the Helmholtz decomposition for vector fields,

$$\mathbf{u} = \nabla\phi + \nabla \times \boldsymbol{\psi}, \quad (2.19)$$

where ϕ is a scalar potential function and $\boldsymbol{\psi}$ is a vector potential function. In the system of the rectangular Cartesian coordinates, $\boldsymbol{\psi} = \psi_x \mathbf{x} + \psi_y \mathbf{y} + \psi_z \mathbf{z}$ and the Helmholtz displacement decomposition is written as

$$u_x = \frac{\partial\phi}{\partial x} + \frac{\partial\psi_z}{\partial y} - \frac{\partial\psi_y}{\partial z}, \quad u_y = \frac{\partial\phi}{\partial y} + \frac{\partial\psi_x}{\partial z} - \frac{\partial\psi_z}{\partial x}, \quad u_z = \frac{\partial\phi}{\partial z} + \frac{\partial\psi_y}{\partial x} - \frac{\partial\psi_x}{\partial y}. \quad (2.20)$$

Plugging the equation (2.19) into the equation of motion (2.18) and taking into account the following relations:

$$\nabla \cdot \nabla\phi = \nabla^2\phi, \quad \text{and} \quad \nabla \cdot \nabla \times \boldsymbol{\psi} = 0,$$

we get

$$\nabla[(\lambda + 2\mu)\nabla^2\phi - \rho\ddot{\phi}] + \nabla \times [\mu\nabla^2\boldsymbol{\psi} - \rho\ddot{\boldsymbol{\psi}}] = 0. \quad (2.21)$$

The equation (2.21) is satisfied if the following uncoupled wave equations are satisfied:

$$\nabla^2\phi - \frac{1}{V_L^2}\ddot{\phi} = 0, \quad (2.22)$$

$$\nabla^2\boldsymbol{\psi} - \frac{1}{V_T^2}\ddot{\boldsymbol{\psi}} = 0, \quad (2.23)$$

where $V_L = (C_{11}/\rho)^{1/2}$ and $V_T = (C_{66}/\rho)^{1/2}$ are the phase velocities of bulk longitudinal and transverse waves⁷, respectively.

In a plate made of an isotropic material with faces normal to the z -axis as illustrated in Fig. 2.2, the wave polarized in the sagittal plane (x, z) is decoupled from the transverse horizontal (TH) wave polarized along the y -axis. For a free plate, or more generally, for an isotropic solid bounded by two parallel free surfaces, the common guided wave with two components is called *Lamb wave* [4] which is related but different to *Rayleigh wave* discovered by Lord Rayleigh in 1888 [6]. One way to interpret the formation of a Lamb wave (LW) and its relation to the Rayleigh wave (RW) is that a RW can propagate independently along each free surface if the thickness of the plate is much larger than the wavelength, and when the thickness becomes comparable to the wavelength, the longitudinal and the transverse components of the RWs are then coupled at both free surfaces. This introduces a characteristic scale (the thickness), gives rise to symmetric or anti-symmetric deformations of the plate (as shown in Fig. 2.2) and leads to the multimode and dispersive waves, i.e. the Lamb waves [31]. The hypothesis of the plane strain motion implies that $u_y = 0$

⁷As a reminder, in the case of the homogeneous isotropic solid material, $C_{44} = C_{55} = C_{66} = (C_{11} - C_{12})/2$, see Eq. (2.12).

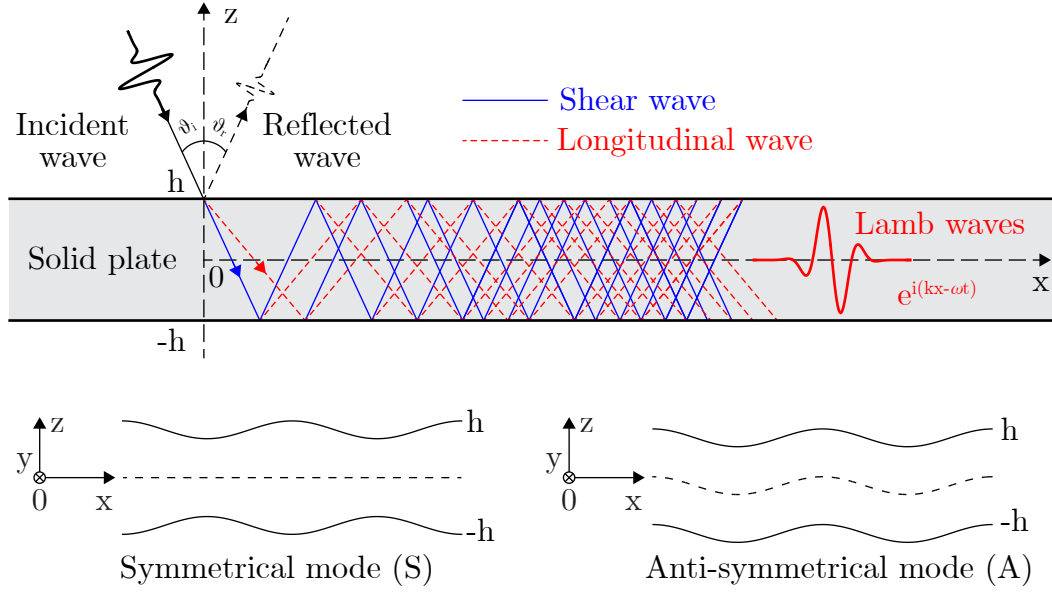


Figure 2.2: Schematic illustration of plane wave interaction at solid surface and Lamb wave in homogeneous isotropic plate with thickness of $2h$ (above) showing deformations of the plate for a symmetrical mode (below left) and an anti-symmetrical mode (below right).

and $\partial \cdot / \partial y = 0$ (i.e. the Lamb wave propagates along x -axis and the diffraction in the y -axis direction is neglected), and then the displacement components introduced in Eq. (2.20) reduce to

$$u_x = \frac{\partial \phi}{\partial x} - \frac{\partial \psi_y}{\partial z}, \quad u_z = \frac{\partial \phi}{\partial z} + \frac{\partial \psi_y}{\partial x},$$

the potentials ϕ and ψ_y (ψ_y is simplified to ψ in the later expressions) satisfy the following propagation equations

$$\frac{\partial^2 \phi}{\partial x^2} + \frac{\partial^2 \phi}{\partial z^2} - \frac{1}{V_L^2} \frac{\partial^2 \phi}{\partial t^2} = 0, \quad (2.24)$$

$$\frac{\partial^2 \psi}{\partial x^2} + \frac{\partial^2 \psi}{\partial z^2} - \frac{1}{V_T^2} \frac{\partial^2 \psi}{\partial t^2} = 0. \quad (2.25)$$

The harmonic solutions of the wave equations (2.24) and (2.25) are searched in the following form

$$\phi = \Phi(z)e^{i(kx - \omega t)}, \quad \psi = \Psi(z)e^{i(kx - \omega t)}.$$

By injecting these solutions into Eq. (2.24) and Eq. (2.25), we obtain

$$\frac{\partial^2 \Phi}{\partial z^2} + p^2 \Phi = 0, \quad \frac{\partial^2 \Psi}{\partial z^2} + q^2 \Psi = 0, \quad (2.26)$$

with

$$p^2 = \frac{\omega^2}{V_L^2} - k^2 \quad \text{and} \quad q^2 = \frac{\omega^2}{V_T^2} - k^2,$$

where ω and k denote the pulsation frequency ($\omega = 2\pi f$) and the wavenumber, respectively. The solutions of Eq. (2.26) are determined by the boundary conditions of the plate for which the normal and tangential stresses, i.e. σ_{zz} and σ_{xz} , must be zero at the free surfaces $z = \pm h$. The expressions of the stresses for an isotropic solid are deduced from Eq. (2.14):

$$\sigma_{xz} = \mu \left(\frac{\partial u_x}{\partial z} + \frac{\partial u_z}{\partial x} \right), \quad (2.27)$$

$$\sigma_{zz} = \lambda \left(\frac{\partial u_x}{\partial x} + \frac{\partial u_z}{\partial z} \right) + 2\mu \frac{\partial u_z}{\partial z}, \quad (2.28)$$

which, in terms of the potentials ϕ and ψ , gives

$$\sigma_{xz} = \mu \left[(q^2 - k^2)\Psi + 2ik \frac{\partial \Phi}{\partial z} \right], \quad (2.29)$$

$$\sigma_{zz} = \mu \left[(k^2 - q^2)\Phi + 2ik \frac{\partial \Psi}{\partial z} \right]. \quad (2.30)$$

The requirements of $\sigma_{xz} = \sigma_{zz} = 0$ at $z = \pm h$ are satisfied simultaneously only if the stresses σ_{xz} and σ_{zz} are even or odd functions of z . The solutions must have different parity and one type of the expressions can be taken as [31]

$$\Phi(z) = A \cos(pz + \alpha), \quad (2.31)$$

$$\Psi(z) = B \sin(qz + \alpha), \quad (2.32)$$

where $\alpha = 0$ in the case where σ_{xz} is even and σ_{zz} is odd or $\alpha = \pi/2$ in the case where σ_{xz} is odd and σ_{zz} is even. In Eq. (2.31), A and B are two constants depending on the initial conditions. The mechanical displacement u_x and u_z are then given by

$$u_x = [ikA \cos(pz + \alpha) - qB \cos(qz + \alpha)]e^{i(kx - \omega t)}, \quad (2.33)$$

$$u_z = [-Ap \sin(pz + \alpha) + ikB \sin(qz + \alpha)]e^{i(kx - \omega t)}. \quad (2.34)$$

Therefore, the two different values of the phase α correspond to the two types (symmetric or anti-symmetric, see the two below subfigures in Fig. 2.2) of Lamb waves:

1. Symmetric modes correspond to the value $\alpha = 0$, where the displacement component u_x , which is tangential to the plate surfaces, is an even function of z and where the displacement component u_z , which is normal to the plate surfaces, is an odd function of z ;
2. Anti-symmetric modes correspond to the value $\alpha = \pi/2$, where the tangential component u_x is an odd function of z and where the normal component u_z is an even function of z .

When $\alpha = 0$ or $\pi/2$, the boundary conditions ($\sigma_{xz} = \sigma_{zz} = 0$ at $z = \pm h$) yield the two following equations by omitting the propagation factor $e^{i(kx - \omega t)}$:

$$(k^2 - q^2)A \cos(ph + \alpha) + 2ikqB \cos(qh + \alpha) = 0, \quad (2.35)$$

$$(k^2 - q^2)B \sin(qh + \alpha) + 2ikqA \sin(ph + \alpha) = 0, \quad (2.36)$$

which could be written in the following matrix form:

$$\begin{bmatrix} (k^2 - q^2) \cos(ph + \alpha) & 2ikq \cos(qh + \alpha) \\ 2ikq \sin(ph + \alpha) & (k^2 - q^2) \sin(qh + \alpha) \end{bmatrix} \cdot \begin{bmatrix} A \\ B \end{bmatrix} = \begin{bmatrix} 0 \\ 0 \end{bmatrix}. \quad (2.37)$$

The compatibility of this linear and homogeneous system requires that the determinant of the system is zero, namely:

$$(k^2 - q^2)^2 \cos(ph + \alpha) \sin(qh + \alpha) + 4k^2 pq \sin(ph + \alpha) \cos(qh + \alpha) = 0. \quad (2.38)$$

Expanding the squared term $(k^2 - q^2)^2$, we have

$$(k^2 - q^2)^2 = (k^2 + q^2) - 4k^2 q^2 = \frac{\omega^4}{V_T^4} - 4k^2 q^2.$$

Using this expansion into the formula (2.38) and after the simplification, we finally obtain the following implicit relation between ω and k :

$$\frac{\omega^4}{V_T^4} = 4k^2 q^2 \left[1 - \frac{p \tan(ph + \alpha)}{q \tan(qh + \alpha)} \right], \quad \text{with } \alpha = 0 \text{ or } \pi/2. \quad (2.39)$$

These two relations of dispersion are called the *Rayleigh-Lamb* equations [31].

2.3.2 Dispersion curves of Lamb waves and ZGV Lamb modes

The Rayleigh-Lamb equation introduced in the previous subsection [see Eq. (2.39)] cannot be solved analytically. Numerical methods must hence be used to find the pairs (ω, k) of each mode. One of them that gives quick access to the dispersion curves of the different modes is based on the search for the roots of the Rayleigh-Lamb equations (2.39), rewritten as:

$$(q^2 - k^2)^2 \cos(ph) \sin(qh) + 4pqk^2 \sin(ph) \cos(qh) = 0, \quad \text{for S modes}, \quad (2.40)$$

$$(q^2 - k^2)^2 \sin(ph) \cos(qh) + 4pqk^2 \cos(ph) \sin(qh) = 0, \quad \text{for A modes}. \quad (2.41)$$

The search for the roots of the equations (2.40) and (2.41) is done numerically by the **fzero** routine of the Matlab software and then optimized by using the Müller's method (other mathematical methods can be also applied for the step of optimization, for example the Newton-Raphson method [67]). The result is a network of curves where each branch corresponds to a propagative Lamb mode. Then the optimized results can be separated and saved as curves for each mode (S or A mode) thanks to a loop counting the number of the existing modes. For details of the calculations as well as the optimization process, readers are welcome to see the Matlab program in Appendix D. There are two ways to number the Lamb modes. A usual way is to number them in the order of their appearance. However, in the case of the ZGV Lamb modes, it has been shown [12, 28] that it is more appropriated to number them according to the number of nodes present in the thickness of the plate [31]. The first symmetric and anti-symmetric mode are denoted S_0 and A_0 , respectively and present no cut-off frequency. With increasing positive frequency, all the other modes show a cut-off frequency f_c and the following rules are used to number them:

- for the symmetric modes:
 - even modes S_{2n} ($n \geq 1$) are such that $f_c \cdot 2h = nV_T$;
 - odd modes S_{2n+1} ($n \geq 0$) are such that $f_c \cdot 2h = \frac{2n+1}{2}V_L$;
- for the anti-symmetric modes:
 - even modes A_{2n} ($n \geq 1$) are such that $f_c \cdot 2h = nV_L$;
 - odd modes A_{2n+1} ($n \geq 0$) are such that $f_c \cdot 2h = \frac{2n+1}{2}V_T$.

In Fig. 2.3, an example of the evolution of the product of the frequency and the thickness ($f \cdot 2h$) is plotted as a function of the ratio of the thickness to the wavelength (kh/π) in the case of an isotropic Aluminum sample ($V_L = 6450$ m/s, $V_T = 3100$ m/s, $\rho = 2700$ kg/m³), where the modes are numbered using the previously-described rules. This current representation (considered as the normalized dispersion curves) makes it possible to quickly find the pairs (f, k) for any plate made of the same material and with thickness $2h$ without recalculating the dispersion curves. The red arrow indicates the position of the first ZGV point, which is further discussed in the following. Note that we consider here only the real roots of the dispersion relations that correspond to propagative Lamb modes. Non-propagative modes (pure imaginary wave number) or attenuated (complex wave number) are not yet taken into account. The reader wishing to know more about these solutions in the near field can consult, for example, the reference [68] or the seminal books [65, 66, 69, 70]. For the study of dispersion relations in anisotropic material, readers are referred to the following references [3, 71, 72].

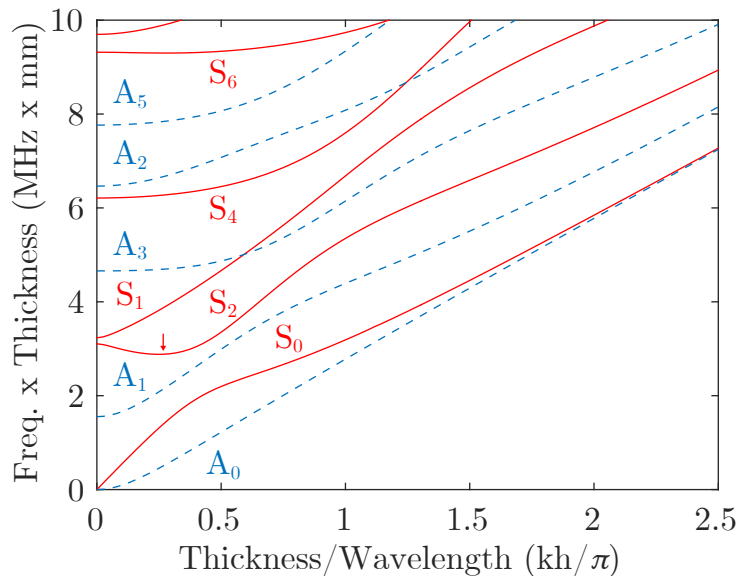


Figure 2.3: Normalized dispersion curves (product $f \cdot 2h$ vs. kh/π) of Lamb waves for both symmetric (red solid lines) and anti-symmetric (blue dashed lines) modes of an homogeneous isotropic Aluminum plate with thickness $2h$. The red arrow indicates the position of the first ZGV point.

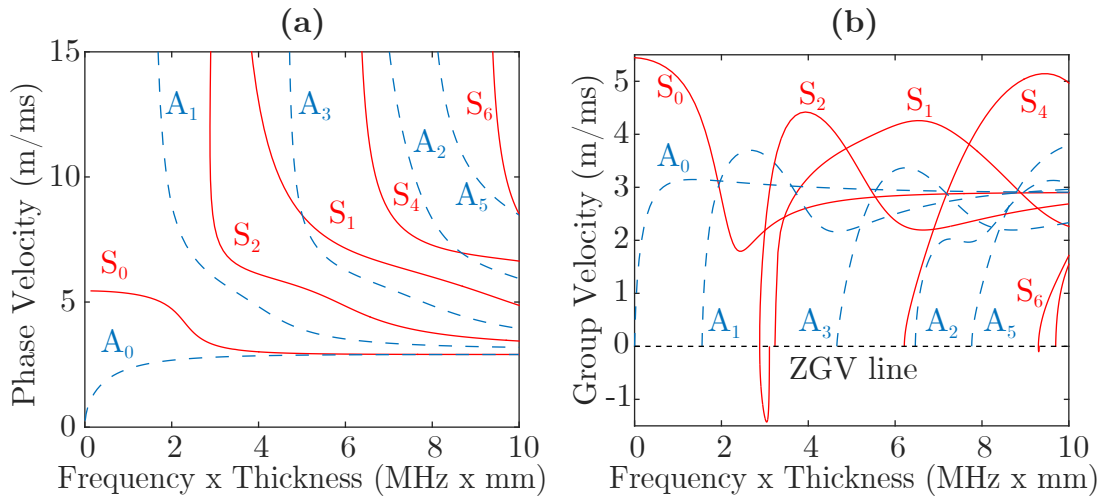


Figure 2.4: Dispersion curves, (a) phase velocity (V_{ph}) and (b) group velocity (V_g) vs. $f \cdot 2h$, of symmetric (red solid lines) and anti-symmetric (blue dashed lines) Lamb modes for an homogeneous isotropic Aluminum plate.

Another typical way to represent the solutions of the dispersion relation is by plotting the velocity as a function of the frequency. Figures 2.4(a) and 2.4(b) show examples of velocity dispersion curves for an isotropic Aluminum plate. Fig. 2.4(a) displays the dispersion curves of phase velocity V_{ph} as a function of the product $f \cdot 2h$, where $V_{ph} = \omega/k$ describes the speed at which a single crest of a wave moves. Fig. 2.4(b) displays the dispersion curves of group velocity V_g vs. $f \cdot 2h$, where $V_g = \partial\omega/\partial k$ describes the speed at which a guided wave packet moves. Note that on the branch of the S_2 mode, there are two points at which the group velocity is zero, between which the group velocity is negative. The first point where the group velocity is zero corresponds to the so-called ZGV Lamb mode: the associated phase velocity is finite. The second point in Fig. 2.4(b) where the group velocity is zero corresponds to a thickness resonance (the first extensional thickness resonance here): the associated phase velocity [divergence of the S_2 branch in Fig. 2.4(a)] is infinite this time since the wavenumber is equal to zero. The frequency at which the latter resonance occurs is the cut-off frequency, in opposition to the frequency at which the former resonance occurs that is called the ZGV resonance frequency. Fig. 2.4(b) also shows that the Aluminum has a second ZGV Lamb mode on the branch of the S_6 mode. In the case where the dissipation due to the material or to the waveguide boundaries is neglected, it is known that there is a rigorous identity between the group velocity and the velocity of energy transport under very general conditions [73]. Therefore, for the ZGV points where the group velocity vanishes while the phase velocity remains finite, the resonances remain locally at the position of the excitation without any energy transfer to the adjacent medium [12].

To have a better understanding of these particular ZGV points, it is important to look not only at the dispersion curves obtained with the real roots of the dispersion relations but also at those obtained with the complex roots, therefore including non-propagating and attenuated/evanescent modes. There are several numerical methods for calculating the complex roots of the Rayleigh-Lamb equations assuming

a complex wavenumber ($k_c = k_r + ik_i$). For example, in 2001, V. Pagneux et al. [74] proposed a method based on the projection of the equations of the elasticity to a spectral basis of orthogonal functions, leading to a classical eigenvalue problem. Although the results obtained by this method are not exact due to truncation of infinite series, they can still be considered as good initial values for an optimization process, such as the Newton-Raphson method or the Müller method. In Fig. 2.5, the dispersion curves of the first three symmetrical Lamb modes solved by this method and then optimized using the Müller method are plotted for a 75 μm -thick isotropic Aluminum plate ($E = 70$ GPa, $\rho = 2700$ kg/m³ and $\nu = 0.35$), assuming there is no dissipation.

We here define that the propagation direction is given by the sign of the group velocity $V_g = \partial\omega/\partial\Re(k)$, which means that where $V_g > 0$, i.e. where ω increases with increasing real part of k , the direction of propagation is along the $+x$ -axis, whereas where $V_g < 0$, the propagation direction is along the $-x$ -axis. Note that in the complex plane, $V_{ph} = \omega/\Re(k)$. In Fig. 2.5 (pp. 32-33), we plot the dispersion curves of the first three symmetrical modes, propagating in both directions: along $+x$ -axis, where the mode are labeled S_0 , S_2 , and S_1 , and along $-x$ -axis, where the mode are labeled S_{-0} , S_{-2} , and S_{-1} . In addition, in figure 2.5, S_0 , S_2 , and S_1 modes are plotted in solid lines and S_{-0} , S_{-2} , and S_{-1} are plotted in dashed lines. The colors of S_0/S_{-0} , of S_2/S_{-2} , and of S_1/S_{-1} modes are blue, green, and red, respectively. In Fig. 2.5(a), the modes are shown in the domain of (k_r, k_i, f) for a 3D view, where k_r is the real part of the wavenumber and k_i is the imaginary part of the wavenumber. To complete the illustration of the dispersion curves, we plot in Fig. 2.5(b) the dispersion curves in the complex wavenumber domain, i.e. (k_r, k_i) , as a top view of Fig. 2.5(a). In Fig. 2.5(c) and (d), the frequency is separately plotted as a function of (c) the real part k_r and (d) the imaginary part k_i of the wavenumber. Fig. 2.5(c) is therefore a front view of Fig. 2.5(a) and Fig. 2.5(d) is a side view of Fig. 2.5(a). In each sub-figure of Fig. 2.5, two black solid circle show the position of the ZGV point as indicated by the black arrows labelled ‘‘ZGV’’. Note that at the ZGV point where k_r is negative, the branches of the modes S_{-1} and S_2 are coincident. Similarly, note that at the ZGV point where k_r is positive, the branches of the modes S_2 and S_{-1} are coincident. Prior to explain why this ZGV mode will be called S_1S_2 in the remaining part of the manuscript, the path of the branches of each mode in the 3D domain (k_r, k_i, f) are now explicitly described using Fig. 2.5(a)-(d):

- for the mode S_0 : the wavenumber is purely real, positive, and increasing with increasing positive frequency, which corresponds to $V_{ph} > 0$ and $V_g > 0$;
- for the mode S_{-0} : the wavenumber is purely real, negative, and decreasing with increasing positive frequency, which corresponds to $V_{ph} < 0$ and $V_g < 0$;
- for the mode S_2 , the path could be split in two:
 1. where the frequency is below that of the ZGV point, the wavenumber is complex with positive real part, decreasing with increasing positive frequency, and with positive imaginary parts, which corresponds to $V_{ph} > 0$ and $V_g < 0$, with attenuation of the mode along the $+x$ direction;
 2. where the frequency is above that of the ZGV point, the wavenumber is purely real, positive, and increasing with increasing positive frequency,

which corresponds to $V_{ph} > 0$ and $V_g > 0$;

- for the mode S_{-2} , the path could also be split in two and is obtain by the symmetry of that of S_2 since $k_{S_{-2}} = -k_{S_2}$:
 1. where the frequency is below that of the ZGV point, the wavenumber is complex with negative real part, increasing with increasing positive frequency, and with negative imaginary parts, which corresponds to $V_{ph} < 0$ and $V_g > 0$, with attenuation of the mode along the $-x$ direction;
 2. where the frequency is above that of the ZGV point, the wavenumber is purely real, negative, and decreasing with increasing positive frequency, which corresponds to $V_{ph} < 0$ and $V_g < 0$;
- for the mode S_1 , the path is a bit more complicated and could be split in four:
 1. where the frequency is below that of the ZGV point, the wavenumber is complex with negative real part, increasing with increasing positive frequency, and positive imaginary parts, which corresponds to $V_{ph} < 0$ and $V_g > 0$, with attenuation of the mode along the $+x$ direction;
 2. where the frequency is above that of the ZGV point and below f_c^1 [where the branch reach the plane $k_r = 0$, see inset in Fig. 2.5(c)], the wavenumber is purely real, negative, and increasing with increasing positive frequency, which corresponds to $V_{ph} < 0$ and $V_g > 0$ [this behavior is called *backward* mode and is therefore labelled S_{1b} in the inset of Fig. 2.5(c)];
 3. where the frequency is above f_c^1 and below f_c^2 [where the branch cross the plane $k_r = 0$ toward positive k_r , see inset in Fig. 2.5(c)], the wavenumber is purely imaginary and positive, which means that this part of the mode is evanescent with decreasing amplitude in the $+x$ direction;
 4. where the frequency is above f_c^2 , the wavenumber is again purely real but positive and increasing with increasing positive frequency, which corresponds to $V_{ph} > 0$ and $V_g > 0$;
- for the mode S_{-1} , the path could also be split in four and is obtain by the symmetry of that of S_1 since $k_{S_{-1}} = -k_{S_1}$:
 1. where the frequency is below that of the ZGV point, the wavenumber is complex with positive real part, decreasing with increasing positive frequency, and negative imaginary parts, which corresponds to $V_{ph} > 0$ and $V_g < 0$, with attenuation of the mode along the $-x$ direction;
 2. where the frequency is above that of the ZGV point and below f_c^1 , the wavenumber is purely real, positive, and decreasing with increasing positive frequency, which corresponds to $V_{ph} > 0$ and $V_g < 0$ [this is also a *backward* mode and is therefore labelled S_{-1b} in the inset of Fig. 2.5(c)];
 3. where the frequency is above f_c^1 and below f_c^2 , the wavenumber is purely imaginary and negative, which means that this part of the mode is evanescent with decreasing amplitude in the $-x$ direction;
 4. where the frequency is above f_c^2 , the wavenumber is again purely real but negative and decreasing with increasing positive frequency, which corresponds to $V_{ph} < 0$ and $V_g < 0$.

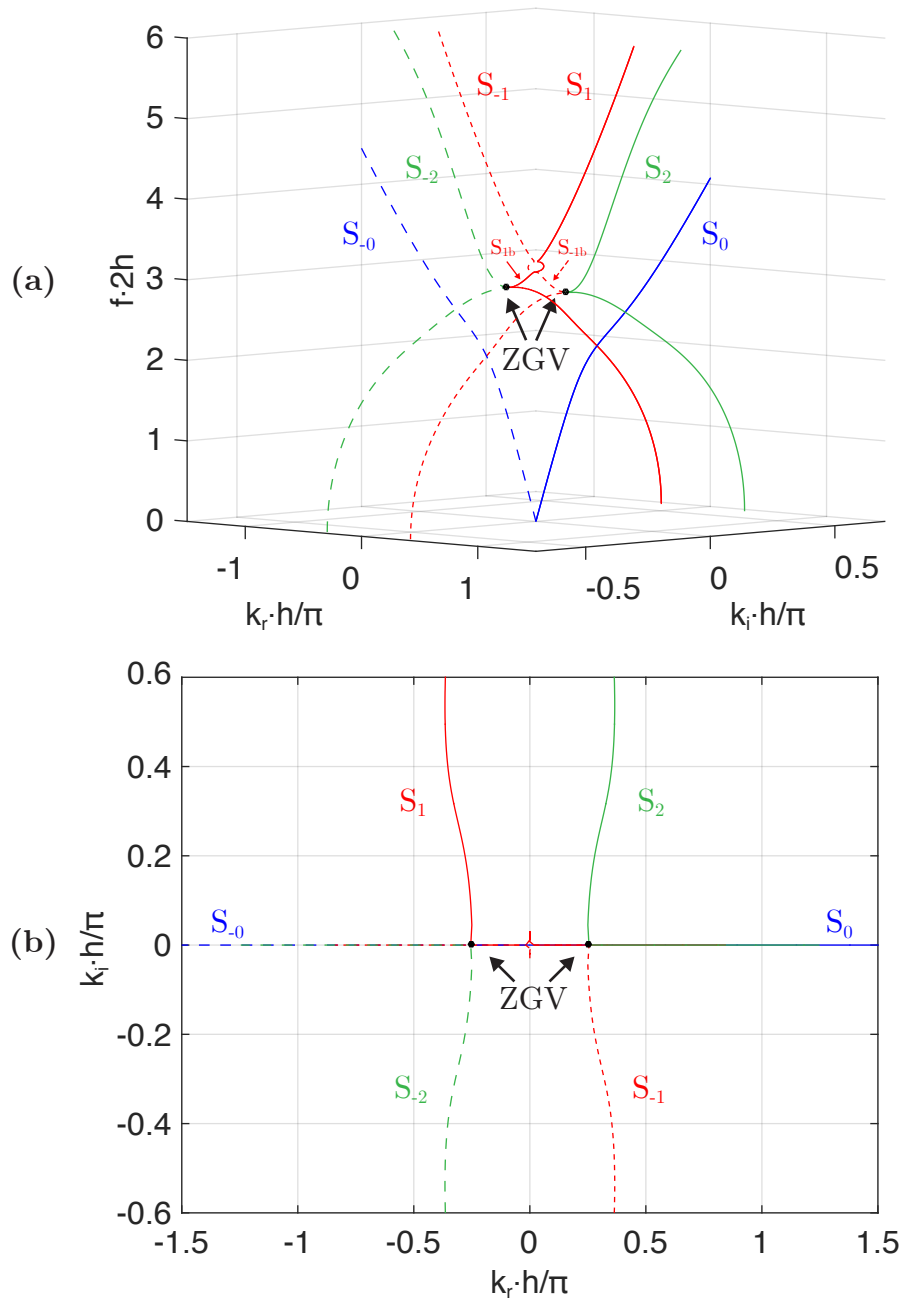


Figure 2.5: (a) Three dimensional view (k_r , k_i , f) of complex dispersion curves of Lamb waves in a $75 \mu\text{m}$ -thick Aluminum plate for the first three symmetrical modes propagating in both $+x$ (solid lines) and $-x$ (dashed lines) direction, with subscript 'b' for backward mode; (b) Top view of the dispersion curves of Lamb modes in the complex wavenumber domain, i.e. k_r vs. k_i .

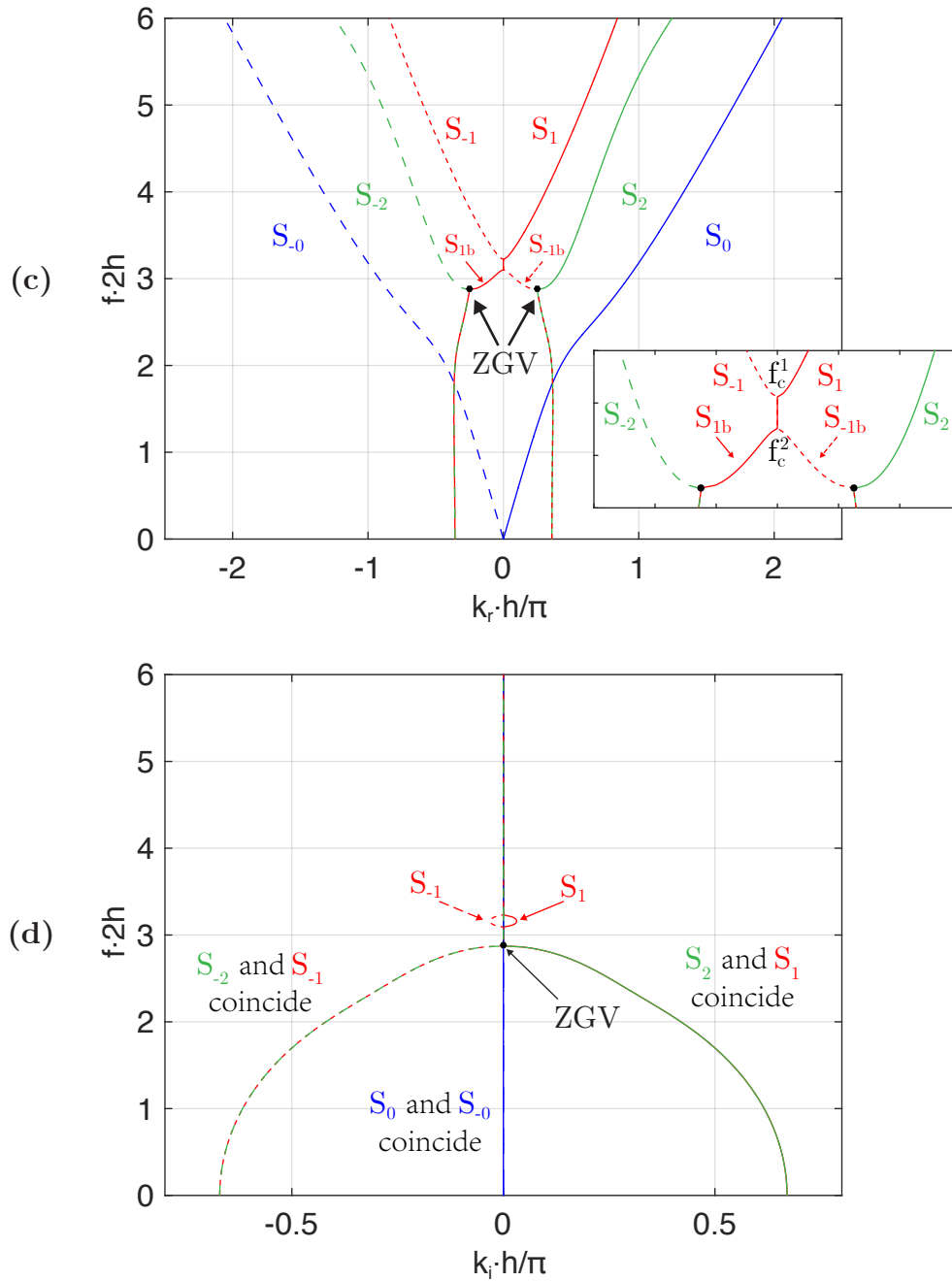


Figure 2.5: (Continued) Dispersion curves of the first three symmetrical Lamb modes in a 75 μm -thick Aluminum plate: frequency as a function of (c) real part and (d) imaginary part of the wavenumber. Note that S_0/S_{-0} , S_1/S_{-1} and S_2/S_{-2} are in blue solid/dashed, yellow solid/dashed and red solid/dashed lines, respectively. The two black solid circles plotted in each subfigure indicates the position of the ZGV point.

It is now proposed to define the terminology chosen to be used in the manuscript regarding ZGV-associated phenomena. For instance, the term “ZGV mode” will be essentially used to depict the monochromatic mode of the plate at the frequency f_{ZGV} that has a standing wave spatial structure, as discussed hereafter. The term “ZGV resonance” will, on the opposite, be used to talk about the resonance effect associated with the existence of the ZGV Lamb mode but accounting also for the frequencies close to that of the ZGV mode where the Lamb waves have non-zero but really small group velocity. For short, experimentally speaking, ZGV resonances are detected and are the sign of the presence of ZGV modes. Last but not least, the term “ZGV point” will be used to denote the position on the dispersion curves where, if the attenuation is neglected, the branches of two modes with ZGV feature are coincident.

Note that the term “ZGV point” hence corresponds to the point on the branch of a mode where the group velocity is zero only in the case, for example, where the branch of the S_2 mode is considered to continuously belong to the real plane, starting from $k = 0$. This was the assumption while describing the dispersion curves calculated in the real plane (see the figures 2.3 and 2.4). In that case, $V_g = \partial\omega/\partial k$ is definite and cancelled at the position of the arrow in Fig. 2.3. Yet, the branch of the S_2 mode does not actually start from $\Re(k) = 0$ in the real plane. The part from $k = 0$ to the “ZGV point” belongs to the S_{-1b} mode. In the specific case of Aluminum presented so far, where the attenuation is neglected, it is seen that the four modes S_2 and S_{-1b} , and S_{-2} and S_{1b} are coincident two by two at ZGV points [black circles in Fig. 2.5(a-d)]. At these points, the four modes have exactly the same frequency f_{ZGV} and the same wavelength, i.e. same absolute value $|k_{ZGV}|$ of the real wavenumber: $k_{ZGV} = k_{S_2}(f_{ZGV}) = -k_{S_{1b}}(f_{ZGV}) = -k_{S_{-2}}(f_{ZGV}) = k_{S_{-1b}}(f_{ZGV})$.

In the case where the material presents some attenuation (always the case in reality), the four branches have non-zero positive (S_2 , S_{1b}) and negative (S_{-2} , S_{-1b}) imaginary parts. Therefore, the branches of the modes S_2 and S_{-1b} , on the one hand, and of the modes S_{-2} and S_{1b} , on the other hand, do not coincide anymore at the ZGV points, which no longer exist. The detected resonance would then either correspond to the interference of the S_2 and S_{1b} modes and/or of the S_{-2} and S_{-1b} modes. The latter statement explains why the ZGV resonance is called S_1S_2 .

For better understanding of the ZGV Lamb mode features, we calculate also the displacement components of the S_1S_2 -ZGV Lamb mode, in a plate of thickness $2h$ and without attenuation, by substituting the constant A in equations (2.33) and (2.34) and neglecting the time dependence $e^{-i\omega t}$:

$$u_x = qB \left[\cos(qz + \alpha) - \frac{2k^2}{k^2 - q^2} \frac{\cos(qh + \alpha)}{\cos(ph + \alpha)} \cos(pz + \alpha) \right] e^{ikx}, \quad (2.42)$$

$$u_z = ikB \left[\sin(qz + \alpha) - \frac{2k^2}{k^2 - q^2} \frac{\cos(qh + \alpha)}{\cos(ph + \alpha)} \sin(pz + \alpha) \right] e^{ikx}. \quad (2.43)$$

For symmetric modes $\alpha = 0$, and taking into account that $k_{S_2}(f_{ZGV}) = -k_{S_{1b}}(f_{ZGV}) =$

k_{ZGV} and that $u_i^{ZGV} = u_i^{ZGVs_1b} + u_i^{ZGVs_2}$, we have

$$u_x^{ZGV}(x, z) = 2qB \left[\cos(qz) - \frac{2k^2}{k^2 - q^2} \frac{\cos(qh)}{\cos(ph)} \cos(pz) \right] \cos(k_{ZGV}x), \quad (2.44)$$

$$u_z^{ZGV}(x, z) = 2ikB \left[\sin(qz) - \frac{2k^2}{k^2 - q^2} \frac{\cos(qh)}{\cos(ph)} \sin(pz) \right] \cos(k_{ZGV}x), \quad (2.45)$$

with

$$p^2 = \frac{(2\pi f_{ZGV})^2}{V_L^2} - k_{ZGV}^2 \quad \text{and} \quad q^2 = \frac{(2\pi f_{ZGV})^2}{V_T^2} - k_{ZGV}^2.$$

The displacement components expressed in Eqs. (2.44)- (2.45) are illustrated in Fig. 2.6.

The figure 2.6(a) shows the axial and normal displacement components, i.e. u_x (in solid blue line) and u_z (in dashed red line), of the S_1S_2 -ZGV mode at $x = 0$ and $t = 0$ with amplitude normalized to the maximal value of $u_x(0, z)$. The figure 2.6(b) shows the distribution of the amplitude of lobes that decreases with increasing distance from the main lobe ($x = 0$) when the considered source is not a line source with infinite length and an infinitesimal width, but a line source with a finite length of 500 μm and an infinitesimal width. The amplitude is normalized by the maximal value at $x = 0$. For calculating the distribution relation $\Upsilon_{ZGV}(x)/\Upsilon_{ZGV}(0)$ in Fig. 2.6(b), we use the following equation

$$\Upsilon_{ZGV}(x) = \int_{-L/2}^{L/2} J_0 \left[k_{ZGV} \sqrt{x^2 + (y - y')^2} \right] e^{-4 \ln 2 (y'^2/L^2)} dy', \quad (2.46)$$

which is the simplified version (the incident laser beam is hypothesized to be normal to the sample surface and to be absorbed at the incident surface) of the fourth equation in Ref. [18]. In Eq. (2.46), L is the length of the line laser source, $y = 0$ is the source center. The zero order Bessel function of the first kind, J_0 , is the interference pattern associated to the normal displacement in the case of the axisymmetric ZGV solution for a point-like source. The integral in Eq. (2.46) therefore represents the continuous sum of point-like source allowing to reconstruct the line source with a finite length of L . Then, the figures 2.6(c) and (d) are the axial (c-1 and d-1) and normal (c-2 and d-2) displacement components associated with the first symmetrical ZGV Lamb mode without (c-1 and c-2) and with (d-1 and d-2) the consideration of the spatial attenuation, i.e. of the decrease of the mode amplitude along the x -axis due to the finiteness of the line source along y -axis. From Fig. 2.6(a), it can be seen that the amplitudes of the normal and tangential component of the displacement associated to the ZGV mode are of the same order of magnitude, although the normal displacement amplitude is weaker. Note that, since the line source that will be used in experiments is not infinite in length, the actual size of the main lobe constituting the interference pattern of the resonance will be slightly larger than that one would have obtained with an infinite line source [see Figs. 2.6(c)-(d)]. From Fig. 2.6(b), it can be deduced that the best position to measure the ZGV resonance with the normal displacement is at the central position of the line source. However, we will see that, if the used optical technique is not sensible to the normal displacement (interferometry) but to its derivative with respect to x (deflectometry),

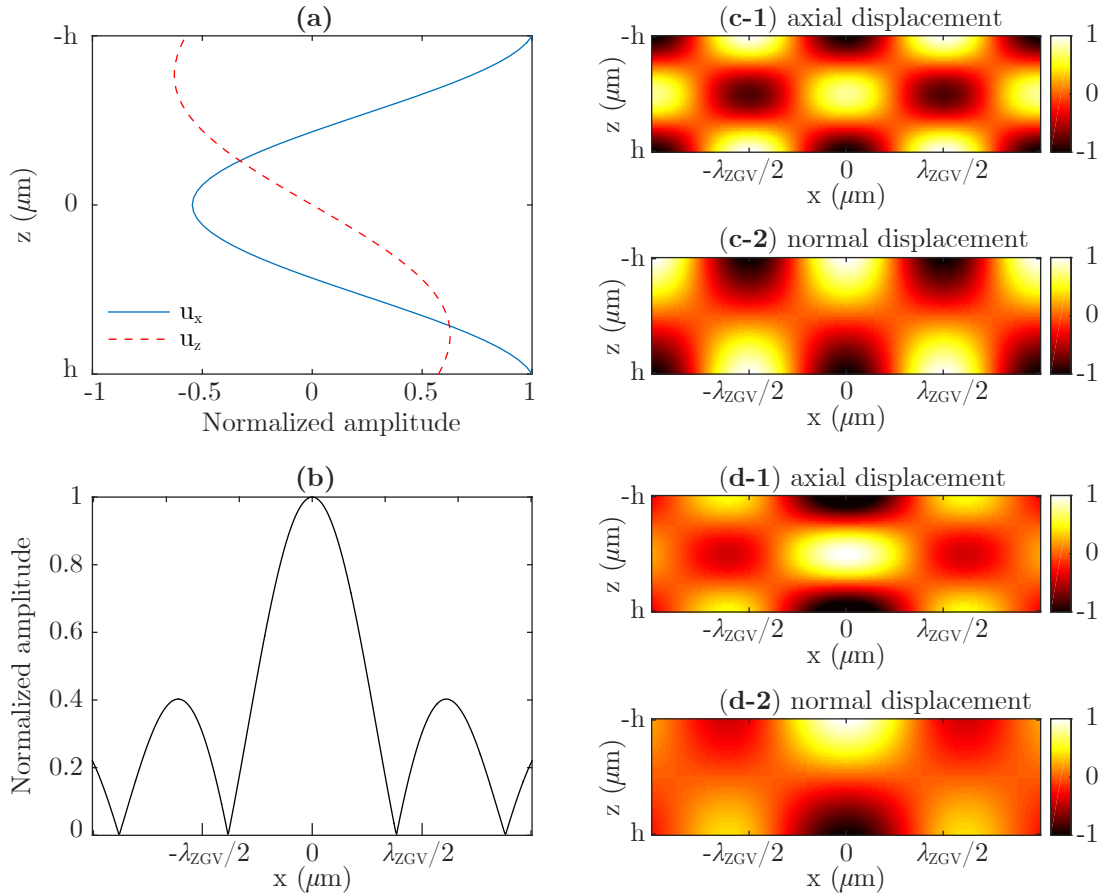


Figure 2.6: (a) Amplitude normalized to the maximal value of $u_x(0, z)$ of the axial u_x (solid line) and the normal (dashed line) displacement components of the S_1S_2 -ZGV mode at the position of excitation ($x = 0$) as a function of the thickness coordinate z ; (b) decrease of the lobe amplitude as a function of the lateral coordinate x , the line source is at $x = 0$ with length of $500 \mu\text{m}$; (c-1,2) axial and normal displacement components associated to the S_1S_2 -ZGV Lamb mode assuming infinite line source and without considering the material damping; (d-1,2) axial and normal displacement components associated to the S_1S_2 ZGV Lamb mode calculated by considering the spatial attenuation (decrease of amplitude along x -axis) due to the finite length of the line source (source length equal to $500 \mu\text{m}$) and still without considering the material damping.

the best position to measure the ZGV resonance will be slightly shifted from the central position.

So far, we have introduced the theoretical background of Lamb waves as well as of the particular case of the ZGV Lamb mode and resonance. In the next section, the current researches using laser-based ZGV Lamb resonances is reviewed, as well as their applications in the field of nondestructive testing/evaluation.

2.3.3 Literature review about ZGV Lamb modes/resonances

In this subsection, several articles published in the last 15 years are chosen for reviewing the topic of ZGV Lamb modes. We start by introducing the experimental observation of ZGV resonances using laser ultrasonics. Then we discuss one of its important application, namely the determination of Poisson's ratio. Another contactless method (air-coupled ultrasonic technique) is also introduced afterwards. Moreover, the excitability of ZGV resonance by laser is introduced which is quite practical for the choice of the experimental focal length of the lens. Finally, the applications of laser-based ZGV resonances for studying anisotropy, for assessing adhesion, and for detecting flaw in composite are reviewed.

2.3.3.1 First experimental observations and analyzes of ZGV resonance

The first achievable experimental observation of ZGV resonance using laser-based technique was presented by C. Prada et al. in 2005 [9]. In this article [9], C. Prada et al. proposed a novel laser-based ultrasonic technique for the inspection of thin plates in which a modulated continuous-wave laser source is used to excite narrow bandwidth Lamb waves. They found that the dominant feature in the acoustic spectrum is a sharp resonance peak that occurs at the minimum frequency of the first-order symmetric Lamb mode, where the group velocity of the Lamb wave goes to zero while the phase velocity remains finite. Moreover, from their published experimental results, they also demonstrated that the ZGV resonance could be generated by a low-power modulated excitation source (1550 nm electroabsorption modulated distributed feedback diode laser with a maximum of 500 mW of averaged power) and be detected by a Michelson interferometer coupled to a lock-in amplifier (frequency-doubled Nd:YAG laser with incident power on photodiode attenuated to be about 3 mW). The experimental phase velocity dispersion relations (solid circles) of the tungsten plate (nominal thickness of 50 μm) measured by the described setup (excitation and detection laser spot sizes were approximately 5 μm and 0.6 μm , respectively) are illustrated in Fig. 2.7 with theoretical calculations (solid lines). The laser source-to-receiver distance was scanned from 10 μm to 600 μm in steps of 10 μm and signals were recorded in a frequency range [40, 48] MHz with a step of 0.1 MHz.

Another experience was also realized in order to evaluate the ZGV point in the frequency domain: the source and the detector were aligned on the epicenter, the excitation laser frequency was then scanned between 38 MHz and 80 MHz in steps of 0.1 MHz, and at each frequency the magnitude of the acoustic signal was recorded. The prominent feature in the spectrum is a sharp resonance (see the fourth figure in Ref. [9]) occurring at 44.6 MHz, which allowed the thickness of the tungsten

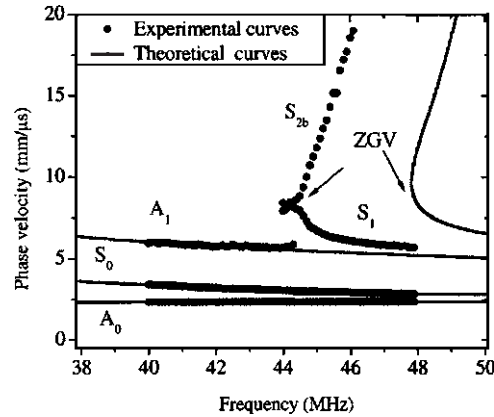


Figure 2.7: Theoretical and experimental phase velocity dispersion curves in vicinity of the ZGV point for a tungsten plate with thickness of $50 \mu\text{m}$ (figure taken from [9]).

plate to being estimated at $50.8 \mu\text{m}$. Based on the obtained results, C. Prada et al. pointed out that one of the most important applications of ZGV resonance is the precise measurement of thickness in micron-scale plates and membranes as well as the mapping of nanoscale thickness variations.

After that, C. Prada focused on the study of the ZGV resonance properties (ringing effects, backward wave propagation and required existence conditions of ZGV mode). In 2008, C. Prada et al. applied another setup system for experience [12]: a pulsed laser for generation (Q-switch Nd:YAG laser with pulse duration of 20 ns and maximal energy of 4 mJ) and a heterodyne interferometer for detecting local vibrations (100 mW frequency doubled Nd:YAG laser, wavelength of 532 nm, i.e. green optical beam). The distance between the source and the detection was varied from zero to 10 mm with a scanning step of $10 \mu\text{m}$. For each probe point, the signal of the normal displacement of the resonance was recorded during a duration of 0.3 ms with sampling rate of 50 MHz. They used the time Fourier transform of the normal displacement for reconstructing the spatial distribution (see Fig. 2.8) of the displacement amplitude resulting from the interferences of the S_1 and S_2 modes, for a given interval of frequency $\in [5.85, 5.93]$ MHz. Considering that energy does not propagate at the ZGV point, the interferences observed far from the source could be explained by the slightly upshift of the wave components (the positive and negative wavenumber values are then not exactly opposite).

Before the conclusions in Ref. [12], C. Prada et al. discussed the relations between the existence of ZGV resonances and the Poisson's ratio of the material for isotropic case. They perform extensive numerical calculations for determining the relation of ZGV frequency vs. Poisson's ratio. The numerical value of shear wave velocity have been arbitrarily chosen and fixed as $V_T = 3.0 \text{ km/s}$, the value of Poisson's ratio varied from 0 to 0.5 with a step of 0.001, and the longitudinal wave velocity V_L is then calculated using the bulk wave velocity ratio $\kappa_{bwr}(\nu) = V_L/V_T = \sqrt{2(1-\nu)/(1-2\nu)}$. After that, they calculated the group velocity by numerical differentiation using the well-known Rayleigh-Lamb equations, the minimum frequencies f_0 corresponding to the ZGV points for each value of ν

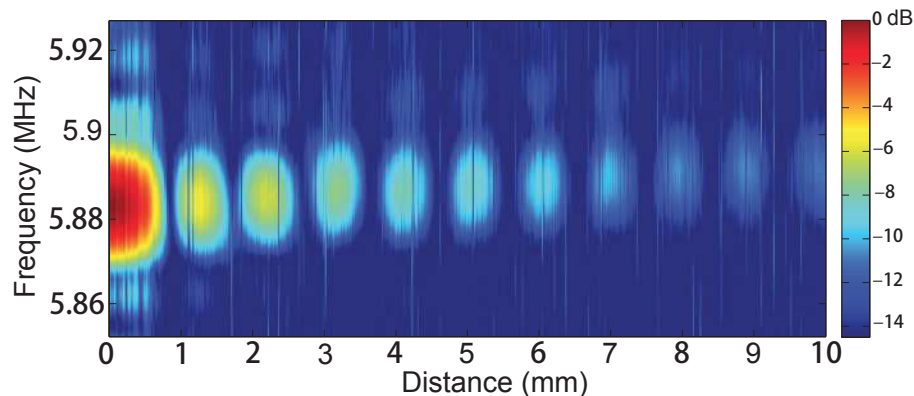


Figure 2.8: Spatial distribution of the displacement amplitude resulting from the interferences of the two Lamb modes S_1 and S_2 in a Duralumin plate with thickness of 0.49 mm (figure taken from [12]).

are then determined by the zero crossings of the group velocity. In Fig. 2.9, the obtained results are shown in a universal plot (first used by Meitzler [75] varying ν from 0 to 0.46) using the dimensionless quantity $2fh/V_T \in [0, 5]$ in ordinate and the Poisson's ratio $\nu \in [0, 0.5]$ in abscissa [12]. In these coordinates, the cutoff frequencies f_c of the odd antisymmetrical Lamb modes A_{2n+1} ($f_c = (2n + 1)V_T/(4h)$, with $n \in \{0, 1, 2, 3, 4\}$) and of the even symmetrical Lamb modes S_{2n} ($f_c = (nV_T)/(2h)$, with $n \in \{1, 2, 3, 4, 5\}$) are horizontal lines in Fig. 2.9 as shown by the labels on the left-hand side of the horizontal solid lines. The cutoff frequencies of the even antisymmetrical Lamb modes A_{2n} ($f_c = (nV_L)/(2h)$, with $n \in \{1, 2, 3, 4, 5\}$) and of the odd symmetrical Lamb modes S_{2n+1} ($f_c = (2n + 1)V_L/(4h)$, with $n \in \{0, 1, 2, 3, 4\}$) are shown by the dash-dotted increasing curves in Fig. 2.9. The calculated ZGV frequency f_0 are also represented in Fig. 2.9 as thick curves. From this representation, it is shown that the existence of a ZGV mode is dependent on the Poisson's ratio and that the ZGV modes appear in a range of Poisson's ratio about the value for which the curves of the cutoff frequency of the modes belonging to the same family (S_{2n} and S_{2m+1} , or A_{2n} and A_{2m+1}) intercept.

The experimental illustration of the above-discussed existence rule of a ZGV mode is presented in Fig. 2.10 where the central subplot is a reproduction of Fig. 2.9 with vertical dotted lines corresponding to the Poisson's ratio of fused Silica ($\nu = 0.172$) and to that of Duralumin ($\nu = 0.338$). The left and right subplots in Figure 2.10 show the dimensionless quantity $2fh/V_T$ as a function of the relative magnitude of the frequency spectra measured in fused Silica and Duralumin, respectively. The resonance peaks on the experimental data occur at the intersection (in the central subplot) of the corresponding vertical dotted lines with the curves revealing the existence of ZGV Lamb modes (solid thick blue and red lines), therefore demonstrating the existence of the ZGV modes S_1S_2 , A_2A_3 , and S_5S_8 in fused Silica and of the ZGV modes S_1S_2 , S_3S_6 , and S_5S_{10} in Duralumin. Note that the peaks at $2fh/V_T = 2$ in fused Silica and at $2fh/V_T = 1.5$ in Duralumin correspond to thickness resonances. For more details, the readers are referred to the third and

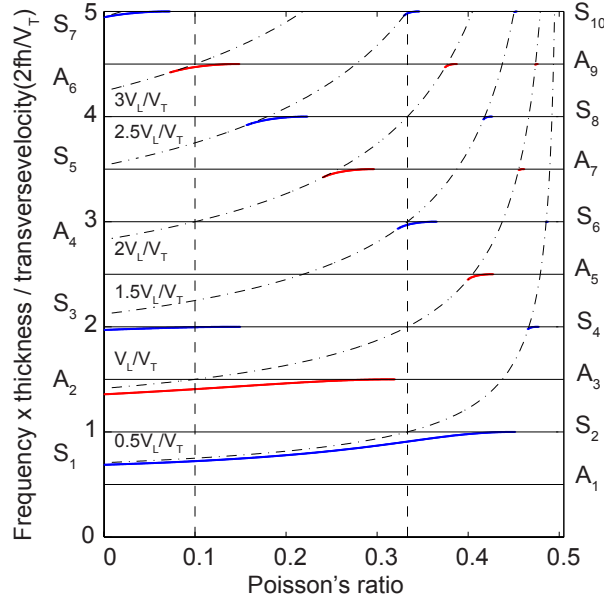


Figure 2.9: Dimensionless cutoff frequencies $2f_ch/V_T$ (horizontal lines) and $2f_ch/V_L$ (dash-dotted curves) and dimensionless minimum (ZGV) frequency $2f_0h/V_T$ vs. Poisson's ratio in the range $0 \leq \nu \leq 0.5$. The ZGV branches (thick lines) appear about crossing points of cutoff frequency curves for modes belonging to the same family: symmetric or anti-symmetric. Vertical dashed lines correspond to the critical values $\nu = 0.1$ and $\nu = 1/3$ (figure taken from [12]).

fourth sections in Ref. [12]

From Fig. 2.10 and other experiments realized in Ref. [12], it is demonstrated that the ratio of two resonance frequencies is independent of the plate thickness $2h$ but depends only on the Poisson's ratio. This last point will be the focus of the next subsection, and the relation between the frequencies of the two first resonances will be shown as an example for explaining this phenomenon.

2.3.3.2 Relation between ZGV frequency and Poisson's ratio

In this subsection, we discuss the relation between the Poisson's ratio of the material and the frequencies of the two first ZGV resonances, called ZGV frequency for simplification. We consider the case where the first ZGV mode is the symmetric S_1S_2 -ZGV mode and the second is the A_2A_3 -ZGV mode. The expressions of their frequency are given as

$$f_1 = f_{S_1S_2} = \beta_1 \frac{V_L}{4h}, \quad \text{with } \beta_1 < 1, \quad (2.47)$$

$$f_2 = f_{A_2A_3} = \beta_2 \frac{3V_T}{4h}, \quad \text{with } \beta_2 < 1, \quad (2.48)$$

where it is reminded that $2h$ stands for the plate thickness.

The coefficients β_1 and β_2 depend only on the Poisson's ratio ν [11, 13, 76], and the relation between β_1 and ν and that between β_2 and ν are illustrated in Fig. 2.11 and Fig. 2.12, respectively. The numerical calculations of the normalized dispersion

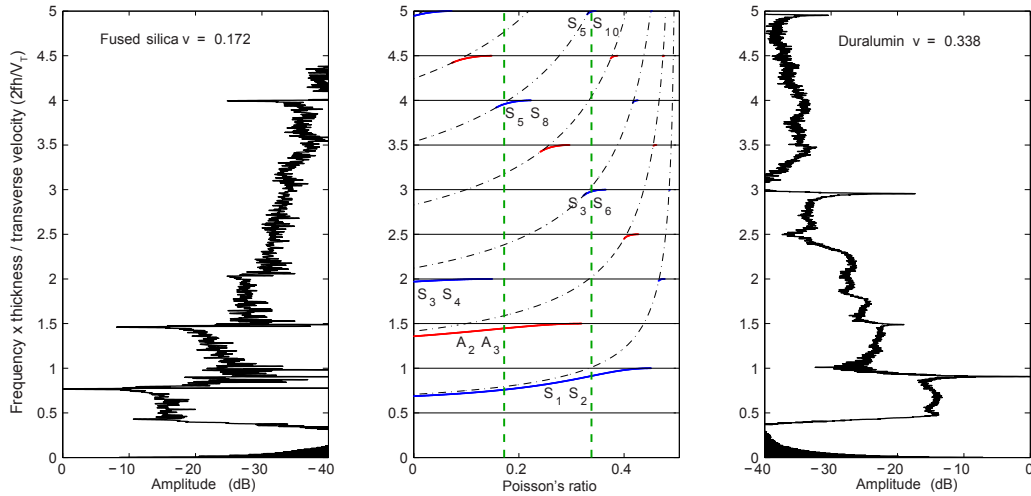


Figure 2.10: Local vibration spectrum of a fused Silica plate of thickness $2h = 1.1$ mm on the left and of a Duralumin plate of thickness $2h = 1.0$ mm on the right. The vertical dotted lines in the central part correspond to the Poisson's ratio of fused Silica $\nu = 0.172$ and of Duralumin $\nu = 0.338$ (figure taken from [12]).

curves for the extraction of such relations (between frequencies and ν) are realized with the same Matlab code used in Appendix D. The value of $\beta_1(\nu)$ or $\beta_2(\nu)$ are calculated discretely by varying the value of ν and then fitted by the polynomial curve (see Fig. 2.11 and Fig. 2.12).

It should be noted that the coefficient β_2 is equal to one for a Poisson's ratio ν greater than 0.31. As explained in Ref. [11], this point can be also observed in Fig. 2.12. The reason is that the A_2A_3 -ZGV mode does not exist anymore after this given value ($\nu = 0.31$) of Poisson's ratio. The coefficient β_2 is therefore equal to 1 since the resonance is then the thickness resonance.

Otherwise, with the known frequencies of the two resonances of the S_1S_2 - and the A_2A_3 -ZGV modes, the Poisson's ratio can be found directly using the ratio of f_2 to f_1 , since this ratio is a bijective function and it depends only on ν :

$$\frac{f_2}{f_1} = 3 \frac{V_T \beta_2}{V_L \beta_1} = 3 \sqrt{\frac{1 - 2\nu}{2(1 - \nu)}} \frac{\beta_2(\nu)}{\beta_1(\nu)}. \quad (2.49)$$

This ratio f_2/f_1 [Eq. (2.49)] is plotted in Fig. 2.13 as a function of ν .

We note here that all these three figures (Figs. 2.11-2.13) are the same as in the Ref. [11] but are all recalculated by the author himself. The discrete points (β_1 , β_2 and f_2/f_1 vs. ν) in these figures are extracted from the theoretical dispersion curves by solving the Rayleigh-Lamb equations [31] for a series of artificial materials with Poisson's ratios varying from 0 to 0.45 with step of 0.01. For each artificial material with a given Poisson's ratio, the Young's modulus (E) and the density (ρ) are arbitrarily chosen from pure Aluminum, i.e. 70 GPa and 2700 kg/m³, respectively.

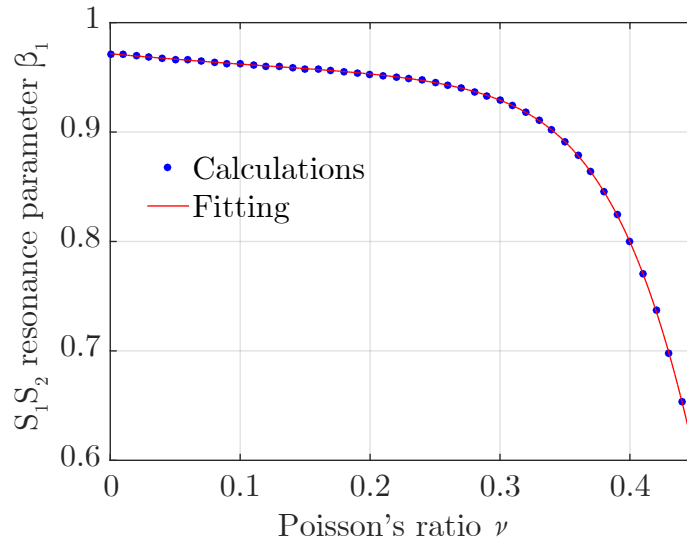


Figure 2.11: First order symmetric ZGV Lamb mode S_1S_2 . Variation of the resonance parameter β_1 vs. Poisson's ratio ν

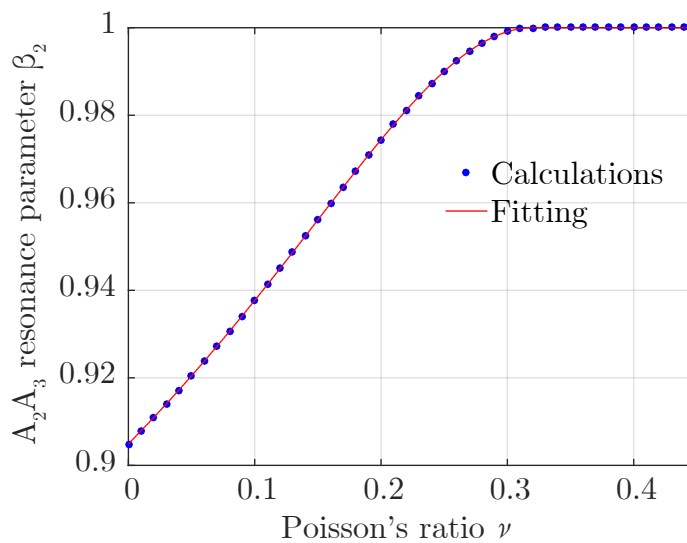


Figure 2.12: Second order antisymmetric ZGV Lamb mode A_2A_3 . Variation of the resonance parameter β_2 vs. Poisson's ratio ν . Note that for $\nu > 0.31$, $\beta_2 = 1$ due to the disappearance of A_2A_3 ZGV mode (resonance is then the thickness resonance).

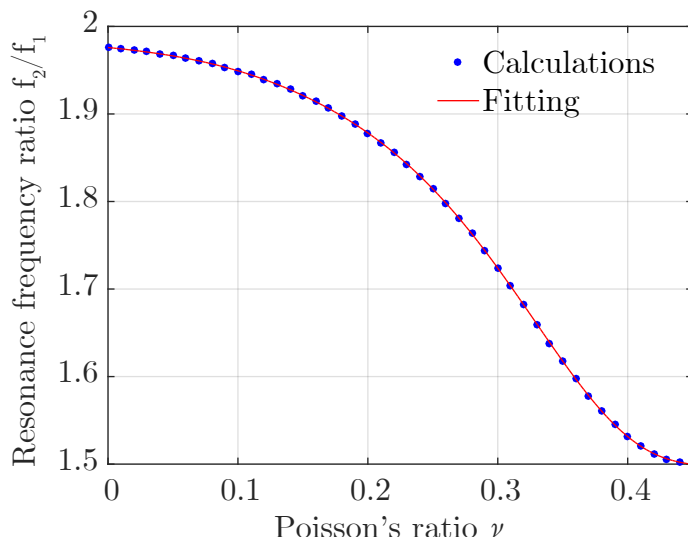


Figure 2.13: Variations of the resonance frequency ratio f_1/f_2 vs. Poisson's ratio ν .

2.3.3.3 Air-coupled imaging with ZGV resonance

In addition to C. Prada's work, there are other researchers who focus on the excitation and detection of the ZGV resonance using non-contact methods. There is a method based on air coupling that, according to the author, is also worth mentioning, and published just two years before the seminal paper of laser-based ZGV resonance [9], that is the C-scan imaging [see Fig. 2.14(b) and (c)] using ZGV resonance frequency [see Fig. 2.14(a)] by S.D. Holland et al. [19].

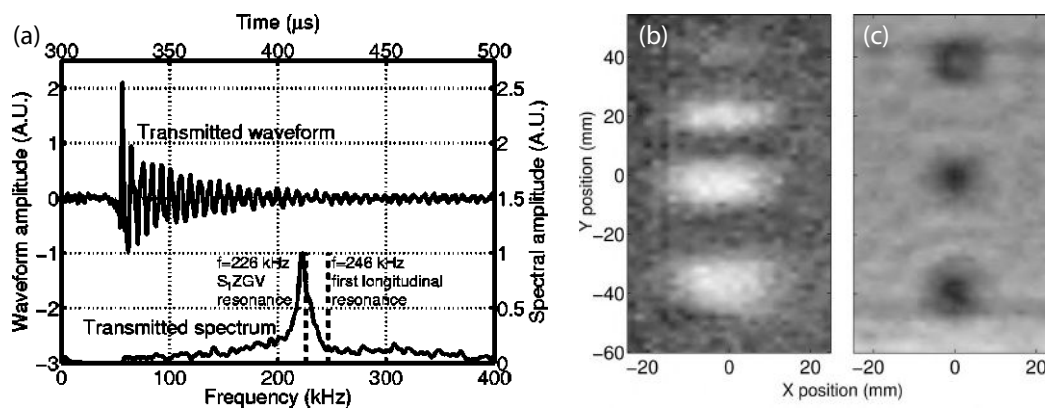


Figure 2.14: (a) Wave form and spectrum of ultrasound transmitted through 5.46-mm Lucite. (b) Air-coupled C-scan image of Scotch-tape strips on Lucite, 218 kHz. (c) Air-coupled C-scan image of Teflon inserts buried within carbon fiber-epoxy, 186 kHz [19].

S.D. Holland et al. pointed that the ZGV resonance couples extremely efficiently from air into a solid medium which dominates other modes by at least 10 dB. Their work proved that the ZGV-resonance-based method could be applied in different

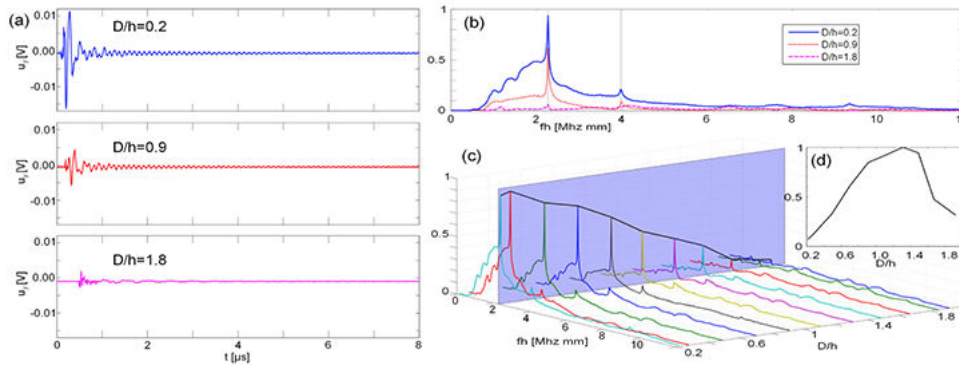


Figure 2.15: (Color online) Results of the experimental investigations of the excitability of ZGV resonances with constant pulse energy: (a) Detected displacement signals for different excitation spot diameters. (b) Spectra for the presented excitation spot diameters in (a). (c) Variation of the spectra of the measured signals with increasing spot diameter. The vertical plane and the line within the plane mark the position of the S_1S_2 -ZGV resonance. (d) Variation of the amplitude of the S_1S_2 -ZGV resonance normalized to constant energy density for each pulse diameter. The maximum at $D/h \approx 1.4$ is apparent (figure taken from [67]).

ranges of solid plates (millimeter scale, sub-MHz range) and still kept a quite good accuracy [19]. The ZGV resonance has been demonstrated to be useful for imaging and for air-coupled ultrasonic nondestructive testing, considering the combination of its efficiency and dominance.

2.3.3.4 Excitability of ZGV resonance by laser

Besides the experimental observation of ZGV resonance by LU, its excitability is also a problem worthy of being investigated by researchers, because when it comes to LU, it is inevitable to explore the excitation condition of photo-acoustic waves in order to obtain a better experimental measurement [77]. This point has motivated many research groups to study the excitability of ZGV resonances by lasers. For example, the work published by O. Balogun et al. [24] using a spot source. In 2015, the Research Center For Non-Destructive Testing (RECENDT) finished a project about the optical excitation and detection of ZGV resonances⁸. In the last article published before the end of this project [67], C.M. Gruensteidl et al. analyzed, experimentally and numerically, the excitability of ZGV resonances using a pulsed laser source in order to find the optical spot size on the sample surface that allows an optimal coupling of the optical energy into the ZGV mode.

Both numerical and experimental results (see Fig. 2.15 for experimental results in tungsten plate with thickness of $2h = 250 \mu\text{m}$) show that the coupling of the laser source into the ZGV mode depends strongly on the ratio of the plate thickness ($2h$) to the spot diameter (D_0) and the optimal case is when $D_0/h \approx 1.5$. This observation is very useful and has a strong practical application for the choice of

⁸<https://www.recendt.at/en/projects-detail/project-zegrove-EN.html>, accessed 09/20/2018.

the objective or of the focalisation lens in laboratory experiment. For example, for a plate with thickness of $100 \mu\text{m}$, the focal length of the lens to use for the optimal generation of the ZGV resonance can be calculated to be $110.7 \mu\text{m}$ for infra-red laser light (wavelength of 1064 nm) with an incident beam diameter (at $1/e^2$) of 2 mm using the Rayleigh range formula for Gaussian beam⁹

$$D_0 = \frac{4\lambda_0 F_0}{\pi D_i}, \quad (2.50)$$

where D_0 and D_i are the spot diameter ($1/e^2$ or FWHM as defined) for the focalised and incident beams, respectively; λ_0 is the optical wavelength and F_0 is the focal length of the focalisation lens. This formula can be found in many seminal books, for instance at page 595 in Ref. [78].

More recently, F. Bruno et al. [25] analyzed also the excitability of ZGV resonances in isotropic plates, both theoretically and experimentally, the difference being that they used also an annular source except the case of a spot. In addition, as pointed in Ref. [25], the optimal radius of the generation laser spot is equal to λ_{ZGV}/π , which is more general than the result in Ref. [67]. For details, readers are referred to Ref. [25].

2.3.3.5 Influence of anisotropy on ZGV mode

ZGV resonances have also been observed by laser ultrasonic techniques in anisotropic plates, in particular by C. Prada et al. [14], on a silicon wafer cut along the crystallographic plane [001]. The detected signal, generated by a pulsed laser (point source), is illustrated in Fig. 2.16(a). The Fourier transform of the signal is shown in Fig. 2.16(b) around the first ZGV resonance and allows identifying three sharp peaks: the peak at 8.03 MHz corresponds to the thickness resonance at the S_2 mode cut-off frequency; the other two peaks at 7.71 MHz and 7.75 MHz correspond to the ZGV resonances for $S_1 S_2$ mode in the [100] and [110] propagation directions, respectively [14]. Then, the authors have changed the generation of Lamb modes from a circular source to an orientable line source. The purpose of the experiment using a line source is to study the behavior of the ZGV resonance frequencies according to the orientation of the line. Fig. 2.16(c) represents the amplitude of the Fourier spectrum as a function of the frequency, from 7.7 to 8.1 MHz , and of the angle that the direction of the line source forms with the [100] direction.

From Fig. 2.16(c), we can observe that the thickness resonance frequency is independent of the source orientation, whereas the ZGV resonance frequency oscillates with a period of 90° . The rest of the article [14] is dedicated to an inversion algorithm which permits the determination of the three elastic constants (C_{11} , C_{12} and C_{44}) of the plate material with excellent accuracy using the experimental measurements. Furthermore, in the article [76], D. Royer et al. showed that ZGV resonance frequency depending on the orientation of the line source in cases of steel and of duralumin laminates. The measurements about anisotropy of materials using a line laser source have also been made in zircaloy tube [79]. For more details about this topic, readers are referred to Refs. [14, 76, 79].

⁹https://en.wikipedia.org/wiki/Gaussian_beam, accessed 09/20/2018.

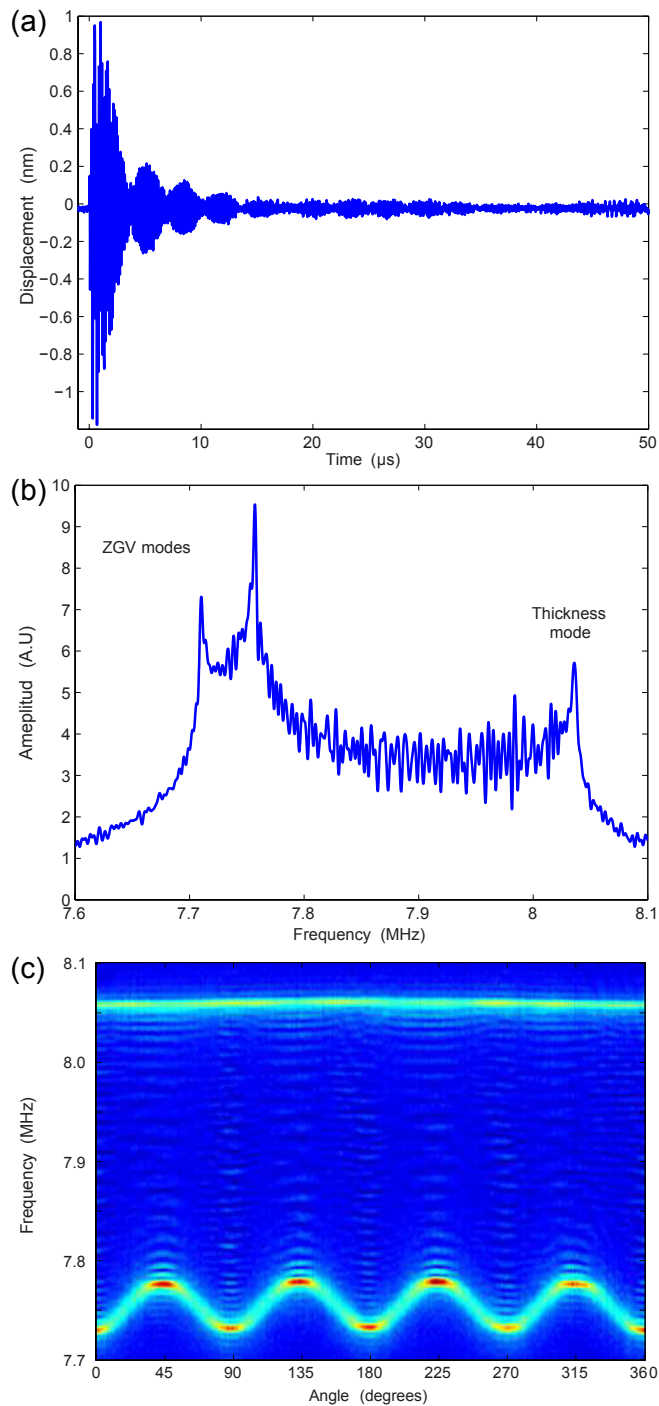


Figure 2.16: In the case of a point laser source, (a) Signal generated by the pulsed laser on a thin silicon plate cut along the crystallographic plane [001] and detected at the same point by the optical probe and (b) expanded view of the S_1S_2 -ZGV resonances and thickness mode resonance. (c) In the case of a line laser source, the amplitude of the Fourier spectrum as a function of the frequency, from 7.7 to 8.1 MHz, and of the angle that the direction of the line source forms with the [100] direction. The thickness resonance frequency is constant while the ZGV resonance frequency oscillates with a 90° period (figure taken from [14]).

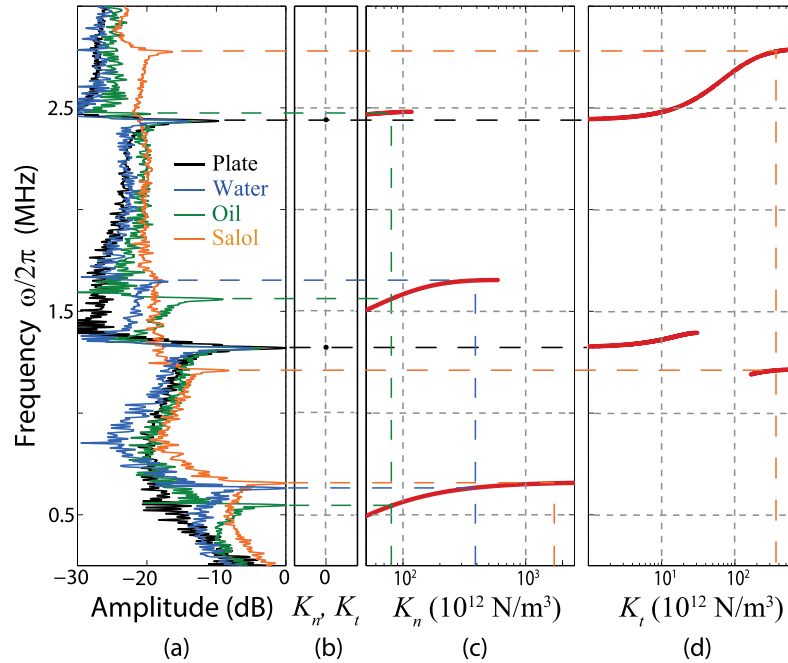


Figure 2.17: (a) Experimental spectra for the three different bonding layers, compared with theoretical ZGV frequencies for (b) a single plate, (c) symmetrical modes, $K_n \in [50; 3000] \times 10^{12} \text{ N/m}^3$, (d) anti-symmetrical modes, $K_t \in [1; 700] \times 10^{12} \text{ N/m}^3$ (figure taken from [16]).

2.3.3.6 ZGV resonance for the analysis of bonded structures

The ZGV resonance was also used for the study of the adhesive bonding between two solid plates. In 2014, S. Mezil et al. developed a contactless technique using ZGV resonances for probing the bonding between two solid plates coupled by a thin layer [16]. Taking into account both the normal and the shear interfacial stresses, S. Mezil et al. modeled the coupling layer between the two solid plates by normal and tangential stiffnesses.

Experimentally, they realized the measurements for several adhesion levels between two glass plates attached by two bulldog clips: a drop of water, of oil, or of salol, and compared with the case without liquid inside (two plates are considered as a single one). The spectra of the four cases are illustrated in Fig. 2.17(a) and compared with the theoretical calculations [see figures 2.17(b), (c) and (d)]. They demonstrated that symmetrical and anti-symmetrical ZGV frequencies depend on the normal stiffness and on the tangential stiffness, respectively. However, since the interfacial shear stiffness is very low, the experimental method is much more sensitive to the normal stiffness rather than to the tangential one. From their results, the proposed method was able to be used for studying multilayer structures after the development of the appropriate modelling. The next year they did so [80] for a trilayer. This article opens a new way for the use of laser-based ZGV resonance, i.e. the study of multilayer structures and potentially the evaluation/characterization of the defects in them.

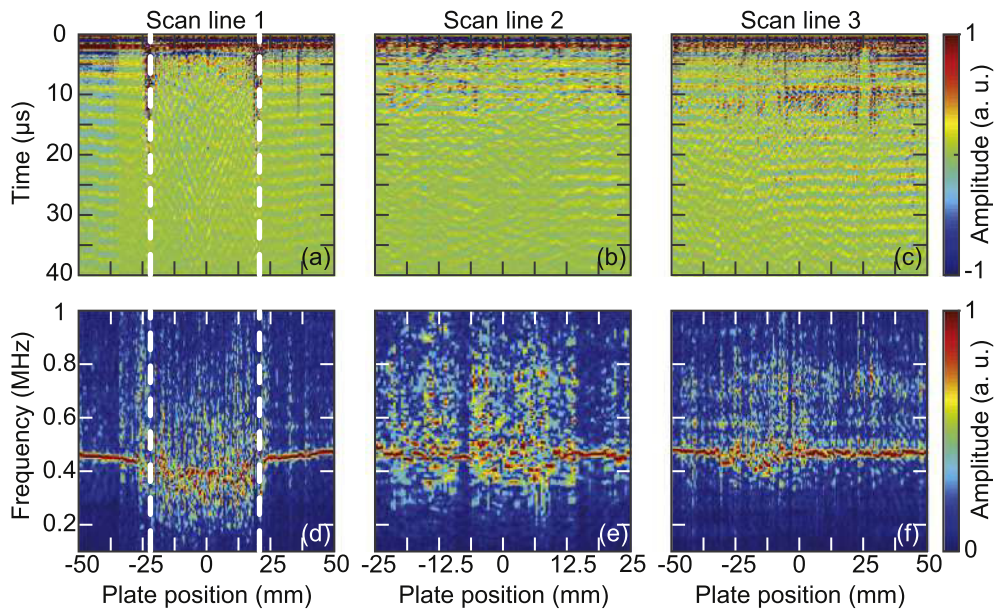


Figure 2.18: Time domain B-scans of the composite plate when the scan line is: (a) line 1 across the impact location, (b) line 2 near the impact location, and (c) line 3 far from the impact location. The related frequency domain B-scans obtained with a Hann time window (respectively d, e and f). Dashed white lines: maximum dimension of the flaw observed optically (figure taken from [50]).

2.3.3.7 ZGV resonance for flaw detection

The ZGV resonances are proven to be useful for detecting flaws in materials [15, 19, 81]. In 2015, just before this PhD work, LAUM has already started a research for flaw detection in composites using ZGV resonance. In this work, F. Faëse et al. used a beam shaping method for the generation laser, in order to enhance ZGV resonances in the probed materials. They applied their method first on an intact Aluminium plate and then in a damaged composite plate. After scanning the sample over healthy and flawed zones (see the Fig. 7 in Ref. [50] for the photo illustration), F. Faëse et al. demonstrated the ability to detect the undersurface flaws in the composite plate. Experimentally, three scanning regions are chosen and the results as well as the frequency spectra are shown in Fig. 2.18. With the help of the prediction of the theoretical models of the defects (or numerical simulations) and of their comparison with the dominant frequencies of the experimental B-scans, the authors of Ref. [50] believed that more information, especially quantitative one can be extracted.

Of course, only one section can not cover such a big theme (i.e. ZGV resonances and their applications). There are numerous other researches on the topic of laser-based ZGV resonances as well as on the theoretical and the numerical study of Lamb wave dispersion relations and ZGV points. For details of these themes, readers are referred to the references [9–19, 24, 26, 50, 67, 72, 80, 82–85] as well as to a review article (version in french) [76] and to the relevant articles cited in these references.

Now that both the experimental technique (laser ultrasonics) and the particular elastic wave (ZGV Lamb mode) that will be used have been introduced, the next

section is now focused to one of the main application that is proposed to be tackled by combining both: the metal fatigue.

2.4 Metal fatigue

The importance of the study of fatigue damage, especially the fatigue in metals, has been constantly recalled and mentioned. The constant reaffirmation of its importance can be found in many reviews and books [86–97], and we will not repeat them here.

In this section, the knowledge about fatigue damage is not new, all the texts are just as a summary of the literature. Please note that for the convenience of reading, the author rephrases all the quoted passages in his own style. Therefore, references to relevant literature have been cited, and articles on the internet and/or web forums have also been referenced by footnotes at the end of each paragraph (website addresses are given). Moreover, in the Chinese-related part (articles, webpages as well as corresponding paper texts), the author himself translated and commented, the document was quoted and well noted that the original text was Chinese (marked “*in Chinese*” after the title).

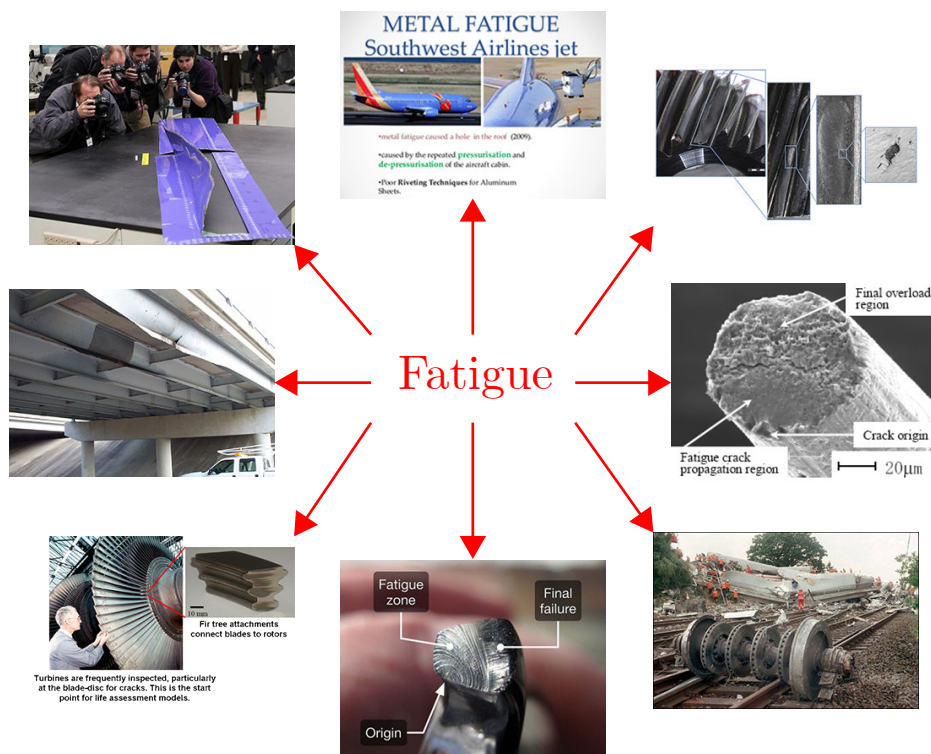


Figure 2.19: Metal fatigue and caused accidents.

2.4.1 About fatigue damage

Fatigue is a deadly killer of all construction machinery as shown in Fig. 2.19. The construction machinery mentioned here includes airplanes flying in the sky, trains

running on the ground, cars and tanks, ships sailing on the sea, submarines, and nuclear power plants, centrifuges, turbine blades and so on.

Although exact numbers are not available, it is expected that at least 50% of the damage of mechanical parts (such as axles, crankshafts, connecting rods, gears, springs, bolts) is fatigue damage [89]. It has also been reported that fatigue failure accounts for 49% of all component damage in aircraft jet engines [98]. In addition, pressure vessels, offshore oil platforms and a variety of welded structures (such as bridges, towers, etc.), even home appliances (including bicycles, wardrobe hinges and kitchen faucet handles, etc.) can be fatigued. Generally the definition of material fatigue¹⁰ is as following: under the cyclic load (stress), the local and permanent damage occurs at a certain point of the material or structure; after sufficient stress (or strain) cycle, the damage accumulation can cause cracks in the material or structure. And the crack is further extended to complete fracture, called fatigue failure [89]. The expression ‘fatigue’ is proposed by Jean-Victor Poncelet¹¹. By the 1950s and 1960s, August Wöhler¹² first measured the $S - N$ curve characterizing fatigue performance and proposed the concept of fatigue limit, which laid the foundation for fatigue research. Fatigue life refers to the cycle of destruction of a material at a given stress (or strain) level. The theory of fatigue mechanics is rich in content [86–88].

The term *Metal Fatigue* based on theory and definition is too flat, we will then list some of the world’s important, deplorable and horrific historical events for interpreting the severity of fatigue damage and the fatal disasters it causes. Here are some notable examples of metal fatigue accidents:

1. a train returning to Paris from the Palace of Versailles crashed in May 1842 at Meudon: after the leading locomotive broke an axle, the carriages behind piled into the wrecked engines and caught fire, at least 55 passengers were killed trapped in the carriages;
2. during the period from 1953 to 1954, three crashes occurred in De Havilland’s *D.H.106 Comet 1* passenger plane, causing the flight of the comet aircraft to be grounded;
3. on 27 March 1977, a “Boeing 747” passenger plane took off at the San Francisco International Airport for 15 minutes, the aircraft crashed sharply due to the failure of the No. 4 engine;
4. according to L’Agence France-Presse, on 20 August 2010, a Boeing 747-438 passenger plane of Qantas Airways, flying from San Francisco to Sydney, suddenly had an engine failure (also caused by fracture of the turbine blades due to metal fatigue) at a height of 25000 feet (about 7.500 meters);

¹⁰[https://en.wikipedia.org/wiki/Fatigue_\(material\)](https://en.wikipedia.org/wiki/Fatigue_(material)), accessed 09/20/2018.

¹¹Jean-Victor Poncelet (1 July 1788 22 December 1867) was a French engineer and mathematician who served most notably as the Commanding General of the École Polytechnique. For details see https://en.wikipedia.org/wiki/Jean-Victor_Poncelet, accessed 09/20/2018.

¹²August Wöhler (22 June 1819 21 March 1914) was a German railway engineer, best remembered for his systematic investigations of metal fatigue.

5. on the evening of July 22, 2013, when a “Boeing 737” passenger plane of South Korea’s East Asian Airlines carrying about 150 people landed in New York, the landing gear broke;
6. on June 3, 1998, the German high-speed train “ICE 884” was suddenly derailed when approaching the Eschede road bridge, the third carriage hit the first beam on the right side of the Eschede road bridge, the road bridge collapsed and then caused the rear compartments collided one after another, killing 101 people and injuring more than 100 people;
7. in 2011, a serious accident causing casualties occurred in a brand escalator in Beijing, after careful analysis by scientific researchers, it was found that the accident was caused by fatigue fracture of a connecting bolt of the escalator drive main unit and the front seat plate;
8. etc¹³ ...

Before finishing this subsection, the author note that all the eight pictures used in Fig. 2.19 are downloaded from the internet and the links corresponding to the related photos are given herein below the text but not directly added on the pictures in the figure: from the top photo, in the clockwise direction, the corresponding links are given in the footnote in order¹⁴.

2.4.2 Features of fatigue

Fatigue damage has several features and characteristics¹⁵, some of which are now listed for the reader to keep them in mind for the remaining of the manuscript:

- there is no obvious macroscopic plastic deformation at break, no obvious omen before fracture, but sudden destruction (suddenness);
- fatigue failure can occur at the maximum value of the cyclic stress, much lower than the tensile strength or yield strength of the material (low stress);
- fatigue failure is the damage caused by repeated loads leading to a result of long-term alternating stress, therefore fatigue damage often takes a certain period of time, which is different from one failure under static load;
- fatigue is very sensitive to defects (such as notches, cracks and tissue defects), since fatigue damage starts from the local, it is highly selective to defects, i.e. the fatigue damage will start from the defects which mechanically is the “weakest”;
- fatigue failure clearly shows the three components of crack occurrence, expansion and final fracture (fatigue fracture).

¹³<http://lxyd.imech.ac.cn/info/detail.asp?infono=17931>, accessed 09/20/2018.

¹⁴www.slideshare.net; www.forgemag.com; www.slideshare.net; <http://archistruct.blogspot.fr>; <http://www.mat-test.com/>; <http://cmg.soton.ac.uk/>; www.seattletimes.com; www.arkansashighways.com, accessed 09/20/2018.

¹⁵<http://www.1cae.com/a/ansys/59/cae-10204.htm>, accessed 09/20/2018.

2.4.3 Classification of fatigue

There are different classification methods for fatigue, and the following classification methods are often encountered in aeroengines. We must understand that different definitions correspond to different classification criteria. For example, high-cycle fatigue and low-cycle fatigue are only divided from failure cycles, and have no relationship with stress state and load conditions. For another example, thermal fatigue mainly describes the loading situation of mechanical components, but has nothing to do with high-cycle and low-cycle fatigue. Therefore, we proposed herein the following several categories of classification for fatigue: 1. high-cycle fatigue and low-cycle fatigue (according to the failure cycle); 2. uniaxial fatigue and multi-axial fatigue (according to stress state); 3. conventional fatigue, high and low temperature fatigue, thermal fatigue, thermomechanical fatigue, corrosion fatigue, contact fatigue, fretting wear fatigue and impact fatigue (according to load conditions and working environment). Note that the cases address in this work lie in the category 1 (low-cycle fatigue) for the application discussed in Chapter 4 and in the category 3 (thermal fatigue) for the application discussed in Chapter 5

2.4.4 Factors affecting metal fatigue

The fatigue strength of materials is extremely sensitive to a variety of external and internal factors. External factors include the shape and size of the part, the surface finish and the conditions of use. The internal factors include the composition of the material itself, the state of the structure, the purity and the residual stress. Subtle changes in these factors can cause fluctuations in material fatigue properties or even large changes. The influence of various factors on fatigue strength is an important aspect of fatigue research. This research will provide a basis for reasonable structural design of parts, as well as the correct selection of materials and rational formulation of various hot and cold processing processes to ensure high fatigue performance of parts. Several main influences of metal fatigue¹⁶ are given here:

1. Effect of stress concentration: The fatigue strengths are conventionally measured with carefully processed smooth specimens. However, actual mechanical parts inevitably have different forms of notches, such as steps, keyways, threads and oil holes. The presence of these notches causes stress concentrations such that the maximum actual stress at the root of the notch is much greater than the nominal stress experienced by the part, and the fatigue damage of the part often begins here.
2. Influence of size factor: Due to the non-uniformity of the material itself and the presence of internal defects, the increase in size leads to an increase in the probability of material damage, thereby reducing the fatigue limit of the material. The existence of size effect is an important issue in applying the fatigue data measured by small samples in the laboratory to large-sized actual parts. Since it is impossible to reproduce the stress concentration, stress gradient,

¹⁶<https://wenku.baidu.com/view/e6526e0a581b6bd97f19eab9.html>, accessed 09/20/2018.

and the like existing on the actual size parts completely on the small sample, the mutual disconnection between the laboratory results and the fatigue damage of some specific parts is caused.

3. Effect of surface processing state: There are always uneven working marks on the machined surface. These marks are equivalent to tiny gaps, which cause stress concentration on the surface of the material, thus reducing the fatigue strength of the material.
4. The impact of the loading experience: In fact, no part is working under the condition of absolutely constant stress amplitude, the overload and secondary load of the actual work of the material will have an impact on the fatigue limit of the material.
5. The influence of chemical composition: The fatigue strength and tensile strength of the material have a close relationship under certain conditions. Therefore, under certain conditions, the alloying elements which can improve the tensile strength can improve the fatigue strength of the material. In comparison, carbon is the most important factor affecting the strength of a material. For example, some impurity elements that form inclusions in steel adversely affect fatigue strength.
6. Effect of heat treatment and microstructure: Different heat treatment conditions will result in different microstructures. Therefore, the effect of heat treatment on fatigue strength is essentially the influence of the microstructure. The material of the same composition, although different in heat treatment, can obtain the same static strength, but the fatigue strength can vary within a relatively large range due to the difference in the structure.
7. Influence of inclusions: The inclusion itself or the hole created by it is equivalent to a small notch. Under the alternating load, stress concentration and strain concentration will occur, which will become a crack source of fatigue fracture, which will adversely affect the fatigue performance of the material. The effect of inclusions on fatigue strength depends not only on the type, nature, shape, size, quantity, and distribution of inclusions, but also on the strength level of the material and of the level and the state of the applied stress.
8. Effects of surface properties and residual stress: The effect of surface state, in addition to the surface finish mentioned above, also includes changes in surface mechanical properties and the effect of residual stress on fatigue strength. The change in the mechanical properties of the surface layer may be caused by the difference in chemical composition and structure of the surface layer, or the surface layer may be caused by deformation strengthening.

For details of numerous studies about metal fatigue, reader are referred to the following articles [91, 93, 96, 99–117], that the author found interesting and worth reading.

In the past half century, lots of methods for fatigue assessment were carried out. Among them, the ultrasound methods, especially the use of acoustic/ultrasonic nonlinearity and nonlinear Lamb waves showed their strong ability for probing fatigue damage as well as for predicting fatigue lifetime [118–138], several related methods will be mentioned again in the chapter 4 and 5. There are also many studies concerned about the fatigue prediction, using not only ultrasound methods, the author cites such articles here for people who may be interested in this topic [97, 119, 124, 134, 139–143].

To conclude this part of the fundamental background dealing with metal fatigue, the author wants to note that the proposal of this work is to develop and to propose a new experimental method to the material scientists expert in fatigue. The aim is therefore not to study in details the influences of the above-mentioned factors affecting metal fatigue but to demonstrate the ability of the proposed method to probe fatigued materials and, therefore, to propose a new experimental tool that would allow experts to perform the detailed study.

2.5 Conclusion

In this chapter, we introduced the basic knowledges about the three principle topics covered in this work: 1. Laser ultrasonic technology; 2. ZGV Lamb modes; 3. Fatigue damage and metal fatigue damage. Through the combing of existing knowledge, we have a general understanding of Lamb waves as well as ZGV Lamb modes in isotropic plate structures, a basic theoretical understanding of laser ultrasonic technology as well as its applications in NDT domain, and a general grasp of the features of the metal fatigue and its current development. Task 1 (see Sec. 1.2) is basically completed in this chapter. The first objective, i.e. to be familiar with Lamb waves and ZGV Lamb modes through Lamb wave dispersion curves, is also theoretically realized. Thus, our focus in the next chapter will be on the understanding and analysis of Lamb waves and ZGV resonances in experiments using laser ultrasonic technique. To sum it up, the elastic guided wave theory recalled herein as well as the literature review of the current researches introduced in this chapter laid a solid foundation for the next study of this work.

Part II

Characterization of homogeneous
isotropic solid thin plates by laser
ultrasonic monitoring of
zero-group-velocity Lamb modes:
intact and damaged cases

In this part, we focus on the study of material damage detected by ZGV Lamb modes. As a first step, we analyze the ultrasonic attenuation by means of reconstruction of the dispersion curves of the Lamb waves, more precisely, around the first ZGV Lamb mode point, for different types of metallic plate. Next, we propose a method for the characterization of progressive fatigue damage, i.e. cumulative fatigue, in solid plates based on the capacity and the efficiency of ZGV resonance frequency for the localization and the imaging of progressive damage during the fatigue lifetime. In the end, the ability of the proposed method for the qualitative and potentially the quantitative prediction of fatigue lifetime is demonstrated in this part. It is also seen here that the study of the ultrasonic attenuation of materials could be a complement for a further understanding of the mechanism/nature of fatigue.

千里之行，始于足下。— 老子·道德经

A journey of a thousand miles begins with a single step. — Laozi · TaoTeChing.

Chapter 3

Experimental study of ultrasonic attenuation in metallic thin plates with laser-based zero-group-velocity Lamb modes and its application for nondestructive evaluation

Contents

3.1	Introduction	58
3.2	ZGV Lamb modes in Aluminum and Copper	59
3.3	Experimental Setup and Measurements	61
3.4	Application of SLaTCoW: estimation of ultrasonic attenuations	64
3.5	Conclusion	69

Keywords: *LU, ZGV Lamb modes, experimental complex dispersion curve, NDT.*

*Gedanken ohne Inhalt sind leer, Anschauungen ohne Begriffe sind blind.
Thoughts without Content are empty, Intuitions without concepts are blind.*

— Immanuel Kant

In this chapter, we present a method to recover complex wavenumber based on the spatial Laplace transform. The method is applied on zero-group-velocity Lamb modes in order to extract the ultrasonic attenuation in different metallic plates of several tens of micrometers-thick. With the spatial Laplace transform, the dispersion curves in the complex plane can be reconstructed and be used for extracting the values of the ultrasonic attenuation, at the scale of several tens of megahertz. The experimental results are compared with values reported in the literature that were measured by other means.

3.1 Introduction

Characterizing the dissipation of inhomogeneous propagating modes remains an open question in several fields of physics. The exploration of this problem attracted and motivated researchers to experimentally measure (via different experimental methods) the ultrasonic attenuation in different materials [144–156], especially the metallic materials which are commonly used in our life, such as Aluminum and Copper [148, 152]. In 1969 and 1971, K.C. Hepfer and J.A. Rayne [146, 148] measured the ultrasonic attenuation of longitudinal waves propagating along principle symmetry directions (i.e. [100], [110] and [111]) in high-purity (99.9999%) Aluminum in a wide range of frequency from 10 MHz up to 510 MHz (discontinuously measured). Several years after, M. Nandanpawar and S. Rajagopalan [152] measured the attenuation using the temperature variation (between 50 to 300 K) of the nonlinearity parameter for longitudinal waves propagating along [100]-axis in Copper at 150 MHz. In this PhD work, we focus on the plate-like structures of metals. For metallic plates, Lamb waves can be excited and are dispersive and multi-mode (as mentioned in chapter 2). So far, it has been possible to obtain the guided wave dispersion curves by applying a double space-time Fourier transform to the normal displacement fields measured in time domain. While other methods than the classical spatial Fourier Transform have been proposed to improve the accuracy of dispersion curve reconstructions, only the real part of the mode was recovered. However, guided waves are complex modes, the imaginary part of which accounts, among others, for the dissipation due to attenuation in materials. This attenuation can be measured for instance by analyzing the wave amplitude decrease with respect to the time (ZGV resonances) [13] or to the propagation distance (propagating waves) [157].

In this Chapter, the propagation of guided waves in sub-millimeter isotropic plates having different attenuation properties is considered. It is proposed to obtain the complex dispersion curves through a single treatment by applying the SLaTCoW method (for Spatial LAplace Transform for Complex Wavenumber recovery) [158], where a spatial Laplace Transform is used instead of the classical spatial Fourier Transform that only gives access to the real part of the complex modes. A cost function (see Sec. 3.4 for details) involving the Laplace transform and a simple model is then minimized to recover the complex wavenumbers. Limitations of other model-based methods that perform complex wavenumber recovery, such as a generalized form of the MUSIC technique [156] to name but one, have been proven to be overcome by the SLaTCoW method [158] since, as opposed to the other methods:

(i) knowing in advance the number of modes is not mandatory, (ii) the use of a simple emitter/receiver configurations is sufficient, and (iii) the interaction/overlap of modes constituting the received signal is not an issue.

The SLaTCoW method is here applied to the case of the S_1S_2 -zero-group-velocity (ZGV) Lamb mode. As already explained in the previous chapter, in the ideal case of a non-attenuating material, two modes reach ZGV points for the same frequency and wavenumber. In the presence of attenuation, the ZGV points with previous features do not exist anymore and the branches of the S_2 and S_{-1} modes never cross a point where, for the same frequency, $k_{S_2} = k_{S_{-1}}$ (see details in Sec. 2.3.2). If one looks to the branches of these modes in that case, they will repel each other: the more the attenuation, the stronger the repulsion.

The presented work in this chapter is organized as follows. The theoretical dispersion curves in the real plane¹ in both Aluminum and copper are shown in Sec. 3.2. The experimental setup and two scanning configurations are introduced in Sec. 3.3. In Sec. 3.4, the SLaTCoW method is then presented and applied to reconstruct the dispersion curves in the complex plane¹ from the experimental data allowing therefore the ultrasonic attenuation of each material to be estimated and presented. In this section, theoretical and experimental dispersion curves are compared for both materials, showing an experimental evidence of the repulsion of both branches in the vicinity of the ZGV mode. Finally, these measured attenuations are compared with values reported in the literature. The results and the potential application of the presented work is discussed and conclude the last section.

3.2 ZGV Lamb modes in Aluminum and Copper

Generally speaking, the propagation of Lamb waves is dispersive. Thus, many studies, both experimental and theoretical/numerical, are focused on the dispersion curves of this kind of guided waves [68, 71, 72, 83, 159–162]. This section is devoted to the analysis of ZGV Lamb modes in metallic materials thanks to the analysis of the dispersion curves in the real plane.

The details of the derivation process of Rayleigh-Lamb equations have been introduced in Sec. 2.3.1 and are not repeated here in the current chapter. Two different sets of dispersion curves are plotted in Fig. 3.1. The first set in Fig. 3.1(a) corresponds to the case of a 71 μm -thick Aluminum plate with elastic properties as shown in the left column of Tab. 3.1. The second set of dispersion curves plotted in Fig. 3.1(b) shows the case of a 74.5 μm -thick Copper plate with elastic properties as shown in the right column of Tab. 3.1. The thicknesses of Aluminum and Copper are chosen to match the thickness of the plates used in experiments (see Sec. 3.3). Moreover, in both Fig. 3.1(a) and (b), the red vertical arrows indicate the position of the first ZGV mode, i.e. the S_1S_2 -ZGV mode, on the dispersion curves. From the

¹The term of ‘*real plane*’ is not really accurate but a shortcut. This term is used in this chapter to speak about the case where the dispersion curves are calculated/shown in the plane where the ordinate is the frequency and where the abscissa is the real part of the complex wavenumber. Note that the term ‘*complex plane*’ will also be used as a shortcut in the case where the dispersion curves are calculated/shown in the domain where the frequency is the z -axis and where the real and imaginary parts of the complex wavenumber are the x - and y -axes, respectively.

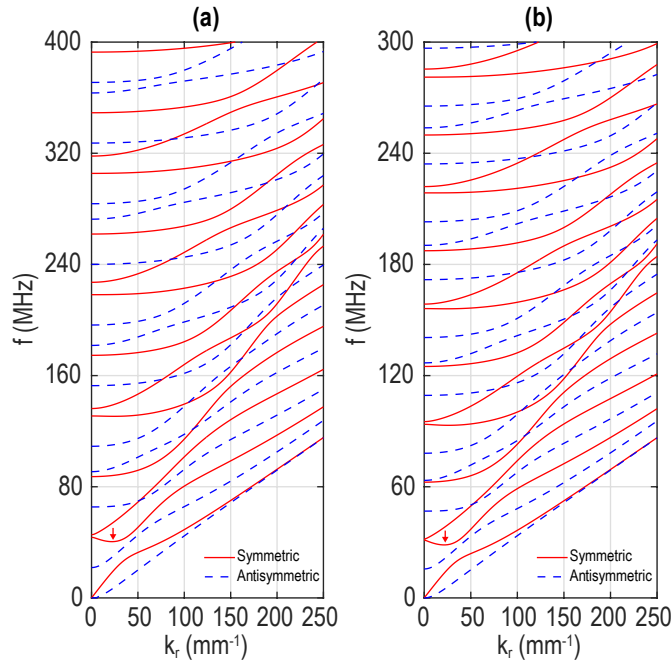


Figure 3.1: Real plane dispersion curves for (a) the Aluminum sample and (b) the Copper sample. The red arrows indicate the position of the S_1S_2 -ZGV mode in each case.

Table 3.1: Elastic properties for Aluminum and Copper samples.

	Aluminum	Copper
Young's modulus (GPa) E	70	130
Poisson ratio ν	0.35	0.34
Density (kg/m^3) ρ	2700	8960
Thickness (μm) $2h$	71.5	74.5
Longitudinal velocity (m/s) V_L	6450	4750
Shear velocity (m/s) V_T	3100	2320

theoretical calculations, we obtain that $f_{S_1S_2} = 40.28$ MHz and $k_{S_1S_2} = 21.93$ mm^{-1} in the case of the 71 μm -thick Aluminum plate [Fig. 3.1(a)] and $f_{S_1S_2} = 28.77$ MHz and $k_{S_1S_2} = 20.38$ mm^{-1} in the case of the 74.5 μm -thick Copper plate [Fig. 3.1(b)], respectively.

After the theoretical calculations of the expected ZGV resonance frequency and wavelength in the plates made of Aluminum and Copper, it is decided to use the same size of the laser spot for the generation of the Lamb modes for both. The experimental setup is now presented in the next section, together with the obtained results from which the ultrasonic attenuation will be extracted.

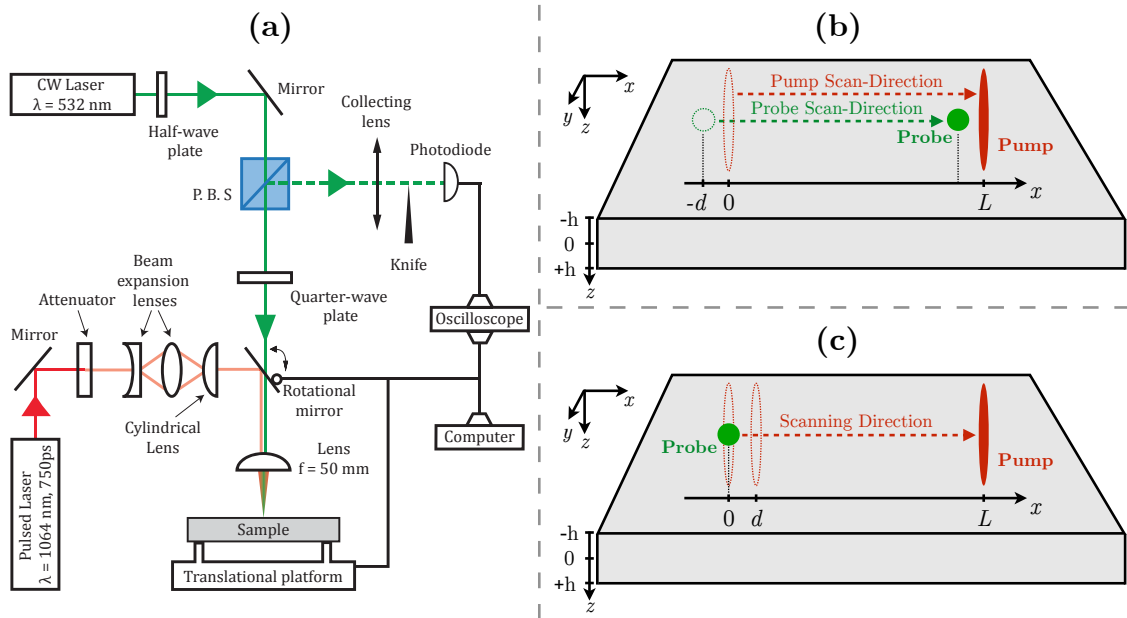


Figure 3.2: Experimental setup (a) and illustration of the two types of scanning: (b) the rotational mirror is fixed with $d = 20 \mu\text{m}$, and then translation plate is moved; (c) the translational plate is fixed, and the mirror rotates.

3.3 Experimental Setup and Measurements

The experimental part of this work consists in understanding and realizing the generation and the detection of the ZGV resonances on both a $71 \mu\text{m}$ -thick Aluminum plate and a $74.5 \mu\text{m}$ -thick Copper plate, and then to plot the experimental dispersion curves in the complex plane. In the next section, the dispersion curves in the complex plane will be recovered from the experimental results, using the SLaTCoW method, proposed by A. Geslain and J.-Ph. Groby [158]. The experimental setup is schematically illustrated in Fig. 3.2(a): the pump laser (pulse duration close to 0.75 ns with a repetition rate of 1 kHz) has an optical wavelength of 1064 nm and is focused into a stretched ellipse, close to a line generation source; another continuous laser (with a wavelength of 532 nm) is focused to a circular spot in the vicinity of the line source and is used for ultrasonic wave detection thanks to the beam deflection technique. Note that this technique is often used for LU probe [32, 77, 163–166]. The calibration of the coincidence of the generation line source and the detection circular spot is controlled by a rotational mirror. The Aluminum plate is attached on a three dimension translational stage.

With this experimental setup, two different kind of scanning can be achieved: (1) in order to characterize the sample thickness, the rotational mirror is fixed to set a distance d between the position of the pump laser and that of the probe laser equal to $20 \mu\text{m}$ and the translation stage is moved [see Fig. 3.2(b)]; (2) in order to make spatio-temporal measurements, the translation stage is fixed and the mirror rotates in order to move the generation from the position $x = 0 \text{ mm}$ where generation and detection are superimposed to the position $x = L$, with a scanning step which is chosen to be equal to $d = 20 \mu\text{m}$ [see Fig. 3.2(c)]. Note that in the configuration

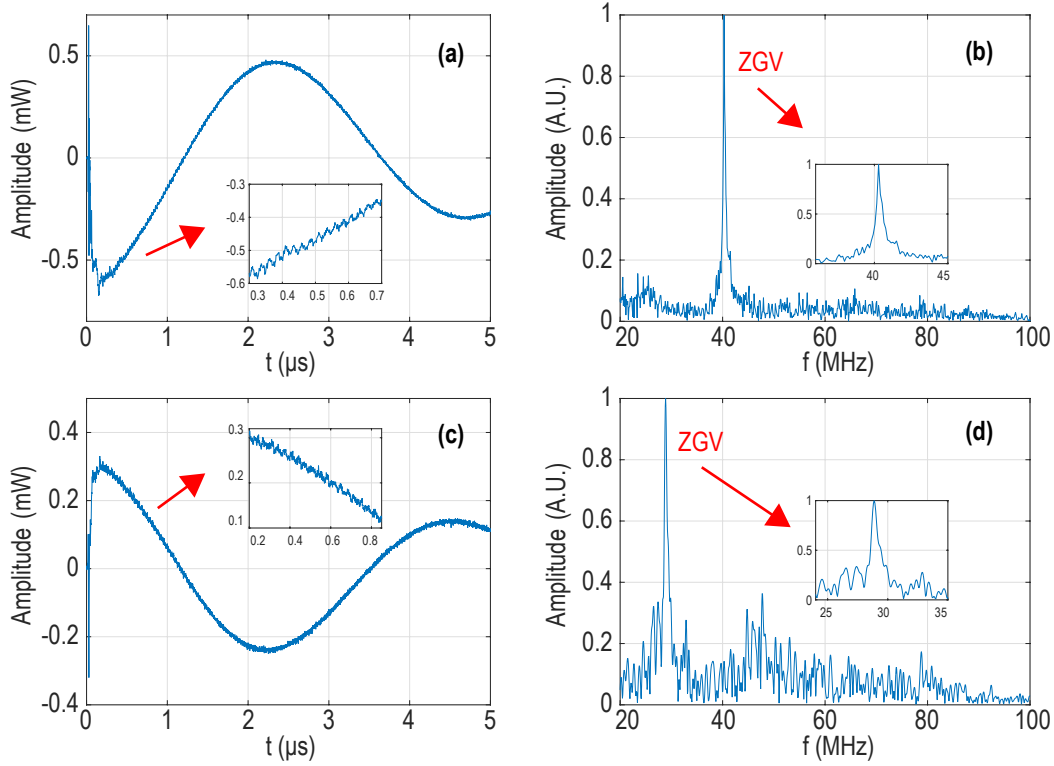


Figure 3.3: Example of measured signal [(a) in Al and (c) in Cu] and its Fourier transform [(b) in Al and (d) in Cu].

(1), the distance d between the pump and the probe is mandatory for the detection of the ZGV resonance since the beam-deflection technique is sensitive to the radial gradient of the normal displacement [which is zero at $x = 0$, i.e. $\partial u_z(x = 0)/\partial x = 0$].

Before the measurements, our sample is polished to improve the reflection of the probe beam, but this changes the thickness of the sample. Considering that the SLaTCoW method is based on the temporal-spatial measurements along a distance on the surface of the sample and that the ZGV frequency is very sensitive (inversely proportional) to the local thickness of the sample, a characterization of this thickness is therefore necessary to find a place on the surface having a constant thickness in order to avoid the influence of the thickness variation on the guided waves during the measurements. The experimental characterization of the thickness change of the plate is carried out by looking at the change of the ZGV frequency. By scanning over 30 mm on the specimens, a zone of constant thickness of 4 mm-long in Al and of 2 mm-long in Cu could be found. Note that there is a great variation of the thickness over the whole plates: $2h \in [70.7 \mu\text{m}, 74.5 \mu\text{m}]$ in the Aluminum plate and $2h \in [71.7 \mu\text{m}, 74.7 \mu\text{m}]$ in the Copper plate.

In Fig. 3.3, we can see the example of a signal measured when the generation and the detection are distant of $d = 20 \mu\text{m}$: (a) in Aluminum and (b) in Copper. The low frequency part of the signal corresponds to the first anti-symmetric mode A_0 which is preponderant. By zooming in on the time signal (inset), we see a higher frequency oscillation which corresponds to the ZGV resonance. If one performs a Fourier transform of this signal [see Figs. 3.3(b) and (d)], a resonance with a very

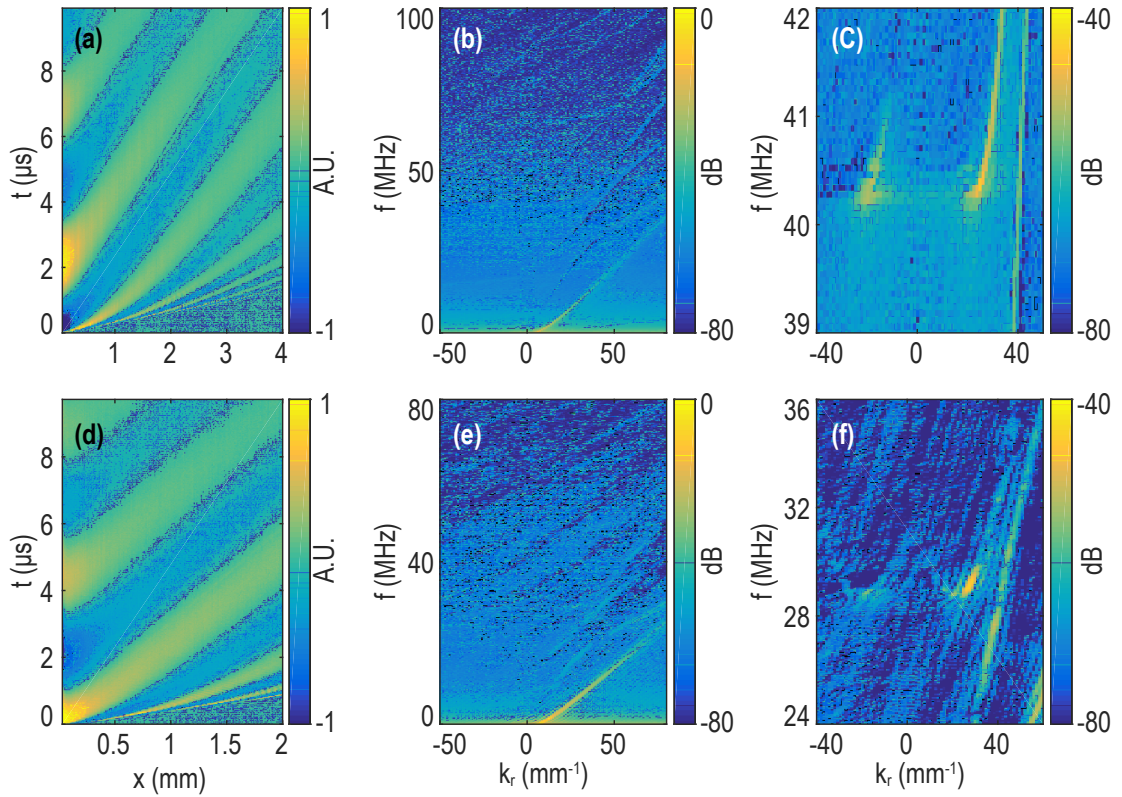


Figure 3.4: Experimental results on Aluminum (a) and Copper (d), their 2DFFT images (b) for Aluminum and (e) for Copper, and zoomed part around the S_1S_2 -ZGV mode for Aluminum (c) and for Copper (f).

good quality factor ($Q_{Al} = 122$ and $Q_{Cu} = 78$) appears around 40 MHz in Al [Fig. 3.3(b)] or 30 MHz in Cu [Fig. 3.3(d)]. The higher quality factor for aluminum than for copper could be related to the grain boundary scatter (copper sample is rolled polycrystalline plate and therefore has some texture).

Spatio-temporal measurements were then carried out using the scanning type shown in Fig. 3.2(c). We note here that Fig. 3.4(a) for Aluminum and Fig. 3.4(d) for Copper show the normalized signal amplitude as a function of x (distance between pump and probe spots) in horizontal axis and of time in vertical axis. Furthermore, from the figures 3.4(a) and (d), the A_0 Lamb mode is mainly observed, i.e. the low frequency content. From these measurements, a double Fourier transform, as shown in the following expression

$$\tilde{u}(k_r, \omega) = \int_0^T \int_0^L u(x, t) e^{-ik_r x} e^{i\omega t} dx dt, \quad (3.1)$$

is applied in order to see the dispersion curves in the real plane, the results of which are as shown in Fig. 3.4(b) for the Al plate and in 3.4(e) for the Cu plate. In the zoomed part around the ZGV point [Fig. 3.4(c) and Fig. 3.4(f)], the three branches of the modes S_1 , S_2 , and A_1 (from left to right) are present. Note that since measurements are made only in one direction, i.e. in the direction of the positive group velocities, the branch of the S_1 mode appears where the real part of

the wavenumber is negative and that of the S_{-1} mode is not present, as expected, therefore showing an experimental example of the discussion in Sec. 2.3.2 in Chapter 2.

From the figures 3.4(b) and (e), we can see with the help of the double Fourier transform that only the real wavenumber information is obtained. Thus, in the next section, a method based on the spatial Laplace transform for the recovery of the experimental dispersion curves in the complex plane (recovery of the real and imaginary parts of the wavenumber) will be introduced. Using these complex dispersion curves, the estimation of the ultrasonic attenuation in materials is then proposed.

3.4 Application of SLaTCoW: estimation of ultrasonic attenuations

The aim of this section is to estimate the ultrasonic attenuation both in Aluminum and in Copper using the comparison between experimental and theoretical dispersion curves in the complex plane. To achieve this, the acronym of the used method to get experimental dispersion curves is SLaTCoW for Spatial LAplace Transform for COMplex Wavenumber recovery, which is focused on the recovery of complex wavenumber information from guided elastic wave measurements. It is first propose to give a brief introduction to this method. Unlike the case of the conventional two-dimensional (space and time) Fourier transform [167, 168], in the SLaTCoW method, after the time-domain Fourier transform

$$\tilde{u}(x, \omega) = \int_0^T u(x, t) e^{i\omega t} dt, \quad (3.2)$$

a spatial Laplace transform is then applied:

$$\bar{u}(s, \omega) = \int_0^L \tilde{u}(x, \omega) e^{-sx} dx, \quad (3.3)$$

where $s = s_r + is_i$ is the complex variable of Laplace. According to Eq. (3.3), it is interesting to note that the quantity $\bar{u}(s, \omega)$ corresponds exactly to the results one would have obtained with a Fourier transform as soon as the imaginary part of s (s_i) is set to zero:

$$\bar{u}[s(s_r, s_i = 0), \omega] = \tilde{u}(k_r, \omega), \quad (3.4)$$

therefore implying that the dispersion curves in the real plane could be retrieved from $\bar{u}[s(s_r, s_i = 0), \omega]$. The idea of the method is to compared the quantity $\bar{u}(s, \omega)$ obtained from the experimental data to a model. Let us assume that the wave field could be written as the sum of the contributions of each of the modes in the frequency domain [158]:

$$\tilde{u}_{th}(x, \omega) = \sum_n \bar{A}^n e^{ik^n x} \Pi(x - L) e^{-i\omega t}, \quad (3.5)$$

where the time dependence has been omitted for clarity and where x denotes the spatial coordinate, \overline{A}^n and k^n are the complex amplitude and the complex wavenumber of the n -th mode, respectively. Note that in our case, the number of modes n is equal to 3 which denotes the three detected Lamb modes: S_2 , S_1 , and A_1 . After applying the Laplace transform to $\tilde{u}_{th}(x, \omega)$, the theoretical expression $\overline{u}_{th}(s, \omega)$ to which the experimental results will be compared takes the following form:

$$\begin{aligned} \overline{u}_{th}(s, \omega) &= \sum_n \overline{A}^n \int_0^L e^{i(-s+k^n)x} e^{-i\omega t} dx \\ &= L \sum_n |\overline{A}^n| \frac{[\sinh(ik^n - s)\frac{L}{2}]}{[-s + ik^n\frac{L}{2}]} e^{i\phi^n + (-s+ik^n)\frac{L}{2}} e^{-i\omega t}. \end{aligned} \quad (3.6)$$

The recovery of the complex wavenumbers of the three modes is finally performed, frequency by frequency, by minimizing the following cost function:

$$f_{opt}(\omega) = \sqrt{\sum_{s_r} \sum_{s_i} \|\overline{u}(s, \omega) - \overline{u}_{th}(s, \omega)\|^2}. \quad (3.7)$$

Note that the minimization is performed under constraints with the Nelder-Mead simplex algorithm with the use of the function *fminsearchbnd* in MATLAB. For details and other applications of the SLaTCoW method which are beyond the scope of this manuscript, the readers are referred to the article of Geslain *et al.* [158].

For the comparison with the experimental results, the theoretical dispersion curves in the complex plane are computed, using the results obtained from the solution of the ‘‘Eigen Value Problem’’ method proposed by V. Pagneux [74] as the initial values for the Mller method (searching for zeros of a complex function), as discussed in Chap.2. The attenuation used to plot the theoretical curves is taken from the literature as 0.4 dB/cm/MHz (measured via longitudinal waves propagating along direction [100]) in Aluminum [146, 148] and as 0.12 dB/cm/MHz (measured via longitudinal waves propagating along the [100]-axis at 150 MHz) in Copper [152]. In Fig. 3.5, the calculated dispersion curves and the results obtained from the measurements by the SLaTCoW method are shown. Fig. 3.5(a)-(b) show the dispersion curves in the real plane (k_r, f) for the Aluminum and the Copper plates, Fig. 3.5(c)-(d) show the dispersion curves in the plane (k_i, f), accordingly: the experimental results for the S_2 mode are depicted by red circles, those for the S_1 mode by blue cross; the dispersion curves calculated without attenuation are in black dash-dotted and dotted lines for the S_2 and S_1 modes, respectively; the dispersion curves calculated with attenuation are in red dashed and blue solid lines for the S_2 and S_1 modes, respectively. Note that, for the sake of the presentation, the measured curve corresponding to the S_1 mode that should have been where k_r is negative in Fig. 3.5(a)-(b) is shown at the position of the mode S_{-1} (positive k_r). Note also that, when close to the position of the ZGV point, the signal-to-noise ratio (SNR) decreases due to the attenuation, which explains why there is no experimental points shown in Fig. 3.5(a)-(d) close to the position of the ZGV point. In Fig. 3.5(c)-(d), the recovered imaginary parts of the wavenumber for the S_1 mode are larger than those recovered for the S_2 mode, which is explained by the smaller

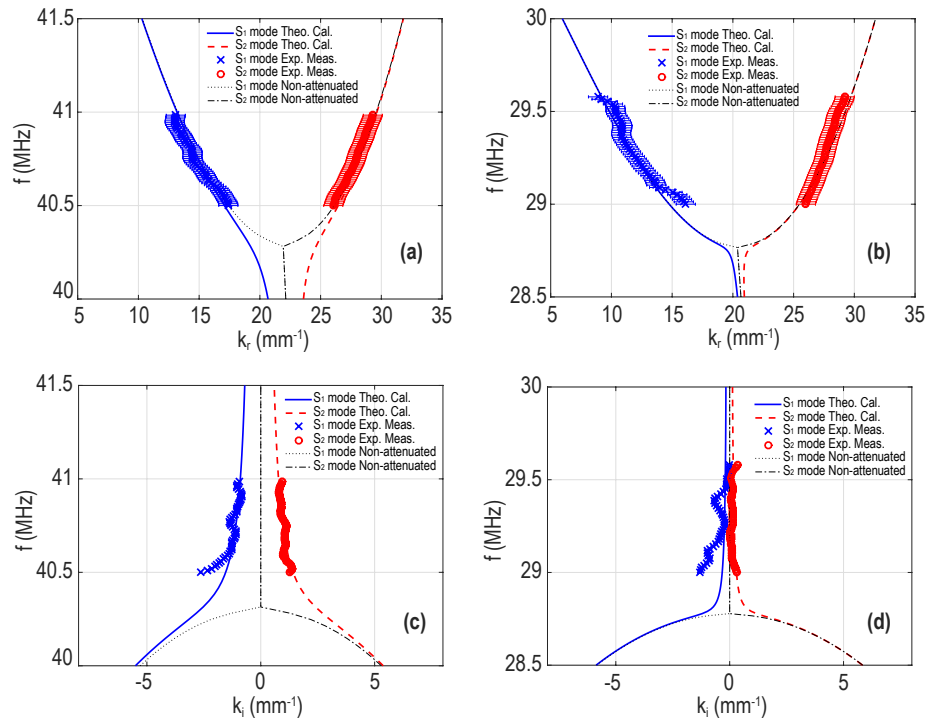


Figure 3.5: Theoretical and experimental dispersion curves in (a-b) the real plane (k_r, f) and (c-d) the plane (k_i, f) for [(a) and (c)] a plate made of Aluminum and [(b) and (d)] a plate made of Copper.

amplitude of the S_1 mode compared to that of the S_2 mode in the measurements [see Fig. 3.4(c) and (f)]. The experimental results show good agreement with the theoretical ones where the attenuation is taken into account. In the real plane, there is no much difference between the case with or without attenuation. However, the effect of the attenuation (repulsion of the branches as discussed in Chap. 2) is clearly observed experimentally when the imaginary part of the wavenumber is recovered [Fig. 3.5(c)-(d)].

The extra information given by k_i is useful to get the ultrasonic attenuation of the tested sample. To do so, a minimization process, with the attenuation as parameter and allowing the best fit (least mean square) of the experimental dispersion curves (in the complex plane) to the theoretical dispersion curves accounting for attenuation, is performed. This process is illustrated in Fig. 3.6. The experimental results shown in Fig. 3.5(c)-(d) in the plane (k_i, f) are reported in Fig. 3.6(a) and Fig. 3.6(b) for the Aluminum and the Copper plates, respectively. The color map shown in Fig. 3.6(a)-(b) stand for the change in the position of the S_2 and S_1 branches with changing the ultrasonic attenuation α from 0 dB/cm/MHz (bright yellow) to 1 dB/cm/MHz (dark blue): the larger the attenuation, the larger the distance between the two branches in the plane (k_i, f). The minimization process is illustrated in Fig. 3.6(c) and Fig. 3.6(d) for the Aluminum and the Copper plates, respectively. The three plotted curves show, as a function of the attenuation α , the quantity Δk_i which is the sum over the frequencies of the absolute-value differences between measured

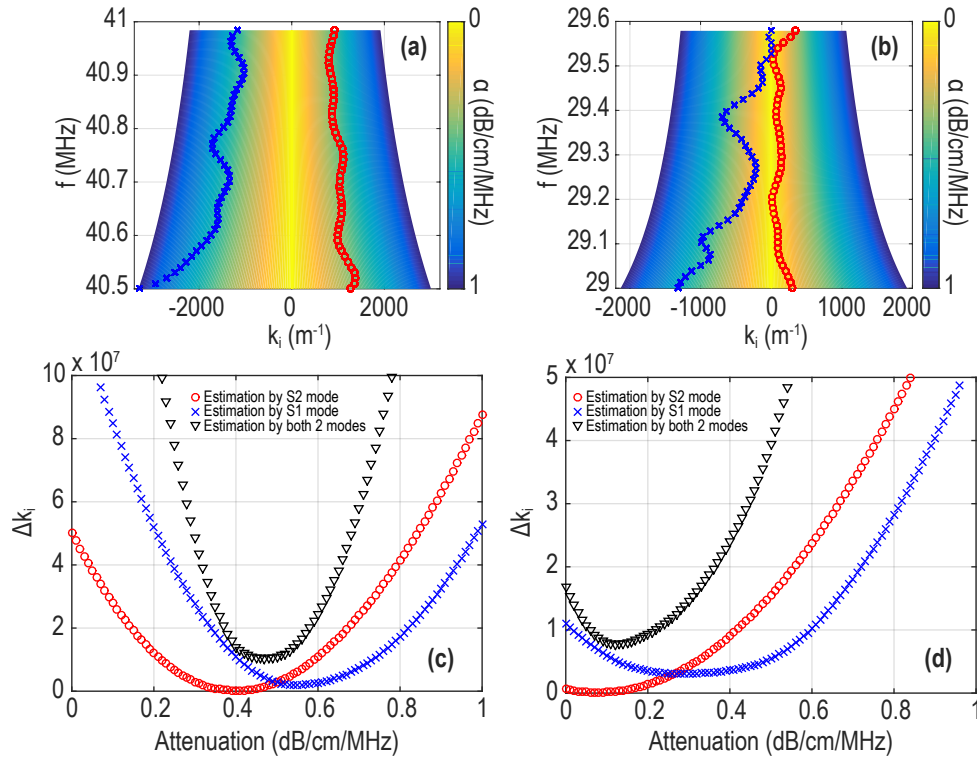


Figure 3.6: Illustration of the minimization process: map in the plane (k_i, f) , for (a) Aluminum and (b) Copper, of the change in the position of the S_2 and S_1 theoretical branches with changing the ultrasonic attenuation α from 0 dB/cm/MHz (bright yellow) to 1 dB/cm/MHz (dark blue), the experimental results shown in Fig. 3.5(c)-(d) are also reported; curves showing the evolution of Δk_i vs. α for (c) Aluminum and (d) Copper, calculated with the S_2 mode (red circles), the S_1 mode (blue crosses), and both the S_2 and S_1 modes (black triangles).

(k_i^{exp}) and calculated (k_i^{th}) imaginary parts of the wavenumbers:

$$\Delta k_i(\alpha) = \sum_{n=1}^N |k_i^{exp}(f_n) - k_i^{th}(f_n, \alpha)|^2. \quad (3.8)$$

In the figures 3.6(c) and (d), the red circles, the blue crosses, and the black triangles represent $\Delta k_i(\alpha)$ in the following three cases: (i) using only experimental and calculated results of the S_2 mode, the attenuation is then named α_2 and is estimated to be 0.40 ± 0.01 dB/cm/MHz in Aluminum and 0.07 ± 0.01 dB/cm/MHz in Copper; (ii) using only experimental and calculated results of the S_1 mode, the attenuation is then named α_1 and is estimated to be 0.54 ± 0.01 dB/cm/MHz in Aluminum and 0.28 ± 0.01 dB/cm/MHz in Copper; (iii) using experimental and calculated results of both the S_2 and S_1 modes, the attenuation is then named α and is estimated to be 0.47 ± 0.01 dB/cm/MHz in Aluminum and 0.12 ± 0.01 dB/cm/MHz in Copper. The obtained ultrasonic attenuation values are shown in Tab. 3.2 together with the one from the literature, for both Aluminum and Copper, which shows good agreement. Note that the proposed precision ± 0.01 comes from the step used in the calculation for the parameter α . For both materials, the attenuation α_1 obtained by using only

the results of the S_1 mode is larger than α_2 obtained with the S_2 mode and than the attenuation reported in the literature α_{lit} , which is due to the smaller amplitude of this mode compared to the amplitude of the S_2 mode in the measurements [see Fig. 3.4(c) and (f)], although both modes should theoretically show the same amplitude.

As shown in Tab. 3.2, the values of the ultrasonic attenuation α estimated in this work is similar to those measured in the literature (in aluminum [146, 148] and in copper [152]), however the mechanisms for phonon attenuation are not the same. Several points should be mentioned here that could explain the difference between values estimated using the proposed method in this work and measured in the literature:

- the samples used in the literature are single crystals (attenuation is mainly due to coupling to electrons mediated by deformation potential), while the samples used in this work are polycrystalline plates (attenuation could be due to grain boundary scatter, interaction with dislocations, etc ...);
- the purity of the samples used in experiments are not exactly the same, for example, in Ref. [148] the purity of Aluminum is 99.999% or 99.999%, but the Aluminum sample used in this work is with purity of 99.0%;
- in the references [148, 152], they measured the ultrasonic attenuation along the principle symmetry directions in materials ([100], [110] and [111] in Aluminum [148] and [100] in Copper [152]), whereas the attenuation obtained in this work is measured along an unknown direction compared to the principle axis of the material;
- the low signal-to-noise ratio due to the attenuation where the estimation is done close to the ZGV point is the main source of measurement uncertainty in the experiment and could also be a source for the discrepancy.

Although the samples used in this study and those measured in the literature are not exactly the same (as pointed by the first point above), the results of ultrasonic attenuation (α) obtained in this work (see Tab. 3.2) are still inspiring. Hence, the comparison with α measured by other means on the same tested sample could lead to strengthen the confidence in our results in order to fully demonstrate the quantitative measurement ability of the proposed method. Furthermore, the all-optical technique proposed in this chapter, based on slowly propagating mode in the vicinity of the ZGV point, could also give access to the local mechanical properties and thickness of the sample by using the value of the ZGV resonance frequency. Therefore, the method shows good ability for determining, at the same time, the mechanical properties and the ultrasonic attenuation of samples with plate-like structures.

Before the conclusion of this chapter, we propose hereby another application of the SLaTCoW method for future work: the monitoring of cumulative damage in materials through the estimation of the ultrasonic attenuation from experimental

[†]Reference [148].

[‡]Reference [152].

Table 3.2: Estimated ultrasonic attenuations in Aluminum and Copper.

	Aluminum	Copper
Attenuation (dB/cm/MHz) α_2	0.40±0.01	0.07±0.01
Attenuation (dB/cm/MHz) α_1	0.54±0.01	0.28±0.01
Attenuation (dB/cm/MHz) α	0.47±0.01	0.12±0.01
Attenuation (dB/cm/MHz) α_{lit}	0.4 [†]	0.12 [‡]

measurements done at different stages of the fatigue process (see details in **Perspectives** on page 135). Indeed, as the material would fatigue, an increase in the ultrasonic attenuation would be expected. Its monitoring should hence be informative and could lead to insightful information about the fatigue progress and stage.

3.5 Conclusion

In conclusion, this chapter presents the application of the SLaTCoW method to the ZGV Lamb modes in order to extract the ultrasonic attenuation of different metallic materials by taking into account the radiation in the air. With spatial Laplace transform, the dispersion curves in the complex plane can be reconstructed and be used for extraction of the values of the ultrasonic attenuation. With the same set of measurements, it is also possible to measure the mechanical properties and the thickness of the tested plate, making the proposed method a handy and versatile tool for material characterization. The experimental results are compared with values reported in the literature which were measured by other means. A minimization procedure is also established by varying the value of attenuation and shows the capacity of this proposed inverse method for estimation of ultrasonic attenuation in metals. It has been also proposed that this method can be very useful in non-destructive evaluation, such as the extraction of attenuation evolution in cumulatively damaged plate structure. Therefore, one of the research focus in the future could be the comparison of the ultrasonic attenuation between intact and damaged (bending, tensile testing, three points testing, ...) specimens for better understanding of the nature of specific type of damages in metallic materials and alloys.

Chapter 4

Laser ultrasonic evaluation of cumulative fatigue damage in thin films using zero-group-velocity Lamb modes

Contents

4.1	Introduction	72
4.2	Description of the fatigue test configuration	74
4.3	Experimental results and analysis	77
4.3.1	Experimental results	77
4.3.2	Analysis	81
4.3.3	Observation of a specimen during the fatigue test under microscope	82
4.4	Empirical model and numerical analyzes	83
4.4.1	Empirical model	83
4.4.2	Numerical model based on FEM	88
4.5	Conclusion	96

Keywords: *ZGV Lamb mode, Cumulative fatigue damage, LU, NDE, FEM.*

The wise man prevents evil rather than using remedies; he avoids pain rather than resorting to relief. — Thomas More

In this part of my work, a non-contact evaluation of cumulative fatigue damage in 75 μm -thick metallic plates is conducted by using the S_1S_2 -ZGV Lamb mode. The tested Aluminum sheets are subjected to fatigue loading, in a two sides clamped compression configuration inducing buckling. An empirical model based on cumulative damage theory completed with a numerical simulation based on finite element method (FEM) are also established, for comparison with the experimental measurements. The observed phenomena along fatigue cycles show the potential for prediction of fatigue lifetime and for qualitative and even quantitative assessment of different stages of fatigue damage in solid plate structures. The quality factor of the ZGV resonance is also experimentally studied and compared with numerical calculations. The difference between the experimental and numerical quality factors is identified as a potential path for the improvement of our empirical modelling in the future.

4.1 Introduction

In the last part of chapter 2, we have seen that the metal fatigue can lead to fatal failure, which makes this topic a research area of great importance for many decades. In chapter 3, we have seen that the all-optical ZGV-resonance-based technique shows good opportunity to measure at once the mechanical properties and the ultrasonic attenuation of plate-like structures. The goal of this chapter is to use the opportunity that gives the ZGV resonances to probe locally the thickness and the mechanical properties of a sample in order to monitor the fatigue life of a metal plate and to propose a reliable and reproducible way to assess at which stage of its fatigue life the metal plate is while being tested.

Material life time prediction, more precisely, the progressive fatigue failure prediction, is indeed always one of the key foundations of safety of the serving equipments, and it is also an important aspect of modern mechanical design and manufacture [86, 87, 169–171]. As a commonly utilized machine component, solid plate structures, such as metallic sheets, are often subjected to fatigue loads in service of engineering. Therefore, the evaluation of the cumulative fatigue damage in thin metallic films is of importance for lifetime prediction and then for reliability and security of practical engineering equipments/machines with such structures in service. During the last two decades, this scientific importance was repeatedly raised not only in the field of metallic materials but also in the field of other kinds of materials such as the composites [89, 91, 92, 95, 108, 139, 172–174].

For more than 70 years and following the seminal work by Miner [175], a tremendous number of research has been dedicated to propose theoretical expressions of an index D providing the cumulative fatigue damage in a material subjected to cyclic loading. This index intends to give an estimate of the state of fatigue of the material. To express the fatigue state, different material or nonmaterial parameters could be used, such as: the ratio between the current number of loading cycles and the number of cycles for the failure to occur, the density, the Young's modulus, the cross-sectional area of the damaged sample, etc. The mathematical expression of the cumulative fatigue damage index not only depends on the chosen parameter

but on empirically- or analytically-based assumption on the fatigue process. For instance, Miner [175] conceptually considered that part of the mechanical energy of the loading is absorbed by the fatigue process at each cycle. The amount of absorbed energy is moreover assumed by Miner to be the same at each cycle, which leads to consider that the cumulative damage linearly increases with the number of cycles, regardless of the loading sequence. This conceptual model has been shown to be limited since the irreversible micro-rupture process associated to D depends nonlinearly on the number of cycles. More realistic models have then been sought. We can cite, for instance, the Lemaitre-Plumtree model [176] that accounts for the fact that, for a strain-controlled cyclic loading, the stress response evolves due to material fatigue, while the Miner's theory states the response does not evolve. The cumulative damage index in the Lemaitre-Plumtree model therefore depends on a damage exponent, that in turn depends on the material mechanical property and on the strain amplitude of the cyclic loading. We focus here on the Miner's and Lemaitre-Plumtree's theory that we use in the following. For further theories and details, the readers are referred to the numerous review articles on the topic of cumulative fatigue damage, among which the author would like to enlighten the review articles by A. Fatemi and L. Yang [97, 140] for their completeness and the important work of method classification allowing a global view of the state of the art of the cumulative damage theory at a glance.

A majority of the reported damage index D evolves monotonously as a function of the number of loading cycles until the sample failure. This monotonous variation makes difficult the prediction of the failure since one should state a threshold after (above or below depending on the evolution of the chosen index) which the fatigue is said to be critical. Yet, if there exists an index which is non-monotonous as a function of loading cycles, it could be an efficient tool for the prediction of the failure as the presence of an extremum does not require the definition of a threshold quantitative value. In 2008, V.V.S. Jaya-Rao et al. [131] used a nonlinear ultrasonic (NLU) harmonic generation system to measure the surface acoustic wave nonlinearity in Aluminum alloy (AA7175-T7351). Their results showed that the evolution of the NLU parameter (A_2/A_1^2) as a function of the normalized fatigue lifetime is non-monotonous since two peaks were present. The observed non-monotonous change of the NLU parameter is therefore a good indicator for predicting the failure of the tested sample. However, their method is based on the propagation of the surface acoustic wave and therefore is a global measurement along the sample, which is not well suited to localize the fatigue cracks nor the fracture zone. To do the latter and to predict, at the same time, the sample failure, a method relying on a local probing of the sample is needed.

Several properties of the sample (geometrical, mechanical, etc.) evolve during the fatigue loading. To exhibit a non-monotonous variation, a parameter should either be sensitive to a property with a non-monotonous variation with loading cycles, which is unusual, or be sensitive to several properties that have opposite influence on it. The ZGV resonance peak is very sensitive to the local thickness [9, 10, 15, 24, 26] and to the local mechanical properties [11, 12] of plates, which both are changing when a sample is subjected to fatigue cycles. When the mechanical properties of the plate, such as the elastic modulus, the Poisson's ratio, and the density, are not

modified, the following relation between the variation Δf of the ZGV frequency f and the variation Δh of the thickness h holds

$$\frac{\Delta f}{f} = -\frac{\Delta h}{h}. \quad (4.1)$$

A decrease in the sample thickness with unchanged mechanical properties will therefore lead to a proportional monotonous increase of the ZGV frequency. In this chapter, we show that the ZGV resonance frequency undergoes a non-monotonous variation during the fatigue progress where the sample failure will occur. At the same time, an obvious difference on the ZGV frequency between damaged and undamaged regions is also clearly observed, which allows locating the fatigue damage. Both the localization and the monitoring of the fatigue process can then be achieved together thanks to the experimentally measured relative variation of the ZGV frequency ($\Delta f/f$) as a function of both the probed position (x) on the sample surface and the number of fatigue loading cycles (N), respectively.

This chapter is organized as follows: In this chapter, the experimental setup and the configuration of the cumulative fatigue tests are first described in Sec. 4.2. The main experimental results are then presented and supported by optical microscope observations in Sec. 4.3. In the following Sec. 4.4, an empirical model based on the cumulative fatigue damage theory is developed and used in a finite element numerical simulation, the purpose of which being to achieve frequency-wavenumber analyzes of the Lamb modes in a fatigued sample. The quality factor of the ZGV resonance is eventually discussed in this section before the conclusion.

4.2 Description of the fatigue test configuration

In order to fatigue the specimen, I have developed a “homemade” fatigue machine using a microcontrolled linear stage. The chosen fatigue test configuration is a two sides clamped compression inducing buckling as illustrated in Fig. 4.1(a). The unloaded plate [bottom in Fig. 4.1(a)] is originally of the length $2L$ with x -axis along the plate surface and z -axis normal to the unloaded plate surface. Each tested Aluminum sheet is first subjected to a compression where the plate buckled [top in Fig. 4.1(a)]: the compression is imposed by moving one of the sides of the fatigue machine where the sample is clamped (the left one in the figure) by $2\Delta L$ along x -axis towards the other side (the right one in the figure). Then a cyclic displacement of the same side (left) is imposed along x -axis, giving rise to the so-called loading cycles, until the specimen failure. Figure 4.1(b) shows the side-view photo of the loaded specimen whose profile is similar to a cosine function as shown in Eq. (4.2). The Fig. 4.1(c) is the top-view picture of the specimen that is unloaded to carry out the opto-acoustic measurements with the setup described in Fig. 3.2(a) in Sec. 3.3 of the previous chapter. Note that when the sample is unloaded, it is also straightened by applying a slight traction in order to obtain a flat surface necessary to get a good signal-to-noise ratio with the technique used for the detection (beam-deflection technique). Note also that the experiments are here done in the scanning configuration where the distance between the pump laser and the probe laser is set and where the sample is scanned [see Fig. 3.2(b)]. The green arrow in Fig. 4.1(c)

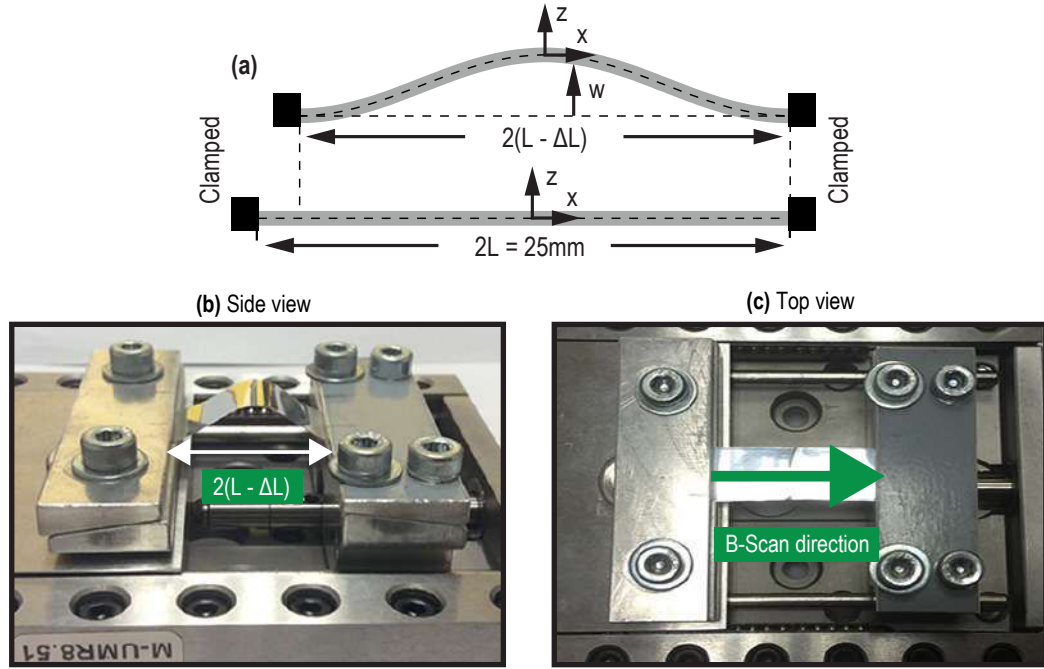


Figure 4.1: Fatigue configuration : (a) Illustration of the plate specimen loaded (top) and unloaded (bottom); (b) side-view photo of the loaded specimen; (c) top-view photo of the unloaded specimen.

denotes the direction of the scan. The unloading of the sample is performed at regular intervals of fatigue loading cycles in order to follow the change in the ZGV frequency all along the fatigue life.

In order to guide the development of the model, the knowledge of the stress distribution to which the plate is subjected while buckling is of interest. The bases of plate buckling are therefore now recalled. The normal deflection of a buckled plate can be expressed as [177]:

$$w(x) = \frac{\delta}{2} \left[1 + \cos \left(\frac{\pi x}{L - \Delta L} \right) \right], \quad (4.2)$$

where $x = 0$ is located in the center of the buckled plate, L is half the length of the plate, ΔL is half the displacement along the x axis of the moving part of the fatigue machine [Fig. 4.1(a)], and δ is the buckling deflection in the center of the specimen defined by [177, 178]:

$$\delta^2 = \frac{16(L - \Delta L)^2}{\pi} \frac{1 - \nu^2}{E} (\sigma_s - \sigma_c). \quad (4.3)$$

In Eq. (4.3), ν is the Poisson's ratio, E is the Young modulus (values are shown in Tab. 4.1 on page 89), σ_s is the central maximal stress, and σ_c is the critical stress. The expression of σ_c for a buckled plate is:

$$\sigma_c = \frac{T_c}{2h} = \frac{\pi^2}{12} \frac{E}{1 - \nu^2} \left(\frac{2h}{L - \Delta L} \right)^2, \quad (4.4)$$

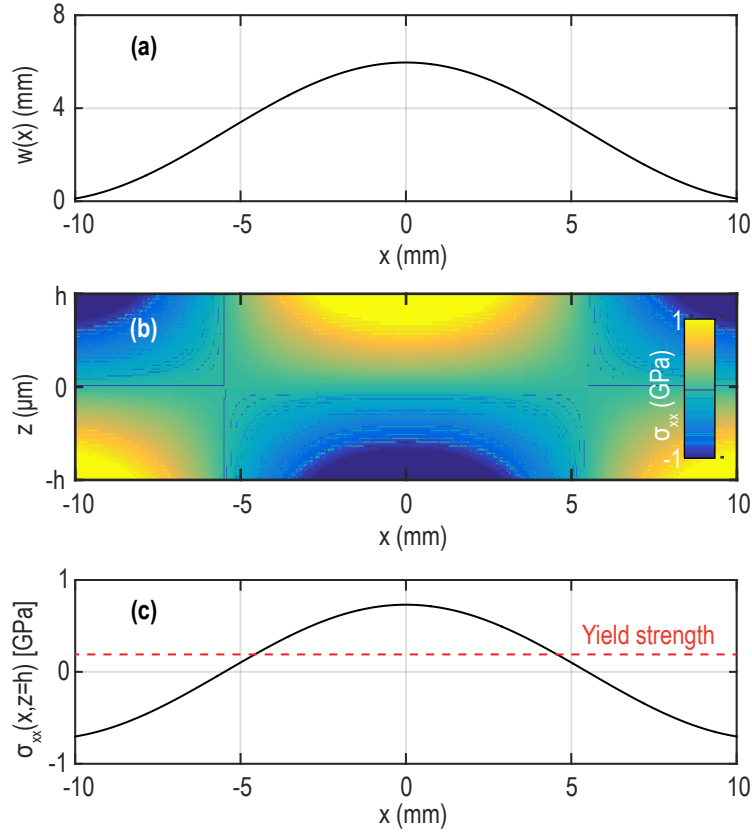


Figure 4.2: Buckling of a thin plate : **(a)** normal deflection of a plate with unloaded length of $2L = 25$ mm and shortening length of $2\Delta L = 5$ mm, **(b)** space distribution of the cross section stress σ_{xx} in (x, z) plane, and **(c)** surface stress distribution $\sigma_{xx}(x, h)$ (solid line) and specimen's tensile yield strength (dashed red line)

where $2h$ is the plate thickness and T_c represents the critical compression load at each clamped side and reads:

$$T_c = \frac{\pi^2}{12} \frac{2hE}{1 - \nu^2} \left(\frac{2h}{L - \Delta L} \right)^2. \quad (4.5)$$

The compression stress (which is also equal to the central maximal stress σ_s) can be obtained from the expression of the shortening ratio $\epsilon = \frac{1-\nu^2}{E} \sigma_s$. The shortening ratio ϵ can be experimentally estimated by using the plate original length and its buckled length as $\epsilon = \Delta L / (L - \Delta L)$ [177]. Then, from the plate bending/buckling theory (see the Eq. 4 in Ref. [179], where simplifications to match our case should be done), we have

$$\sigma_{xx}(x, z) = -\frac{12Dz}{(2h)^3} \frac{\partial^2 w}{\partial x^2}(x), \quad \forall (x, z) \in [-(L - \Delta L), L - \Delta L] \times [-h, h], \quad (4.6)$$

where $D = (2h)^3 E / [12(1 - \nu^2)]$. The formulation of the stress distribution of a buckled plate is eventually obtained:

$$\sigma_{xx}(x, z) = \frac{\delta \pi^2 E}{16(1 - \nu^2)(L - \Delta L)^2} z \cos \left[\frac{\pi x}{L - \Delta L} \right]. \quad (4.7)$$

In Fig. 4.2, the calculated buckled plate deflection (a), the cross section stress distribution $\sigma_{xx}(x, z)$ (b), and the surface ($z = h$) stress distribution (c) are presented in the case of an Aluminum plate. In Fig. 4.2(c) the dashed horizontal line stands for the tensile yield strength of Aluminum [86]. For more details on the buckling plate theory, readers are referred to the following references [177–181]. In our experiment, the specimen is unloaded at regular intervals of 500 cycles from the fatigue test system and probed each time using the pump-probe laser technique shown in Fig. 3.2(a) on page 61 to get the values of the S_1S_2 -ZGV resonance frequency along the scanning path. This means that for each position during the scanning, an opto-acoustic signal is measured and saved for spectral analysis. For each set of measurements, the scanning length, chosen to be 10 mm, corresponds to the estimated damaged region width, according to the value of the tensile yield strength and the stress distribution calculation [see Fig. 4.2(c)]. The scan is performed with a step of $100 \mu\text{m}$, i.e. 101 points of detection in total. The used motorized actuator provides a 50 mm travel range with a minimum incremental motion of $0.1 \mu\text{m}$, which is sufficiently accurate for our measurements.

Note that the measurements on the intact specimen are saved as the reference in order to make the comparison with all the other ones after the specimen is damaged.

4.3 Experimental results and analysis

4.3.1 Experimental results

In Fig. 4.3, an example of (a) a received laser ultrasonic temporal signal and (b) its frequency spectrum is plotted. A sharp peak at $\sim 38 \text{ MHz}$ [see inset in Fig. 4.3(b)] is observed and corresponds to the S_1S_2 -ZGV resonance frequency.

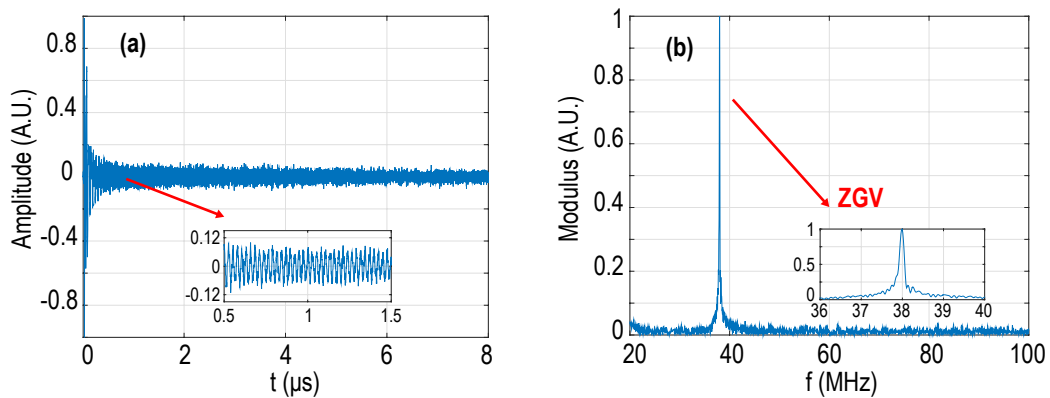


Figure 4.3: **(a)** Example of a received laser ultrasonic temporal signal on the intact specimen ($N = 0$) and **(b)** its fast Fourier transform (FFT) with a sharp peak corresponding to the S_1S_2 -ZGV resonance frequency

Several representative spatial distributions of the Fourier transform (FT) spectrum (magnitude normalized by the ZGV peak value) for different numbers N of fatigue cycles are depicted in Fig. 4.4 for the frequency range (y -axis) [30, 45] MHz and the scanning range x (x -axis) $[-5, 5]$ mm: (a) intact sample ($N = 0$), (b)

$N = 4000$, (c) $N = 6000$, (d) $N = 8000$, (e) $N = 9000$, and (f) $N = 11000$. The extracted ZGV frequency values in Fig. 4.4 are denoted by purple dashed lines.

The ZGV frequency values extracted in the intact case [see Fig. 4.4(a)] are considered as the reference. It is seen that the frequency value is not unique, even in the intact case, and lies in the range [38.45, 38.66] MHz due to initial thickness variation. The original thickness $2h$ of the intact specimen is therefore determined to lie in the interval [74.3, 74.7] μm . While the number N of fatigue cycles increases, an obvious increase of the ZGV frequency is observed in the center of the measurements (maximum increase at $x = 0.1$ mm) [see Fig. 4.4(b-e)]. The increase is mainly caused by the decrease of the local thickness in the fatigued region. After ~ 10500 fatigue cycles, a decrease of the ZGV frequency begins to emerge, as shown in Fig. 4.4(f) at $N = 11000$ for example. This drop in the ZGV frequency pursues until the specimen fails after about 12000 cycles.

Two other specimens (named specimen 2 and specimen 3) have also been prepared and subjected to the same experimental procedure. Their failure occurs after ~ 16000 loading cycles and after ~ 14000 loading cycles, respectively. In order to simplify the redaction and since the same phenomena as the one described above occur, the experimental results (the normalized FT spectra as in Fig. 4.4) will not be repeatedly presented here. The hypothesis of the decrease of the specimen's thickness will be shown true with the help of the observations under optical microscope of a fourth prepared Aluminum sheet (that failed after ~ 33000 cycles) presented in Sec. 4.3.3.

From Fig. 4.4, three main points could be explored : (1) the obvious difference in ZGV frequency between damaged and undamaged regions [see Fig. 4.4(b)-(e)]; (2) the monotonic increase of the ZGV frequency in the fatigued region to a certain level of fatigue [mainly caused by the change in the thickness, as explained by the relation between the thickness and the ZGV frequency in Eq. (4.1)]; (3) the abrupt decrease [see Fig. 4.4(f)] of the ZGV frequency before the specimen failure.

For a better observation of the third point, the variation of the ZGV frequency at $x = 0.1$ mm (central part of the fatigue zone) is extracted from the images and is plotted in Fig. 4.5(a) for specimen 1, where the error bars stand for $f_n/(f_0Q_n)$, with f_n the ZGV frequency after n cycles and Q_n the Q factor of the corresponding resonance.

The maximum value at 10000 loading cycles divides the curve into two different parts: (i) the monotonic increase where the thickness change is mainly at play and (ii) the abrupt decrease before specimen failure that could be explained by the drop in elastic stiffness [141, 182] and by the interaction between the ZGV resonance and the presence [155, 183–185] of dislocations/cracks in the specimen. Note that fatigue softening of materials can be found not only in metals [186, 187] but also in other types of materials, such as polymer [136] and composite materials [188]. The corresponding $\Delta f/f$, extracted from the three fatigue monitoring tests carried out on the three specimens (1, 2, and 3), are plotted in Fig. 4.5(b), showing identical variations in normalized fatigue lifetime scale, although the failure occurs at different amounts of loading cycles. This reproducible, non-monotonous parameter variation [see Fig. 4.5(b)], thanks to the existence of an extremum just prior to the fracture of the specimen (each time ~ 80 % of the fatigue lifetime), might establish

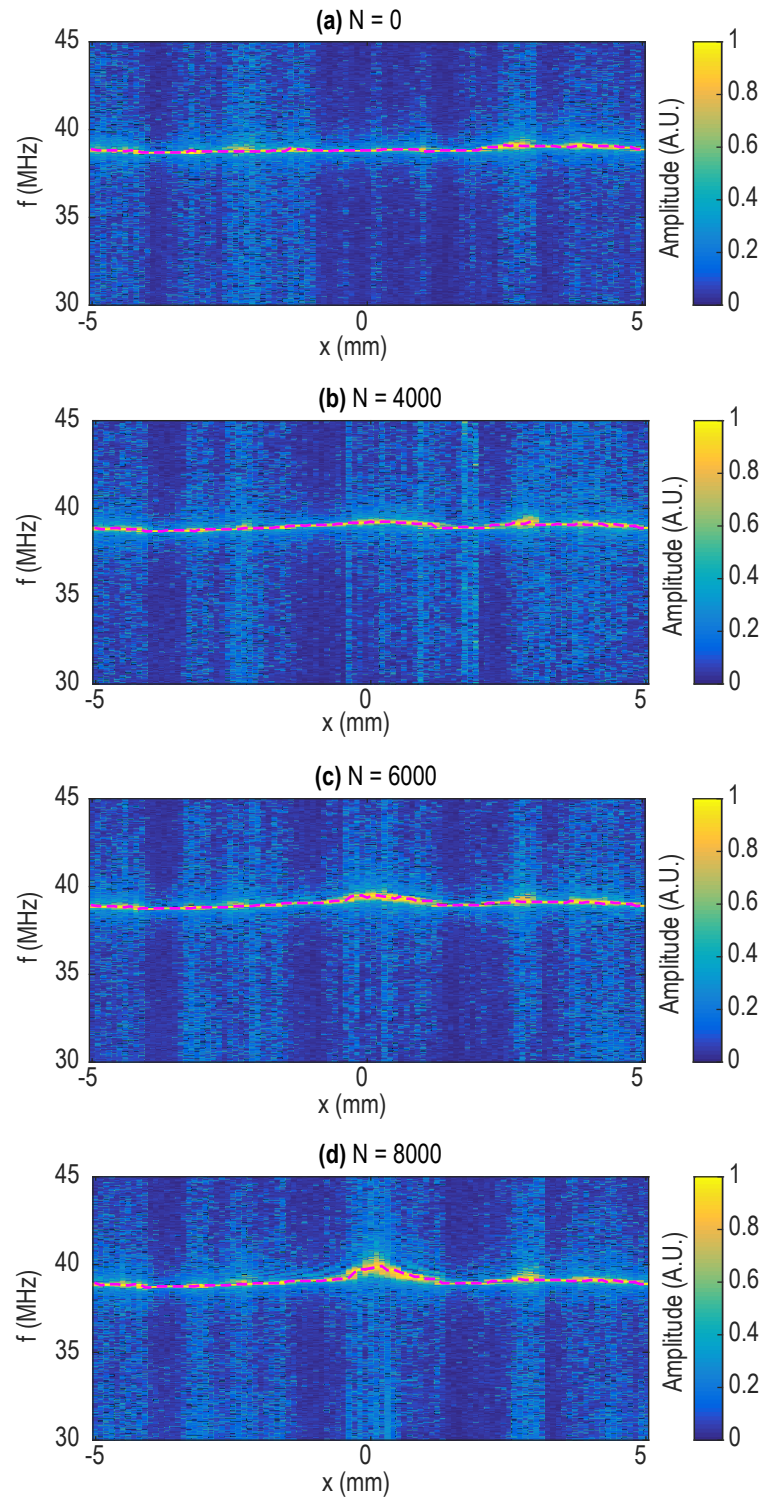


Figure 4.4: Several chosen experimental measurements : amplitude spectrum density as a function of frequency (f) and specimen position (x) for loading cycles (a) $N = 0$, (b) $N = 4000$, (c) $N = 6000$, (d) $N = 8000$, (e) $N = 9000$, and (f) $N = 11000$.

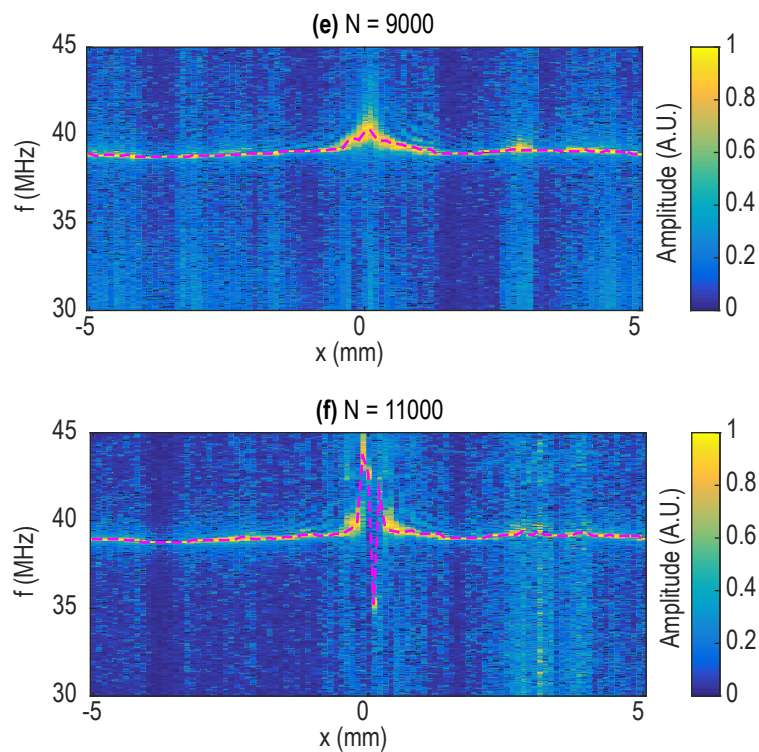


Figure 4.4: (Color online) Continued.

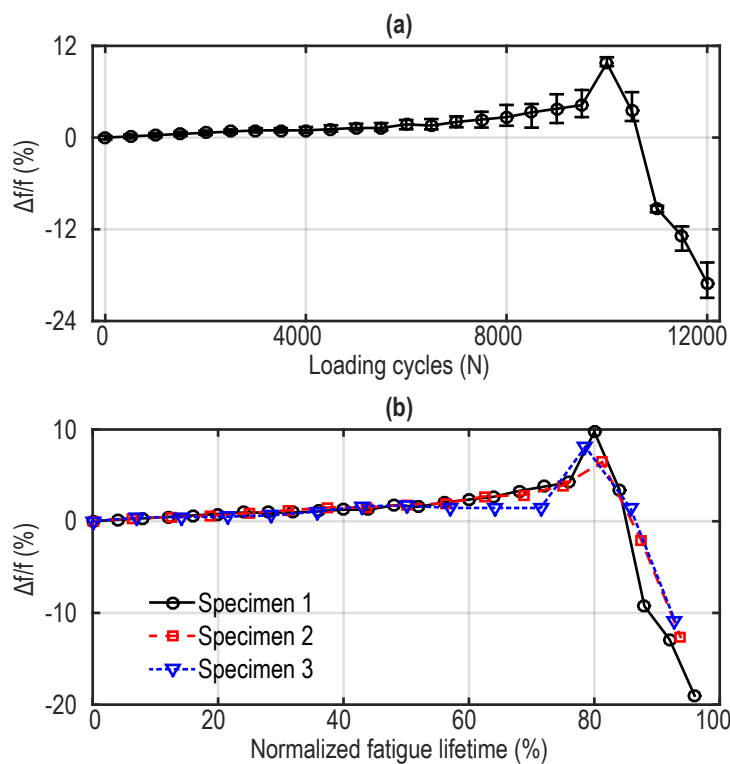


Figure 4.5: (a) Experimental evolution of $\Delta f/f$ (with error bars) as a function of fatigue duration at the center ($x = 0.1$ mm) of specimen 1. (b) Comparison of the evolution of $\Delta f/f$ measured in specimens 1, 2, and 3 (failure at approximately 12500, 16000, and 14000 cycles) as a function of normalized fatigue lifetime.

a quantitative empirical law characterizing the fatigue stage of any tested sample and could be an effective tool for predicting fatigue life.

4.3.2 Analysis

To analyze the experimental results, the spatial distributions of the variation of the ZGV frequency (depicted by the solid red lines in Fig. 4.4) are plotted on the same graph in Fig. 4.6 for the measurement done from 0 cycle to 9500 cycles, i.e. before the drop of the ZGV frequency. From Fig. 4.6, the spatial distributions could be qualitatively split into three zones: (1) the Zone I in the central part is similar to the curve of a narrow Gaussian function, this zone could be mainly associated to the cumulative damage; (2) the Zone II corresponds to the two adjacent portions close to the central zone which looks like a cosine function and could be associated to the influence of the residual buckling stress that is a cosine function as shown in Eq. (4.7); (3) the Zone III, away from the fatigued region, shows an offset of the ZGV resonance frequency which may be caused by the traction applied to the specimen when it is unloaded and straightened in order to obtain a flat surface for allowing a good acousto-optic detection during the spatial scanning measurements.

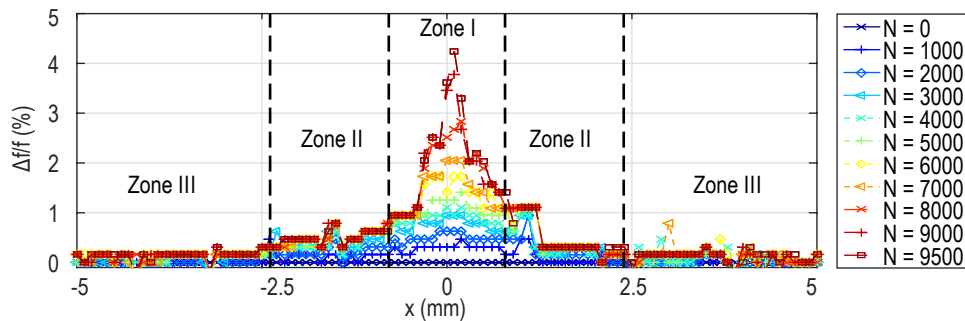


Figure 4.6: Experimental measurements of the spatial distribution of the ZGV resonance frequency for different fatigue cycles ($N = 0, 1000, 2000, \dots, 9000, 9500$) and their qualitative classification in three regions.

Moreover, from the experimental observations [see Fig. 4.4(c-e) and Fig. 4.6], as mentioned in Sec. 4.3.1, a very clear local increase of the ZGV resonance frequency in the center of the scanned area is observed. By considering the inversely proportional relation between the variation of the ZGV frequency and that of the plate thickness [see Eq. (4.1)] where the mechanical properties remain unchanged, the observed frequency increase is proposed to be explained by the local decrease of the plate thickness caused by the buckling-induced fatigue damage. In order to strengthen this analysis of the experimental results, the assumption that the decrease of the thickness is mainly at play here needs to be confirmed, for instance by a direct observation under optical microscope which is discussed in the next sub-section 4.3.3.

4.3.3 Observation of a specimen during the fatigue test under microscope

As discussed in Sec. 4.3.1, the hypothesis of the decrease of the thickness of the tested plates needs experimental approval via direct observation such as with the use of light microscope. Therefore, for better understanding of the progression and existence of the fatigue damage, we prepared another Aluminum specimen, with the similar size as the first three measured in this chapter, in order to take photos with a light microscope during the fatigue test until the failure. For a more precise observation of each stage of the damage during the fatigue progress, the loaded compression length is decreased to be $2\Delta L = 3$ mm (before it was 5 mm) in order to increase the number of fatigue loading cycles before failure. The specimen failure occurs in this case after ~ 33000 loading cycles. Three chosen photos are presented in Fig. 4.7(a-c), which are the top-view on the surface of the specimen after (a) 30000 cycles, (b) 32000 cycles, and (c) 33000 cycles.

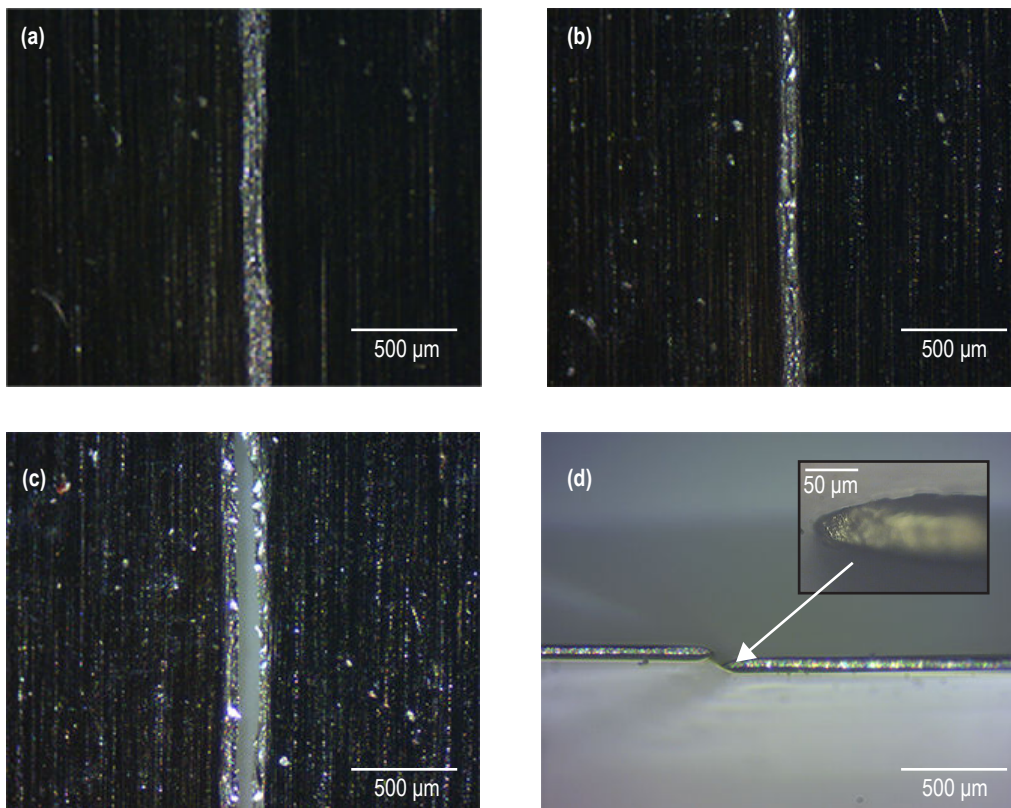


Figure 4.7: Top-view photos through optical microscope of the fatigue progression on a specimen at (a) 30000 cycles, (b) 32000 cycles, and (c) ~ 33000 cycles (specimen failure). (d) Side-view of the broken specimen after 33000 cycles under optical microscope showing symmetrical decrease of the thickness around the fracture.

In Fig. 4.7(a) and (b), an evident damage is seen in the center of the photos as a brighter zone than the surrounding material. Note that, while dark vertical line within the bright zone and corresponding to micro-crack are barely visible after

30000 cycles [see Fig. 4.7(a)], the specimen shows a clearly visible open crack with a very narrow width after 32000 cycles [see Fig. 4.7(b)], i.e. just some few cycles before its failure. In Fig. 4.7(c), the photo after the specimen broke into two pieces is shown.

From Fig. 4.7(a-c), it is very clear that there exists a visible vertical damage area (visible width of about $100\ \mu\text{m}$) in the center of the photos caused by the accumulation of the buckling induced fatigue. A fourth photo [see Fig. 4.7(d)] shows the side-view of the broken specimen. The decrease of the thickness in the middle of the tested specimen can be clearly observed. A zoomed image is also presented in the inset in Fig. 4.7(d), showing an evident symmetrical decrease of the thickness along the normal-to-the-plate-surface direction. Similar phenomena of a symmetrical thickness decrease around the crack have been also observed post-mortem, for the first three samples (not shown here).

The spatial distribution of the ZGV resonance frequency up to 9500 cycles for specimen 1 discussed in the previous section as well as the above demonstration of a symmetrical decrease of the thickness around the crack location will be used for the construction of an empirical model of the thickness variation with respect to the number of cycles N , in turn used in a numerical model for frequency-wavenumber (f-k) analysis of the Lamb waves, as detailed in the next section 4.4.

4.4 Empirical model and numerical analyzes

To analyze the influence of the local variation of the plate thickness on the Lamb modes in general, and on the ZGV Lamb mode in particular, it is proposed to develop a numerical model. The aim of such a model, simulating the propagation of the laser-generated elastic waves in a plate having non uniform thickness, is to have a handy tool for parametric analyzes. From Fig. 4.7(d) in Sec. 4.3.3, especially the zoomed part in the inset, the decrease of the thickness provides the original idea for establishing an empirical model of the thickness distribution of the plate, to use in the numerical model, that takes into account the variation of the thickness in the (x, z) plane and independent of y owing to the symmetry imposed by the fatigue configuration [see Eq. (4.7)]. In this section, we therefore first introduce the empirical model of the evolution with the loading cycles of the thickness distribution. This model is based on the cumulative fatigue damage theory. The mathematical expression of the thickness distribution is then used for the numerical simulations, the results of which are analyzed and eventually compared to the experimental results discussed in Sec. 4.3.

4.4.1 Empirical model

The numerous empirically- or analytically-based theories of cumulative fatigue damage provide different definitions of the local damage index D depending on the observable and observed parameter. Following the above-discussed experimental observations, it is here proposed to relate the definition of D to the variation of the cross-section, i.e. to the thickness variation, of the specimen under repeatedly loading.

For each spatial position of the measurements, the decrease of the local cross section is equal to the product of the local variation of the thickness [$h(N, x) - h(0, x) = 2\Delta h(N, x) \leq 0$] and the differential of the variable y (dy). Note that when the sample is intact ($N = 0$), $\Delta h(0, x)$ is zero for all x . For a given number of loading cycles N , the remaining local cross section of the specimen is denoted as $\tilde{A}(N, x) = 2(h(0, x) + \Delta h(N, x))dy$. Then, the experimental local damage index $\tilde{D}(N, x)$ is proposed to be defined as follows:

$$\tilde{D}(N, x) = \frac{\tilde{A}(N, x) - \tilde{A}(0, x)}{\tilde{A}(0, x)} = \frac{\Delta h(N, x)}{h(0, x)}. \quad (4.8)$$

Note that, since $\Delta h(N, x)/h(0, x)$ decreases from 0 ($N = 0$) to -1 ($N = N_f$) as N increases, so is the damage index \tilde{D} . According to Eq. (4.1), the chosen experimental local damage index is therefore equal to the opposite of the ratio of the variation of the ZGV resonance frequency [$\Delta f(N, x)$] to the ZGV frequency when the sample is intact [$f_{ZGV}(0, x)$]:

$$\tilde{D}(N, x) = -\frac{f_{ZGV}(N, x) - f_{ZGV}(0, x)}{f_{ZGV}(0, x)} = -\frac{\Delta f(N, x)}{f_{ZGV}(0, x)}. \quad (4.9)$$

Since the proposed experimental local damage index $\tilde{D}(N, x)$ is related to the local relative variation of the plate thickness, it is now proposed to formulate a theoretical model of the damage index, denoted D , based on the fatigue theory, in order to have at hand an empirical model of $\Delta h(N, x)/h(x)$ to implement in the numerical model discussed in the next subsection 4.4.2. The theoretical damage index $D(N, x)$ is proposed to be the sum of three terms corresponding to the three different influences over the three zones discussed in Sec. 4.3.2:

$$D(N, x) = -[a_c D_c(N, x) + a_b D_b(N, x) + a_t D_t(N)] , \quad (4.10)$$

where a_c , a_b , and a_t stand for constant coefficients allowing the overall balance between the contribution of D_c , D_b , and D_t , respectively, to the theoretical damage index D . Note that the minus sign in front of the square brackets in Eq. (4.10) stands for the fact that D is imposed to be negative, since \tilde{D} is negative. Three origins of the fatigue damage are therefore considered in the theoretical model: (i) D_c that accounts for the cumulative damage, (ii) D_b that accounts for the global damage induced by the buckling-caused residual stress, and (iii) D_t that accounts for the global traction applied to the specimen allowing the laser ultrasonic measurements (need of a flat surface, see Sec. 4.2). The expression of these three terms are now separately proposed and discussed.

Although it is not true in the current fatigue test since the controlled parameter is the imposed displacement of a clamped side of the plate, it is considered that the cyclic loading is strain-controlled. Therefore, the part of the theoretical damage index associated to the cumulative damage, D_c , is proposed to be modelled using the Lemaitre-Plumtree rule [140, 141, 182] that accounts for the evolution of the stress response of the material due to the material fatigue in a strain-controlled

cyclic loading:

$$D_c(N, x) = \left[1 - \left(1 - \frac{N}{N_f} \right)^{1/(1+P_N)} \right] \exp \left[-4 \ln 2 \frac{(x - \Delta x)^2}{\sigma^2} \right], \quad (4.11)$$

where N_f is the number of cycles to produce a critical amount of damage (as outlined in Ref. [176]) and P_N , a dimensionless quantity, represents the damage exponent which depends on the plastic strain amplitude. Note that the value of P_N can range from one-digit number to two-digit number [182]. In Eq. (4.11), the Lemaitre-Plumtree rule dictates the dependence of D_c on N . Assuming that the cumulative damage is concentrated in the center of the plate where the imposed fatigue stresses are the largest [see Fig. 4.2(c)], the spatial distribution of the effect of the cumulative damage is proposed to be modeled with a narrow Gaussian distribution along the scanning distance x with the parameters σ (FWHM) to control its width and Δx to control the position of its maximum. The Gaussian distribution is here proposed after the experimental observations of the spatial distribution of the relative variation of the ZGV frequency (see Fig. 4.6) and that of the optical microscope [see inset in Fig. 4.7(d)]. According to the stress distribution [see Fig. 4.2(c)], the extent of the damage in the centre of the plate should increase quicker than that in the side parts. The Gaussian distribution width σ should thus rigorously decrease as N increases, hence concentrating the damage more and more to the center. Yet, looking at the experimental results of the distribution in Fig. 4.6, the Gaussian distribution width in Zone I is observed to be quasi-constant. It has thus been assumed to set σ to be constant in Eq. (4.11).

For the other two terms of D , D_b and D_t , the Miner-linear damage hypothesis [140, 175] is considered to model their dependence on N : linear dependence of the form N/N_f . Indeed, it is assumed that the metal fatigue is weaker in Zone II and Zone III and, therefore, that the stress response evolves linearly with N . Since the buckling-caused residual stress has the form of a cosine function with respect to x [see Eq. (4.7)], so is the spatial distribution of D_b , which leads to the following expression:

$$D_b(N, x) = \frac{N}{N_f} \left| \cos \left(\pi \frac{x - \Delta x}{L + \delta l} \right) \right|, \quad (4.12)$$

where δl stands for the elongation of the specimen due to the traction (assumed to be the same for all unloading) and the absolute value accounts for the fact that, whether the loading stress is positive or negative, it contributes to the damage the same way. Note that the latter is an assumption to simplify the model and barely correct since it is known that materials usually present greater yield strength in compression than in tension. The global traction applied to the plate and related to D_t is assumed to be uniaxial, implying that its effect on the plate thickness does not depend on x and therefore that:

$$D_t(N) = \frac{N}{N_f}. \quad (4.13)$$

Following Eqs. (4.10)-(4.13), the expression of the theoretical damage index

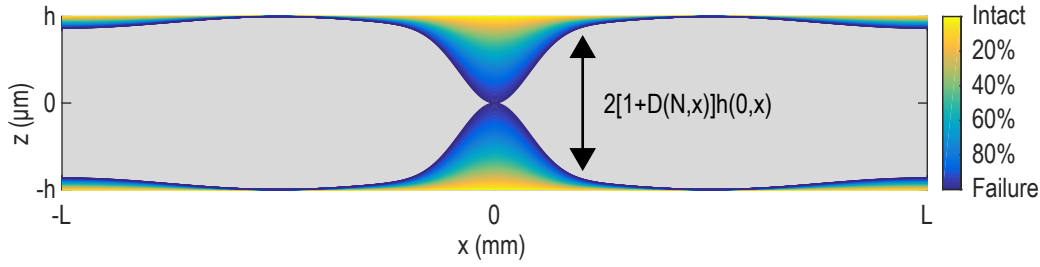


Figure 4.8: Illustration of the change in the specimen profiles caused by the fatigue damage. The gray background represents the remaining section of the plate after N_f fatigue cycles and the different color shades stand for the evolutive profiles of the plate subjected to fatigue damage: from the intact situation (light yellow) to the failure (dark blue) as indicated by the color bar. Numerical values of the input parameters for the calculation are: $P_N = 50$, $\sigma = 1$ mm, $\Delta x = 0$ mm, $2L = 25$ mm, $\delta l = 0.1$ mm, $a_c = 0.98$, $a_b = a_t = 0.01$, and the ratio $N/N_f \in [0\%, 100\%]$.

$D(N, x)$ eventually reads:

$$D(N, x) = - \left\{ a_c \left[1 - \left(1 - \frac{N}{N_f} \right)^{1/(1+P_N)} \right] \exp \left[-4 \ln 2 \frac{(x - \Delta x)^2}{\sigma^2} \right] + a_b \frac{N}{N_f} \left| \cos \left(\pi \frac{x - \Delta x}{L + \delta l} \right) \right| + a_t \frac{N}{N_f} \right\}. \quad (4.14)$$

Note that, at the center of the fatigue zone ($x = \Delta x$), D_c , D_b , and D_t equal to 1 for $N = N_f$, meaning that $D(N_f, \Delta x) = -(a_c + a_b + a_t)$. Since the minimum of D is -1 according to the chosen definition of the experimental local damage index \tilde{D} , the sum of the three coefficients is therefore imposed to be equal to 1. Assuming that $\tilde{D} = D$, the thickness distribution of the plate after N loading cycles therefore reads:

$$2h(N, x) = 2 [1 + D(N, x)] h(0, x). \quad (4.15)$$

Using Eq. (4.15), an illustration of the influence of the fatigue damage on the plate thickness is proposed in Fig. 4.8, where the following numerical values of the parameters are used: $P_N = 50$, $\sigma = 1$ mm, $\Delta x = 0$ mm, $2L = 25$ mm, $\delta l = 0.1$ mm, $a_c = 0.98$, $a_b = a_t = 0.01$, and the ratio $N/N_f \in [0\%, 100\%]$. The color shades in Fig. 4.8 stand for the evolutive profiles of the plate subjected to fatigue damage: from the intact situation (light yellow) to the failure (dark blue) as indicated by the color bar. Note that the damaged profiles on the top and the bottom sides of the plate (see Fig. 4.8) look well appropriate to match the experimental observations of the distribution of the relative variation of the ZGV frequency [see Fig. 4.7(d)].

Now that the model of the evolution of the thickness distribution of the plate with the number of loading cycles has been established, it is proposed to look for the parameters of that model to use in the numerical modeling of the next section. The parameters of the theoretical model to use are the ones that would allow the best fitting of the theoretical damage index D to the experimental damage index \tilde{D} . The known parameters are fixed as follow for the specimen 1: $N_f = 12500$,

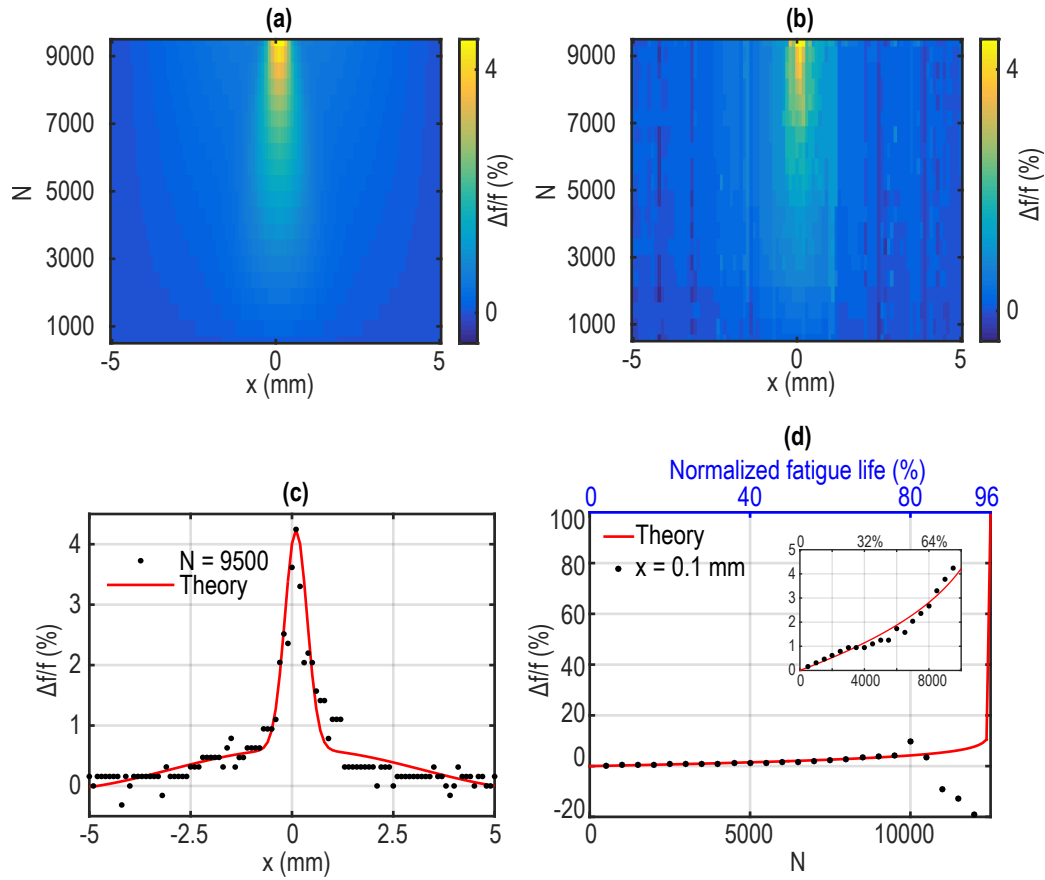


Figure 4.9: Comparison between theoretical model and experimental results: (a) distribution of theoretically calculated $\Delta f/f$ as a function of the number of loading cycles N and of the lateral position x ; (b) distribution of experimental $\Delta f/f$ as a function of the number of loading cycles N and of the lateral position x ; (c) comparison between experimental results and the theoretical fitting after 9500 fatigue cycles; (d) theoretical and experimental evolution of $\Delta f/f$ in the center of the fatigued region (at $x = \Delta x = 0.1$ mm) as a function of the number of the loading cycles N .

$\Delta x = 0.1$ mm, and $2L = 25$ mm. The recovery of all the other parameters in Eq. (4.14) is therefore achieved by minimizing the quadratic relative differences between \tilde{D} and D as shown in the following cost function \mathcal{F} , under the constraints that $a_c + a_b + a_t = 1$:

$$\mathcal{F}(P_N, \sigma, \delta l, a_c, a_b, a_t) = \sum_N \sum_x \left\| \tilde{D}(N, x) - D(N, x, P_N, \sigma, \delta l, a_c, a_b, a_t) \right\|^2. \quad (4.16)$$

The minimization is performed under constraints with the Nelder-Mead simplex algorithm by using the Matlab function `@fminsearch`.

After the inverse estimation from Eq. (4.16), the unknown parameters are determined to be: $P_N = 44.37$, $\sigma = 0.58$ mm, $\delta l = 0.1$ mm, $a_c = 0.99$, $a_b = 0.004$, and $a_t = 0.006$. We note here that the minimization is done by considering only $N \in [0, 9500]$, because the proposed model accounts exclusively for the thickness

change and not for the softening (drop of the ZGV frequency as shown in Sec. 4.3).

In Fig. 4.9, the spatial distribution of the relative variation of the ZGV frequency $\Delta f/f$ is plotted as a function of the number of fatigue loading cycles for: (a) the theoretical case using the previously determined parameters and assuming that $\Delta f/f$ is equal to $-D$ [Eq. (4.14)] and (b) the experimental case. The comparison between the theory (solid lines) and the experimental measurements (points) for two specific cases, i.e. the spatial distribution of $\Delta f/f$ at $N = 9500$ and the evolution of $\Delta f/f$ as a function of loading cycles in the center of the fatigued zone ($x = \Delta x = 0.1$ mm) are also illustrated in Figs. 4.9(c)-(d), respectively. From Fig. 4.9(a-c), good agreement is shown between the experimental results and the opposite of the cumulative fatigue damage index. In Fig. 4.9(d), the experimental measurements and the theoretical calculations agree well in for $N \in [0, 9500]$, as shown in the inset. After $N = 9500$, the solid red line (theory) is separated and continue to increase where the experimental results decreases. This is because the empirical model is proposed by considering only the thickness variation (as explained in previous paragraph). For details of the huge amount of other theoretical models of cumulative damage which are out of the scope of this paper, readers are referred to the following reviews/articles [140, 141, 176, 182] and also to the references in these publications.

To conclude this subsection, it worth stressing out that the model is not meant to be exact or strictly rigorous. Indeed, for this empirically-based theoretical model to be fully validated, further direct micro-observation, by electron microscope for example, should have been performed but are out of the scope of my work. Having explained the underside of the expressions composing the model, the latter is supposed to correctly depict the fatigue-based thickness change of the plate. It is now proposed to use the theoretical expression of the plate thickness distribution $2h(N, x)$ [see Eq. (4.15)] to define the geometry of the fatigued plate in a numerical model purposing to perform frequency-wavenumber (f-k) analyzes of the Lamb modes in such a fatigued sample.

4.4.2 Numerical model based on FEM

The numerical calculations to perform f-k analyzes of the Lamb modes in a fatigued sample are realized using a commercial software (Comsol MultiphysicsTM) based on the finite element method (FEM). By considering that our laser beam is focused to a line, the problem is simplified to a two-dimensional problem in the (x, z) plane owing to the symmetry imposed by the source shape, and the acoustic wave equation in its vectorial expression is written as:

$$\nabla \cdot [\mathbf{C} : (\nabla + \nabla^t)\mathbf{u}] - \rho \frac{\partial^2 \mathbf{u}}{\partial t^2} = \mathbf{S}, \quad (4.17)$$

where \mathbf{C} is the 4th order stiffness tensor, \mathbf{u} is the displacement field, ρ stands for the density of the material, and the source term \mathbf{S} in the right hand part is the gradient of the thermal stresses induced by the laser absorption, expressed as:

$$\mathbf{S} = [S_x, S_z]^T = \nabla \cdot [\mathbf{C} : \bar{\alpha} \Delta T]. \quad (4.18)$$

Table 4.1: Mechanical, thermal and optical properties of Aluminum plate used in this work for both theoretical calculations and numerical simulations.

	Value
Young's modulus (GPa) E	70
Poisson ratio ν	0.35
Density (kg/m^3) ρ	2700
Thickness (μm) $2h$	75
Pulse energy (μJ) I	70
Pulse duration (ns) τ	0.75
Pulse wavelength (nm) λ_L	1064
Pulse FWHM (μm) d	20
Absorption coefficient (%) η	6~7
Heat Capacity ($\text{J}/\text{kg}\cdot\text{K}$) C_p	897
Thermal expansion ($1/\text{K}$) α	$2.3\cdot 10^{-5}$
Penetration depth (nm) $1/\beta$	8.98
Thermal conductivity ($\text{W}/\text{m}\cdot\text{K}$) κ	237

In Eq. (4.18), $\bar{\alpha}$ is the thermal dilatation tensor. The temperature rise $T = T(x, z, t)$ could be calculated by solving the heat equation [189]:

$$\rho C_p \frac{\partial T(x, z, t)}{\partial t} - \kappa \nabla^2 T(x, z, t) = \beta I_0 e^{-\beta z} f(t) G(x), \quad (4.19)$$

where C_p is the heat capacity per unit mass of the material, $I_0 = \eta I$ is the absorbed intensity of the laser beam, β is the optical absorption coefficient, $f(t)$ is the normalized time distribution of the laser intensity and $G(x)$ is the Gaussian distribution of the normalized laser intensity expressed as:

$$G(x) = \frac{2}{d} \sqrt{\frac{\ln 2}{\pi}} \exp\left[-4 \ln 2 \frac{x^2}{d^2}\right],$$

with d the full width at half maximum (FWHM). In Eq. (4.19), κ represents the thermal conductivity, the operator $\nabla^2 = \frac{\partial^2}{\partial x^2} + \frac{\partial^2}{\partial z^2}$ denotes the Laplacian.

Knowing that the optical penetration depth ($1/\beta$) is small in the case of Aluminum (~ 9 nm at 1064 nm), the volume source is chosen to be replaced, in the numerical model, by a shear stress dipole with a short pulse duration, as indicated in the reference [38]. Note that all the necessary-to-the-model parameters for Aluminum can be found in Tab. 4.1.

The two-dimensional FEM model is therefore constructed in the following usual order:

1. the geometry is defined,
2. the boundary conditions are set (for instance, the shear stress dipole at the surface),
3. the mesh is parameterized,

4. the solver parameters are chosen adequately (for instance, the time step) to solve the above-described wave equation [see Eq. (4.17) with $\mathbf{S} = \mathbf{0}$] in two dimensions.

First, the geometry of the plate is defined. The plate is chosen to be split in three parts. The central part ranges in $x = [-3.75, 3.75]$ mm and is the one from which the calculations will be used for analyzes. In order to avoid the reflections from the left and right vertical boundaries of the central part, two symmetric perfect matching layers (PML), with gradient high loss, are added to the left and right ends of the model at $x = \pm 3.75$ mm. In the central part, the geometry of the plate evolves as a function of the loading cycles N . This evolution is provided by the theory proposed in Sec. 4.4.1 [see Eqs. (4.14)-(4.15) and Fig. 4.8]. For each given N , despite the changes in the geometry of the model, there are clear and uniform definitions of boundary conditions on the four sides of the modelled plate (upper, lower, left, and right surfaces). The upper and lower surfaces of the two-dimensional model are set to be free. Those upper and lower surfaces in the intact case ($N = 0$) are chosen to be flat and located at $z = +h$ and $z = -h$, respectively, with $2h = 75 \mu\text{m}$. In the cases of the damaged plate, the positions of the upper and lower surfaces are represented by functions of x and of N : $z_{up}(N, x) = +h(1 + D(N, x))$ and $z_{lo}(N, x) = -h(1 + D(N, x))$, respectively (see the colored profiles in Fig. 4.8). The right-end surface of the right PML and the left-end surface of the left PML are set to be free, although it does not change much if they are set to be fixed. The last boundary conditions to impose is the shear stress dipole at the lower surface. The temporal distribution $f(t)$ of the generation source is a Gaussian function which can be written as

$$f(t) = \frac{2}{\tau} \sqrt{\frac{\pi}{\ln 2}} \exp\left(-4 \ln 2 \frac{t^2}{\tau^2}\right), \quad (4.20)$$

where τ is the temporal pulse duration. Note that while setting f to be the temporal distribution of the acoustic source, the choice is made to calculate the velocity field instead of the displacement field, mainly for numerical stability reason.

To finish the parametrization of the model, the central part of the geometry is meshed by setting the mesh geometry to be triangular and the mesh step to be $1 \mu\text{m}$. The finite element meshes are therefore fine enough (compared to the ZGV mode wavelength, about $300 \mu\text{m}$ in the studied case) near the excited zone in order to obtain the transient velocity field with a good spatial accuracy. The PML are meshed using a much coarser mesh size of $15 \mu\text{m}$ in order to save computing time. Finally, the time step is chosen to be 1 ns (equal to the experimental acquisition time step) and the total time of the simulation is set to be $5 \mu\text{s}$ which is long enough for Fourier transform with a relative good accuracy. It should be noted here that the only physical model used in Comsol is the model of **Solid Mechanics** (see details in Appendix C on page 171).

The simulated results by the above-described model in the case an intact ($N = 0$) plate of Aluminum are shown in Fig. 4.10: **(a)** first eleven temporal opto-acoustic signals (normal velocity of the front surface ($z = -h$) calculated by numerical simulations from the epicenter ($x = 0 \text{ mm}$) to $x = 0.1 \text{ mm}$ with a step of $10 \mu\text{m}$ and **(b)**

their Fourier spectrum; **(c)** zoom for $x \in [-0.2, 0.2]$ mm of the spatial distribution of the normalized amplitude of the normal velocity at 15 ns after the wave generation. From Fig. 4.10(a), we can see clearly the temporal oscillation corresponding to the ZGV resonance in both the excitation position ($x = 0$) and the detected points far from it ($x = 0.01, 0.02 \dots 0.1$ mm). An evident decrease of the amplitude of the ZGV resonance is also observed due to the spatial distribution related to an interference pattern as discussed previously. From Fig. 4.10(b), three main information can be obtained: (i) a sharp peak, corresponding to the ZGV resonance at a frequency of about 38.42 MHz, is always observed in the frequency spectrum from the epicenter to $x = 0.1$ mm; (ii) a second relatively weaker peak around 62.10 MHz is also seen which corresponds to the cut-off frequency of the A_2 resonance (there is no A_2A_3 -ZGV resonance in the studied case due to the chosen material with a Poisson's ratio of 0.35 [11]); note that this peak can be used for the estimation of the Poisson's ratio of the used material (see chapter 2); (iii) a sharp peak around 125 MHz is obtained and corresponds to the S_3S_6 -ZGV resonance, which can also be used for estimating the Poisson's ratio [28] if experimentally detected. From Fig. 4.10(c), standard wavefronts of longitudinal waves (represented by L), shear waves (represented by T), and waves reflected at the back surface of the plate ($z = h$), with mode conversion (LT) or not (2L), are respectively observed. The Rayleigh waves (R in black) propagating only at the surface where the generation have been set ($z = -h$) are also observed. All these numerical results demonstrate the good numerical reproduction of the usual features observed in laser ultrasonic experiments conducted on metals and therefore validate the developed model.

The numerical model is then run four times, each time only changing the parameter N (the number of loading cycles) and therefore the geometry of the plate: $N \in [0, 4000, 9500, 10000]$. The Fig. 4.11 depict four snapshot of the normalized normal velocity distribution within the whole range of valid calculations $[(x, z) \in [-3.75, 3.75] \times [-0.0375, 0.0375]]$ mm². Note that each snapshot is taken at a time corresponding to approximately 90 periods of the S_1S_2 -ZGV resonance, i.e. at $t \cong 90/f_{ZGV}(N, 0)$ for the sake of the comparison. In Fig. 4.11(a), the classical interference pattern of a ZGV resonance is seen between -1 mm and 1 mm, while the propagating modes has escaped the area of the wave generation and propagates towards the left- and right-end of the plates with different group velocities. In Fig. 4.11(b)-(d) where the plate is damaged, the same observations could be made, although the spatial extend of the ZGV-related interference pattern in the central part seems to decrease as N increases. Qualitatively, this is due to the expected decrease of the ZGV wavelength with decreasing thickness of the plate.

For a better understanding of the influence of the fatigue damage on the Lamb modes, a set of spatio-temporal signals are also probed along the surface profile $z_i o(N, x)$ by the numerical model. For each damage level (each loading cycles N), 376 numerical signals are saved with a numerical spatial scanning step of $10 \mu\text{m}$ from $x = 0$ mm to $x = L_{\text{num}} = 3.75$ mm. For each saved signal, the duration of the signal is set to be $T_{\text{num}} = 5 \mu\text{s}$ with a temporal calculation step of 1 ns (i.e. a numerical sampling rate equals to 1 Gs/s).

With these simulated calculations, it is possible to carry out the two dimensional

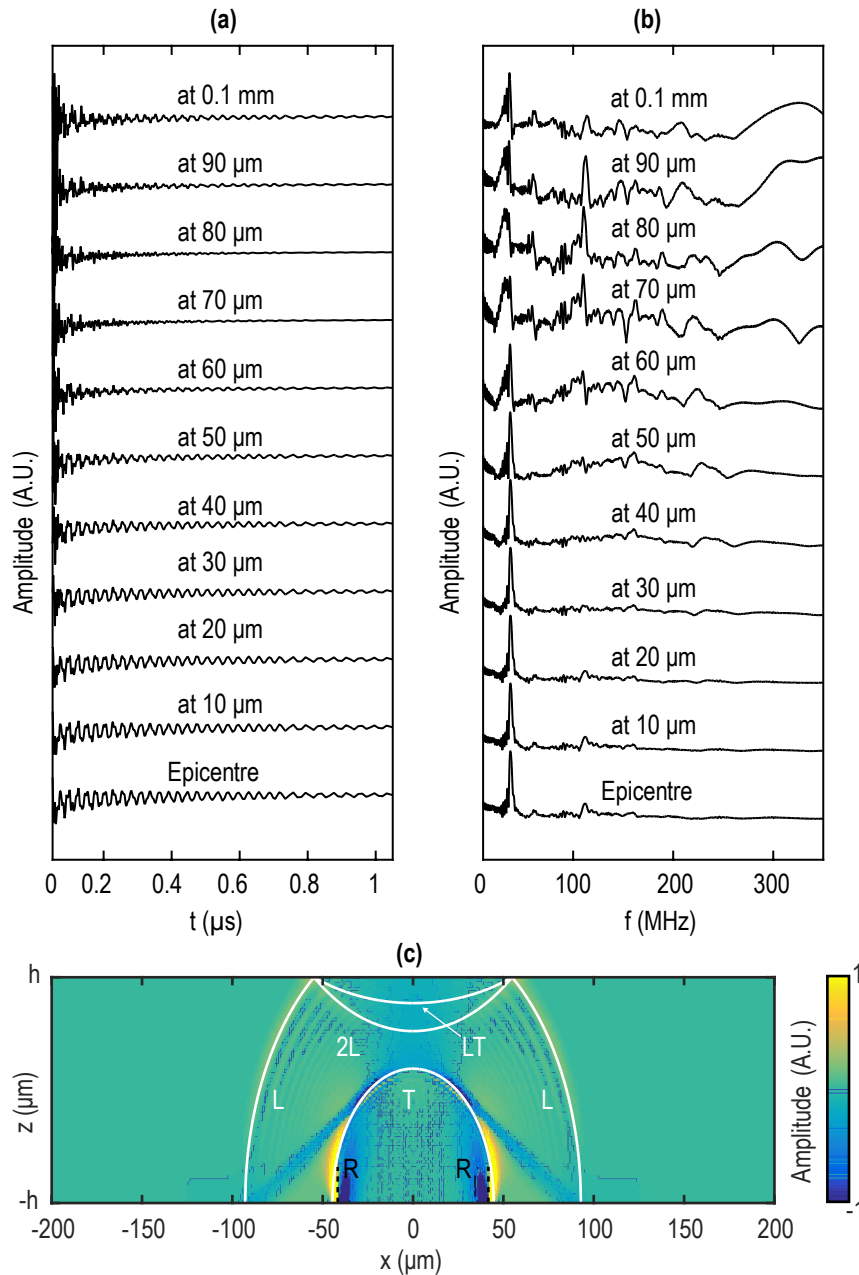


Figure 4.10: Results of the numerical simulations for the intact specimen ($N = 0$) : (a) first eleven temporal opto-acoustic signals (normal velocity of the front surface [$z = -h$] calculated by numerical simulations from the epicenter ($x = 0$ mm) to $x = 0.1$ mm with a step of $10 \mu\text{m}$ and (b) their Fourier spectrum; (c) zoom for $x \in [-0.20, 0.2]$ mm of the spatial distribution of the normalized amplitude of the normal velocity in a $75 \mu\text{m}$ -thick Aluminum plate at 15 ns after the wave generation.

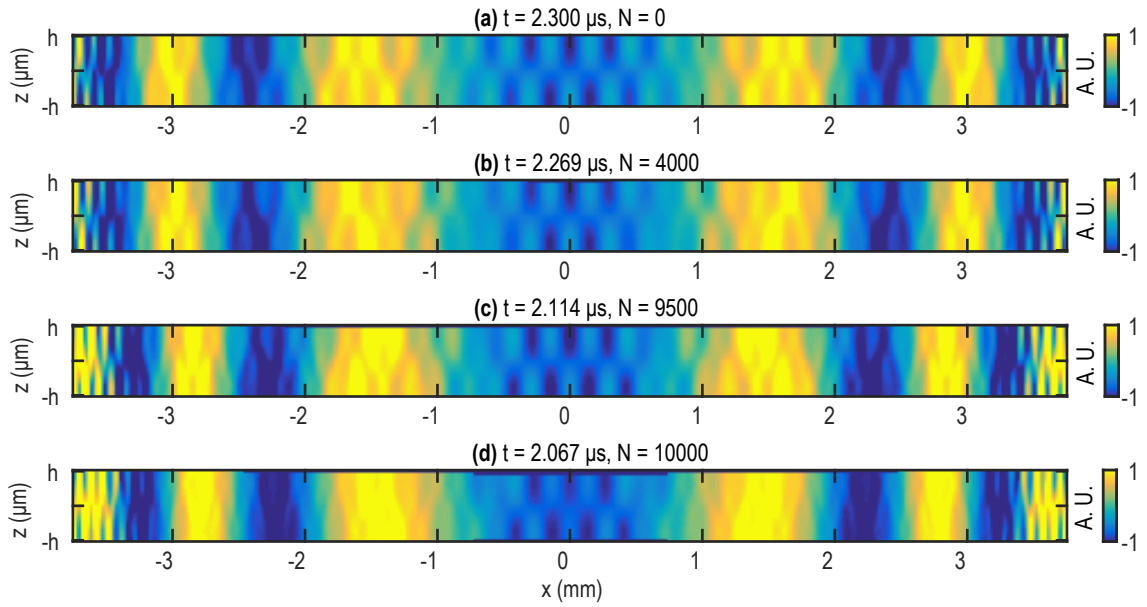


Figure 4.11: Numerical simulations of the normal velocity distribution at about 90 periods, i.e. $t \cong 90/f(N)$, for intact ($N = 0$) and damaged ($N = 4000, 9500$ and 10000) specimens, taking into account the reduction of thickness as illustrated in Fig. 4.8.

Fourier transform (2D-FT)

$$\tilde{u}(k, f) = \int_0^{T_{\text{num}}} \int_0^{L_{\text{num}}} u(x, t) e^{-ikx} e^{i2\pi ft} dx dt, \quad (4.21)$$

in order to look at the f - k diagram in the real wavenumber plane. The numerical f - k diagram (that corresponds to the dispersion curves only in the intact case) are calculated by the 2D-FT for the four selected cases of different levels of damage in Fig. 4.12: (a) $N = 0$ [$\Delta h(0, 0) = 0\%$], (b) $N = 4000$ [$\Delta h(4000, 0) = 1.16\%$], (c) $N = 9500$ [$\Delta h(9500, 0) = 3.76\%$], and (d) $N = 10000$ [$\Delta h(10000, 0) = 4.43\%$].

Since the numerical detection is only made in one direction, i.e. in the direction of increasing x (positive group velocities), and since the group velocity and the phase velocity of the S_1 mode are of opposite sign as introduced in Sec. 2.3.2, the phase velocity of S_1 is thus negative. The S_1 wavenumbers are therefore negatives and hence shown in the negative part of the wavenumbers axis ($k < 0$) in Fig. 4.12(a-d). From these f - k diagram, especially the one in Fig. 4.12(d), it can be straightforwardly seen, by comparison with the intact case in Fig. 4.12(a), that the ZGV point is shifted to the right-up side from its original position. It means that both the frequency (f) and the real wavenumber (k) are changed with the kind of local damage of a thin plate that a buckling fatigue test induces. This explains the reason of the change of the ZGV resonance profile shown in Fig. 4.11(d).

The information presented in Fig. 4.12 is a kind of averaged wave response of the laterally inhomogeneous plate to the photo-excitation in terms of averaged (k, ω) characteristics of the acoustic modes. In an aperiodically inhomogeneous plate, these curves of the modes in the (k, ω) plane, are expected to depend both on the

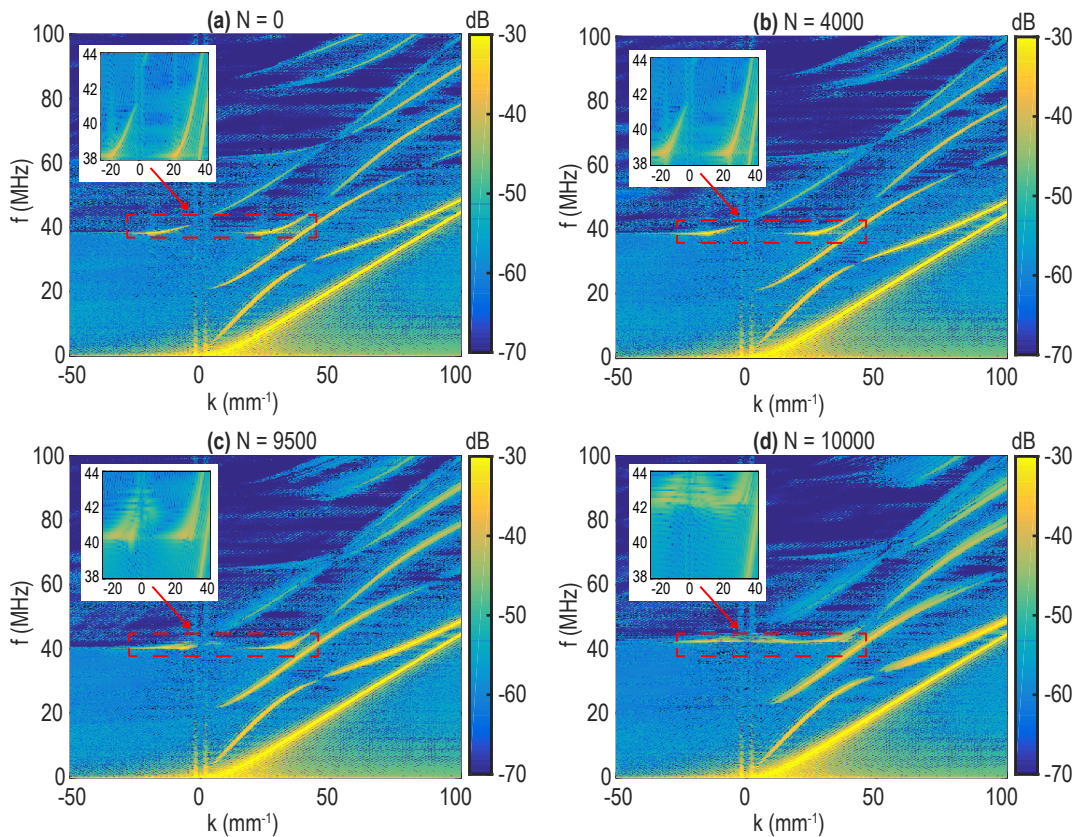


Figure 4.12: f - k diagram for the analyzes of the Lamb modes propagating in (a) an intact plate and (b-d) a damaged plate calculated from a set of 376 temporal signals with a spatial scanning step of $10 \mu\text{m}$ from $x = 0 \text{ mm}$ to $x = L_{\text{num}} = 3.75 \text{ mm}$. Each temporal signal is calculated for a duration of $5 \mu\text{s}$ with a time step of 1 ns .

position of the tested region and on its lateral dimension. However, the obtained (k, ω) curves are still informative in the sense that their modification with increasing damage (when the position and the dimension of the tested region is fixed) reflects the damage progress and could be applied for its evaluation. For example, the up-shift of the curves is a signature of the diminishing thickness of the plate. It is the most visible/pronounced in Fig. 4.12 near the ZGV point because, in our simulated geometry, the photo-excitation of the acoustic modes is centered on the maximum of the thickness variations and the modes with the lowest group velocity (like those near the ZGV point) spend larger time in the modified region and are therefore the most sensitive to its parameters. This statement is in accordance with the general statement that the ZGV mode is more suitable for the spatially localized testing of the plates than the propagative modes. The diminishing of the plate thickness should result in the increase of the ZGV frequency, in the diminishing of the wavelength (increasing of the wavenumber) and could qualitatively explain the shift of the ZGV point observed in Fig. 4.12 with increased fatigue. Another noticeable feature in Fig. 4.12 is the increase of the curves width with the progression of damage. This effect could be qualitatively associated to the inhomogeneous broadening of the spectral lines. Actually, it can be precisely related to inhomogeneous

broadening for the acoustic modes with the wavenumber much larger than the inverse of the characteristic scale of the plate inhomogeneity, i.e. the lateral dimension of the thickness variation in this case. These modes propagate indeed locally like in locally-homogeneous plates with modified parameters (geometrical acoustic approximation) and their spectral lines broadening could be obtained by spatial averaging of the local spectral lines. However, for waves with the wavenumbers smaller than the inverse of the inhomogeneity characteristic scale, the observed broadening could be much more complicated to evaluate quantitatively because the structure of the mode having wavelengths comparable to the scale of the inhomogeneity could be modified. Furthermore, another remarkable phenomenon is observed: a short branch of dispersion curve with negative group velocity appears for small $k_r > 0$ just above the first ZGV frequency and below the corresponding cut-off frequency of the same branch, as noticeable in the inset of Fig. 4.12(d). Similar phenomenon is also seen in Fig. 4.12(c), although much weaker. At present, we attribute these features to the increased scattering of the Lamb waves at the inhomogeneity of the plate. Further research is required thereafter in order to get a clearer understanding of this interesting feature.

The mathematical expression of the thickness profile of the plate after a given number of loading cycles has been proposed based on the experimental observations of $\Delta f/f$. In the previous Sec. 4.4.1, it has been shown that the proposed theory agrees very well with the experimental data. It is now proposed to compare the theory with the relative variation of the ZGV frequency at the center of the fatigue zone where $\Delta f/f$ is now extracted from the numerical simulation. This will somehow demonstrate that the developed numerical model reproduces the same trend as the one observed experimentally.

The comparison between the theoretical model and numerical validation in the center of the fatigued region ($x = 0$) is plotted in Fig. 4.13(a) as a function of N , where N is chosen to remain below 10000, i.e. N is in the range where, experimentally, $\Delta f/f$ only increases and where it is assumed that only the thickness profile change is at play. The solid line represents the theoretical variation of $\Delta f/f$ calculated by the Eq. (4.14) at $x = 0$ mm. The solid circles represent the variation of $\Delta f/f$ extracted from the FT of the temporal signal simulated at $x = 0$ mm for $N \in [0, 10000]$ (simulations run every 500 loading cycles). The error bars in Fig. 4.13(a) stand for $f(N)/[f(0)Q(N)]$, with $f(N)$ the ZGV frequency at $x = 0$ mm after N cycles and $Q(N)$ the quality (Q) factor of the corresponding resonance. Note that the Q factor is defined as $Q = f/(f_2 - f_1)$, where f is the ZGV resonance frequency at which the gain is maximum and f_2 and f_1 are the frequencies higher and lower than f at which the gain is -6dB than the maximum. From Fig. 4.13(a), a good agreement between the theoretical and the numerical calculations is shown, where the slight discrepancy could be explained by numerical errors/approximations. This shows that the experimentally-observed variation of the ZGV resonance frequency is mainly related to the change in the thickness profile of the plate caused by the fatigue process.

To analyze further, the numerical Q factors are compared to the experimental Q factors as a function of N (or normalized fatigue lifetime N/N_f) in Fig. 4.13(b). The results shown in Fig. 4.13(b) are twofold. First, the experimental and numerical Q

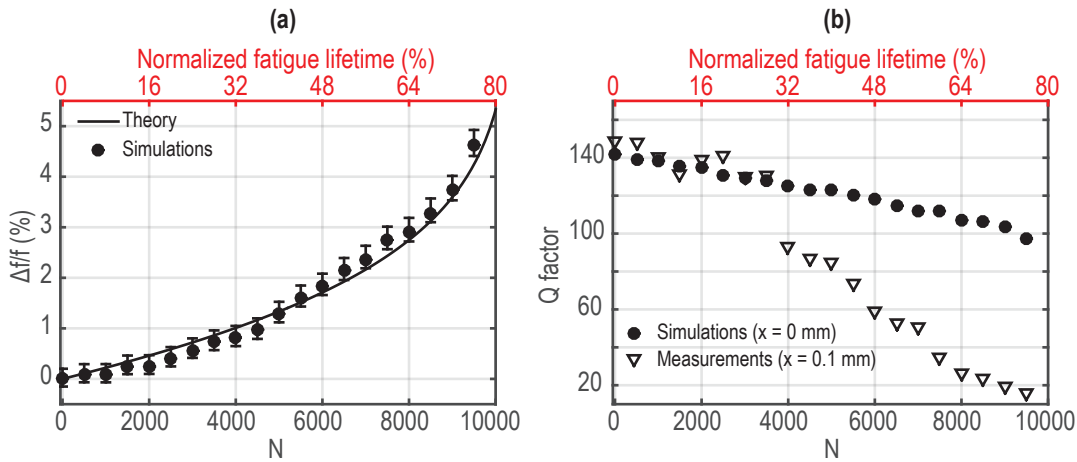


Figure 4.13: **(a)** Theoretical (solid line) and numerical evolution (solid circles) of the relative variation of the ZGV frequency at the center of the fatigued region as a function of the loading fatigue cycles N ; **(b)** Comparison of the experimental (triangles) and the numerical (solid circles) Q factors as a function of N .

factors match pretty well for $N \in [0, 3500]$ ($N/N_f \in [0, 32]$ %) and this demonstrates a decrease in the Q factor of the ZGV resonance as N increases, i.e. as the thickness change due to fatigue damage is increasingly pronounced. Second, a linear downward trend of the Q factor is particularly evident in our model where other changes of the material (damping property, mechanical property, ...) are not considered, whereas an abrupt decrease of the experimental Q factor is observed from $N = 3500$ to $N = 4000$. Those important observations lead to three important comments to point out: (i) no damping factor is considered in this numerical model, while the Q factor decreases as N increases, both for simulations and experiments, meaning that the attenuation of the resonance can be only influenced by the local geometry of the plate; (ii) the good match of the simulations and of the experimental measurements confirms that our proposed empirical model well describes the fatigue process at the early stage of the fatigue life ($N/N_f < 32\%$); (iii) the drop of the experimental Q factor at $N = 4000$ and the change of the decreasing slope after that could be the interesting manifestation of the start of the changes in the material elastic parameters. To complete the empirically-based theoretical model and the numerical model, the change of material properties with the loading cycles should be considered.

4.5 Conclusion

In conclusion, this chapter presents a non-contact laser ultrasonics evaluation of cumulative fatigue damage in thin solid plates by monitoring a ZGV resonance frequency. A “homemade” machine has been developed to perform fatigue tests in the configuration of a two-sides-clamped compression inducing buckling. The experimental results demonstrate the ability of this method for (i) locating damage, (ii) predicting fatigue lifetime and (iii) assessing qualitatively and potentially quantitatively the cumulative fatigue damage levels during the fatigue process.

For better understanding of the evolution of the thickness distribution in the specimen during fatigue test and of its effect on the ZGV resonance frequency, an empirically-based theoretical model of the evolution of the thickness distribution with the cumulative fatigue damage and a numerical model, based on finite element method, purposing to perform frequency-wavenumber (f-k) analyzes of the Lamb modes in fatigued metal plates have been proposed.

The developed theoretical model have shown good agreement with the experimental results up to a certain amount of fatigue damage, which allows assuming that the change in the thickness distribution due to the cumulative thickness is at major play up to 80% of the fatigue lifetime. The analyzes, based on the numerical simulations, of the relative change of the ZGV resonance frequency with the fatigue process have confirmed the latter statement. The last comparison between the quality factor of the ZGV resonance calculated with the numerical results and the experimental results has furthermore shown that the dramatic drop of the Q factor after 32% of the fatigue lifetime experimentally observed cannot be explained by the change in the thickness distribution. This is the clear demonstration that the current model limited to take into account the fatigue-based thickness variation is not yet complete. Thus, a more complete model taking also into account the change in the mechanical properties of the sample as the fatigue damage increases should be developed in the future to be closer to the reality. Such a model could be used for better explanation of the experimental observations among the whole fatigue progression, even after the abrupt decrease of the ZGV resonance frequency. Moreover, other methods of cumulative damage tests (bending, tensile tests, creep, three points testing, thermal aging, etc.) could be applied to metallic sheets in order to study/analyze the feasibility, the applicability, and the limits of our method for evaluating cumulative fatigue damage under different situations.

For future works, on one hand, we will focus on the imaging of the fatigue damage for analyzing the limits and the capacities of the presented method, especially at few loading cycles, when the damage is barely visible. On the other hand, the energy loss along the imaginary parts of the dispersion curves around the ZGV point seems interesting to recover, with the method discussed in Chap. 3 for instance, and to follow with fatigue lifetime in order to propose a proper model accounting for the evolution of the quality factor, which needs additional research. In addition, as mentioned several times in Sec. 4.4.2, a future work on the establishment of a more complete empirically-based theoretical model accounting for the change in the mechanical properties is important and necessary (a preliminary study about this point is introduced in chapter **Perspectives**, see Fig. P.1 on page 137). With the consideration of the combination of the local variation of the thickness and the local changes of the elastic constants, our proposed model can be much more close to the reality, i.e. the experimental measurements, and would be useful for a deep understanding of each stage of the fatigue allowing masterizing the overview of the whole fatigue process.

Last but not least, by considering the potential capacity of the presented method for quantitative prediction of fatigue progress, one possible prospect of this work could be the assessment of fatigue damage in different stages, especially before the specimen failure. This could be achieved by combining the proposed method with

either chemical methods (such as etch-pit technique [190], precipitation technique [170]), physical techniques (such as transmission electron microscopy [185], or X-ray diffraction technique [191]), in order to further reveal the nature of such damage and to formally identify the material mechanisms leading to this extremum in the ZGV resonance frequency in order to reach a fully quantitative (local) damage evaluation of fatigued samples.

Part III

Extending application of laser-based
zero-group-velocity Lamb modes:
nonlinearity extraction and texture
imaging

In this part, following the successful study of the cumulative fatigue damage due to mechanical loading, the choice has been made to consider new benchmarks for the laser-based ZGV Lamb modes. First, it is proposed to study the case of thermal damage in highly elastically nonlinear Aluminum alloy and therefore to concentrate the efforts towards the observation of some nonlinear phenomena with the ZGV modes, which is also one of the goals of this PhD work, as pointed in the introductory chapter of this manuscript (Chap. 1). Then, the analysis and the ZGV-mode-based imaging of highly textured Copper plate is proposed, as the first minor step for extending the method to different potential applications in the field of material science.

穷则变，变则通，通则久。 — 《周易·系辞下》

When it is exhausted, it mutates; by mutation it achieves continuity; by continuity it endures long. — «Yijing».

Chapter 5

Evolution of a nonlinear parameter in heat-treated metallic plates evaluated with laser-based zero-group-velocity Lamb modes

Contents

5.1	Introduction	102
5.2	Experimental samples	103
5.3	Experimental setup and example of a detected signal . .	105
5.4	Pseudo-Phase-Plane (PPP) analysis	106
5.5	Signal processing model	109
5.6	Evolution of the nonlinear parameter with the thermal fatigue	111
5.7	Discussion on the influence on the ZGV resonance of the temperature rise caused by laser absorption	116
5.7.1	Temperature rise influence on ZGV resonance frequency in Aluminum alloys (AlAl-5083)	117
5.7.2	Influence of the temperature rise due to the pulsed laser .	118
5.8	Conclusions	119

Keywords: *Nonlinearity; thermal aging; laser ultrasonics; ZGV.*

*Calling the subject nonlinear dynamics is like calling zoology 'nonelephant studies'.
— Stanislaus Ulam*

In this chapter, the measurements of a nonlinear parameter via contactless generation and detection of laser-intensity-dependent ZGV resonances are carried out in order to characterize the thermal aging of an Aluminum alloy. The experiments are realized on Aluminum alloy specimens (Al6061-T6) which have been heat-treated at 220 °C for different times (0 min, 20 min, 40 min, 1 h, 2 h, 10 h, 100 h, 1000 h) after a heat treatment of 4 hours at 540 °C and which therefore present different levels of thermal aging. From the experimental observation, the fractional change in the nonlinear parameter agrees well with the variation in the yield strength, which demonstrates the potential of the presented results for evaluating the thermal damages. Therefore, the variation of the nonlinear parameter of the ZGV resonance could be considered as an indicator of the level of thermal aging of the Aluminum alloy.

5.1 Introduction

Nonlinear problems are of interest to engineers [192], biologists [193], physicists [194, 195], mathematicians [196, 197], and many other scientists because most systems are inherently nonlinear in nature [198]. In physics and dynamics, nonlinear phenomena are often observed, such as the resonance frequency shift [186, 199–208], in various kinds of motions as well as in different materials. Moreover, nonlinear ultrasonic technique is also widely used for assessing the damage or for the characterization of materials [136, 209–212]. In the last two decades, the nonlinear Surface Acoustic Waves (NL-SAWs) [213–216] as well as the nonlinear Lamb waves [217–219] have been used for fundamental research and nondestructive testing and evaluation (NDT&E). For fatigue damage characterization, acoustic nonlinearity can be used as a good parameter because of its capacity for probing the processes of crack growth [220] and of dislocation movement [172].

After the study of cumulative mechanical fatigue of metallic plates in the previous chapter, and as the first step for extending laser-based ZGV resonance method to other cumulative damage tests, it is proposed to generate and detect ZGV resonances with the expectation of being sensitive to nonlinear phenomena in samples with a different type of damage than the mechanical fatigue damage. The aim is to extract useful information from ZGV resonances in order to non-destructively characterize the damaged samples. The latter correspond to the second goal of the experimental part of the present PhD work (see the **General Introduction** on page 1).

The acoustic nonlinearity is ubiquitous in many materials (glass, metal, polymer...) and can be defined in different ways and measured by multiple methods [129, 221–224]. Early this century, H. Ogi et al. proposed a method for prediction of fatigue lifetime in steels using SAW nonlinearity with the help of contactless acoustic transduction in order to avoid background nonlinearity caused by coupling agents and the transducer itself [172]. One year later, X. Jacob et al. [221] measured the nonlinearity of longitudinal acoustic waves propagating in solids using a method based on the detection of the phase modulation resulting from the parametric interaction between a high frequency acoustic wave and a lower frequency acoustic pulse. Besides nonlinear longitudinal and Rayleigh waves, Lamb wave is another mean

for probing nonlinearity, such as through the effect of second harmonic generation [129, 222]. Some of the investigations are closely related to an actual engineering problem, i.e. the material fatigue lifetime prediction [129, 131, 222].

In the last decade, the researchers in ISNDE (Intelligent Sensing & Nondestructive Evaluation Laboratory, Hanyang University, Seoul, South Korea) developed the NDE technique based on SAWs [132, 135, 212, 225–228]. Recently, they have focused on the development of the NDE technique for material degradations based on NL-SAWs via both contact and non-contact methods [49, 229]. Using SAWs is useful and effective for thick specimen. However, the developed NDE technique [49] based on SAWs are restricted to probe the sample within a few wavelength under the guiding surface. On the opposite, Lamb waves are well suited to probe the whole thickness of a plate-like structure. In order for the probing to be local, the ZGV features of some specific Lamb modes show great interest. Therefore, the will to develop of a NDE technique based on ZGV resonance emerged and an international cooperation between ISNDE and LAUM began. The main research objective of this cooperation is the development of the contactless NDE technique for material degradations based on ZGV resonances for thin metal plates using laser ultrasonics. The variations of a nonlinear parameter of the ZGV resonance obtained on thin metal plates (thickness of $\sim 100 \mu\text{m}$) in LAUM will be compared with that obtained on blocks of the same material (thickness of 40 mm) using SAWs based methods at ISNDE.

The present chapter is organized as follows. The experimental samples and devices are introduced in Sec. 5.2 and in Sec. 5.3, respectively. Then an example of the received signal in the experiment with the chosen nonlinear analysis method is presented in Sec. 5.4 and the signal processing model allowing the extraction of nonlinear parameter from ZGV resonance is introduced in Sec. 5.5. After that, in Sec. 5.6, the experimental results on the evolution of this nonlinear parameter with increasing heat-treatment time are presented and compared with those measured by two other methods. Finally, before the conclusion, the effect of temperature rise on the ZGV frequency caused by the pump laser is discussed in Sec. 5.7 to demonstrate that the observed phenomena have other origins than just the temperature rise.

5.2 Experimental samples

First of all, we introduce the specimens used in this part and the thermal fatigue preparation process applied to them. The specimens are provided kindly by our collaborators Dr. Hogeon Seo and Prof. Kyung-Young Jhang, from Hanyang University, Seoul, South Korea. The specimens (with size of $80 \times 20 \times 0.1 \text{ mm}^3$) were cut from blocks made of the Aluminum alloy Al6061-T6 via wire-cut electrical discharge machining under the same conditions in order to standardize the flatness and roughness of the surfaces to be inspected. The eight samples surrounded by acoustic absorbers (Blu Tack) are illustrated in Fig. 5.1 and numbered from 1 to 8 corresponding to different heat-treated durations.

It should be noted here that, before optoacoustic measurements, the thickness of each sample is preliminarily measured via the micrometer screw gauge (with a precision of $\pm 0.001 \text{ mm}$), and an evident variation of the thickness due to the

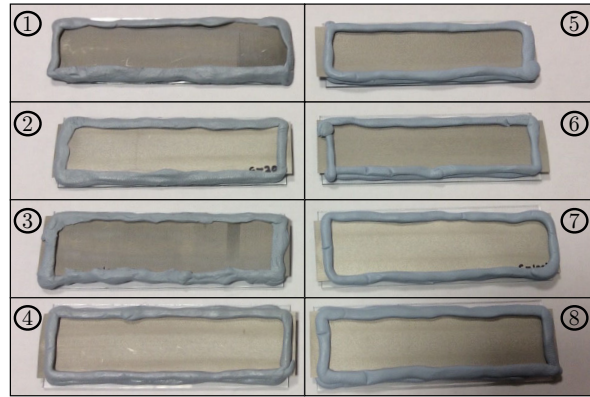


Figure 5.1: Experimental specimens heat-treated for different durations numbered from 1 (0 min of heat-treatment) to 8 (1000 h of heat-treatment).

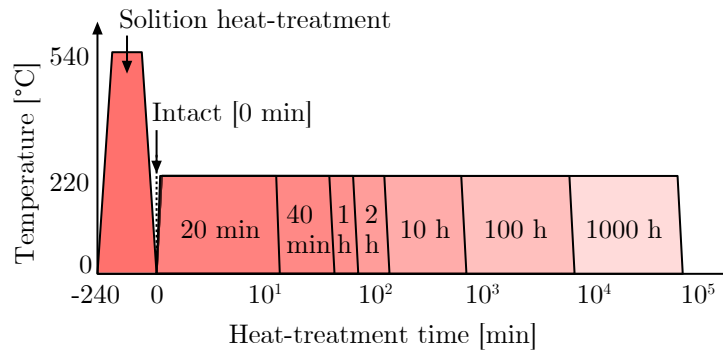


Figure 5.2: Schematic representation of the heat-treatment processes for Aluminum alloy blocks [49].

fabrication process (when cut from the Aluminum alloy blocks) is observed along the length of each sample (the thickness varies from $\sim 80 \mu\text{m}$ to $\sim 120 \mu\text{m}$, i.e. about $\pm 20\%$ of variation). For this, it is here proposed to treat only one signal from each sample, in order to see if an encouraging tendency could be revealed or not. For the proposed method, aiming to characterize the thermal damage, it would be necessary to get rid of the influence of thickness variation on ZGV resonance frequency. It is also proposed here to disregard the absolute value of the measured nonlinear parameter and to concentrate on its variation relative to the sample number 1..

The heat-treatment processes applied to the Aluminum alloy blocks are illustrated in Fig. 5.2. Before inducing thermal aging to the specimens, they were heat-treated equally in a solution for 4 h at $540 \text{ }^\circ\text{C}$ and then water-cooled quickly. Subsequently, each sample was heat-treated at $220 \text{ }^\circ\text{C}$, about 35% of the melting temperature, for different durations (specimen 1: 0 min, specimen 2: 20 min, specimen 3: 40 min, specimen 4: 1 h, specimen 5: 2 h, specimen 6: 10 h, specimen 7: 100 h, specimen 8: 1000 h) to induce gradually increasing level of thermal aging.

The theoretical dispersion curves of Lamb modes in the thermal-aged Aluminum plates are calculated using the properties of each sample measured in Ref. [49]. Here, the dispersion curves of sample 1 are plotted in Fig. 5.3 assuming that the thickness is $100 \mu\text{m}$. The mechanical properties used for the calculations are given

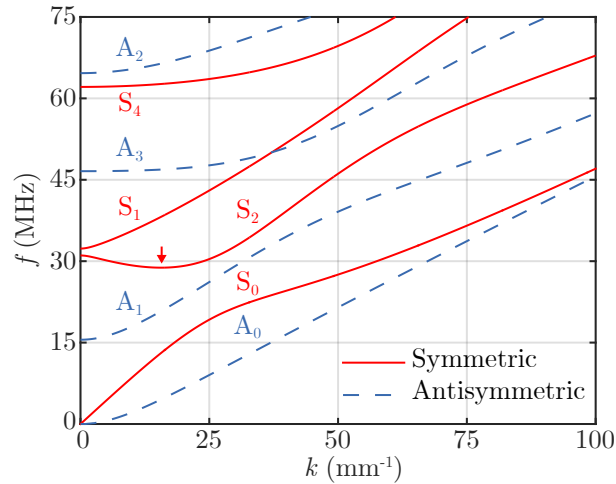


Figure 5.3: Dispersion curves of Lamb modes in the Aluminum alloy plate with thickness of $100 \mu\text{m}$ for both A (dashed blue lines) and S (solid red lines) modes. The red arrow denotes the position of the first ZGV mode.

in Tab. 5.1 on page 116. The S_1S_2 -ZGV frequency is calculated to be 28.83 MHz in the case where the thickness is equal to $100 \mu\text{m}$.

5.3 Experimental setup and example of a detected signal

The experimental setup is schematically illustrated in Fig. 5.4 : the pump laser (pulse duration of $\sim 0.75 \text{ ns}$ with a repetition rate of 1 kHz) has an optical wavelength of 1064 nm and is focused into circular spot (diameter $\sim 100 \mu\text{m}$); another continuous laser (interferometer BossaNova Tempo with a wavelength of 532 nm) is focused to a circular spot (diameter $\sim 60 \mu\text{m}$). The calibration of the overlapping/separation of the generation and the detection circular spots is controlled by two rotating mirrors. The Aluminum plate is attached on a three dimension translational platform. In this work, only the translation along x -direction is used in order to achieve the B-scan measurements, the scanning direction is denoted by a double-headed arrow in Fig. 5.4. In Fig. 5.4, the dashed rectangle around the convex lens (focal length equals to 50 mm) represents an oblique translational platform in order to adjust the spot size of the generation laser beam.

In Fig. 5.5, we plot an example of a received laser ultrasonic temporal signal and its frequency spectrum before [see Fig. 5.5(a) and Fig. 5.5(b)] and after [see Fig. 5.5(c) and Fig. 5.5(d)] the application of a bandpass numerical filtering aiming at isolating the ZGV resonance peak. A sharp peak at $\sim 28 \text{ MHz}$ (the frequency is matching the one extracted from the dispersion curves in Fig. 5.3) is observed and corresponds to the S_1S_2 -ZGV resonance in Aluminum alloy. The numerical bandpass filter is using a *Kaiser* window and the following parameters are set: the low cut-off frequency is 24 MHz and the high cut-off frequency is 32 MHz (i.e. $\sim f_{ZGV} \pm 4 \text{ MHz}$), the frequencies at the edge of the start and the stop of the pass band are

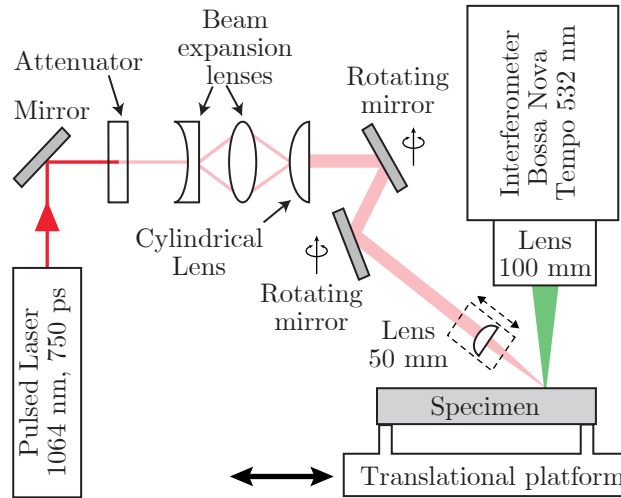


Figure 5.4: Experimental setup.

20 MHz and 36 MHz (i.e. $\sim f_{ZGV} \pm 8$ MHz), respectively, and the attenuation in the first and the second stop bands are 1 dB and 60 dB, respectively¹. Two main advantages of the use of such a filter are: the central band is narrow enough to isolate the ZGV resonance keeping its profile; the stop band (wider one) can filter out the non-useful information away from the ZGV resonance. The signal presented in Fig. 5.5 will also be used for nonlinear dynamic analysis that will be introduced in the next section.

Here in the illustrative example, we assume that nonlinearity manifests itself in a time variation of the oscillation frequency, caused by the dependence of the sample elastic parameters on the amplitude of the oscillations.

5.4 Pseudo-Phase-Plane (PPP) analysis

The Phase Plane (PP) or Pseudo-Phase Plane (PPP) Analysis are often used for the study of nonlinear dynamics [230–236]. It is here proposed to use this visualization tool in order to detect if some nonlinear phenomena are present in the experimental signals measured on the thermal-aged samples or not. Note that it is out of the scope of this manuscript to deeply analyze the phase portrait and that, by consequence, only the useful information for the comprehension of PP and of PPP will be provided below.

Before the application of PPP to the signal in Fig. 5.5, we explain the basic idea of PPP with two theoretical signals: a linear signal with respect to time and a nonlinear signal with respect to time. The linear signal is a general and normalized sinusoidal oscillation with exponential decrease. Its expression as well as the

¹For more details, see <https://fr.mathworks.com/help/signal/ref/kaiserwin.html> and <https://fr.mathworks.com/help/dsp/ref/fdesign.bandpass.html>, accessed 10/18/2018

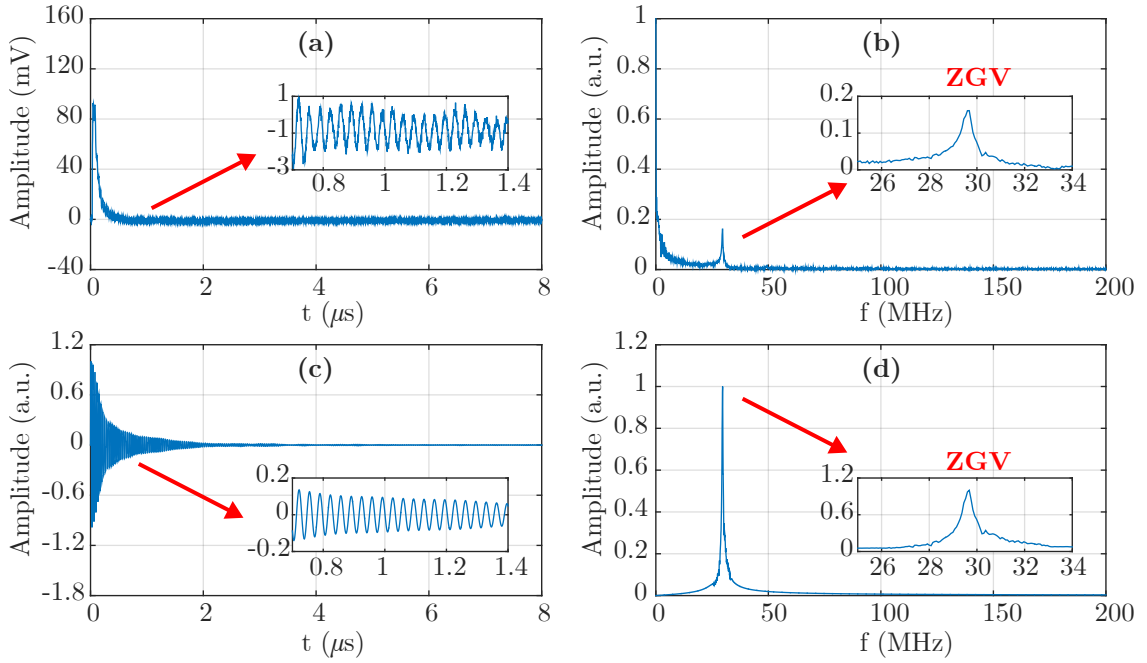


Figure 5.5: One example of the temporal received signal on sample 1 before (a) and after (c) bandpass filtering, and its frequency spectrum before (b) and after (d) bandpass filtering. The sharp peak corresponds to the ZGV resonance peak.

expression of its derivative with respect to time t are:

$$u(t) = e^{-\alpha t} \cos(\omega t), \quad (5.1)$$

$$\dot{u}(t) = \frac{du}{dt}(t) = -\alpha u(t) - \omega e^{-\alpha t} \sin(\omega t). \quad (5.2)$$

The expression of the nonlinear signal, together with that of its derivative, is chosen to be:

$$u_{NL}(t) = e^{-\alpha t} \cos(\omega t + \beta \omega t^2), \quad (5.3)$$

$$\dot{u}_{NL}(t) = \frac{du_{NL}}{dt}(t) = -\alpha u(t) - \omega(1 + 2\beta t)e^{-\alpha t} \sin(\omega t + \beta \omega t^2). \quad (5.4)$$

The phase plane in both cases (linear and nonlinear) consists in a parametric representation where $x = u(t)$ or $x = u_{NL}(t)$ and $y = \dot{u}(t)$ or $y = \dot{u}_{NL}(t)$, respectively. The PP are depicted in Fig. 5.6(a) for the linear case and in Fig. 5.6(c) for the nonlinear case. The numerical values of the parameters used for the calculations are $\omega = 2\pi \cdot 29.5$ rad/ μ s, $\alpha = 2.6$ μ s $^{-1}$, $\beta = 0.01$ μ s $^{-1}$ and $t \in [0, 10]$ μ s. The chosen values are close to that of the experimental data extracted from the signal in Fig. 5.5 as will be explained later. To plot the PP with experimental results, it is necessary to measure both a parameter and its derivative as a function of time. Such information may not be possible to measure every time. In the case of laser ultrasonics, it is indeed usual to measure only one of them, either the displacement or the velocity. However, due to the temporal derivative relation existing between both, it is possible to visualize the phase portrait in a pseudo-phase plane that consists in a parametric representation where $x = u(t)$ or $x = u_{NL}(t)$ and $y = u(t + T)$

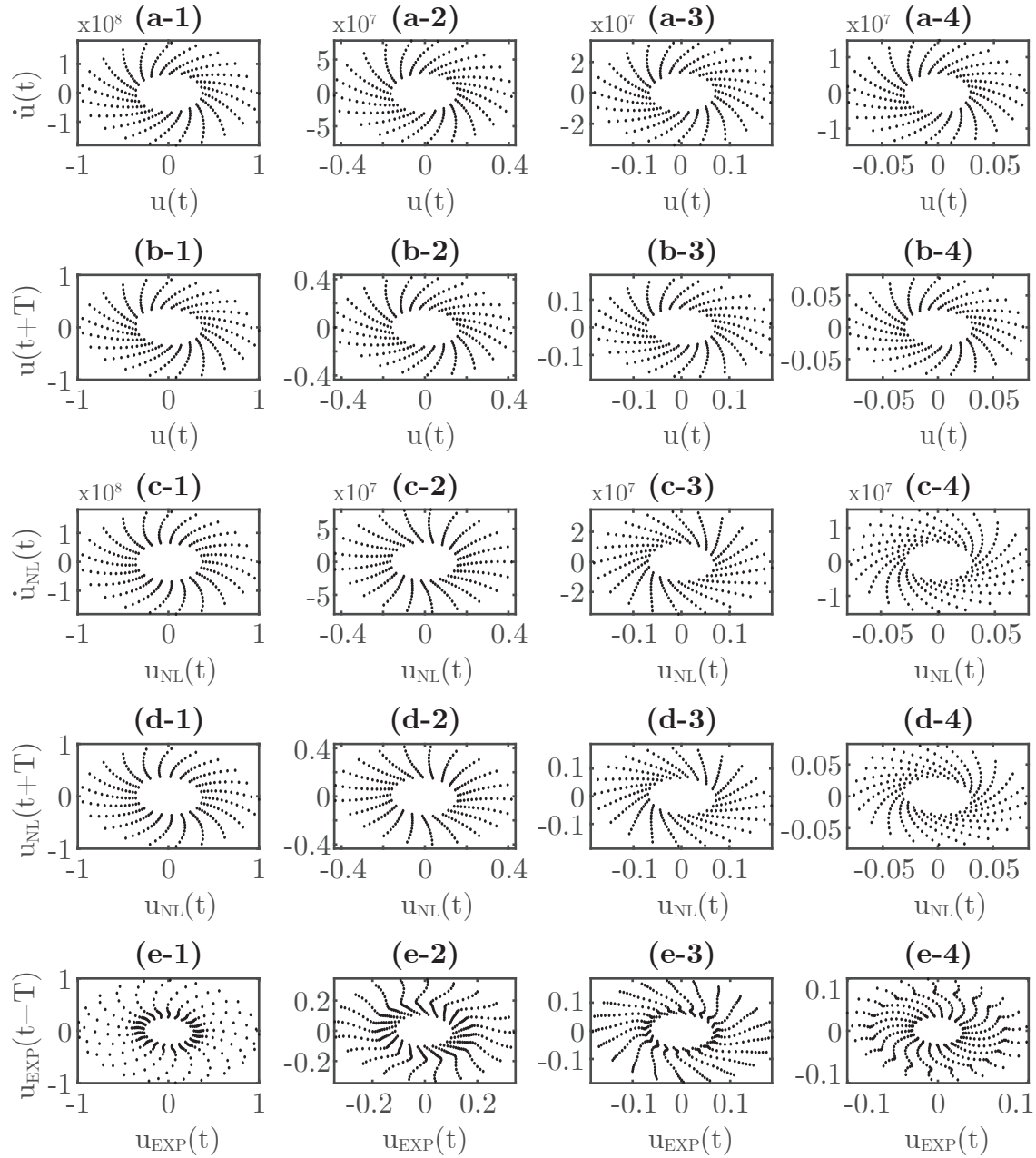


Figure 5.6: (a) Phase Plane for the linear signal for different values of t_{ini} : (a-1) $0 \mu\text{s}$, (a-2) $0.32 \mu\text{s}$, (a-3) $0.64 \mu\text{s}$, and (a-4) $0.96 \mu\text{s}$; (b) Pseudo-Phase Plane with $T = 12 \text{ ns}$ for the linear signal for different values of t_{ini} : (b-1) $0 \mu\text{s}$, (b-2) $0.4 \mu\text{s}$, (b-3) $0.8 \mu\text{s}$, and (b-4) $1.2 \mu\text{s}$; (c) Phase Plane for the nonlinear signal for different values of t_{ini} : (c-1) $0 \mu\text{s}$, (c-2) $0.32 \mu\text{s}$, (c-3) $0.64 \mu\text{s}$, and (c-4) $0.96 \mu\text{s}$; (d) Pseudo-Phase Plane with $T = 12 \text{ ns}$ for the nonlinear signal for different values of t_{ini} : (d-1) $0 \mu\text{s}$, (d-2) $0.4 \mu\text{s}$, (d-3) $0.8 \mu\text{s}$, and (d-4) $1.2 \mu\text{s}$; (e) PPPs reconstructed using experimental result with $T = 12 \text{ ns}$ for different values of t_{ini} : (e-1) $0 \mu\text{s}$, (e-2) $0.4 \mu\text{s}$, (e-3) $0.8 \mu\text{s}$, and (e-4) $1.2 \mu\text{s}$.

or $y = u_{NL}(t + T)$, respectively, where the delay time T should be chosen wisely. The PPP for the linear and nonlinear signals are plotted in Fig. 5.6(b) and Fig. 5.6(d), respectively, where $T = 12$ ns.

In order to observe the change on the phase of the oscillations with increasing time, the PP and the PPP, both for linear and for nonlinear signals, are plotted with four different times t_{ini} at which the parametric representation start. These four initial times are associated to the numbering of the subplots in Fig. 5.6: for the PP [(a) and (c)] the numbering corresponds to the following t_{ini} (1) $0 \mu\text{s}$, (2) $0.32 \mu\text{s}$, (3) $0.64 \mu\text{s}$, and (4) $0.96 \mu\text{s}$; for the PPP [(b) and (d)] the numbering corresponds to the following t_{ini} (1) $0 \mu\text{s}$, (2) $0.4 \mu\text{s}$, (3) $0.8 \mu\text{s}$, and (4) $1.2 \mu\text{s}$. Note that, as t_{ini} increases, the extrema values in the PP and the PPP decrease, since the amplitude of both signals exponentially decreases. With the comparison between Fig. 5.6(a) and (b) and between Fig. 5.6(c) and (d), it is seen that the phase planes and the pseudo-phase planes agree with the use of the previously-listed parameters. The most important feature of the PP and of the PPP is the direct visualization of phase change with respect to time. For instance, in Fig. 5.6(a)-(b) where the signal is linear, the phase portrait is exactly the same, no matter the value of the chosen time to start the parametric representation. However, in Fig. 5.6(c)-(d) where the signal is nonlinear, the phase portrait changes. While it is looking as a counter-clockwise turning spiral when t_{ini} is less than $0.4 \mu\text{s}$, it looks as a clockwise turning spiral when t_{ini} is greater than $0.4 \mu\text{s}$. The latter means that the PPP should allow to visualize any phase change with increasing time in the experimental results.

It is then proposed to apply the PPP representation with the same parameters (T and t_{ini}) to the filtered experimental data normalized by its maximum amplitude [see Fig. 5.5(c)]. The results are shown in Fig. 5.6(e). Similar changes of the spiral turning directions than the one shown in Fig. 5.6(d) are found in Fig. 5.6(e). This demonstrates that the phase portrait of the experimental data changes with increasing time, which means that the signal is nonlinear. Note that the phase portrait is yet more complicated than the one depicted in the case of $u_{NL}(t)$, which means that the temporal function associated to the experimental results is more complicated than the proposed expression in Eq. (5.3). Thus, in the next section, we introduce another signal model and propose a model-based signal processing method for analyzing the data and for extracting/quantifying a nonlinear parameter contained in the experimental observations (the frequency variation as a function of the amplitude).

5.5 Signal processing model

The model of the nonlinear oscillating signal that will be used to extract the nonlinear parameters from the experimental signals with a minimization process is now introduced. We start from the physical observations for nonlinear resonances, where the inverse of the quality factor Q can be written as a function of the current amplitude $A = A(t)$ of the wave, which is time-dependent, as follows:

$$\frac{1}{Q(A)} \approx \frac{1 + a_1 A}{Q_0}, \quad (5.5)$$

where Q_0 is the quality factor when the amplitude of the oscillating signal is small, i.e. in the linear regime, and where a_1 and a_2 stand for the nonlinear dependence of the inverse of Q with the current amplitude. Still based on physical observations; the relative shift of the oscillation frequency $\Delta f/f_0$, with f_0 the oscillation frequency in the linear regime, can also be written as:

$$\frac{\Delta f}{f_0} \approx b_1 A, \quad (5.6)$$

where b_1 is the nonlinear parameter associated to the change in frequency due to a change in the current amplitude of the wave. The instantaneous frequency then reads:

$$f(A) = f_0 + b_1 f_0 A. \quad (5.7)$$

We assume a temporal signal of the general form,

$$u(t) = ae^{-\psi(t)} \cos \phi(t), \quad (5.8)$$

with a magnitude equal to

$$A(t) = |u(t)| = ae^{-\psi(t)}, \quad (5.9)$$

where

$$\psi(t) = \frac{\pi f[A(t)]}{Q[A(t)]} t = \frac{\pi f_0}{Q_0} t [1 + a_1 A(t)] [1 + b_1 A(t)]. \quad (5.10)$$

As a reminder, the relation between the quality factor Q , the damping ratio ξ , and the decay time τ is expressed as following: $Q = \frac{1}{2\xi} = \frac{\tau\omega_0}{2}$ with $\omega_0 = 2\pi f$. At the leading order in correction terms, we have,

$$\psi(t) \approx a_0 t [1 + (a_1 + b_1)ae^{-a_0 t}], \quad (5.11)$$

where $a_0 = \pi f_0/Q_0$. In order to determine $\phi(t)$ we start from $f(t) \approx f_0(1 + b_1 ae^{-a_0 t})$ and we check that

$$\lim_{t \rightarrow \infty} f(t) = f_0, \lim_{t \rightarrow \infty} A(t) = 0, \lim_{t \rightarrow \infty} Q(A(t)) = Q_0.$$

As we have by definition $f(t) = \frac{1}{2\pi} \frac{\partial \phi(t)}{\partial t}$, then $\phi(t) = 2\pi \int f(t) dt - C$, where C is a constant. If we start at $t = 0$ with the maximum of a signal (of the cosinus signal), we have the requirement that $\phi(t = 0) = 0$. Then, we eventually get,

$$\phi(t) = \omega_0 \left(t - \frac{b_1}{a_0} ae^{-a_0 t} + \frac{b_1}{a_0} a \right). \quad (5.12)$$

We then have to minimize the coefficients f_0 , Q_0 (or a_0), a_1 , b_1 . Some of these coefficients may be useless, which has to be checked depending on the problem. For the simplest and normalized ($a = 1$) case where we have considered only the quadratic nonlinearity on frequency the following normalized formulation of the signal is then obtained:

$$u(t) = ae^{-a_0 t [1 + (a_1 + b_1)ae^{-a_0 t}]} \cos \left[\omega_0 \left(t - \frac{b_1}{a_0} ae^{-a_0 t} + \frac{b_1}{a_0} a \right) \right]. \quad (5.13)$$

Yet, our preliminary minimization trials have demonstrated that the fits are much more sensitive to the accumulating-with-time amplitude-dependent phase shift than to the deviations of the amplitude decay expressed in the exponential term. Therefore a simplified formula is decided to be used where the nonlinear term is removed from the exponential:

$$u(t) = ae^{-a_0t} \cos \left[\omega_0 \left(t - \frac{b_1}{a_0} ae^{-a_0t} + \frac{b_1}{a_0} a \right) \right]. \quad (5.14)$$

Note that in this simplified expression, the only nonlinear parameter remaining is b_1 . For extracting the nonlinear parameter b_1 from our measurements, the expression in Eq. (5.14) will be used to fit the experimental signals, as discussed in the next section.

5.6 Evolution of the nonlinear parameter with the thermal fatigue

In this section, we present the results of the evolution of the nonlinear parameter b_1 in the heat-treated sample for different treatment durations. Before applying the proposed signal processing (minimization between the model and the experimental signals), the observed signals are filtered. To minimize the processing of the original signal and to stay as close as possible to the ZGV waveform when filtering, it has been decided to use the `smooth` function in Matlab as a low pass filter. The smoothed signal indeed contains the low frequency variation in the signal and, by subtracting the smoothed signal from the original data, a signal devoided of low frequencies is obtained.

An example of the processing is shown in Fig. 5.7. The top figure shows the original data (black dotted line), the smoothed signal (red dashed line), and the filtered signal (blue solid line). The inset in the top part is a zoom on the beginning of the signal. From that figure, it can be seen that, although the signal has been registered for 10 μ s, the amplitude of the ZGV resonance decreases quite fast. In order to perform the fitting of the model to the experimental signal where the ZGV resonance is actually still at play, it is proposed to set a signal-to-noise ratio (SNR) threshold below which the corresponding measured signals will be disregarded. This is illustrated in the bottom part of Fig. 5.7 showing the instantaneous SNR of the signal estimated by considering the noise level of the recorded signal before $t = 0$. The threshold is fixed at 5 dB. The signal is therefore cut in the example after 2 μ s for avoiding the useless information, i.e. the part with SNR less than 5 dB is not considered.

From each of the eight tested samples, one measured signal is used in the following. All the eight received signals are processed using the `smooth` function as described above and the results of the filtering are illustrated in Fig. 5.8.

The inverse estimation of the parameter a_0 (related to Q_0) and of the nonlinear parameter b_1 is performed for each signal by minimizing the following cost function:

$$f_{cost}(a_0, b_1) = \sum_t V(t) \times \|u_{exp}(t) - u_{theo}(t, a_0, b_1)\|^2, \quad (5.15)$$

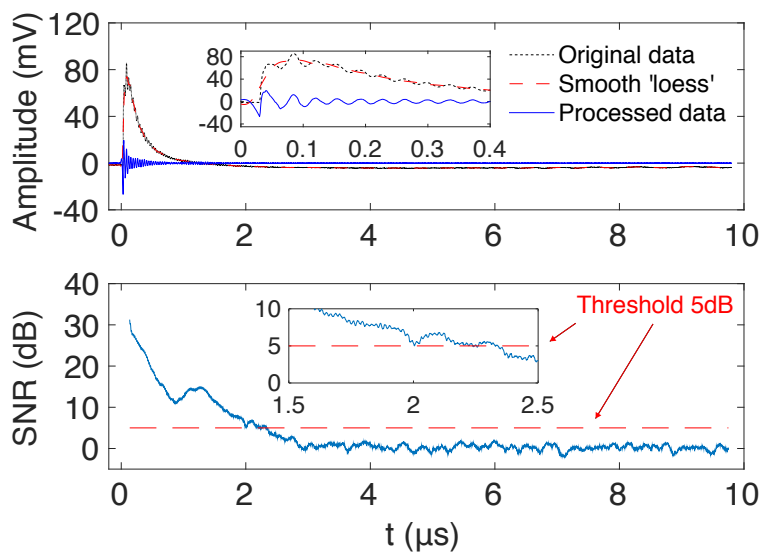


Figure 5.7: (Top) An example of the processing for a received signal using the `smooth` function: original data (black dotted line), smoothed signal (red dashed line), and filtered signal (blue solid line); (Bottom) Instantaneous SNR of the processed signal as a function of time. The red dashed horizontal line shows the threshold of 5 dB below which the signal is considered as noise.

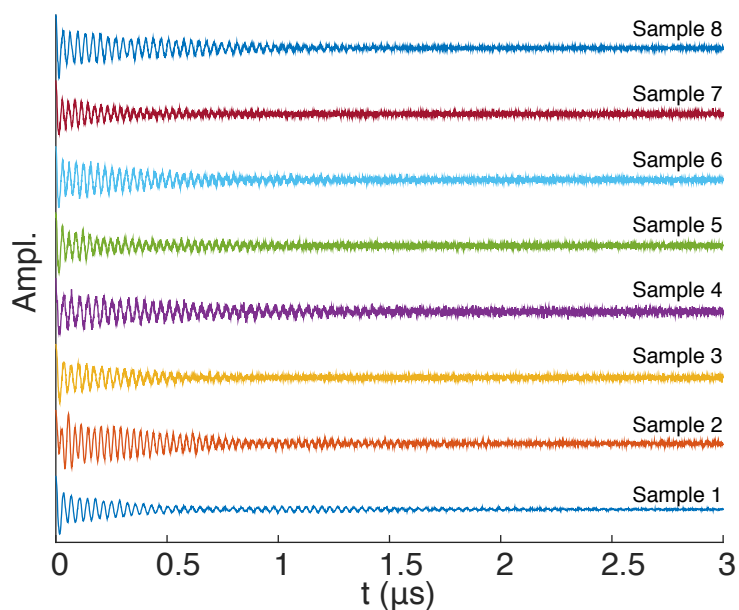


Figure 5.8: Results in the eight samples of the signal filtering with the `smooth` function.

where $V(t)$ is defined as

$$V(t) = \begin{cases} 1 & \text{for } \text{SNR}(t) \geq \text{Threshold}, \\ 0 & \text{for } \text{SNR}(t) < \text{Threshold}. \end{cases} \quad (5.16)$$

The minimization is performed under constraints with the Nelder-Mead simplex algorithm with the use of the function `fminsearch` in Matlab with values of ‘MaxFunEvals’ and ‘MaxIter’ set to be 1E10, which is sufficiently large for optimization. The images of the values of f_{cost} as a function of a given range for a_0 and for b_1 are illustrated in Fig. 5.9 for visualizing if a global minimum exists in each case and if the global minimum is not surrounded by local minimum to which the minimization process could converge due to bad first guess. Fig. 5.9 clearly shows that for these 8 signals the minimum is global and that the minimization should not be an issue. This shows also that the proposed method seems feasible. The values of b_1 are therefore estimated and are given in the Tab. 5.1. Other basic information about samples is also given in this table².

As already said, these samples were kindly prepared by our colleagues from ISNDE from Aluminum alloy blocks that had been already tested by them. In the Ref. [49], they reported two nonlinear parameters from two methods using the non-linearity of the Rayleigh wave. β'_1 has been measured with a contact method for generation and detection, while β'_2 has been measured with a semi-contact method (laser for generation and transducer for detection). They have shown that the non-linearity measured by these two methods was in good agreement one to another, but also with the variation of the yield strength due to thermal aging. In order to compare our estimated nonlinear parameter to those estimated by our colleagues from ISNDE, we calculate the fractional change of b_1 and compare with the other measured nonlinearity variations in different stages of thermal aging (see Fig. 5.10).

In accordance with the study of our collaborators [49], the general precipitation sequence of 6000-series Al-Mg-Si alloy is as follows: super-saturated solid solution \rightarrow co-clusters \rightarrow Guinier-Preston I (spherical-shaped) \rightarrow needle-shaped \rightarrow rod-shaped \rightarrow plate-shaped. The last three stages are named as $\hat{\beta}$ (plate-shape), $\hat{\beta}'$ (rod-shape) and $\hat{\beta}''$ (needle-shape) for representing the precipitation phase in the 6000-series Al-Mg-Si alloy. As the thermal aging proceeded, the samples went through these stages one by one, and the gradual transition at different stages provides a fractional change on the acoustic nonlinearity [49]. H. Seo et al. measured the magnitudes of the fundamental and second harmonic frequency components (A_1 and A_2 , respectively) of bulk acoustic waves and calculated the relative acoustic nonlinearity parameter with $\beta' = A_2/A_1^2$ which is widely used [45, 134, 213, 216, 218, 222, 237, 238]. The fractional change $\bar{\beta}'$ is also calculated using $\bar{\beta}' = (\beta'_{aged} - \beta'_{intact})/\beta'_{intact}[\%]$. Those are the quantity plotted in Fig. 5.10 blue dashed lines connecting square symbols ($\bar{\beta}'_1$) and red dash-dotted lines connecting downward triangle symbols ($\bar{\beta}'_2$). The fractional change of b_1 , plotted as black solid line with disk symbol in the same Fig. 5.10, shows the same variations as $\bar{\beta}'_1$ and $\bar{\beta}'_2$ with respect to the heat-treatment

²The constants (longitudinal velocity V_L , shear velocity V_T , Young modulus E and Poisson’s ratio ν) presented here are measured by using Aluminum alloy blocks, for details, please see the Tab. 2 in the reference [49]

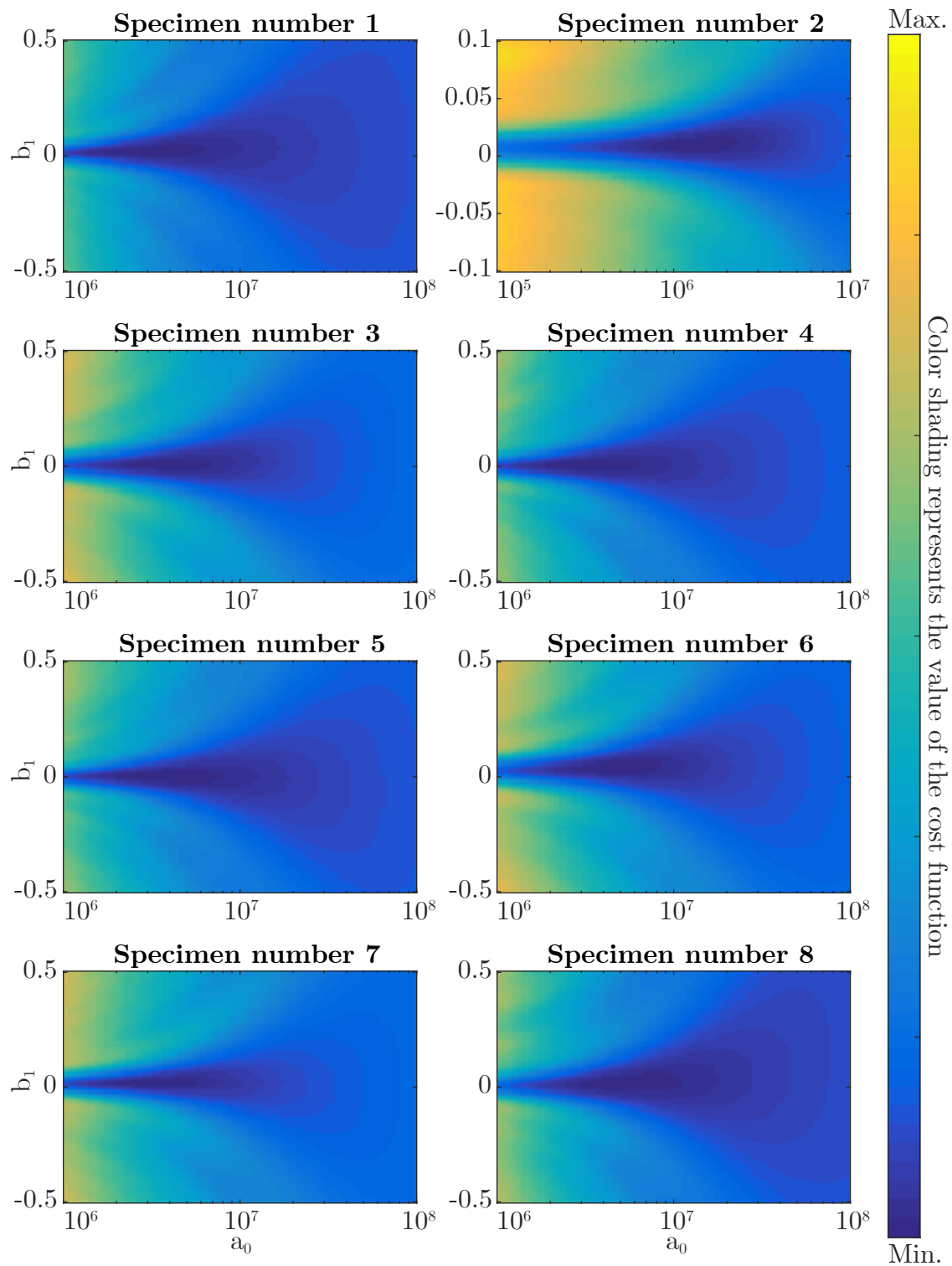


Figure 5.9: Representations of the cost function used in the minimization process as a function of the coefficients a_0 and b_1 .

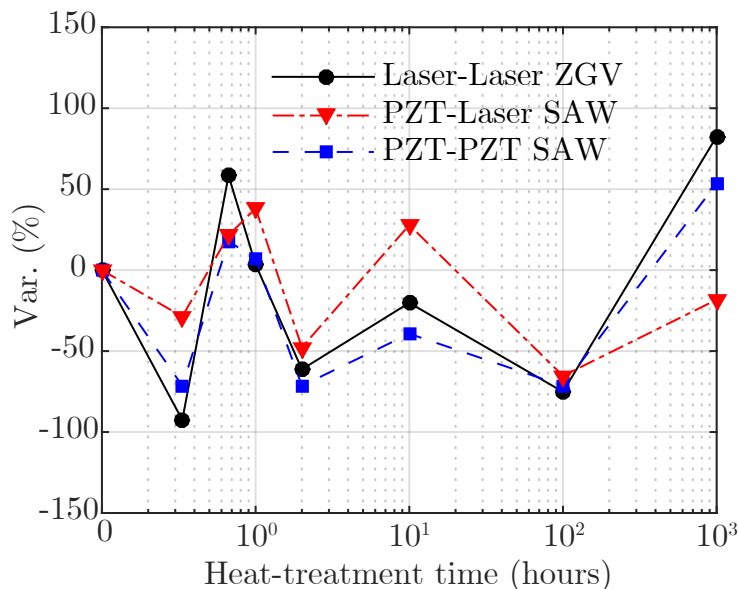


Figure 5.10: Evolution of $\bar{\beta}'_1$ (blue dashed line with square symbols), of $\bar{\beta}'_2$ (red dash-dotted line with downward triangle symbols), and of the fractional change of b_1 (black solid line with disk symbols) according to the heat-treatment durations.

time. This shows the potential of the nonlinear parameter of ZGV resonances to account for thermal aging.

Linear in wave-amplitude deviations of the inverse quality factor and of the oscillation frequency in our Eqs. (5.5) and (5.6) are the typical features of the lowest order (quadratic) hysteretic nonlinearity, which manifests itself in linear variations with wave amplitude of the real and imaginary parts of the elastic modulus [203, 239, 240]. Our ability to fit the experimental data, assuming a frequency shift changing linearly with wave amplitude, indicates that the observed nonlinear phenomena is due to hysteretic quadratic nonlinearity, because it cannot be associated with the elastic nonlinearities. Quadratic elastic nonlinearity does not shift the oscillation frequency because it does not modify the velocity of the harmonic acoustic waves propagation. Cubic elastic nonlinearity could introduce a frequency shift but this shift would be quadratic and not linear in the wave amplitude [240]. We can then conclude from this that we have revealed a thermal fatigue leading to the modifications in the hysteretic quadratic nonlinearity of the material. At the same time hysteretic quadratic nonlinearity does not contribute to the generation of the second harmonic in the finite-amplitude acoustic waves [203, 239, 240]. Generation of the second harmonic is the manifestation of the elastic quadratic nonlinearity [240–242]. So in the experiments on the second harmonic generation of SAWs conducted in ISNDE of Hanyang University Seoul the elastic quadratic nonlinearity of the considered samples was revealed and tested as a function of the thermal fatigue. Thus, the correlation of the data obtained by us and our colleagues from ISNDE of Hanyang University Seoul, which is evidenced in Fig. 5.10 indicates that these two different quadratic material nonlinearities, hysteretic and elastic, are both present in the tested material and vary proportionally as a function of the materials modifications

Table 5.1: Longitudinal velocity V_L , shear velocity V_T , Young modulus E , Poisson's ratio ν of the used samples and nonlinear parameters measured by different approaches for different heat-treatment time (T_{heat}): PZT-PZT SAW contact method (β'_1), Laser-PZT SAW semi-contact method (β'_2) and Laser-Laser ZGV resonance contactless method (b_1).

T_{heat}	0 min	20 min	40 min	1 h	2 h	10 h	100 h	1000 h
V_L (m/s)	6406	6362	6401	6402	6387	6415	6382	6382
V_T (m/s)	3168	3203	3177	3175	3195	3198	3191	3212
E (GPa)	72.61	73.78	72.99	72.84	73.47	73.67	73.48	74.32
β'_1	0.028	0.008	0.033	0.030	0.008	0.017	0.008	0.043
β'_2	4.908	3.500	5.966	6.779	2.565	6.276	1.703	4.013
b_1	0.0201	0.0015	0.0318	0.0208	0.0078	0.0160	0.0050	0.0367

introduced by thermal fatigue.

As pointed in the article [49] published by H. Seo et al.: “In monitoring the relative acoustic nonlinearity parameter, not only the value itself but also its history is taken into consideration. ... it is necessary to identify the characteristics of acoustic nonlinearity change through preliminary research such as this study about the change in acoustic nonlinearity caused by the thermal aging of Aluminum alloy. Especially, applying the relative acoustic nonlinearity measurement to structural health monitoring (SHM) with such preliminary knowledge, its feasibility and effectiveness can be even better manifested.” The agreement between the fractional changes in the relative nonlinear parameters between the contact and semi-contact SAWs methods, and the fully contactless ZGV resonance method in the Aluminum alloy is an experimental basis for the demonstration that the measurement of nonlinear parameters via SAWs and guided waves is of interest in the analysis of thermal fatigue.

5.7 Discussion on the influence on the ZGV resonance of the temperature rise caused by laser absorption

During the experiments using lasers, a topic that can never be avoided is the discussion on the laser-caused temperature rise and its influence on the assessed samples. Moreover, the frequency shift of ZGV resonance in Aluminum membrane by varying the incident laser power (resonance frequency decreased as laser power increased) has been already observed by O. Balogun et al. [24]. Therefore, the aim of this section is to ascertain that the frequency change observed in the precedent section cannot be explain by the temperature rise itself.

5.7.1 Temperature rise influence on ZGV resonance frequency in Aluminum alloys (AlAl-5083)

In this subsection, we consider the worst case (i.e. Aluminum alloys 5083) in which the variation of elastic properties, due to a given temperature rise, is the greatest compared to other Aluminum alloys 1100, 7005 and 7075 [243]. This is done in order to estimate the maximum possible thermal effects caused by temperature rise and since the actual temperature dependence of the elastic properties of our samples are not known. Therefore, in this study, we calculate the temperature rise influence on S_1S_2 -ZGV frequency in Aluminum alloys (AlAl-5083) by considering the following temperature dependent properties: Young modulus (E), thickness ($2h$), shear modulus (G) and Poisson's ratio (ν). The formula used for calculation of the temperature dependant elastic constant is [243]:

$$C_{case} = C_0 - \frac{s}{e^{T_{case}/T} - 1}, \quad (5.17)$$

where C_{case} is any elastic constants (for C_l longitudinal and C_t shear elastic constant in our problem), C_0 , s and T_{case} are adjustable parameters described in Ref. [243], and T is the temperature. The value of C_{case} at $T=0$ K is C_0 and $-s/T_{case}$ is the high-temperature limit of the temperature derivative dC/dT . The values of C_0 , s and T_{case} for both longitudinal (t_l) and shear (t_t) cases are given in Table IV of Ref. [243] and are equal to: $C_0 = 115.10$ GPa for l -mode and 30.67 GPa for t -mode, respectively; $s = 9.26$ GPa for l -mode and 3.81 GPa for t -mode, respectively; and $t_l = 235.3$ K, $t_t = 206.7$ K. Then, several material properties can be calculated as a function of the temperature, here are the formula for the shear modulus G , the Young modulus E , and the Poisson's ratio ν :

$$G = C_t; \quad (5.18)$$

$$E = \frac{3G(C_l - \frac{4}{3}C_t)}{(C_l - C_t)}; \quad (5.19)$$

$$\nu = E/2G - 1. \quad (5.20)$$

The temperature dependence of the material thickness h is given by [24]:

$$h = h_0(1 + \alpha_t \Delta T), \quad (5.21)$$

where h_0 is the plate thickness at room temperature, α_t the thermal expansion coefficient, and ΔT the temperature rise.

Table 5.2: Theoretical ZGV frequency variations and related temperature rise by considering thermal dependent E , G , h and Poisson ratio ν .

Δf (%)	0.1	0.2	0.5	1	2
ΔT (K)	4.78	9.64	24.74	51.79	114.16

The room temperature (T_0) used is $20^\circ C$ (293.15K). Finally, we inversely estimate the corresponding temperature rise values (extracted from fitting curve in Fig. E.5 in the Appendix E) from the fitting relation for different cases of $\Delta f = 0.1\%$, 0.2% , 0.5% , 1% and 2% in Tab. 5.2. For details of the calculations, see Appendix E.

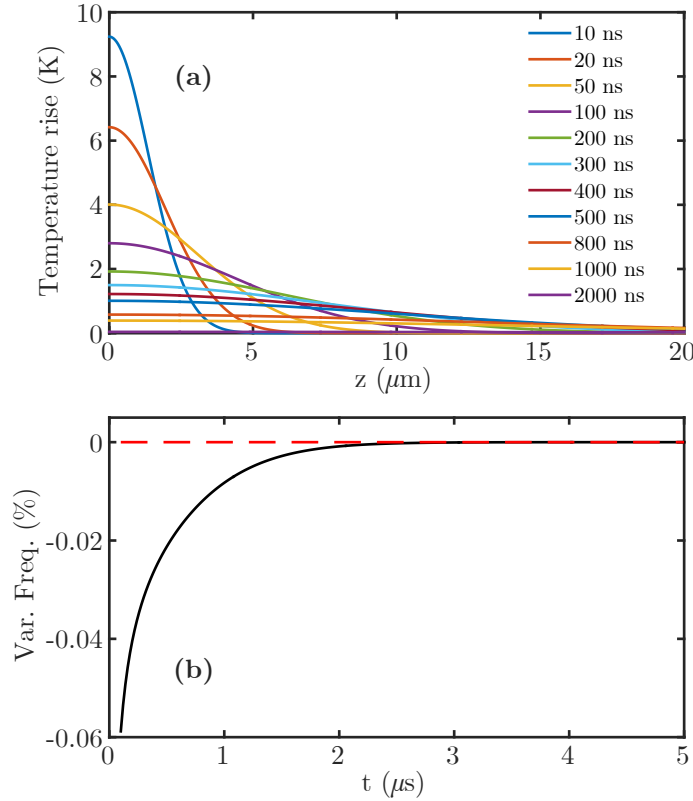


Figure 5.11: Laser-induced temperature rise and its influence on the shift of the ZGV frequency. (a) Temperature rise due to pulsed laser as a function of depth at different time; (b) ZGV resonance frequency variation as a function of time in the position of the exciting point.

5.7.2 Influence of the temperature rise due to the pulsed laser

Following the same ideology, introduced above, in this paragraph, we discuss the influence of the temperature rise due to the pulsed laser. The equation used for calculating the temperature rise due to the pulsed laser [30, 32] is given here:

$$\Delta T(r, z, t) = \frac{Q}{\pi K} \sqrt{\frac{\kappa}{\pi}} \int_0^t \frac{q(t-t')}{\sqrt{t'(4\kappa t' + a^2)}} \exp\left(-\frac{z^2}{4\kappa t'} - \frac{r^2}{4\kappa t' + a^2}\right) dt', \quad (5.22)$$

where Q is the absorbed energy, K is the thermal conductivity in room temperature, κ is the thermal diffusivity, $2a$ is the laser beam diameter and $q(t) = (t/\tau^2) \exp(-t/\tau)$ with τ the pulse duration.

In our case, for theoretical calculations, the absorbed energy is set to be the maximum value of $50 \mu\text{J}$ that our laser in experiments can reach. The laser pulse duration is $\tau = 750 \text{ ps}$, the laser beam radius is experimentally estimated to be 0.105 mm . With all the numerical values, we plot herein the temperature rise due to the pump laser at the excitation position ($r = 0$) as a function of depth z for different time in Fig. 5.11(a). From Fig. 5.11(a), we can find out that after about $2 \mu\text{s}$ (standard repetition rate of the pump laser is 1 kHz , corresponding to 1 ms

delay between consecutive laser pulses), the thermal influence of pump laser almost completely disappeared. By the way, the level of the temperature rise is less than 10 K from 10 ns (note that we start the treatment of the experimental on ZGV oscillation at $\sim 100 \mu\text{s}$, which is much longer than 10 ns), which is very weak in our case.

With the help of the Matlab code based on the program in Appendix D, we calculate the frequency variation of the ZGV resonances in Aluminum alloys (see Sec. 5.7.1 for ideology) at $z = 0$. The equation (5.22) can be then simplified in case of that r and z are all zeros, like:

$$\Delta T(0, 0, t) = \frac{Q}{\pi K} \sqrt{\frac{\kappa}{\pi}} \int_0^t \frac{q(t-t')}{\sqrt{t'(4\kappa t' + a^2)}} t', \quad (5.23)$$

The frequency variation of the ZGV resonance due to pump laser for a given Aluminum alloy, considering the changes on the following temperature dependent properties: Young modulus (E), thickness ($2h$), shear modulus (G), and Poisson's ratio (ν), is shown in Fig. 5.11(b). From Fig. 5.11(b), the variation of the frequency is less than 0.06%, from t just after $0.1 \mu\text{s}$ to $2 \mu\text{s}$ and later, which is much lower than the ZGV frequency variation in experiment (for example, for the sample number 1, the detected variation is of about 2%). The influence of the pump laser used in this work is quite weak compared to the experimentally observed frequency variation as a function of the amplitude.

5.8 Conclusions

In this chapter, measurements of nonlinear parameter via contactless generation of ZGV Lamb waves are carried out in order to characterize the thermal aging of an Aluminum alloy. The experiments are realized on Aluminum alloy specimens (Al6061-T6) which have been heat-treated at $220 \text{ }^\circ\text{C}$ for different times (0 min, 20 min, 40 min, 1 h, 2 h, 10 h, 100 h, 1000 h) after a preliminary heat treatment and had therefore the different levels of thermal aging. From the experimental observation, the fractional change in the nonlinear parameter agrees well with the variation in the yield strength, which demonstrates the potential of the presented results for evaluating the thermal damages. Therefore, the variation of the nonlinear parameter of the ZGV resonance could be considered as an indicator of the level of thermal aging of the Aluminum alloy. We are currently performing the experiments of one-dimensional lateral scanning to evaluate the spatial distribution of the nonlinear parameter in the samples.

Chapter 6

Application of laser-based ZGV resonances to characterize the texture in rolled metallic plates

Contents

6.1	Introduction	122
6.2	Experimental setup	124
6.3	Effect of the anisotropy of the Copper sample on the ZGV frequency	125
6.4	Study of the texture of the anisotropic Copper plate by using laser-based ZGV resonance	126
6.4.1	Results of the 1D experimental scanning measurements	127
6.4.2	Results of the 2D experimental scanning measurements	127
6.5	Conclusions	129

Keywords: *ZGV Lamb modes, LU, Anisotropy, Texture.*

To improve is to change; to be perfect is to change often.
— Winston Leonard Spencer- Churchill

In this chapter, the laser-based ZGV resonance technique is used for characterizing the grain microstructure in a high purity Copper sample at the micrometric scale. A Copper block, made of randomly oriented crystallites, is subjected to a rolling process giving rise to a plate structure which is highly textured and presents a transversely isotropic elastic behavior (three elastic constants). Due to this anisotropy, the ZGV resonance does not appear like the usual unique peak but as multiple adjacent peaks with different amplitudes. Two approaches are proposed here for imaging the texture by means of information extracted from the ZGV resonance multiple peaks. The image is obtained in one case by using the value of the ZGV resonance frequency presenting the maximum amplitude within the different peaks composing the resonance. In the second case, the 2D distributions of the spectral density at a given frequency around the ZGV resonance peaks are used. The obtained images with both methods present similar features corresponding to the rolling direction. Thanks to the ZGV resonance multiple peaks in the frequency spectrum, the here-presented preliminary analyzes is strongly encouraging, although further experiments and signal analyzes are needed to fully capture the whole promises of this technique for texture characterization. The observed phenomena show important implications for the use of the laser-based ZGV resonance method for the analysis of textured samples. Potential applications of this method contain the evaluation of the development of recrystallized microstructure in high purity Copper as well as the monitoring of the texture changes during high temperature processing.

6.1 Introduction

In materials science, the word *texture* is used to describe the distribution of crystallographic orientations of the crystallites in a polycrystalline sample. The crystallites orientation of polycrystalline materials should generally be random. However, due to the manufacturing process, most grains can have similar crystal orientations, which is called texture or preferred orientation.

Generally speaking, the reason for the texture is usually that the metal is subjected to a drawing, rolling or extrusion process, so that the grains inside the metal are aligned in the same direction. The production of texture will highlight the elastic anisotropy: if there is no texture, the orientation of the crystallites is random, and the sample anisotropy will be offset; if there is orientational order, the anisotropy will be particularly prominent. Therefore, the texture has a significant influence on the elastic properties of the metal having large single-crystal elastic anisotropy considering the important role of the grain microstructure on the mechanical properties of the processed metal [244].

Traditionally, texture or orientation distribution analysis is performed using X-ray diffraction [191] or electron backscatter diffraction (EBSD) [174, 245]. An alternative technique, resonant ultrasound spectroscopy (RUS) utilizing contact transducers, is also an efficient tool for measuring mechanical properties as well as for characterizing bulk texture of materials [202, 246, 247]. This also motivated continuously researchers in different groups to develop novel contactless techniques for the

evaluation of texture using measurements of acoustic properties. In the last decade, the laser-based resonant ultrasound spectroscopy (LRUS) has been proven to be useful for nondestructive evaluation of textured materials [244, 248–252], especially the previous works achieved by D.H. Hurley et al. [244, 250] which focus on the development and applications of LRUS to study texture in pure metals.

In the study published in Ref. [250], they used *in situ* LRUS to characterize the development of a recrystallized microstructure in a high purity Copper sample, combined with electron backscatter data to prove that the majority of this shift is due to changes in the polycrystal average elastic stiffness tensor, driven by changes in texture, and that changes in dislocation density and pinning length are of secondary influences. Just two years later, in their other work [244], LRUS is applied for studying texture in Copper samples having two distinct grain microstructures: one is processed with four passes of equal channel angular extrusion (ECAE) and consists of randomly oriented crystallites (leading to isotropic elastic property of the polycrystal in average with only two elastic constants), and the other is imparted by means of rolling a fully annealed material to a 97.5% thickness reduction and has a textured microstructure (leading to anisotropic elastic property of the polycrystal in average with three elastic constants). The laser-based experimental setup schematics as well as the EBSD micrographs of samples used in the two works, i.e. in [250] and in [244], are illustrated in Fig. 6.1(a) and Fig. 6.1(b), respectively, for giving a basic idea of LRUS and its applications for the author himself and the readers.

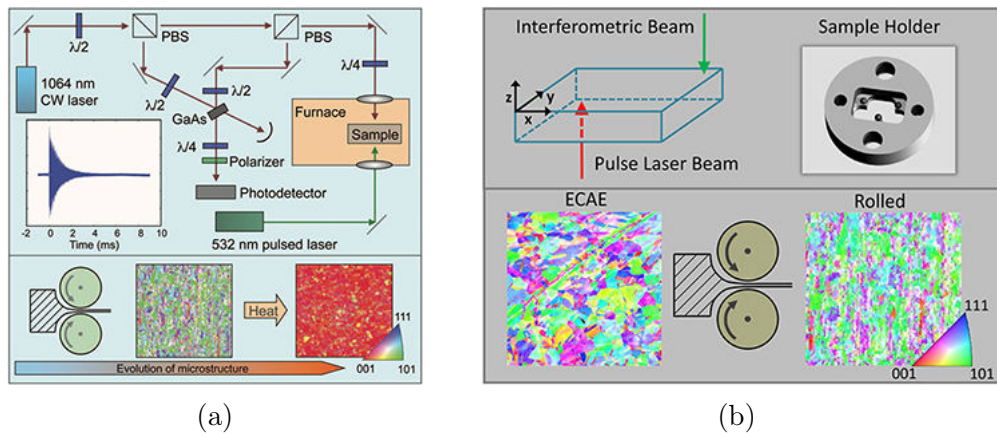


Figure 6.1: (a) Top: Experimental setup. A pulsed Nd:YAG laser is used for ultrasonic generation and a photorefractive interferometer is used to detect out-of-plane surface motion. The inset in the bottom left shows the ultrasonic ring-down in the sample after laser excitation. Bottom: Details of microstructure evolution. A texture is imparted by rolling. A well defined cube texture is formed upon annealing [250]. (b) Top left: generation and detection beams strike corner of sample. Top right: sample holder. Bottom: EBSD micrographs of ECAE and rolled samples [244].

In the end of the later paper [244], based on the experimental results, D.H. Hurley et al. pointed out that LRUS is a robust technique for the ECAE sample but not proper for rolling sample, since the inversion procedure for RUS was insensitive for anisotropic materials. One question comes thereby: how to develop a proper

method for anisotropic material by improving LRUS? As discussed in Chap. 2, ZGV resonance frequency has been proven to be sensitive to the anisotropy of the plate material [14] (see Fig. 2.16). As discussed by C. Prada et al. in Ref. [14], ZGV resonances can possibly provide an excellent accuracy for the determination of the three elastic constants of a transversely isotropic plate through an appropriate inversion algorithm. Therefore, the laser-based ZGV resonances appear as good candidates for evaluation of textured materials.

In summer of 2017, Dr. D.H. Hurley visited in LAUM for a short period and met the author and his supervisor, Dr. S. Raetz. After fruitful discussion between the three, Dr. D.H. Hurley kindly proposed to provide a piece of the Copper sample used in Ref. [250] for preliminary tests of the ability to characterize textured materials using laser-generated and laser-detected ZGV Lamb modes. With the experimental setup in Le Mans, the ZGV resonance was successfully generated and detected on the provided $\sim 300 \mu\text{m}$ -thick Copper plate. Unfortunately, experiments were suspended due to the process of the PhD work at that moment (analysis of the thermally-fatigued samples). With a little regret for not having completely achieved the goals of this part of the work due to the time constraints of a PhD, the current observations are presented in this chapter as preliminary results. The structure of this chapter is as follows: at first, the experimental setup for this work, already presented in details in the previous chapter, is quickly reminded; then a typical temporal photoacoustic signal received on the high purity Copper sample is shown and the effect of the anisotropy is discussed from its frequency spectrum; the preliminary experimental results of one- and two-dimensional scanning measurements are then analyzed to propose the imaging of the texture of the Copper sample; finally, preliminary conclusions and future steps are drawn.

6.2 Experimental setup

The experimental setup is schematically illustrated in Fig. 6.2 which is developed based on the setup used in chapter 5: the pump laser (pulse duration of $\sim 0.75 \text{ ns}$ with a repetition rate of 1 kHz) has an optical wavelength of 1064 nm and is focused into circular spot (diameter $\sim 100 \mu\text{m}$); another continuous laser (interferometer BossaNova Tempo with a wavelength of 532 nm) is focused to a circular spot (diameter $\sim 60 \mu\text{m}$). The calibration of the overlapping/separation of the generation and the detection circular spots is controlled by two rotating mirrors. The Copper plate is attached to a two-dimensional motorized translation stage. In this study, both x -axis and y -axis directions are used to achieve the C-scan measurements in order to produce the 2D images which will be presented after. The scanning directions are denoted by a cross double-headed arrow in Fig. 6.2.

The sample used in this work is the high purity Copper plate with nominal dimensions $70.5 \times 71.5 \times 0.3 \text{ mm}^3$, rolled from a Copper block with randomly oriented crystallites. A textured microstructure was imparted by rolling a fully annealed sample and a 99.6% thickness reduction was produced during the rolling process, leading to an average grain size for the rolled sample of $1.5 \mu\text{m}^2$ [250]. Note that y -axis corresponds to the rolling direction. The experimental measurement axial center

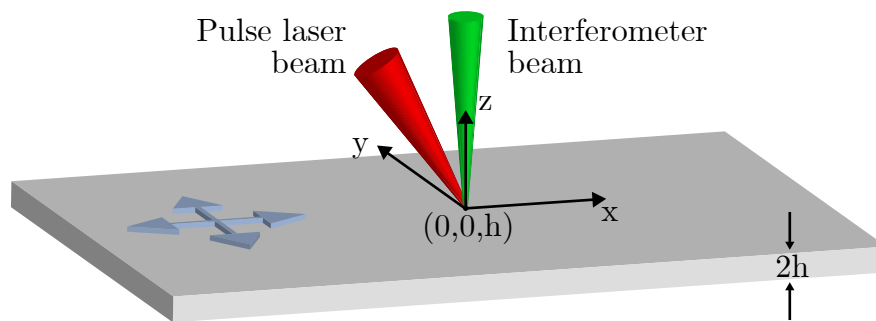


Figure 6.2: Experimental setup.

($x = y = 0$) is chosen to be approximately at the central position of the sample. The first step of the experiments is to achieve a point measurement, then to carry two one-dimensional (1D) scanning measurements along x - and y -axis, respectively, and finally to run a two-dimensional (2D) scanning measurements. For the 1D measurements, the sample is scanned along two lines, $x \in [-10 \text{ mm}, 10 \text{ mm}]$ at $y = 0$ mm corresponding to the horizontal line and $y \in [-10 \text{ mm}, 10 \text{ mm}]$ at $x = 0$ mm corresponding to the vertical line, with a scanning step of $100 \mu\text{m}$. For the 2D scanning, a square of $5 \times 5 \text{ mm}^2$ is chosen with $(x, y) \in [-2.5 \text{ mm}, 2.5 \text{ mm}]^2$, with both scanning steps equal to $200 \mu\text{m}$. The analysis of the point measurement is now proposed to illustrate the influence of the anisotropy of the Copper sample on the ZGV resonance.

6.3 Effect of the anisotropy of the Copper sample on the ZGV frequency

An example of an opto-acoustic temporal signal (measured at $x = 0$ mm and $y = 0$ mm) and its frequency spectrum normalized in amplitude is plotted in Fig. 6.3(a) and (b), respectively. In Fig. 6.3(a), the high-amplitude measured normal displacement at the beginning of the signal is associated to the low-order propagating Lamb mode (i.e. A_0 mode). While this mode propagates away from the generation area as time increases, the ZGV resonance remains in this area as shown by the inset presenting a zoom on the signal from $1 \mu\text{s}$ to $3 \mu\text{s}$. The latter is confirmed in Fig. 6.3(b) where a sharp peak at 7.33 MHz is found and corresponds to the S_1S_2 -ZGV resonance frequency. The theoretical ZGV frequency value could have been calculated from the anisotropic dispersion curves using the method proposed by T. Hussain et al. [72] with the values of the elastic constants of the sample given in the appendix of Ref. [250]. Note that this calculation is not done at present time but will be definitely performed in the near future.

The inset of Fig. 6.3(b) depicts a zoom of the frequency spectrum between 6 MHz and 9 MHz . It shows an important feature of the ZGV resonance in this Copper plate: the ZGV resonance does not appear as the usual unique peak (in the case of an isotropic material) but as multiple (here two) adjacent peaks with different amplitudes. At present, this can be explained and hypothesized as follows

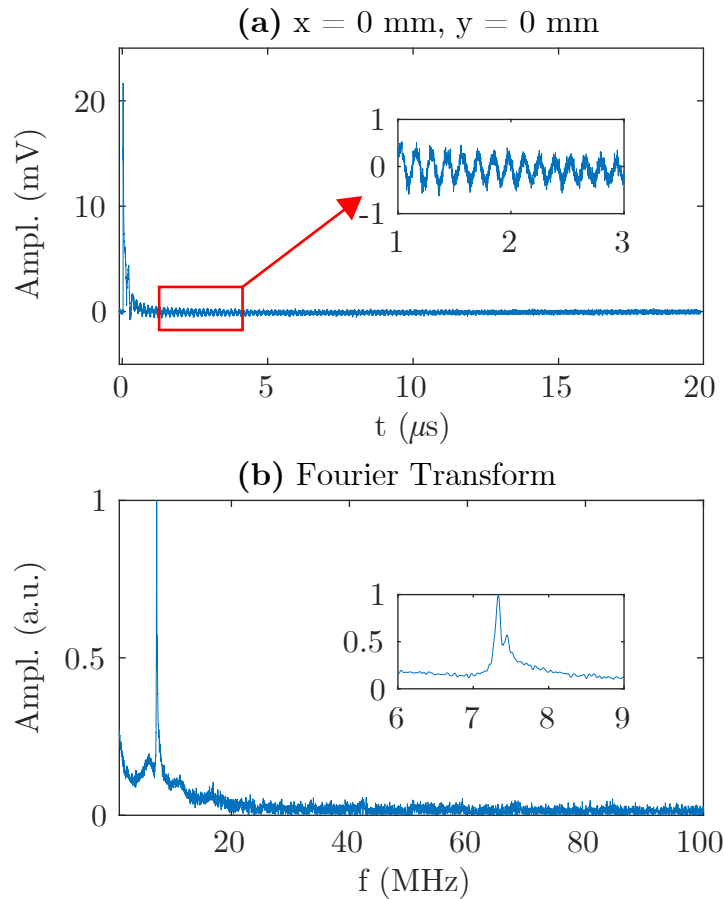


Figure 6.3: (a) An example of the received opto-acoustic signal and (b) its frequency spectrum normalized in amplitude.

[14]: since the sample is anisotropic (due to its texturing) and since the laser used for the elastic wave generation is focused to a circular spot, several resonances with different frequencies and associated to ZGV Lamb modes in different propagation directions are excited. Therefore the observed ZGV resonance contains oscillations with different but adjacent frequencies, surely containing information on the local orientation/texture that could be used for imaging purpose.

6.4 Study of the texture of the anisotropic Copper plate by using laser-based ZGV resonance

In this section, the previously-discussed features of the ZGV resonance in the tested Copper plate are used to analyze the texture of the plate, first from two 1D scanning measurements and then from a 2D scanning measurement. Note that the here-presented analyzes, although strongly encouraging, are preliminary and that further experiments and signal analyzes are needed to fully capture the whole promises of this technique for texture characterization.

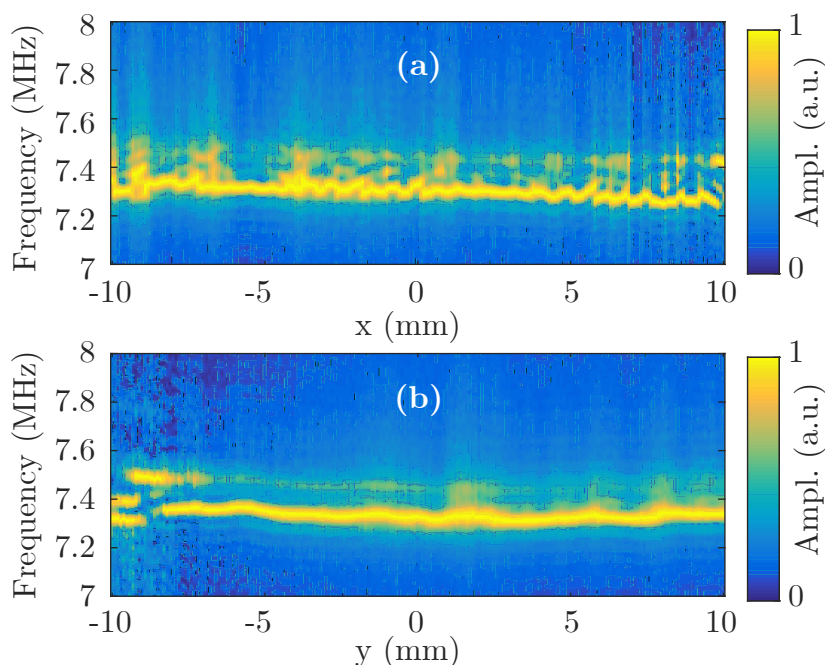


Figure 6.4: Distribution of the frequency in the frequency range of the ZGV resonance multiple peaks as a function of the scanning positions along (a) the x -axis and (b) the y -axis.

6.4.1 Results of the 1D experimental scanning measurements

The distribution of the frequency in the frequency range of the ZGV resonance multiple peaks is plotted as a function of the scanning positions in Fig. 6.4. Fig. 6.4(a) shows the results of the horizontal scanning measurements (along x -axis) and Fig. 6.4(b) shows the results of the vertical scanning measurements (along y -axis). From Fig. 6.4(a) and (b), it appears that most of the ZGV resonance peak with the maximum amplitude have frequency values about 7.3 MHz. It can be also noticed that the frequency variation along the x -axis are more pronounced than along the y -axis. Actually, when rolling along y -axis, it could somehow be conceived that the rolling device is itself inhomogeneous along x -axis and, thus, produces more inhomogeneity along x -axis than along y -axis. This could explain the frequency variation along x -axis together with the fact that the rolls could be misaligned along that direction. It is also clear from Fig. 6.4(a) and (b) that the feature of the multiple peaks due to the material anisotropy is more likely to be seen while scanning along x -axis than along y -axis. Note also that the frequency at which the peak amplitude is maximum does not always correspond to the frequency of the first peak. The latter may occur due to the local texture/anisotropy of the sample and should be deeper analyzed.

6.4.2 Results of the 2D experimental scanning measurements

A $5 \times 5 \text{ mm}^2$ 2D scanning of the sample is performed to analyze further the ability of the technique to image the texture. Through the signal processing of the experimen-

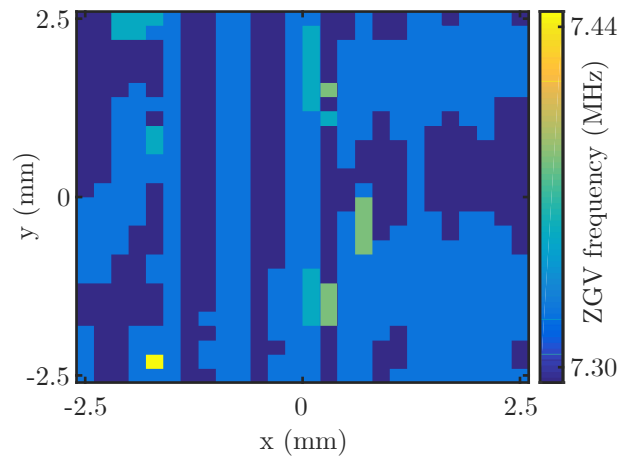


Figure 6.5: 2D distribution of the frequency associated to the peak with the maximum amplitude within the ZGV resonance multiple peaks as a function of the position on the plate.

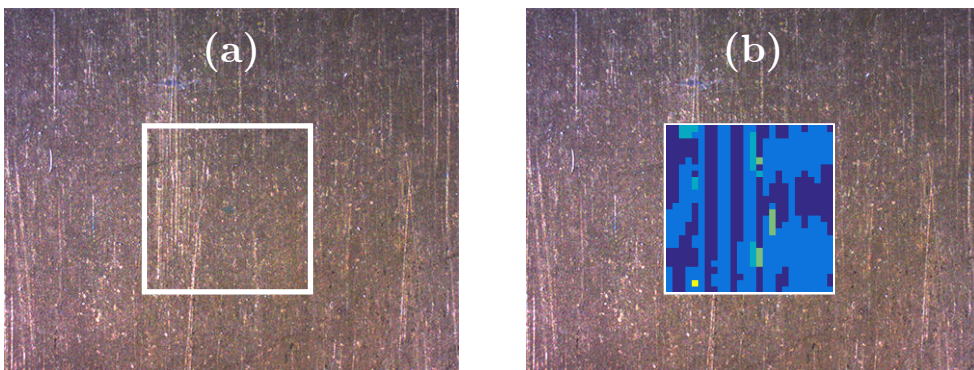


Figure 6.6: Comparison between (a) the photo under optical microscope and (b) the image obtained with the spatial distribution of f_{max} . The white square approximately corresponds to the measured area on the sample.

tal data, two different parameters are proposed and tested as contrast parameter for the imaging: (i) the frequency, denoted f_{max} in the following, associated to the peak with the maximum amplitude within the ZGV resonance multiple peaks, (ii) the spectral density of a given frequency in the range spanned by the ZGV resonance multiple peaks.

In Fig. 6.5, we plot the 2D spatial distribution of f_{max} on the Copper sample covering a square of $5 \times 5 \text{ mm}^2$. A photo of the sample surface under optical microscope is also shown in Fig. 6.6(a) with a white square approximately corresponding to the measured area on the sample. Fig. 6.6(b) with the image obtained with the spatial distribution of f_{max} is presented for comparison. From these two figures, it can be qualitatively stated that the changes of the value of the frequency corresponding to the spectral maximum in the multi-peak ZGV resonance depict the orientation of the rolling since the parameters seem to change more along the x -axis than along the y -axis. To have more qualitative information, the 2D distribution of the spectral density at specific frequencies in the ZGV resonance multiple peaks

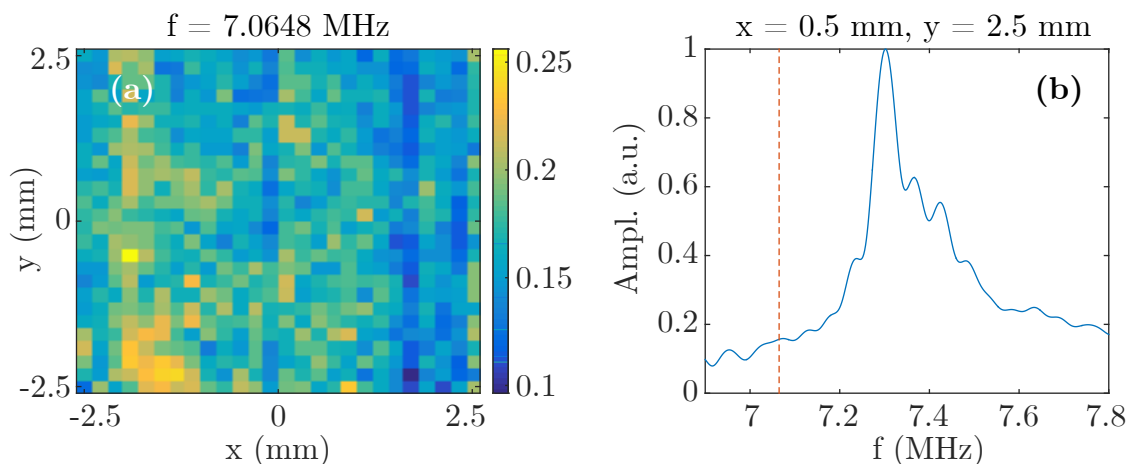


Figure 6.7: (a) 2D distribution example of the spectral density at $f = 7.0648$ MHz and (b) the frequency spectrum of one measured position (at $x = 0.5$ mm and $y = 2.5$ mm) showing at least three peaks of resonances. position.

should be studied.

The results using the second contrast parameter (the spectral density) for a frequency $f = 7.06$ MHz chosen rather arbitrary inside the multi-peak ZGV resonance is illustrated in Fig. 6.7(a) and the frequency spectrum of one measured position (at $x = 0.5$ mm and $y = 2.5$ mm) is shown in Fig. 6.7(b) with a vertical dashed red line corresponding to the chosen frequency. Note that in Fig. 6.7(b), there are at least three peaks composing the multi-peak ZGV resonance contrary to the spectrum shown in Fig. 6.3(b). This clearly strengthens the statement that this multiple peaks feature comports a lot of information.

Fig. 6.8 shows the obtained 2D distribution of the spectrum amplitude at (a) $f = 7.05$ MHz, (b) $f = 7.11$ MHz, (c) $f = 7.17$ MHz, (d) $f = 7.22$ MHz, (e) $f = 7.28$ MHz, (f) $f = 7.34$ MHz, (g) $f = 7.39$ MHz, (h) $f = 7.45$ MHz, and (i) $f = 7.51$ MHz. The brightest part of the images corresponds to several peaks in the spectrum [see Fig. 6.7(b)] at $f = 7.28$, 7.34 and 7.45 MHz. These brightest parts depict straight vertical line, i.e. straight line in the direction of the rolling process, which is strongly encouraging for the ability of the proposed method for texture imaging.

6.5 Conclusions

As a preliminary result, some of the figures (see Fig. 6.4, Fig. 6.5, and Fig. 6.8) shown in this chapter are sufficient to demonstrate the feasibility and the potentials of the proposed method, based on the ZGV Lamb mode for one-dimensional and two-dimensional imaging of pure metal textures. Due to the time limit of this project, no further experimental exploration will be conducted here, at least before the manuscript is drafted. However, from the results of the preliminary experiments, this work highlights the ability of the method to get image of the texture of high purity recrystallized metal Copper.

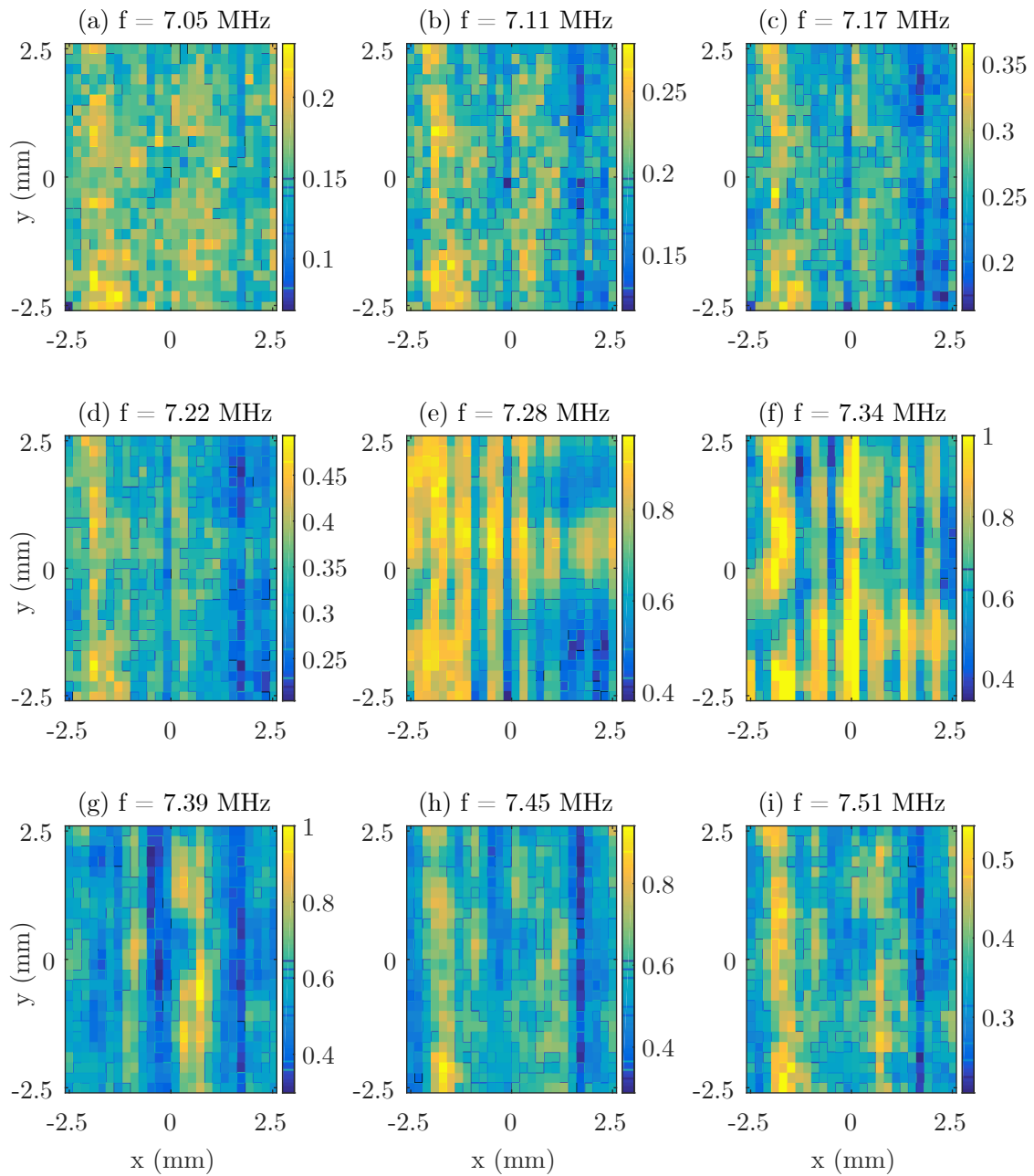


Figure 6.8: 2D distribution of the spectral density at (a) $f = 7.05$ MHz, (b) $f = 7.11$ MHz, (c) $f = 7.17$ MHz, (d) $f = 7.22$ MHz, (e) $f = 7.28$ MHz, (f) $f = 7.34$ MHz, (g) $f = 7.39$ MHz, (h) $f = 7.45$ MHz, and (i) $f = 7.51$ MHz.

As the focus of future research, several experimental operations based on the developed experimental system and processing methods are proposed herein: (i) C-scan optoacoustic measurements on the specimen for a larger scanning surface with a better spatial resolution, for example a square of $20 \times 20 \text{ mm}^2$ with a step of $100 \mu\text{m}$; (ii) heating of the high purity copper rolled plate and application of the method for assessing texture changes, anisotropic properties and the recrystallized microstructure during high temperature processing. For achieving the last goal, either a mini furnace based chamber as shown in Fig. 6.1(b) [250] for global heating of the sample or the use of a supplemental laser [47] for local heating of the sample can be potentially considered.

General conclusion

The work presented in this PhD thesis is concerned with the applications of laser-based ZGV Lamb modes for NDT&E, and in particular for nondestructive characterization and/or evaluation of metallic plates, damaged from mechanical or thermal fatigue. In the first part of this thesis, we reviewed and sorted out the fundamental knowledge required in this work. In the second part, we studied ZGV Lamb mode as well as its sensitivity and ability for fatigue prediction, in isotropic homogeneous solid thin plate, using both experimental measurements and numerical simulations for understanding the observed phenomena. In the last part, the monitoring of mechanical fatigue damage has been achieved by analyzing the ZGV resonance. Then, two prospective studies has been started, with the objective to investigate, i) non-linear phenomena with ZGV resonance in thermally damaged alloys and, ii) texture analysis with ZGV resonance in anisotropic materials.

In this work, the Lamb wave dispersion relations of isotropic homogeneous solid plates with given thickness in both real and complex wavenumber domain are studied using a Matlab code (see appendix D). The separation of the complex dispersion curves of the S_1 and S_2 modes around the ZGV point are analyzed for the purpose of the study of material dissipation. Experimental dispersion curves are reconstructed in real and complex wavenumber planes, using 2D Fourier transform and spatial Laplace transform on spatio-temporal opto-acoustic measurements, respectively. An inverse algorithm is also developed for estimating the material attenuation in both Aluminum and Copper. The extracted values of ultrasonic attenuation (Chap. 3) show good agreement with the results in the literature.

This research has led to the development of a method to assess the fatigue cumulative effect in thin solid plates subjected to mechanical cyclic loading. Experimental results in chapter 4 demonstrated the sensitivity of the ZGV resonance frequency to cumulative fatigue damage, and its ability for monitoring and localizing the associated damage. We could also take on the possibility to predict fatigue lifetime. Thereby, the fully non-contact laser based method proposed here is suitable for probing defects at micro-metric scale and follow their spatial and property evolution. A numerical model based on finite element method (realized with Comsol) is also developed, with the help of the established empirical theory to parametrize the cumulative fatigue progress, in order to analyze the effect of fatigue on the Lamb modes, especially close to the ZGV point.

After the second part (chapters 3 and 4), our focus of research shifts to nonlinear considerations (chapter 5). Thermally-fatigued Aluminum alloys are used as samples for the evaluation of nonlinearity, via the amplitude-dependent laser-based ZGV resonance. The results previously obtained by contact (generation and detection

by piezo-electric transducers), and semi-contact (detection by laser) methods are compared to our fully contactless (laser ultrasonics) method. Results of the observed nonlinear phenomena in the same materials with various thermal aging progress are compared and advantages / shortcomings of each method are discussed. Finally in Chapter 6, preliminary results are introduced on the laser-based ZGV resonance method for assessing micro-structure changes of textured material. Promising results are found, showing the ability of the laser-based ZGV resonance method to reveal texture in polycrystals. Obviously, further work is needed to understand better the origin of the observed nonlinearity of the laser-based ZGV resonance, and possibly use it for material characterization purpose. For the full application of the method to texture characterization, further experiments and comparisons to other methods are required too.

Finally, we note that the end of this work does not mean completion, but a new beginning leading to the future, whether it's about Lamb waves, or about laser ultrasound, metal fatigue, nonlinearity, nondestructive testing, anisotropy, textures, etc. In view of this, the comments, discussions and prospects on this work will be given in the next chapter.

La dernière démarche de la raison est de reconnaître qu'il y a une infinité de choses qui la surpassent. Elle n'est que faible si elle ne va jusqu'à connaître cela.

Reason's last step is the recognition that there are an infinite number of things which are beyond it. It is simply feeble if it does not go as far as realizing that.

— Blaise Pascal

Perspectives

There are several prospects to this PhD work. We classify the envisioned future studies in the following five categories (noted by **I** to **V**) which were already discussed a bit in each chapter.

I In this work, the experimental study of the ultrasonic attenuation in metals, making use of the spatial Laplace transform applied to ZGV Lamb mode, shows its potential for non-destructive evaluation. The extraction of attenuation parameter evolution in a cumulatively damaged plate structure could be for instance achieved in this way. The specimen would need to be fatigued and damaged locally along the lateral direction (y -axis). For this purpose, the fatigue configuration used in chapter 4 can be applied for the preparation of the specimen. This can help us to better understand the influence of fatigue on the dissipation and also to reveal the mechanisms of metal fatigue. We propose then the application of the SLaTCoW method: the monitoring of cumulative damage in materials through ultrasonic attenuation estimated from experimental measurements at different stages of the fatigue process. The different steps to follow for achieving this goal (monitoring) are:

- (1) before the sample is fatigued, estimate the ultrasonic attenuation (as the reference) in the intact sample via the method used in Chap. 3;
- (2) cyclically load the sample to induce the fatigue (tensile load for example);
- (3) unload the sample from the fatigue configuration after 1000 cycles, for example, and repeat the spatio-temporal measurement at exactly the same positions on the sample as during the reference measurement in step (1);
- (4) apply the SLaTCoW method for estimating the ultrasonic attenuation by using the measurements done in step 3;
- (5) repeat steps (2-4) until sample failure and record the total loading cycles as fatigue life.

Finally, the variation of ultrasonic attenuation after different amounts of fatigue loading cycles can be calculated using the reference one, measured on the intact sample, allowing the material scientists to have access to the evolution of ultrasonic attenuation as a function of fatigue lifetime in a chosen material.

II Concerning the assessment of cumulative fatigue in metals, several points should be noted:

- (i) The laser ultrasonic technique using ZGV resonance frequency applied in our work can be extended to obtain two-dimensional (x - and y -axis) or even three dimensional (with consideration of the fatigue lifetime) images for fatigue damage. Before doing this study, the limits and capacities of the presented method should be analyzed, especially at low cycles of fatigue lifetime when the damage is invisible on the surface of the specimen, i.e. before existence of fatigue caused cracks;
- (ii) A future work on the establishment of a more complete empirically-based theoretical model is important and necessary. With the consideration of the combination of the local variation of thickness and the local changes of elastic constants, our new model should be much more close to the reality, i.e. the experimental measurements, and will be useful for deep understanding of each stage of the fatigue as well as the whole fatigue process;
- (iii) After the empirically-based theoretical model is improved, this model can be used in our numerical simulations for a better comparison with the experimental measurements in order to better understand the observed phenomena;
- (iv) Considering that there is potential in the presented method for quantitative prediction of fatigue progress, one possible prospect of this work could be the assessment of fatigue damage at different stages. This could be done, especially before the specimen failure, by using chemical methods (such as etch-pit technique [190] or precipitation technique [170]) or physical techniques (such as transmission electron microscopy [185] or X-ray diffraction [191]), in order to further reveal the nature of such damage;
- (v) The waves reflected and mode-converted at fatigued zone before the existence of cracks are also interesting (this phenomenon is not shown in this work as it's not the main purpose of this PhD thesis, but was presented as a bonus observation in the *AFPAC* conference in 2017, Marseille France). The authors think that a nonlinear frequency-mixing photo-acoustic imaging [253] might be also useful for extracting supplemental information and this could be also one of the research direction for a future study.

As a first step for improving our proposed empirical model and as pointed out in (ii) above, the influence of the following parameters can be studied separately: Young's modulus (E), Poisson's ratio (ν), material density (ρ), longitudinal and shear acoustic velocity (V_L , V_T).

It must be mentioned here that for the study of each parameter, only the isotropic case is considered and the plate thickness is set to be a constant without any local variation. By varying some elastic parameters one by one, we extract the ZGV mode frequency from the calculated dispersion curves, and some nonlinear but monotonic relations (except for the Poisson's ratio ν) are found. These relations could be used to verify our hypothesis proposed

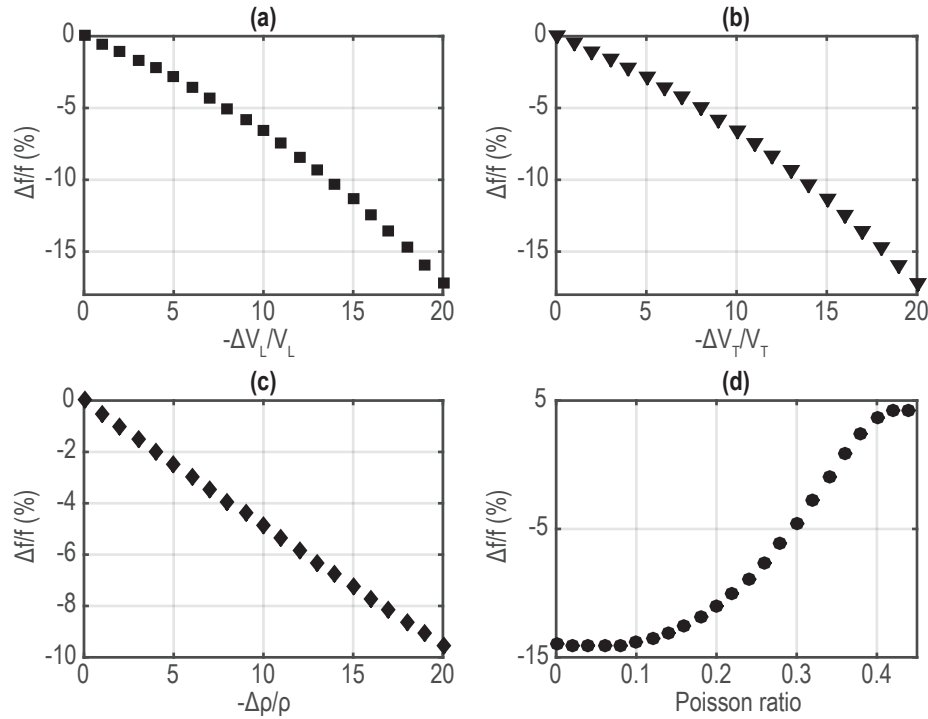


Figure P.1: Calculated variation of the ZGV resonant frequency V.S. variation of several considered elastic constants: (a) longitudinal and (b) shear acoustic velocity, (c) density, and (d) Poisson ratio.

at the beginning of this paragraph. The relative monotonous relations are represented as:

$$\frac{\Delta f}{f} \propto \frac{\Delta V_L}{V_L}, \frac{\Delta V_T}{V_T} \text{ and } \frac{\Delta \rho}{\rho}.$$

In Fig. P.1, for a general view, we give the relations between the variation of the $S_1 S_2$ ZGV resonance frequency and several considered plate parameters (i.e. longitudinal/shear acoustic velocity, density and Poisson's ratio). From Fig. P.1(a-c), monotonic decrease relations can be found. The nonlinear relation between $\Delta f/f$ and the Poisson's ratio [see Fig. P.1(d)] is non-monotonic but quasi-monotonic in the interval of $\nu \in [0.2, 0.4]$.

We are now working on the combination of the local variation of thickness and the local evolution of the mechanical properties as a function of the number of cycles to locally implement in the FEM modelling both variations in order to achieve a more complete numerical simulation, closer to the reality.

III About the investigation of nonlinearity in thermally-fatigued metal using ZGV resonance, one important supplemental manipulation is to experimentally evaluate the influence of the temperature rise caused by pulsed laser, probe laser or both. To achieve this, new experiments need to be realized, especially the

experiment of the measurement of the frequency shift as a function of the incident optical power by varying the pump laser intensity while the probe laser intensity is fixed.

IV The additional manipulations that could be carried out for the future study of the texture in pure Copper plate as mentioned in chapter 6 are:

- (i) the C-scan optoacoustic measurements on the specimen for a much larger size, for example a square of $20 \times 20 \text{ mm}^2$ with a step of $100 \mu\text{m}$ (estimated measurement duration is about 112.225 hours);
- (ii) from the current observation, for some received signals, several peaks (2 or even 3) are found in the FFT spectrum (possibly caused by the rolling process of the preparation of the metal plate), and this gives us an opportunity to produce the imaging by using the frequency peak amplitude as a function of a narrow band around the ZGV resonance frequency in order to extract more information from the experimental measurements;
- (iii) the next step after the previous two is to develop a new way for heating the sample and then to apply the ZGV resonance method in order to assess the anisotropy and the recrystallized microstructure in the high purity Copper rolled plate. Here are two possible examples: establishing a mini furnace to put the sample inside [250]; adding a supplemental laser [47] for locally heating the sample in order to achieve this goal.

V The last point is truly out of the current work but quite interesting, that is the study of ZGV resonance under extreme conditions. The experimental observation of laser generated and detected guided waves at ultra-high pressure using diamond anvil cell (up to several tens of GPa) could indeed be interesting. Supplemental theoretical calculations (based on elastic waveguide theory) and numerical simulations (based on the COMSOL code introduced in chapter 4) can be used for the sample dimensioning and can help to do comparison with experimental observations. On a long term basis, such experiments can be extended to the investigation of Earth's minerals in field of geophysics .

Que pour examiner la vérité il est besoin, une fois en sa vie, de mettre toutes choses en doute autant qu'il se peut

In order to seek truth, it is necessary once in the course of our life, to doubt, as far as possible, of all things.

— René Descartes

Bibliography

- [1] Martin Maldovan. Sound and heat revolutions in phononics. *Nature*, 503(7475):209–217, 2013.
- [2] L. He, H. Zhu, X. Qiu, and G. Du. 声学理论与工程应用. 科学出版社, 2006 (in Chinese).
- [3] G. Neau. *Lamb waves in anisotropic viscoelastic plates. Study of the wave fronts and attenuation*. PhD thesis, Mechanical Engineering Department, L’Universite de Bordeaux, 2003.
- [4] Horace Lamb. On waves in an elastic plate. *Proc. R. Soc. A*, 93(648):114–128, 1917.
- [5] E. B. Christoffel. Sur une classe particulière de fonctions entières et de fractions continues. *Ann. Mat. Pura Appl.*, 8(1):1–10, 1877.
- [6] Lord Rayleigh. On the free vibrations of an infinite plate of homogeneous isotropic elastic matter. *Proc. London Math. Soc.*, s1-20(1):225–237, 1888.
- [7] Alexander Graham Bell. On the production and reproduction of sound by light. *Am. J. Sci.*, 20(118):305–324, 1880.
- [8] Sergey Nikitin. *Laser ultrasonics in a diamond anvil cell for investigation of simple molecular compounds at ultrahigh pressures*. Theses, Université du Maine, 2015.
- [9] C. Prada, O. Balogun, and T. W. Murray. Laser-based ultrasonic generation and detection of zero-group velocity lamb waves in thin plates. *Appl. Phys. Lett.*, 87(19):194109, 2005.
- [10] Dominique Clorennec, Claire Prada, Daniel Royer, and Todd W. Murray. Laser impulse generation and interferometer detection of zero group velocity lamb mode resonance. *Appl. Phys. Lett.*, 89(2):024101, 2006.
- [11] D. Clorennec, C. Prada, and D. Royer. Local and noncontact measurements of bulk acoustic wave velocities in thin isotropic plates and shells using zero group velocity lamb modes. *J. Appl. Phys.*, 101(3):034908, 2007.
- [12] C. Prada, D. Clorennec, and D. Royer. Local vibration of an elastic plate and zero-group velocity lamb modes. *J. Acoust. Soc. Am.*, 124(1):203–212, 2008.

-
- [13] C. Prada, D. Clorennec, and D. Royer. Power law decay of zero group velocity lamb modes. *Wave Motion*, 45(6):723–728, 2008.
- [14] C. Prada, D. Clorennec, T. W. Murray, and D. Royer. Influence of the anisotropy on zero-group velocity lamb modes. *J. Acoust. Soc. Am.*, 126(2):620–625, 2009.
- [15] D. Clorennec, C. Prada, and D. Royer. Laser ultrasonic inspection of plates using zero-group velocity lamb modes. *IEEE Trans. Ultrason. Ferroelectr. Freq. Control.*, 57(5):1125–1132, 2010.
- [16] Sylvain Mezil, Jérôme Laurent, Daniel Royer, and Claire Prada. Non contact probing of interfacial stiffnesses between two plates by zero-group velocity lamb modes. *Appl. Phys. Lett.*, 105(2):021605, 2014.
- [17] J. Laurent, D. Royer, and C. Prada. Temporal behavior of laser induced elastic plate resonances. *Wave Motion*, 51(6):1011–1020, 2014.
- [18] S. Raetz, J. Laurent, T. Dehoux, D. Royer, B. Audoin, and C. Prada. Effect of refracted light distribution on the photoelastic generation of zero-group velocity lamb modes in optically low-absorbing plates. *J. Acoust. Soc. Am.*, 138(6):3522–3530, 2015.
- [19] Stephen D. Holland and D. E. Chimenti. Air-coupled acoustic imaging with zero-group-velocity lamb modes. *Appl. Phys. Lett.*, 83(13):2704–2706, 2003.
- [20] Stephen D. Holland and D. E. Chimenti. High contrast air-coupled acoustic imaging with zero group velocity lamb modes. *Ultrasonics*, 42:957–960, 2004.
- [21] M.-L. Li, M.-X. Deng, and G.-J. Gao. Selective generation of ultrasonic lamb waves by electromagnetic acoustic transducers. *Chin. Phys. B*, 25(12):124301–124301, 2016.
- [22] M Ph Papaelias, C Roberts, and C L Davis. A review on non-destructive evaluation of rails: State-of-the-art and future development. *Proc. Inst. Mech. Eng. Part F : J. Rail Rapid Transit*, 222(4):367–384, 2008.
- [23] P. Wilcox, M. Lowe, and P. Cawley. Omnidirectional guided wave inspection of large metallic plate structures using an emat array. *IEEE Trans. Ultrason. Ferroelectr. Freq. Control.*, 52(4):653–665, 2005.
- [24] O. Balogun, T. W. Murray, and C. Prada. Simulation and measurement of the optical excitation of the s1 zero group velocity lamb wave resonance in plates. *J. Appl. Phys.*, 102(6):064914, 2007.
- [25] François Bruno, Jérôme Laurent, Paul Jehanno, Daniel Royer, and Claire Prada. Laser beam shaping for enhanced zero-group velocity lamb modes generation. *J. Acoust. Soc. Am.*, 140(4):2829–2838, 2016.

- [26] M. Cès, D. Clorennec, D. Royer, and C. Prada. Thin layer thickness measurements by zero group velocity lamb mode resonances. *Rev. Sci. Instrum.*, 82(11):114902, 2011.
- [27] Olivier Xeridat. *Etude expérimentale de la propagation, de la diffusion et de la localisation des ondes de Lamb*. Theses, Université Nice Sophia Antipolis, 2011.
- [28] Maximin Cès. *Etude théorique et expérimentale des résonances mécaniques locales de modes guidés par des structures complexes*. Theses, Université Paris-Diderot - Paris VII, 2012.
- [29] Sylvain Mezil. *Nonlinear optoacoustics method for crack detection and characterization*. Theses, Université du Maine, 2012.
- [30] Daniel Royer. *Génération et détection optiques d'ondes élastiques*. Techniques de l'ingénieur, 1996.
- [31] D. Royer and E. Dieulesaint. *Elastic Waves in Solids I: Free and Guided Propagation*, volume I. Springer Berlin Heidelberg, 2000.
- [32] D. Royer and E. Dieulesaint. *Elastic Waves in Solids II: Generation, Acousto-optic Interaction, Applications*, volume II of *Advanced Texts in Physics*. Springer Berlin Heidelberg, 2000.
- [33] John Tyndall. Action of an intermittent beam of radiant heat upon gaseous matter. *Proc. R. Soc.*, 31:307–317, 1880.
- [34] W. C. Röntgen. On tones produced by the intermittent irradiation of a gas. *Philos. Mag.*, 11(68):308–311, 1881.
- [35] G. A. Askaryan, A. M. Prokhorov, G. F. Chanturiya, and G. P. Shipulo. The effects of a laser beam in a liquid. *J. Exptl. Theoret. Phys. (U.S.S.R.)*, 44:2180, 1963.
- [36] R. M. White. Elastic wave generation by electron bombardment or electromagnetic wave absorption. *J. Appl. Phys.*, 34(7):2123–2124, 1963.
- [37] R. M. White. Generation of elastic waves by transient surface heating. *J. Appl. Phys.*, 34(12):3559–3567, 1963.
- [38] C.B. Scruby and L.E. Drain. *Laser Ultrasonics Techniques and Applications*. Taylor & Francis, 1990.
- [39] Vitalyi E. Gusev and A. A. Karabutov. *Laser optoacoustics*. American Institute of Physics, 1993.
- [40] T. Kundu. *Ultrasonic Nondestructive Evaluation: Engineering and Biological Material Characterization*. CRC Press, 2003.
- [41] John F. Ready. *Effects of High-Power Laser Radiation*. Elsevier Science, 1971.

- [42] Alexey Lomonosov, Andreas P. Mayer, Peter Hess, Henry E. Bass Moises Levy, and Richard Stern. *3. Laser-based surface acoustic waves in materials science*, volume 39, pages 65–134. Academic Press, 2001.
- [43] J. Krautkrämer and H. Krautkrämer. *Ultrasonic Testing of Materials*. Springer Berlin Heidelberg, 1990.
- [44] W. R. Scott and P. F. Gordon. Ultrasonic spectrum analysis for nondestructive testing of layered composite materials. *J. Acoust. Soc. Am.*, 62(1):108–116, 1977.
- [45] Christian Bermes, Jin-Yeon Kim, Jianmin Qu, and Laurence J. Jacobs. Non-linear lamb waves for the detection of material nonlinearity. *Mech. Syst. Signal Process.*, 22(3):638–646, 2008.
- [46] D. Dhital and J. R. Lee. A fully non-contact ultrasonic propagation imaging system for closed surface crack evaluation. *Exp. Mech.*, 52(8):1111–1122, 2012.
- [47] C. Ni, N. Chigarev, V. Tournat, N. Delorme, Z. Shen, and V. E. Gusev. Probing of laser-induced crack closure by pulsed laser-generated acoustic waves. *J. Appl. Phys.*, 113(1):014906, 2013.
- [48] Peipei Liu, Hoon Sohn, Tribikram Kundu, and Suyoung Yang. Noncontact detection of fatigue cracks by laser nonlinear wave modulation spectroscopy (Inwms). *NDT&E Int.*, 66:106–116, 2014.
- [49] Hogeon Seo, Jihyun Jun, and Kyung-Young Jhang. Assessment of thermal aging of aluminum alloy by acoustic nonlinearity measurement of surface acoustic waves. *Res. Nondestr. Eval.*, 28(1):3–17, 2017.
- [50] F. Faëse, S. Raetz, N. Chigarev, C. Mechri, J. Blondeau, B. Campagne, V. E. Gusev, and V. Tournat. Beam shaping to enhance zero group velocity lamb mode generation in a composite plate and nondestructive testing application. *NDT&E Int.*, 85:13–19, 2017.
- [51] Liang Song, Konstantin Maslov, and Lihong V. Wang. Section-illumination photoacoustic microscopy for dynamic 3d imaging of microcirculation in vivo. *Opt. Lett.*, 35(9):1482–1484, 2010.
- [52] Song Hu, Bin Rao, Konstantin Maslov, and Lihong V. Wang. Label-free photoacoustic ophthalmic angiography. *Opt. Lett.*, 35(1):1–3, 2010.
- [53] Joon-Mo Yang, Ruimin Chen, Christopher Favazza, Junjie Yao, Chiye Li, Zhilin Hu, Qifa Zhou, K. Kirk Shung, and Lihong V. Wang. A 2.5-mm diameter probe for photoacoustic and ultrasonic endoscopy. *Opt. Express*, 20(21):23944–23953, 2012.
- [54] J. Cuffe, O. Ristow, E. Chávez, A. Shchepetov, P-O. Chapuis, F. Alzina, M. Hettich, M. Prunnila, J. Ahopelto, T. Dekorsy, and C. M. Sotomayor Torres. Lifetimes of confined acoustic phonons in ultrathin silicon membranes. *Phys. Rev. Lett.*, 110:095503, 2013.

- [55] P. A. Mante, J. F. Robillard, and A. Devos. Complete thin film mechanical characterization using picosecond ultrasonics and nanostructured transducers: experimental demonstration on sio₂. *Appl. Phys. Lett.*, 93(7):071909, 2008.
- [56] Andreas Zerr, Nikolay Chigarev, Ovidiu Brinza, Sergey M. Nikitin, Alexey M. Lomonosov, and Vitalyi Gusev. Elastic moduli of η -ta₂n₃, a tough self-healing material, via laser ultrasonics. *Phys. Status Solidi RRL*, 6(12):484–486, 2012.
- [57] Maju Kuriakose, Samuel Raetz, Nikolay Chigarev, Sergey M. Nikitin, Alain Bulou, Damien Gasteau, Vincent Tournat, Bernard Castagnede, Andreas Zerr, and Vitalyi E. Gusev. Picosecond laser ultrasonics for imaging of transparent polycrystalline materials compressed to megabar pressures. *Ultrasonics*, 69:259–267, 2016.
- [58] Maju Kuriakose, Nikolay Chigarev, Samuel Raetz, Alain Bulou, Vincent Tournat, Andreas Zerr, and Vitalyi E Gusev. In situ imaging of the dynamics of photo-induced structural phase transition at high pressures by picosecond acoustic interferometry. *New. J. Phys.*, 19(5):053026, 2017.
- [59] Maju Kuriakose, Samuel Raetz, Qing Miao Hu, Sergey M. Nikitin, Nikolay Chigarev, Vincent Tournat, Alain Bulou, Alexey Lomonosov, Philippe Djemia, Vitalyi E. Gusev, and Andreas Zerr. Longitudinal sound velocities, elastic anisotropy, and phase transition of high-pressure cubic h₂O ice to 82 gpa. *Phys. Rev. B*, 96:134122, 2017.
- [60] F. Decremps, M. Gauthier, S. Ayrinhac, L. Bove, L. Belliard, B. Perrin, M. Morand, G. Le Marchand, F. Bergame, and J. Philippe. Picosecond acoustics method for measuring the thermodynamical properties of solids and liquids at high pressure and high temperature. *Ultrasonics*, 56:129–140, 2015.
- [61] Sergey M. Nikitin, Nikolay Chigarev, Vincent Tournat, Alain Bulou, Damien Gasteau, Bernard Castagnede, Andreas Zerr, and Vitalyi E. Gusev. Revealing sub- μ m and μ m-scale textures in h₂o ice at megabar pressures by time-domain brillouin scattering. *Sci. Rep.*, 5:9352, 2015.
- [62] William A. Bassett. Diamond anvil cell, 50th birthday. *High Press. Res.*, 29(2):163–186, 2009.
- [63] Arthur L. Ruoff, Hui Xia, and Qing Xia. The effect of a tapered aperture on x-ray diffraction from a sample with a pressure gradient: Studies on three samples with a maximum pressure of 560 gpa. *Rev. Sci. Instrum.*, 63(10):4342–4348, 1992.
- [64] R. M. Jones. *Mechanics Of Composite Materials, Second Edition*. Taylorand Francis, 1999.
- [65] J.D. Achenbach. *Wave Propagation in Elastic Solids*. Applied Mathematics and Mechanics Series. North-Holland Publishing Company, 1973.

- [66] B.A. Auld. *Acoustic fields and waves in solids*, volume II of *Acoustic Fields and Waves in Solids*. Wiley, 1973.
- [67] Clemens M. Grünsteidl, István A. Veres, and Todd W. Murray. Experimental and numerical study of the excitability of zero group velocity lamb waves by laser-ultrasound. *J. Acoust. Soc. Am.*, 138(1):242–250, 2015.
- [68] F. Simonetti and M. J. S. Lowe. On the meaning of lamb mode nonpropagating branches. *J. Acoust. Soc. Am.*, 118(1):186–192, 2005.
- [69] R.D. Mindlin. Mathematical theory of vibrations of elastic plates. In *11th Annual Symposium on Frequency Control*, pages 1–40, 1957.
- [70] I.A. Viktorov. *Rayleigh and Lamb waves: physical theory and applications*. Ultrasonic technology. Plenum Press, 1970.
- [71] L. P. Solie and B. A. Auld. Elastic waves in free anisotropic plates. *J. Acoust. Soc. Am.*, 54(1):50–65, 1973.
- [72] Takasar Hussain and Faiz Ahmad. Lamb modes with multiple zero-group velocity points in an orthotropic plate. *J. Acoust. Soc. Am.*, 132(2):641–645, 2012.
- [73] M. A. Biot. General theorems on the equivalence of group velocity and energy transport. *Phys. Rev.*, 105:1129–1137, 1957.
- [74] V. Pagneux and A. Maurel. Determination of lamb mode eigenvalues. *J. Acoust. Soc. Am.*, 110(3):1307–1314, 2001.
- [75] Allen H. Meitzler. Backward-wave transmission of stress pulses in elastic cylinders and plates. *J. Acoust. Soc. Am.*, 38(5):835–842, 1965.
- [76] Daniel Royer, Dominique Clorenec, and Claire Prada. Caractérisation de plaques et de tubes par modes de lamb à vitesse de groupe nulle. *I2M*, 10:73–94, 2010.
- [77] Sylvain Mezil, Nikolay Chigarev, Vincent Tournat, and Vitalyi Gusev. All-optical probing of the nonlinear acoustics of a crack. *Opt. Lett.*, 36(17):3449–3451, 2011.
- [78] Eugene Hecht. *Optics (4th Edition)*. Addison Wesley, 2001.
- [79] M. Cès, D. Royer, and C. Prada. Characterization of mechanical properties of a hollow cylinder with zero group velocity lamb modes. *J. Acoust. Soc. Am.*, 132(1):180–185, 2012.
- [80] Sylvain Mezil, Francois Bruno, Samuel Raetz, Jérôme Laurent, Daniel Royer, and Claire Prada. Investigation of interfacial stiffnesses of a tri-layer using zero-group velocity lamb modes. *J. Acoust. Soc. Am.*, 138(5):3202–3209, 2015.

- [81] Yi-Te Tsai and Jinying Zhu. Simulation and experiments of airborne zero-group-velocity lamb waves in concrete plate. *J. Nondestruct. Eval.*, 31(4):373–382, 2012.
- [82] M. Cès, D. Clorennec, D. Royer, and C. Prada. Edge resonance and zero group velocity lamb modes in a free elastic plate. *J. Acoust. Soc. Am.*, 130(2):689–694, 2011.
- [83] Eduardo Kausel. Number and location of zero-group-velocity modes. *J. Acoust. Soc. Am.*, 131(5):3601–3610, 2012.
- [84] Jérôme Laurent, Daniel Royer, Takasar Hussain, Faiz Ahmad, and Claire Prada. Laser induced zero-group velocity resonances in transversely isotropic cylinder. *J. Acoust. Soc. Am.*, 137(6):3325–3334, 2015.
- [85] Vitalyi E. Gusev, Alexey M. Lomonosov, Chenyin Ni, and Zhonghua Shen. Self-action of propagating and standing lamb waves in the plates exhibiting hysteretic nonlinearity: Nonlinear zero-group velocity modes. *Ultrasonics*, 80:34–46, 2017.
- [86] N.E. Dowling, K.S. Prasad, and R. Narayanasamy. *Mechanical Behavior of Materials: Engineering Methods for Deformation, Fracture, and Fatigue*. Always learning. Pearson, 2012.
- [87] R.I. Stephens, A. Fatemi, R.R. Stephens, and H.O. Fuchs. *Metal Fatigue in Engineering*. A Wiley-Interscience publication. John Wiley & Sons, 2000.
- [88] J.A. Bannantine, J.J. Comer, and J.L. Handrock. *Fundamentals of Metal Fatigue Analysis*. Prentice Hall, 1990.
- [89] M. Kamal and M. M. Rahman. Advances in fatigue life modeling: A review. *Renew. Sust. Energ. Rev.*, 82(Part 1):940–949, 2018.
- [90] Lenka Kunčická, Radim Kocich, and Terry C. Lowe. Advances in metals and alloys for joint replacement. *Prog. Mater. Sci.*, 88:232–280, 2017.
- [91] André Pineau, David L. McDowell, Esteban P. Busso, and Stephen D. Antolovich. Failure of metals ii: Fatigue. *Acta Mater.*, 107(Supplement C):484–507, 2016.
- [92] Brian L. V. Bak, Carlos Sarrado, Albert Turon, and Josep Costa. Delamination under fatigue loads in composite laminates: A review on the observed phenomenology and computational methods. *Appl. Mech. Rev.*, 66(6):060803, 2014.
- [93] N. L. Post, S. W. Case, and J. J. Lesko. Modeling the variable amplitude fatigue of composite materials: A review and evaluation of the state of the art for spectrum loading. *Int. J. Fatigue*, 30(12):2064–2086, 2008.
- [94] Guang-Zhong Wang. 材料疲劳断裂研究的现状和发展. *Bull. Chin. Acad. Sci.*, 3:204–208, 1993 (in Chinese).

- [95] P J Withers. Residual stress and its role in failure. *Rep. Prog. Phys.*, 70(12):2211, 2007.
- [96] Joris Degrieck and Wim Van Paeppegem. Fatigue damage modeling of fibre-reinforced composite materials: Review. *Appl. Mech. Rev.*, 54(4):279–300, 2001.
- [97] L. Yang and A. Fatemi. Cumulative fatigue damage mechanisms and quantifying parameters: A literature review. *J. Test. Eval.*, 26(2):89–100, 1998.
- [98] S. Suresh. *Fatigue of Materials*. Cambridge University Press, Cambridge, 1998.
- [99] N. H. POLAKOWSKI. Softening of cold-worked metals under cyclic strains. *Nature*, 171:173, 1953.
- [100] A. K. HEAD and F. H. HOOKE. Fatigue of metals under random loads. *Nature*, 177:1176, 1956.
- [101] A. N. MAY. Fatigue under random loads. *Nature*, 192:158–159, 1961.
- [102] J. H. Cantrell and K. Salama. Acoustoelastic characterisation of materials. *Int. Mater. Rev.*, 36(1):125–145, 1991.
- [103] X. J. Lou, M. Zhang, S. A. T. Redfern, and J. F. Scott. Local phase decomposition as a cause of polarization fatigue in ferroelectric thin films. *Phys. Rev. Lett.*, 97:177601, 2006.
- [104] X. J. Lou, M. Zhang, S. A. T. Redfern, and J. F. Scott. Fatigue as a local phase decomposition: A switching-induced charge-injection model. *Phys. Rev. B*, 75:224104, 2007.
- [105] F. Kun, H. A. Carmona, J. S. Andrade, and H. J. Herrmann. Universality behind basquin’s law of fatigue. *Phys. Rev. Lett.*, 100:094301, 2008.
- [106] K. Lu, L. Lu, and S. Suresh. Strengthening materials by engineering coherent internal boundaries at the nanoscale. *Science*, 324(5925):349, 2009.
- [107] Xiaoyan Li, Yujie Wei, Lei Lu, Ke Lu, and Huajian Gao. Dislocation nucleation governed softening and maximum strength in nano-twinned metals. *Nature*, 464:877–880, 2010.
- [108] P. Li, S. X. Li, Z. G. Wang, and Z. F. Zhang. Fundamental factors on formation mechanism of dislocation arrangements in cyclically deformed fcc single crystals. *Prog. Mater. Sci.*, 56(3):328–377, 2011.
- [109] Dongchan Jang, Xiaoyan Li, Huajian Gao, and Julia R. Greer. Deformation mechanisms in nanotwinned metal nanopillars. *Nat. Nanotechnol.*, 7:594–601, 2012.

- [110] Y. Morris Wang, Frederic Sansoz, Thomas LaGrange, Ryan T. Ott, Jaime Marian, Troy W. Barbee Jr, and Alex V. Hamza. Defective twin boundaries in nanotwinned metals. *Nat. Mater.*, 12:697–702, 2013.
- [111] Lan Wei-LaPierre, Ellie M. Carrell, Simona Boncompagni, Feliciano Protasi, and Robert T. Dirksen. Orail-dependent calcium entry promotes skeletal muscle growth and limits fatigue. *Nat. Commun.*, 4:2805, 2013.
- [112] Haofei Zhou, Xiaoyan Li, Shaoxing Qu, Wei Yang, and Huajian Gao. A jogged dislocation governed strengthening mechanism in nanotwinned metals. *Nano Lett.*, 14(9):5075–5080, 2014.
- [113] Daniel Marino, Jin-Yeon Kim, Alberto Ruiz, Young-Sang Joo, Jianmin Qu, and Laurence J Jacobs. Using nonlinear ultrasound to track microstructural changes due to thermal aging in modified 9%cr ferritic martensitic steel. *NDT&E Int.*, 79:46–52, 2016.
- [114] K. Lu. Stabilizing nanostructures in metals using grain and twin boundary architectures. *Nat. Rev. Mater.*, 1:16019, 2016.
- [115] Jared L. Zitnay, Yang Li, Zhao Qin, Boi Hoa San, Baptiste Depalle, Shawn P. Reese, Markus J. Buehler, S. Michael Yu, and Jeffrey A. Weiss. Molecular level detection and localization of mechanical damage in collagen enabled by collagen hybridizing peptides. *Nat. Commun.*, 8:14913, 2017.
- [116] Qingsong Pan, Haofei Zhou, Qihong Lu, Huajian Gao, and Lei Lu. History-independent cyclic response of nanotwinned metals. *Nature*, 551:214, 2017.
- [117] S. Kozinov and M. Kuna. Simulation of fatigue damage in ferroelectric polycrystals under mechanical/electrical loading. *J. Mech. Phys. Sol.*, 116:150–170, 2018.
- [118] Mikael Amura, Michele Meo, and F. Amerini. Baseline-free estimation of residual fatigue life using a third order acoustic nonlinear parameter. *J. Acoust. Soc. Am.*, 130(4):1829–1837, 2011.
- [119] Mikael Amura and Michele Meo. Prediction of residual fatigue life using nonlinear ultrasound. *Smart Mater. Struct.*, 21(4):045001, 2012.
- [120] John H. Cantrell and William T. Yost. Nonlinear ultrasonic characterization of fatigue microstructures. *Int. J. Fatigue*, 23:487–490, 2001.
- [121] John H. Cantrell. Substructural organization, dislocation plasticity and harmonic generation in cyclically stressed wavy slip metals. *Proc. R. Soc. Lond. A*, 460(2043):757–780, 2004.
- [122] J. H. Cantrell. Quantitative assessment of fatigue damage accumulation in wavy slip metals from acoustic harmonic generation. *Philos. Mag.*, 86(11):1539–1554, 2006.

- [123] John H. Cantrell. Dependence of microelastic-plastic nonlinearity of martensitic stainless steel on fatigue damage accumulation. *J. Appl. Phys.*, 100(6):063508, 2006.
- [124] John H. Cantrell. Ultrasonic harmonic generation from fatigue-induced dislocation substructures in planar slip metals and assessment of remaining fatigue life. *J. Appl. Phys.*, 106(9):093516, 2009.
- [125] Anthony J. Croxford, Paul D. Wilcox, Bruce W. Drinkwater, and Peter B. Nagy. The use of non-collinear mixing for nonlinear ultrasonic detection of plasticity and fatigue. *J. Acoust. Soc. Am.*, 126(5):EL117–EL122, 2009.
- [126] Mingxi Deng, Ping Wang, and Xiafu Lv. Experimental observation of cumulative second-harmonic generation of lamb-wave propagation in an elastic plate. *J. Phys. D: Appl. Phys.*, 38(2):344, 2005.
- [127] Mingxi Deng, Ping Wang, and Xiafu Lv. Experimental verification of cumulative growth effect of second harmonics of lamb wave propagation in an elastic plate. *Appl. Phys. Lett.*, 86(12):124104, 2005.
- [128] Weihua Deng, Changpin Li, and Jinhua Lü. Stability analysis of linear fractional differential system with multiple time delays. *Nonlinear Dyn.*, 48(4):409–416, 2007.
- [129] Mingxi Deng and Junfeng Pei. Assessment of accumulated fatigue damage in solid plates using nonlinear lamb wave approach. *Appl. Phys. Lett.*, 90(12):121902, 2007.
- [130] Ming Hong, Zhongqing Su, Qiang Wang, Li Cheng, and Xinlin Qing. Modeling nonlinearities of ultrasonic waves for fatigue damage characterization: Theory, simulation, and experimental validation. *Ultrasonics*, 54(3):770–778, 2014.
- [131] V. V. S. Jaya Rao, Elankumaran Kannan, Raghu V. Prakash, and Krishnan Balasubramaniam. Fatigue damage characterization using surface acoustic wave nonlinearity in aluminum alloy aa7175-t7351. *J. Appl. Phys.*, 104(12):123508, 2008.
- [132] Kyung-Young Jhang, Jaeik Lee, and Taehun Lee. Acoustic nonlinearity of surface wave in a fatigued aluminum alloy specimen. *Mater. Trans.*, 53(2):303–307, 2012.
- [133] J. Y. Kim, J. Qu, L. J. Jacobs, J. W. Littles, and M. F. Savage. Acoustic nonlinearity parameter due to microplasticity. *J. Nondestruct. Eval.*, 25(1):28–36, 2006.
- [134] Jin-Yeon Kim, Laurence J. Jacobs, Jianmin Qu, and Jerrol W. Littles. Experimental characterization of fatigue damage in a nickel-base superalloy using nonlinear ultrasonic waves. *J. Acoust. Soc. Am.*, 120(3):1266–1273, 2006.
- [135] Tae Hun Lee and Kyung Young Jhang. Experimental investigation of nonlinear acoustic effect at crack. *NDT&E Int.*, 42(8):757–764, 2009.

- [136] Peter B. Nagy. Fatigue damage assessment by nonlinear ultrasonic materials characterization. *Ultrasonics*, 36(1–5):375–381, 1998.
- [137] Yikuan Wang, Ruiqi Guan, and Ye Lu. Nonlinear lamb waves for fatigue damage identification in frp-reinforced steel plates. *Ultrasonics*, 80:87–95, 2017.
- [138] Jianfeng Zhang and Fu-Zhen Xuan. Fatigue damage evaluation of austenitic stainless steel using nonlinear ultrasonic waves in low cycle regime. *J. Appl. Phys.*, 115(20):204906, 2014.
- [139] A. Aid, A. Amrouche, B. Bachir Bouiadjra, M. Benguediab, and G. Mesmacque. Fatigue life prediction under variable loading based on a new damage model. *Mater. Design*, 32(1):183–191, 2011.
- [140] A. Fatemi and L. Yang. Cumulative fatigue damage and life prediction theories: a survey of the state of the art for homogeneous materials. *Int. J. Fatigue*, 20(1):9–34, 1998.
- [141] Jean Lemaitre and Jacques Dufailly. Damage measurements. *Eng. Fract. Mech.*, 28(5):643–661, 1987.
- [142] B. SUN, L. YANG, and Y. GUO. A high-cycle fatigue accumulation model based on electrical resistance for structural steels. *Fatigue Fract. Eng. Mater. Struct.*, 30(11):1052–1062, 2007.
- [143] X J Sun, C C Wang, J Zhang, G Liu, G J Zhang, X D Ding, G P Zhang, and J Sun. Thickness dependent fatigue life at microcrack nucleation for metal thin films on flexible substrates. *J. Phys. D: Appl. Phys.*, 41(19):195404, 2008.
- [144] R. J. Kolouch and K. A. McCarthy. Ultrasonic attenuation in copper. *Phys. Rev.*, 139:A700–A701, 1965.
- [145] M. J. Lea and E. R. Dobbs. Ultrasonic attenuation measurements in normal and superconducting zinc. *Phys. Lett. A*, 27(8):556–557, 1968.
- [146] K. C. Hepfer and J. A. Rayne. Ultrasonic attenuation in aluminum. *Physics Letters A*, 30(5):281–282, 1969.
- [147] D. H. R. Price and C. D. W. Wilkinson. Frequency dependence of ultrasonic attenuation in zinc oxide at room temperature. *Appl. Phys. Lett.*, 16(12):480–482, 1970.
- [148] K. C. Hepfer and J. A. Rayne. Ultrasonic attenuation in aluminum. *Phys. Rev. B*, 4:1050–1064, 1971.
- [149] S. K. Kor, U. S. Tandon, and G. Rai. Ultrasonic attenuation in copper, silver, and gold. *Phys. Rev. B*, 6:2195–2197, 1972.
- [150] C. R. Cleavelin and B. J. Marshall. Ultrasonic-attenuation determination of the anisotropic energy gap in superconducting zinc. *Phys. Rev. B*, 10:1902–1911, 1974.

- [151] B. M. Gitis. Sound absorption in metals at high temperatures. *Sov. Phys.-JETP*, 40:181–187, 1974.
- [152] M. Nandanpawar and S. Rajagopalan. Ultrasonic attenuation in copper and the temperature dependence of the nonlinearity parameter. *Phys. Rev. B*, 18:5410–5412, 1978.
- [153] J. D. Aussel and J. P. Monchalin. Measurement of ultrasound attenuation by laser ultrasonics. *J. Appl. Phys.*, 65(8):2918–2922, 1989.
- [154] Michael D Gilchrist. Attenuation of ultrasonic rayleigh-lamb waves by small horizontal defects in thin aluminium plates. *Int. J. Mech. Sci.*, 41:581–594, 1999.
- [155] Agnès Maurel, Vincent Pagneux, Felipe Barra, and Fernando Lund. Wave propagation through a random array of pinned dislocations: Velocity change and attenuation in a generalized granato and lücke theory. *Phys. Rev. B*, 72:174111, 2005.
- [156] J.-G. Minonzio, J. Foiret, M. Talmant, and P. Laugier. Impact of attenuation on guided mode wavenumber measurement in axial transmission on bone mimicking plates. *J. Acoust. Soc. Am.*, 130(6):3574–3582, 2011.
- [157] G. Rix, C. Lai, and A. Spang Jr. In situ measurement of damping ratio using surface waves. *J. Geotech. Geoenviron. Eng.*, 126(5):472–480, 2000.
- [158] A. Geslain, S. Raetz, M. Hiraiwa, M. Abi Ghanem, S. P. Wallen, A. Khanolkar, N. Boechler, J. Laurent, C. Prada, A. Duclos, P. Leclaire, and J.-P. Groby. Spatial laplace transform for complex wavenumber recovery and its application to the analysis of attenuation in acoustic systems. *J. Appl. Phys.*, 120(13):135107, 2016.
- [159] W. H. Prosser, Michael D. Seale, and Barry T. Smith. Time-frequency analysis of the dispersion of lamb modes. *J. Acoust. Soc. Am.*, 105(5):2669–2676, 1999.
- [160] Marc Niethammer, Laurence J. Jacobs, Jianmin Qu, and Jacek Jarzynski. Time-frequency representations of lamb waves. *J. Acoust. Soc. Am.*, 109(5):1841–1847, 2001.
- [161] Kailiang Xu, Dean Ta, Petro Moilanen, and Weiqi Wang. Mode separation of lamb waves based on dispersion compensation method. *J. Acoust. Soc. Am.*, 131(4):2714–2722, 2012.
- [162] A. G. Every. Intersections of the lamb mode dispersion curves of free isotropic plates. *J. Acoust. Soc. Am.*, 139(4):1793–1798, 2016.
- [163] M. A. Olmstead, N. M. Amer, S. Kohn, D. Fournier, and A. C. Boccara. Photothermal displacement spectroscopy: An optical probe for solids and surfaces. *Appl. Phys. A*, 32(3):141–154, 1983.

- [164] Joshua E. Rothenberg. Observation of the transient expansion of heated surfaces by picosecond photothermal deflection spectroscopy. *Opt. Lett.*, 13(9):713–715, 1988.
- [165] Constant A. J. Putman, Bart G. De Grooth, Niek F. Van Hulst, and Jan Greve. A detailed analysis of the optical beam deflection technique for use in atomic force microscopy. *J. Appl. Phys.*, 72(1):6–12, 1992.
- [166] J. Higuët, T. Valier-Brasier, T. Dehoux, and B. Audoin. Beam distortion detection and deflectometry measurements of gigahertz surface acoustic waves. *Rev. Sci. Instrum.*, 82(11):114905, 2011.
- [167] D. Alleyne and P. Cawley. A two-dimensional fourier transform method for the measurement of propagating multimode signals. *J. Acoust. Soc. Am.*, 89(3):1159–1168, 1991.
- [168] W. Gao, C. Glorieux, and J. Thoen. Laser ultrasonic study of lamb waves: determination of the thickness and velocities of a thin plate. *Int. J. Eng. Sci.*, 41(2):219–228, 2003.
- [169] A. J. KENNEDY. A new detection of fatigue damage in metals. *Nature*, 179(4573):1291–1292, 1957.
- [170] G.E. Dieter. *Mechanical metallurgy*. Metallurgy and metallurgical engineering series. McGraw-Hill, 1961.
- [171] Jamie J. Kruzic. Predicting fatigue failures. *Science*, 325(5937):156, 2009.
- [172] Hirotsugu Ogi, Masahiko Hirao, and Shinji Aoki. Noncontact monitoring of surface-wave nonlinearity for predicting the remaining life of fatigued steels. *J. Appl. Phys.*, 90(1):438–442, 2001.
- [173] J. Schijve. Fatigue of structures and materials in the 20th century and the state of the art. *Int. J. Fatigue*, 25(8):679–702, 2003.
- [174] M. A. Meyers, A. Mishra, and D. J. Benson. Mechanical properties of nanocrystalline materials. *Prog. Mater. Sci.*, 51(4):427–556, 2006.
- [175] M.A Miner. Cumulative damage in fatigue. *J. Appl. Mech.*, 12(3):A159–A164, 1945.
- [176] J. Lemaitre and A. Plumtree. Application of damage concepts to predict creep-fatigue failures. *J. Eng. Mater. Technol.*, 101(3):284–292, 1979.
- [177] John W. Hutchinson. *Stresses and failure modes in thin films and multilayers*. Department of Solid Mechanics, Technical University of Denmark, Denmark, 1996.
- [178] B. Cotterell and Z. Chen. Buckling and cracking of thin films on compliant substrates under compression. *Int. J. Fract.*, 104(2):169–179, 2000.

- [179] Herzl Chai and Charles D. Babcock. Two-dimensional modelling of compressive failure in delaminated laminates. *J. Compos. Mater.*, 19(1):67–98, 1985.
- [180] Marta Lewicka, L. Mahadevan, and Mohammad Reza Pakzad. The föppl-von kármán equations for plates with incompatible strains. *Proc. R. Soc. A*, 467(2126):402, 2010.
- [181] J. L. Beuth. Cracking of thin bonded films in residual tension. *Int. J. Sol. Struct.*, 29(13):1657–1675, 1992.
- [182] A. Plumtree and B. P. D. O’Connor. Damage accumulation and fatigue crack propagation in a squeeze-formed aluminium alloy. *Int. J. Fatigue*, 11(4):249–254, 1989.
- [183] Laura J. Pyrak-Nolte, Jianping Xu, and Guy M. Haley. Elastic interface waves propagating in a fracture. *Phys. Rev. Lett.*, 68:3650–3653, 1992.
- [184] Nicolas Mujica, Maria Teresa Cerda, Rodrigo Espinoza, Judit Lisoni, and Fernando Lund. Ultrasound as a probe of dislocation density in aluminum. *Acta Mater.*, 60(16):5828–5837, 2012.
- [185] Felipe Barra, Rodrigo Espinoza-González, Henry Fernández, Fernando Lund, Agnès Maurel, and Vincent Pagneux. The use of ultrasound to measure dislocation density. *JOM*, 67(8):1856–1863, 2015.
- [186] M. W. Barsoum, M. Radovic, T. Zhen, P. Finkel, and S. R. Kalidindi. Dynamic elastic hysteretic solids and dislocations. *Phys. Rev. Lett.*, 94:085501, 2005.
- [187] S. J. Li, L. E. Murr, X. Y. Cheng, Z. B. Zhang, Y. L. Hao, R. Yang, F. Medina, and R. B. Wicker. Compression fatigue behavior of ti-6al-4v mesh arrays fabricated by electron beam melting. *Acta Mater.*, 60(3):793–802, 2012.
- [188] Natalie Rauter, Rolf Lammering, and Tim Kühnrich. On the detection of fatigue damage in composites by use of second harmonic guided waves. *Compos. Struct.*, 152:247–258, 2016.
- [189] Samuel Raetz, Thomas Dehoux, and Bertrand Audoin. Effect of laser beam incidence angle on the thermoelastic generation in semi-transparent materials. *J. Acoust. Soc. Am.*, 130(6):3691–3697, 2011.
- [190] W. G. Johnston and J. J. Gilman. Dislocation velocities, dislocation densities, and plastic flow in lithium fluoride crystals. *J. Appl. Phys.*, 30(2):129–144, 1959.
- [191] B.D. Cullity and S.R. Stock. *Elements of X-ray Diffraction, Third Edition*. Prentice-Hall, 2001.
- [192] S. Prajna, P. A. Parrilo, and A. Rantzer. Nonlinear control synthesis by convex optimization. *IEEE Trans. Automat. Contr.*, 49(2):310–314, 2004.

- [193] Michael J. Korenberg and Ian W. Hunter. The identification of nonlinear biological systems: Volterra kernel approaches. *Ann. Biomed. Eng.*, 24(2):250–268, 1996.
- [194] M. W. Barsoum, A. Murugaiah, S. R. Kalidindi, and T. Zhen. Kinking nonlinear elastic solids, nanoindentations, and geology. *Phys. Rev. Lett.*, 92:255508, 2004.
- [195] Vadas Gintautas and Alfred W. Hübler. Resonant forcing of nonlinear systems of differential equations. *Chaos*, 18(3):033118, 2008.
- [196] Edward N. Lorenz. Deterministic nonperiodic flow. *J. Atmos. Sci.*, 20(2):130–141, 1963.
- [197] Robert M. May. Simple mathematical models with very complicated dynamics. *Nature*, 261:459–467, 1976.
- [198] J.F. de Canete, C. Galindo, and I. Garcia-Moral. *System Engineering and Automation: An Interactive Educational Approach*. Springer Berlin Heidelberg, 2011.
- [199] Koen E-A. Van Den Abeele, Alexander Sutin, Jan Carmeliet, and Paul A. Johnson. Micro-damage diagnostics using nonlinear elastic wave spectroscopy (news). *NDT&E Int.*, 34(4):239–248, 2001.
- [200] Paul A. Johnson and Xiaoping Jia. Nonlinear dynamics, granular media and dynamic earthquake triggering. *Nature*, 437:871, 2005.
- [201] V. Gusev and V. Tournat. Amplitude- and frequency-dependent nonlinearities in the presence of thermally-induced transitions in the preisach model of acoustic hysteresis. *Phys. Rev. B*, 72:054104, 2005.
- [202] M. Radovic, M. W. Barsoum, A. Ganguly, T. Zhen, P. Finkel, S. R. Kalidindi, and E. Lara-Curzio. On the elastic properties and mechanical damping of Ti_3SiC_2 , Ti_3GeC_2 , $\text{Ti}_3\text{Si}_0.5\text{Al}_0.5\text{C}_2$ and Ti_2AlC in the 300–1573 k temperature range. *Acta Mater.*, 54(10):2757–2767, 2006.
- [203] C. Inserra, V. Tournat, and V. Gusev. Characterization of granular compaction by nonlinear acoustic resonance method. *Appl. Phys. Lett.*, 92(19):191916, 2008.
- [204] A. Novak, M. Bentahar, V. Tournat, R. El Guerjouma, and L. Simon. Nonlinear acoustic characterization of micro-damaged materials through higher harmonic resonance analysis. *NDT&E Int.*, 45(1):1–8, 2012.
- [205] J. Cabaret, P. Béquin, G. Theocharis, V. Andreev, V. E. Gusev, and V. Tournat. Nonlinear hysteretic torsional waves. *Phys. Rev. Lett.*, 115:054301, 2015.
- [206] Marcel C. Remillieux, Robert A. Guyer, Cédric Payan, and T. J. Ulrich. Decoupling nonclassical nonlinear behavior of elastic wave types. *Phys. Rev. Lett.*, 116:115501, 2016.

- [207] D. Davidovikj, F. Alijani, S. J. Cartamil-Bueno, H. S. J. van der Zant, M. Amabili, and P. G. Steeneken. Nonlinear dynamic characterization of two-dimensional materials. *Nat Commun*, 8(1):1253, 2017.
- [208] Chongyue Yi, Pratiksha D. Dongare, Man-Nung Su, Wenxiao Wang, Debadri Chakraborty, Fangfang Wen, Wei-Shun Chang, John E. Sader, Peter Nordlander, Naomi J. Halas, and Stephan Link. Vibrational coupling in plasmonic molecules. *PNAS*, 114(44):11621–11626, 2017.
- [209] Andreas P. Mayer. Surface acoustic waves in nonlinear elastic media. *Phys. Rep.*, 256(4–5):237–366, 1995.
- [210] R.A. Guyer and P.A. Johnson. Nonlinear mesoscopic elasticity: evidence of a new class of materials. *Phys. Today*, 52:30–36, 1999.
- [211] W. J. N. de Lima and M. F. Hamilton. Finite-amplitude waves in isotropic elastic plates. *J. Sound Vib.*, 265(4):819–839, 2003.
- [212] Kyung-Young Jhang. Nonlinear ultrasonic techniques for nondestructive assessment of micro damage in material: A review. *Int. J. Precis. Eng. Man.*, 10(1):123–135, 2009.
- [213] Jan Herrmann, Jin-Yeon Kim, Laurence J. Jacobs, Jianmin Qu, Jerrol W. Little, and Michael F. Savage. Assessment of material damage in a nickel-base superalloy using nonlinear rayleigh surface waves. *J. Appl. Phys.*, 99(12):124913, 2006.
- [214] Peter Hess. Surface acoustic waves in materials science. *Phys. Today*, 55(3):42–47, 2002.
- [215] Al. A. Kolomenskii, A. M. Lomonosov, R. Kuschnerit, P. Hess, and V. E. Gusev. Laser generation and detection of strongly nonlinear elastic surface pulses. *Phys. Rev. Lett.*, 79:1325–1328, 1997.
- [216] Simon V. Walker, Jin-Yeon Kim, Jianmin Qu, and Laurence J. Jacobs. Fatigue damage evaluation in a36 steel using nonlinear rayleigh surface waves. *NDT&E Int.*, 48:10–15, 2012.
- [217] Christoph Pruell, Jin-Yeon Kim, Jianmin Qu, and Laurence J. Jacobs. Evaluation of plasticity driven material damage using lamb waves. *Appl. Phys. Lett.*, 91(23):231911, 2007.
- [218] C. Pruell, J. Y. Kim, J. Qu, and L. J. Jacobs. A nonlinear-guided wave technique for evaluating plasticity-driven material damage in a metal plate. *NDT&E Int.*, 42(3):199–203, 2009.
- [219] Peng Zuo, Yu Zhou, and Zheng Fan. Numerical and experimental investigation of nonlinear ultrasonic lamb waves at low frequency. *Appl. Phys. Lett.*, 109(2):021902, 2016.

- [220] Alexei Moussatov, Vitalyi Gusev, and Bernard Castagnède. Self-induced hysteresis for nonlinear acoustic waves in cracked material. *Phys. Rev. Lett.*, 90:124301, 2003.
- [221] Xavier Jacob, Christophe Barrière, and Daniel Royer. Acoustic nonlinearity parameter measurements in solids using the collinear mixing of elastic waves. *Appl. Phys. Lett.*, 82(6):886–888, 2003.
- [222] Christian Bermes, Jin-Yeon Kim, Jianmin Qu, and Laurence J. Jacobs. Experimental characterization of material nonlinearity using lamb waves. *Appl. Phys. Lett.*, 90(2):021901, 2007.
- [223] Bart Sarens, Georgios Kalogiannakis, Christ Glorieux, and Danny Van Hemelrijck. Full-field imaging of nonclassical acoustic nonlinearity. *Appl. Phys. Lett.*, 91(26):264102, 2007.
- [224] F. Vander Meulen and L. Haumesser. Evaluation of b/a nonlinear parameter using an acoustic self-calibrated pulse-echo method. *Appl. Phys. Lett.*, 92(21):214106, 2008.
- [225] Kyung-Young Jhang and Kyung-Cho Kim. Evaluation of material degradation using nonlinear acoustic effect. *Ultrasonics*, 37(1):39–44, 1999.
- [226] TAE-HUN LEE, IK-HWANG CHOI, and KYUNG-YOUNG JHANG. The nonlinearity of guided wave in an elastic plate. *Mod. Phys. Lett. B*, 22(11):1135–1140, 2008.
- [227] Kyung Young Jhang, Taehyung Nam, Sung Ho Choi, Tae Hun Lee, and Chungseok Kim. Bending fatigue evaluation of al6061 alloy by laser-generated surface wave. In *Experimental Mechanics and Materials*, volume 83 of *Applied Mechanics and Materials*, pages 19–21. Trans Tech Publications, 2011.
- [228] Kim Chung-Seok and Jhang Kyung-Young. Acoustic nonlinearity of a laser-generated surface wave in a plastically deformed aluminum alloy. *Chin. Phys. Lett.*, 29(12):120701, 2012.
- [229] Sungho Choi, Hogeon Seo, and Kyung-Young Jhang. Noncontact evaluation of acoustic nonlinearity of a laser-generated surface wave in a plastically deformed aluminum alloy. *Res. Nondestr. Eval.*, 26(1):13–22, 2015.
- [230] Henry D. I. Abarbanel, Reggie Brown, John J. Sidorowich, and Lev Sh. Tsimring. The analysis of observed chaotic data in physical systems. *Rev. Mod. Phys.*, 65:1331–1392, 1993.
- [231] Lucas de Carvalho Pagliosa and Rodrigo Fernandes de Mello. Applying a kernel function on time-dependent data to provide supervised-learning guarantees. *Expert Syst. Appl.*, 71:216–229, 2017.
- [232] B. F. Feeny and G. Lin. Fractional derivatives applied to phase-space reconstructions. *Nonlinear Dyn.*, 38(1):85–99, 2004.

- [233] Matthew B. Kennel, Reggie Brown, and Henry D. I. Abarbanel. Determining embedding dimension for phase-space reconstruction using a geometrical construction. *Phys. Rev. A*, 45:3403–3411, 1992.
- [234] F. Lima, J. Machado, and M. Crisostomo. Pseudo phase plane, delay and fractional dynamics. *JESA*, 42:1037–1051, 2008.
- [235] Miguel F. M. Lima and J. A. Tenreiro Machado. Representation of robotic fractional dynamics in the pseudo phase plane. *Acta Mech. Sin.*, 27(1):28–35, 2011.
- [236] I. TRENDAFILOVA and H. VAN BRUSSEL. Non-linear dynamics tools for the motion analysis and condition monitoring of robot joints. *Mech. Syst. Signal Process.*, 15(6):1141–1164, 2001.
- [237] Christoph Pruell, Jin-Yeon Kim, Jianmin Qu, and Laurence J Jacobs. Evaluation of fatigue damage using nonlinear guided waves. *Smart Mater. Struct.*, 18(3):035003, 2009.
- [238] K. H. Matlack, J. J. Wall, J.-Y. Kim, J. Qu, L. J. Jacobs, and H.-W. Viehrig. Evaluation of radiation damage using nonlinear ultrasound. *J. Appl. Phys.*, 111(5):054911, 2012.
- [239] V. Gusev, C. Glorieux, W. Lauriks, and J. Thoen. Nonlinear bulk and surface shear acoustic waves in materials with hysteresis and end-point memory. *Phys. Lett. A*, 232(1):77–86, 1997.
- [240] Vitalyi Gusev, Vincent Tournat, and Bernard Castagnède. *Nonlinear Acoustic Phenomena in Micro-inhomogenous Media*, chapter 17, pages 431–471. ISTE, 2010.
- [241] O.V. Rudenko and S.I. Soluian. *Theoretical foundations of nonlinear acoustics*. Studies in Soviet science. Consultants Bureau, 1977.
- [242] Vincent Tournat, Vitalyi Gusev, and Bernard Castagnède. *Non-destructive Evaluation of Micro-inhomogenous Solids by Nonlinear Acoustic Methods*, chapter 18, pages 473–503. ISTE, 2010.
- [243] E. R. Naimon, H. M. Ledbetter, and W. F. Weston. Low-temperature elastic properties of four wrought and annealed aluminium alloys. *J. Mater. Sci.*, 10(8):1309–1316, 1975.
- [244] David H. Hurley, Stephen J. Reese, and Farhad Farzbod. Application of laser-based resonant ultrasound spectroscopy to study texture in copper. *J. Appl. Phys.*, 111(5):053527, 2012.
- [245] K. S Kumar, H Van Swygenhoven, and S Suresh. Mechanical behavior of nanocrystalline metals and alloys. *Acta Mater.*, 51(19):5743–5774, 2003.

- [246] A. Migliori, J. L. Sarrao, William M. Visscher, T. M. Bell, Ming Lei, Z. Fisk, and R. G. Leisure. Resonant ultrasound spectroscopic techniques for measurement of the elastic moduli of solids. *Physica B*, 183(1):1–24, 1993.
- [247] Julian Maynard. Resonant ultrasound spectroscopy. *Phys. Today*, 49:26–31, 1996.
- [248] S. J. Reese, K. L. Telschow, T. M. Lillo, and D. H. Hurley. On the establishment of a method for characterization of material microstructure through laser-based resonant ultrasound spectroscopy. *IEEE Trans. Ultrason. Ferroelectr. Freq. Control.*, 55(4):770–777, 2008.
- [249] Hanuš Seiner, Lucie Bodnárová, Petr Sedlák, Miloš Janeček, Ondřej Srba, Robert Král, and Michal Landa. Application of ultrasonic methods to determine elastic anisotropy of polycrystalline copper processed by equal-channel angular pressing. *Acta Mater.*, 58(1):235–247, 2010.
- [250] D. H. Hurley, S. J. Reese, S. K. Park, Z. Utegulov, J. R. Kennedy, and K. L. Telschow. In situ laser-based resonant ultrasound measurements of microstructure mediated mechanical property evolution. *J. Appl. Phys.*, 107(6):063510, 2010.
- [251] F. Farzbod and D. H. Hurley. Using eigenmodes to perform the inverse problem associated with resonant ultrasound spectroscopy. *IEEE Trans. Ultrason. Ferroelectr. Freq. Control.*, 59(11):2470–2475, 2012.
- [252] Farhad Farzbod. Resonant ultrasound spectroscopy for a sample with cantilever boundary condition using rayleigh-ritz method. *J. Appl. Phys.*, 114(2):024902, 2013.
- [253] Sylvain Mezil, Nikolay Chigarev, Vincent Tournat, and Vitalyi Gusev. Two dimensional nonlinear frequency-mixing photo-acoustic imaging of a crack and observation of crack phantoms. *J. Appl. Phys.*, 114(17):174901, 2013.

Appendix A

Synthesis of scientific publications,
communications and activities during
this thesis work

A.1 Articles

1. G. Yan, S. Raetz, N. Chigarev, V. Gusev, V. Tournat, Characterization of progressive fatigue damage in solid plates by laser ultrasonic monitoring of ZGV Lamb modes, *Phys. Rev. Applied*, 9, 061001 (2018).
2. G. Yan, S. Raetz, N. Chigarev, J. Blondeau, V. Gusev, V. Tournat, Laser ultrasonic evaluation of cumulative fatigue damage in thin films using ZGV Lamb modes, *J. Appl. Phys.*, submitted.
3. G. Yan, S. Raetz, J-Ph. Groby, A. Duclos, A. Geslain, N. Chigarev, V. E. Gusev and V. Tournat, Experimental study of ultrasonic attenuation in metallic thin plates by using laser-generated zero-group velocity Lamb modes, *Appl. Sci.*, in preparation.

A.2 Conferences

1. G. Yan et al, Zero-group velocity guided waves in laser hypersonics: an accurate tool to probe mechanical properties and nonlinear phenomena at the micro-metric scale, Flash Doctoral Seminar 2016, 12 Janvier, Le Mans, France.
2. G. Yan et al, Etude expérimentale des modes de Lamb à vitesse de groupe nulle (ZGV) dans le plan complexe des nombres d'ondes, CFA 2016, 11-15 Avril, Le Mans, France.
3. G. Yan et al, Experimental complex dispersion curve by use of spatial Laplace transform: application to ZGV Lamb modes, LU 2016, Lenz, Austria.
4. G. Yan et al, All-optical evaluation of cumulative fatigue damage in solid plates using ZGV Lamb modes, AFPAC 2017, Marseille, France.
5. G. Yan et al, Evaluation tout optique de l'endommagement cumulatif causé par fatigue dans des plaques solides micrométriques en utilisant un mode de Lamb à vitesse de groupe nulle (ZGV), CMOI-FLUVISU 2017, Le Mans, France.
6. G. Yan et al, ZGV guided waves in laser hypersonics, ED-SPIGA Séminaire 2017, Nante, France.
7. G. Yan et al, Laser ultrasonic evaluation of cumulative damage in thin films using ZGV Lamb mode, ICPPP 2017, Bilbao, Spain.
8. G. Yan et al, Non-Contact Monitoring of Fatigue Damage in Metallic Plates Using Laser-Generated Zero-Group Velocity Lamb Waves, ICU 2017, December 18-20, Honolulu Hawaii.
9. G. Yan et al, Non-contact study of heat-treated metallic plates using acoustic nonlinearity of zero-group-velocity (ZGV) Lamb modes, CFA 2018, 23-27 Avril, Le Havre, France
10. G. Yan et al, Evolution of the acoustic nonlinearity in heat-treated metallic plates evaluated with laser-based zero-group velocity (ZGV) Lamb modes, LU 2018, 9-13 July, Nottingham, UK.

A.3 Posters

1. G. Yan et al, Laser-generated zero group velocity (ZGV) Lamb mode for non-destructive fatigue evaluation, Son et Lumière 2017, Les Houches, France.

2. G. Yan et al, Son et lumière : ondes acoustiques générées par laser pour ECND, 15ème Forum Jeunes Recherches, 17 Novembre 2017, Le Mans, France.

A.4 Activities

1. Scientific diffusion in science festival, La Flèche, France 2015;
2. Volunteer for the organization of the 13th French Congress of Acoustics, 2016;
3. Cultural diffusion in Trophy School Day, Le Mans, France 2017;
4. Participation of ‘Son et Lumière’ International School, Les Houches, France 2017;
5. Local organizer of Laser Ultrasonics Hub Date, Le Mans, 12 Oct. 2017;
6. Volunteer for the organization of the 5th Symposium on the Acoustics of PoroElastic Materials, Le Mans, France 2017.

A.5 Teaching

A.5.1 Tutorial and Practical courses

Advanced Instrumentation: data acquisition and spectral analysis (2nd year of B.Sc degree, 32h); Simulations of Phenomena in Physical Sciences (3rd year of B.Sc degree, 48h); Upgrading of Digital Tools: Matlab (3rd year of B.Sc degree, 8h); Geometrical optics (2nd year of B.Sc degree, 32h); Fluid mechanics (3rd year of B.Sc degree, 72h);

A.5.2 Supervisions

Project about laser-ultrasonic Lamb modes in solid plate (1st year of M.Sc degree); Internship about mechanical characterisation of porous materials (2nd year of M.Sc degree).

A.6 Formations

During the three year, the author is totally trained for 210 hours of formations, within 151 hours of professional formations (72%) and 59 hours of scientific formations (28%).

Appendix B


Additional details of the part of
cumulative fatigue damage (CFD) in
Chapter 4: published article

PHYSICAL REVIEW APPLIED 9, 061001 (2018)

Letter

Characterization of Progressive Fatigue Damage in Solid Plates by Laser Ultrasonic Monitoring of Zero-Group-Velocity Lamb Modes

Guqi Yan, Samuel Raetz,* Nikolay Chigarev, Vitalyi E. Gusev, and Vincent Tournat†
 LAUM, Le Mans Université, UMR CNRS 6613, Avenue Olivier Messiaen, 72085 Le Mans Cedex 9, France

 (Received 15 December 2017; revised manuscript received 27 April 2018; published 19 June 2018)

We propose a method for nondestructive characterization of progressive fatigue damage in solid plates, using a zero-group-velocity (ZGV) Lamb mode generated and detected by lasers. Our experimental results depict a nonmonotonous change in the ZGV mode frequency with an increasing number of loading cycles, and more importantly its drastic decrease prior to the specimen failure. We report three experiments on three specimens made of aluminum, which fail after different numbers of loading cycles. Despite this difference, the three nonmonotonous variations of the ZGV mode frequency with an increasing number of loading cycles are superimposed when plotted as a function of the normalized fatigue lifetime. This feature stresses out the potential of the technique to locate fatigue damage, to predict the fatigue lifetime, and to qualitatively, and even quantitatively, assess the different stages of fatigue damage in micrometer- to potentially centimeters-thick solid plates.

DOI: [10.1103/PhysRevApplied.9.061001](https://doi.org/10.1103/PhysRevApplied.9.061001)

I. INTRODUCTION

Solid structures, such as metallic sheets, are generally subjected during their lifetime to numerous stresses (mechanical, thermal, chemical, neutron-ion irradiation), causing fatigue and leading inexorably to damage or even failure of the specimen. It is therefore of utmost importance, in many industrial contexts, to nondestructively assess the cumulative fatigue damage in solid structures used in manufactured products, for their reliability, quantification of health, and certification of security. This challenge has been continuously recalled to be of scientific importance over the last decade [1–5].

Ultrasonic methods were often used for fatigue assessments by detecting acoustic nonlinearity, crack length, elasticity, and the accumulation of damage [6–12]. Laser ultrasonic (LU) techniques have demonstrated increasingly high capabilities in the nondestructive evaluation (NDE) of the mechanical properties of materials [13–21]. Their specific advantages, such as high spatial resolution, large bandwidth, and noncontact character, when compared to conventional ultrasonic methods based on piezoelectric transducers, are particularly appealing. In parallel, the recently implemented laser-based zero-group-velocity (ZGV) Lamb modes have proven to be an efficient tool to probe locally and accurately the thickness or the mechanical properties of plates, as well as to detect defects [22–29]. Yet, the use of LU monitoring of ZGV Lamb modes in solid plates, in order to evaluate or image the sample's damage, especially the fatigue-induced

damage, has not been reported, while it could be useful for both modeling developments and practical applications.

Over the last three decades, much research has been dedicated to proposing measurable physical parameters informative of the fatigue stage of a material, subjected to fatigue test. In this frame, parameters such as damage index, Young's modulus, density, and cross-sectional area, have demonstrated changes with respect to the fatigue lifetime [30–37]. However, the variation of these parameters were all reported to be monotonous (either decreasing or increasing) with the fatigue of the material, which necessitates somehow a definition (often rather arbitrary) of a quantitative threshold denoting a given fatigue stage. Therefore, an index which shows a robust nonmonotonous trend as a function of the amount of loading cycles or fatigue lifetime, would have the important advantage of defining by itself a threshold in the fatigue process, easily detected and surely related to the onset or domination of specific physical processes.

We report here on the monitoring of ZGV Lamb mode frequency along fatigue damage progression in a solid plate made of aluminum. Specifically, the change in the frequency of the first symmetrical ZGV Lamb mode is analyzed as a function of both the fatigue lifetime and the probing location on the sample. In addition to a spatial image of the damage, we observe a reproducible nonmonotonous trend in the evolution of the ZGV mode frequency, with a single extremum occurring consistently for different tests at about 80% of the fatigue lifetime. The thickness of the here-tested plates is 75 μm . Yet, the technique is sound for micrometer-thick-to-centimeters-thick plates, depending on the pulsed generation laser characteristics (pulsed duration, energy).

*samuel.raetz@univ-lemans.fr

†vincent.tournat@univ-lemans.fr

YAN, RAETZ, CHIGAREV, GUSEV, and TOURNAT

PHYS. REV. APPLIED 9, 061001 (2018)

II. ZERO-GROUP-VELOCITY LAMB MODES

Lamb waves are the acoustic eigenmodes guided in a freestanding plate [38–40]. A ZGV Lamb mode results from the interference of two Lamb waves coexisting for a unique couple of frequency and wave number but spatially counter-propagating. This specific type of Lamb mode exhibits an anomalous behavior since the group velocity $V_g = d\omega/dk$ vanishes, while the phase velocity remains finite. The mechanical energy associated with a ZGV mode is, therefore, locally trapped at the excitation area, which leads to a sharp resonance of the plate. Because of the local feature of this resonance, its frequency value is informative of the local mechanical properties or thickness. For a single homogeneous plate, the Rayleigh-Lamb equations can be written as a function of the dimensionless frequency $\Omega = 2h\omega/(\pi c_T)$ and the dimensionless wave number $\xi = 2kh/\pi$, where $2h$ stands for the plate thickness, ω for the pulsation, c_T for the shear wave velocity, and k for the wave number [38–40]. Therefore, if the elastic parameters of the plate remain unchanged, the frequency shift Δf ($\propto \Delta\omega$) of the ZGV mode is associated with the change of the plate thickness Δh :

$$\frac{\Delta f}{f} = -\frac{\Delta h}{h}. \quad (1)$$

The relation (1) is useful for NDE purposes [29,41–43] and will be used in the following to explain the experimentally revealed phenomena. It is also important to note that the spatial resolution of our method is scalable with the plate thickness since the ZGV mode wavelength is of the order of twice the plate thickness. This feature, therefore, probably limits the potential of our technique to detect small fatigue zones in a centimeters-thick plate.

III. FATIGUE SETUP AND LASER ULTRASONIC EXPERIMENTAL SETUP

In this Letter, a homemade fatigue machine is used for cyclic loading of a 75- μm -thick aluminium plate in a two-sides-clamped compression configuration inducing buckling [see Fig. 1(c)]. The buckling is achieved by imposing one of the clamped end of the plate of length $2L$ to move by $2\Delta L$ along the x axis [see Fig. 1(c)]. The analytical expression of the normal deflection $w(x)$ of the plate neutral line in this buckling configuration is [44]

$$w(x) = \frac{\delta}{2} \left[\cos\left(\frac{\pi(x-L+\Delta L)}{L-\Delta L}\right) - 1 \right], \quad (2)$$

where δ is the buckling deflection at the center of the specimen ($x = 0$). From Eq. (2), the stress $\sigma_{xx}(x, z)$ is then readily deduced [45]:

$$\sigma_{xx}(x, z) = Az \cos\left(\frac{\pi(x-L+\Delta L)}{L-\Delta L}\right), \quad (3)$$

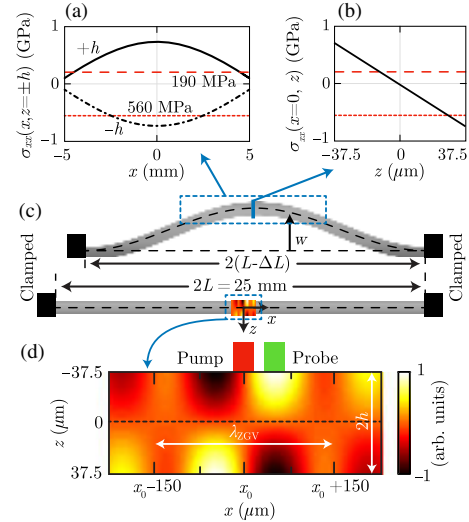


FIG. 1. (a) Surface ($z = \pm h$) stress profiles of the buckled solid plate and (b) section (at $x = 0$ mm) stress distribution with $\Delta L = 2$ mm. (c) Schematic presentation of the loaded and unloaded plate. (d) x component of the normal displacement gradient ($\partial u_z/\partial x$) associated with the first symmetrical ZGV Lamb mode ($2h = 75 \mu\text{m}$).

where $A = -\delta\pi^2 E/[2(L-\Delta L)^2(1-\nu^2)]$, E and ν standing for the Young's modulus and the Poisson's ratio, respectively. Here, the zero of the local $z = z(x)$ axis, normal to the plate surfaces, is chosen in the middle plane of the plate. In our experiment, the length of the plate is $2L = 25$ mm and the imposed x displacement is $2\Delta L = 4$ mm, leading to a buckling deflection of $\delta = 5.83$ mm. In that case, and using $E = 70$ GPa and $\nu = 0.35$ (corresponding to aluminum), the stress distribution at $z = \pm h$ is plotted in Fig. 1(a) as a function of x . The red dashed line and dotted line represent the tensile (approximately 190 MPa) and compressive (approximately 560 MPa) yield strengths of the tested aluminum specimen, respectively. Please note that the compressive yield strength has been taken from p. 152 of Ref. [46]. From Fig. 1(a), it can be stated that the most fatigued part of the plate is expected to be located at $x = 0$, since the maximum difference between the applied stress and the tensile-compressive yield stress occurs at this location [see Figs. 1(a) and 1(b)]. Note that the fatigue could be expected for all points from $x = 0$ to $x \approx \pm 5$ mm with a continuous decrease in magnitude since the applied stresses approach the yield stresses as the distance from $x = 0$ mm increases. This low-cycle fatigue is in our case most probably related to the propagation of surface flaws than to dislocation mechanisms. In order to perform the measurements of the variation of the ZGV mode frequency along the fatigued plate, the loading is stopped at regular intervals of cycles. The

scan of the unloaded plate in front of the laser ultrasonic setup is performed over the interval $x \in [-5; 5]$ mm, with a scan step of $100 \mu\text{m}$, using a motorized actuator with a minimum incremental motion of $0.1 \mu\text{m}$.

The laser ultrasonic experimental setup used to monitor the ZGV mode frequency is composed of (i) a pulsed Nd:YAG laser (1064 nm, pulse duration close to 0.75 ns, repetition rate of 1 kHz) focused to a stretched ellipse (small diameter approximately $20 \mu\text{m}$ and large diameter approximately $500 \mu\text{m}$) on the sample surface to generate the first symmetrical ZGV Lamb mode among others, and (ii) a CW laser (532 nm) focused to a circular spot (diameter approximately $20 \mu\text{m}$) in the vicinity of the line source to detect the local resonance thanks to the beam-deflection technique [20,47]. Since the beam-deflection technique is sensitive to the radial gradient of the normal displacement (u_z), a small shift of about $40 \mu\text{m}$ has been used between generation and detection spots, for the detection of the ZGV mode. This is illustrated in Fig. 1(d), also showing the distribution of the x component of the normal displacement gradient ($\partial u_z / \partial x$) associated with the first symmetrical ZGV Lamb mode. Note that the specimen is unloaded at regular intervals of 500 cycles in the conducted experiments and that a reference scan has been achieved on the intact specimen and saved for comparison with results at different fatigue stages.

IV. RESULTS AND DISCUSSION

An example of a measured temporal photoacoustic signal is displayed in Fig. 2(a). The slowly oscillating background corresponds to the first antisymmetric mode A_0 which is preponderant. By enlarging the time signal [inset in Fig. 2(a)], a higher frequency oscillation corresponding to the ZGV resonance is visible. The Fourier transform (FT) of the signal in Fig. 2(a) is calculated and its normalized magnitude with respect to the ZGV peak value is plotted in the frequency range of 20–100 MHz in Fig. 2(b). A resonance is visible at 38.78 MHz, having a measured quality factor of 149. In Fig. 2(c), the red solid line exhibits the spatial distribution of the ZGV resonance frequency after 9500 fatigue loading cycles, which is extracted from the normalized FT magnitude. A very clear frequency increase is observed in the center of the sample (maximum increase at position $x = 0.1$ mm), primarily due to the local decrease of the thickness in this fatigued region.

The relative variation $\Delta f/f$ of the ZGV frequency measured after N cycles compared to the reference ZGV frequency (measured on the intact specimen) is calculated as a function of the sample position and of the number of loading cycles and displayed in Fig. 3(a). Three main results emerge from this plot: (i) the obvious distinction on ZGV frequency between damaged and undamaged regions; (ii) the monotonic increase of ZGV frequency in the fatigue region up to 10 000 cycles, mainly caused by thickness changes, as expected from Eq. (1); (iii) the abrupt decrease of the ZGV

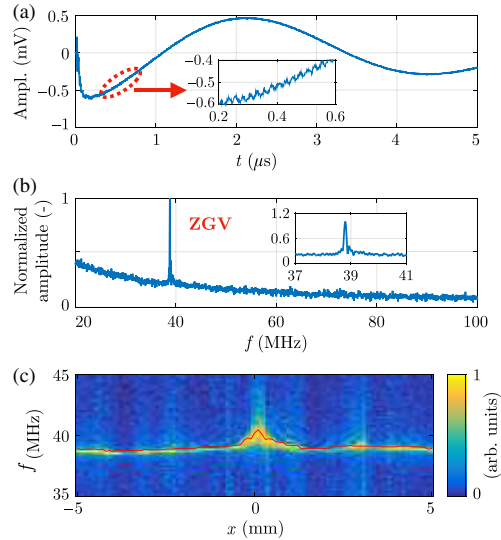


FIG. 2. (a) Example of a received temporal photoacoustic signal measurement and (b) its spectrum with a sharp peak corresponding to the ZGV resonance frequency. (c) Spectrum magnitude normalized by the ZGV peak value as a function of frequency and sample position after 9500 fatigue loading cycles, the red solid line represents the spatial distribution of the estimated ZGV resonance frequency.

frequency before specimen failure. For a better appreciation of this last point, the variation of the ZGV frequency at $x = 0.1$ mm is extracted from the image and is plotted in Fig. 3(b); error bars stand for $f_n/(f_0 Q_n)$, with f_n the ZGV frequency after n cycles, Q_n the Q factor of the corresponding resonance. The maximum value at 10 000 loading cycles divides the curve into two different parts: (i) the monotonic increase where the thickness change is mainly at play and (ii) the abrupt decrease before specimen failure that could be explained by the drop in elastic stiffness [30,48] and by the interaction between the ZGV mode and the dislocations and cracks present in the specimen [12,49–51]. Note that fatigue softening of materials can be found not only in metals [37,52], but also in other types of materials, such as polymer [6], composite materials [53], and so on.

Following these experimental results, it can be stated that the proposed method is sensitive to cumulative fatigue damage [see Figs. 2(c) and 3(a)]. Moreover, even without knowing the exact position of the damaged zone before observation, which could be a limitation of some other methods [35,54], it can be located thanks to the frequency image as depicted in Fig. 2(c). Last but not least, unlike other damage indexes presented in the literature [6,9,30–37,48], the nonmonotonic evolution of the variation $\Delta f/f$ of the ZGV resonance frequency shows the potential for quantitative assessment of the fatigue lifetime [see Fig. 3(b)]. Even

YAN, RAETZ, CHIGAREV, GUSEV, and TOURNAT

PHYS. REV. APPLIED 9, 061001 (2018)

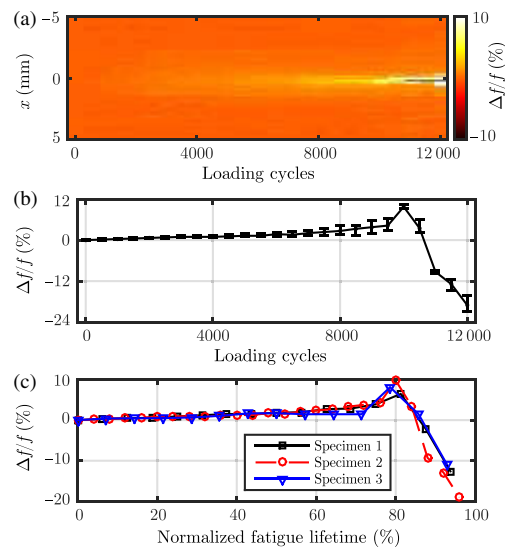


FIG. 3. (a) Spatial distribution of the relative variation of the ZGV mode frequency vs fatigue cycles. (b) Experimental evolution of $\Delta f/f$ (with error bars) as a function of fatigue duration at the specimen center ($x = 0.1$ mm). (c) Comparison between $\Delta f/f$ evolutions measured in specimens 1, 2, and 3 (failure at approximately 16 000, 12 500, and 14 000 cycles) as a function of normalized fatigue lifetime.

if ascertaining which side of the peak corresponds to the correct measurement of the fatigue state might be seen as a limitation of our technique when the material is not continuously monitored, two consecutive measurements of this frequency at a small fatigue cycle interval would suffice to ascertain to which side of the peak belongs the current state. Overcoming this limitation is currently under development and should be addressed in follow-up papers. Three fatigue monitoring tests have been carried out on three samples and the corresponding $\Delta f/f$ are plotted in Fig. 3(c), showing identical variations in normalized fatigue lifetime scale, although failure occurs at different amounts of loading cycles. This reproducible, nonmonotonous parameter variation [see Fig. 3(c)], thanks to the existence of an extremum just prior to the fracture of the specimen (approximately 80% of the fatigue lifetime), might establish a quantitative empirical law characterizing a sample's fatigue stage and could be an effective tool for predicting fatigue life.

V. CONCLUSION

In conclusion, this Letter presents a noncontact laser ultrasonics evaluation of cumulative fatigue damage in thin solid plates by monitoring a ZGV Lamb mode frequency. The experimental results demonstrate the ability of this method for (i) locating damage, (ii) predicting fatigue

lifetime, and (iii) assessing qualitatively and potentially quantitatively, the cumulative fatigue damage levels during fatigue process. For better understanding of elastic property changes and of thickness distribution in the specimen, numerical simulations (based on the finite element method, for example) are necessary and are under development. One of the prospects of this work is to formally identify the material mechanisms leading to this extremum in ZGV Lamb mode frequency using, e.g., electron microscope imaging, in order to reach a fully quantitative (local) damage evaluation of a sample [55,56].

- [1] P. J. Withers, Residual stress and its role in failure, *Rep. Prog. Phys.* **70**, 2211 (2007).
- [2] J. J. Kruzic, Predicting fatigue failures, *Science* **325**, 156 (2009).
- [3] P. Li, S. X. Li, Z. G. Wang, and Z. F. Zhang, Fundamental factors on formation mechanism of dislocation arrangements in cyclically deformed fcc single crystals, *Prog. Mater. Sci.* **56**, 328 (2011).
- [4] A. Pineau, D. L. McDowell, E. P. Busso, and S. D. Antolovich, Failure of metals II: Fatigue, *Acta Mater.* **107**, 484 (2016).
- [5] M. Kamal and M. M. Rahman, Advances in fatigue life modeling: A review, *Renew. Sustain. Energ. Rev.* **82**, 940 (2018).
- [6] P. B. Nagy, Fatigue damage assessment by nonlinear ultrasonic materials characterization, *Ultrasonics* **36**, 375 (1998).
- [7] C. Bermes, J. Kim, J. Qu, and L. J. Jacobs, Experimental characterization of material nonlinearity using Lamb waves, *Appl. Phys. Lett.* **90**, 021901 (2007).
- [8] J. H. Cantrell and W. T. Yost, Nonlinear ultrasonic characterization of fatigue microstructures, *Int. J. Fatigue* **23**, 487 (2001).
- [9] M. Deng and J. Pei, Assessment of accumulated fatigue damage in solid plates using nonlinear Lamb wave approach, *Appl. Phys. Lett.* **90**, 121902 (2007).
- [10] V. V. S. Jaya Rao, E. Kannan, R. V. Prakash, and K. Balasubramaniam, Fatigue damage characterization using surface acoustic wave nonlinearity in aluminum alloy AA7175-T7351, *J. Appl. Phys.* **104**, 123508 (2008).
- [11] C. Pruell, J. Kim, J. Qu, and L. J. Jacobs, Evaluation of plasticity driven material damage using Lamb waves, *Appl. Phys. Lett.* **91**, 231911 (2007).
- [12] L. J. Pyrak-Nolte, J. Xu, and G. M. Haley, Elastic Interface Waves Propagating in a Fracture, *Phys. Rev. Lett.* **68**, 3650 (1992).
- [13] C. B. Scruby and L. E. Drain, *Laser Ultrasonics Techniques and Applications* (Taylor & Francis, London, 1990).
- [14] D. Royer and E. Dieulesaint, *Elastic Waves in Solids II: Generation, Acousto-optic Interaction, Applications*, Advanced Texts in Physics Vol. II (Springer, Berlin, Heidelberg, 2000).
- [15] P. Hess, Surface acoustic waves in materials science, *Phys. Today* **55**, No. 3, 42 (2002).
- [16] A. K. Kromine, P. A. Fomitchov, S. Krishnaswamy, and J. D. Achenbach, Laser ultrasonic detection of surface breaking discontinuities: Scanning laser source technique,

- Mater. Eval. **58**, 173 (2000), <https://www.scholars.northwestern.edu/en/publications/laser-ultrasonic-detection-of-surface-breaking-discontinuities-sc>.
- [17] S. Dixon, B. Cann, D. L. Carroll, Y. Fan, and R. S. Edwards, Non-linear enhancement of laser generated ultrasonic Rayleigh waves by cracks, *Nondestr. Test. Eval.* **23**, 25 (2008).
- [18] C. Thomsen, J. Strait, Z. Vardeny, H. J. Maris, J. Tauc, and J. J. Hauser, Coherent Phonon Generation and Detection by Picosecond Light Pulses, *Phys. Rev. Lett.* **53**, 989 (1984).
- [19] A. I. A. Kolomenskii, A. M. Lomonosov, R. Kuschneireit, P. Hess, and V. E. Gusev, Laser Generation and Detection of Strongly Nonlinear Elastic Surface Pulses, *Phys. Rev. Lett.* **79**, 1325 (1997).
- [20] S. Mezil, N. Chigarev, V. Tourmat, and V. Gusev, All-optical probing of the nonlinear acoustics of a crack, *Opt. Lett.* **36**, 3449 (2011).
- [21] C. Ni, N. Chigarev, V. Tourmat, N. Delorme, Z. Shen, and V. E. Gusev, Probing of laser-induced crack closure by pulsed laser-generated acoustic waves, *J. Appl. Phys.* **113**, 014906 (2013).
- [22] C. Prada, O. Balogun, and T. W. Murray, Laser-based ultrasonic generation and detection of zero-group velocity Lamb waves in thin plates, *Appl. Phys. Lett.* **87**, 194109 (2005).
- [23] D. Clorennec, C. Prada, D. Royer, and T. W. Murray, Laser impulse generation and interferometer detection of zero group velocity Lamb mode resonance, *Appl. Phys. Lett.* **89**, 024101 (2006).
- [24] D. Clorennec, C. Prada, and D. Royer, Local and noncontact measurements of bulk acoustic wave velocities in thin isotropic plates and shells using zero group velocity Lamb modes, *J. Appl. Phys.* **101**, 034908 (2007).
- [25] S. Mezil, F. Bruno, S. Raetz, J. Laurent, D. Royer, and C. Prada, Investigation of interfacial stiffnesses of a tri-layer using zero-group velocity Lamb modes, *J. Acoust. Soc. Am.* **138**, 3202 (2015).
- [26] C. Prada, D. Clorennec, and D. Royer, Local vibration of an elastic plate and zero-group velocity Lamb modes, *J. Acoust. Soc. Am.* **124**, 203 (2008).
- [27] C. Prada, D. Clorennec, T. W. Murray, and D. Royer, Influence of the anisotropy on zero-group velocity Lamb modes, *J. Acoust. Soc. Am.* **126**, 620 (2009).
- [28] S. Raetz, J. Laurent, T. Dehoux, D. Royer, B. Audoin, and C. Prada, Effect of refracted light distribution on the photoelastic generation of zero-group velocity lamb modes in optically low-absorbing plates, *J. Acoust. Soc. Am.* **138**, 3522 (2015).
- [29] F. Faëse, S. Raetz, N. Chigarev, C. Mechri, J. Blondeau, B. Campagne, V. E. Gusev, and V. Tourmat, Beam shaping to enhance zero group velocity Lamb mode generation in a composite plate and nondestructive testing application, *NDT&E Int.* **85**, 13 (2017).
- [30] A. Plumtree and B. P. D. O'Connor, Damage accumulation and fatigue crack propagation in a squeeze-formed aluminium alloy, *Int. J. Fatigue* **11**, 249 (1989).
- [31] A. Fatemi and L. Yang, Cumulative fatigue damage and life prediction theories: A survey of the state of the art for homogeneous materials, *Int. J. Fatigue* **20**, 9 (1998).
- [32] B. Sun, L. Yang, and Y. Guo, A high-cycle fatigue accumulation model based on electrical resistance for structural steels, *Fatigue Fract. Eng. Mater. Struct.* **30**, 1052 (2007).
- [33] X. J. Sun, C. C. Wang, J. Zhang, G. Liu, G. J. Zhang, X. D. Ding, G. P. Zhang, and J. Sun, Thickness dependent fatigue life at microcrack nucleation for metal thin films on flexible substrates, *J. Phys. D* **41**, 195404 (2008).
- [34] J. H. Cantrell, Ultrasonic harmonic generation from fatigue-induced dislocation substructures in planar slip metals and assessment of remaining fatigue life, *J. Appl. Phys.* **106**, 093516 (2009).
- [35] M. Amura, M. Meo, and F. Amerini, Baseline-free estimation of residual fatigue life using a third order acoustic nonlinear parameter, *J. Acoust. Soc. Am.* **130**, 1829 (2011).
- [36] A. Aid, A. Amrouche, B. Bachir Bouiadjra, M. Benguediab, and G. Mesmacque, Fatigue life prediction under variable loading based on a new damage model, *Mater. Des.* **32**, 183 (2011).
- [37] S. J. Li, L. E. Murr, X. Y. Cheng, Z. B. Zhang, Y. L. Hao, R. Yang, F. Medina, and R. B. Wicker, Compression fatigue behavior of Ti-6Al-4V mesh arrays fabricated by electron beam melting, *Acta Mater.* **60**, 793 (2012).
- [38] J. D. Achenbach, *Wave Propagation in Elastic Solids* (North-Holland Publishing Company, Amsterdam, 1973).
- [39] B. A. Auld, *Acoustic Fields and Waves in Solids* (R. E. Krieger Publishing Company, Malabar, FL, 1990), Vol. 2.
- [40] D. Royer and E. Dieulesaint, *Elastic Waves in Solids* (Masson, Paris, 1999), Vol. 1.
- [41] D. Clorennec, C. Prada, and D. Royer, Laser ultrasonic inspection of plates using zero-group velocity Lamb modes, *IEEE Trans. Ultrason. Ferroelectr. Freq. Control* **57**, 1125 (2010).
- [42] M. Cès, D. Clorennec, D. Royer, and C. Prada, Thin layer thickness measurements by zero group velocity Lamb mode resonances, *Rev. Sci. Instrum.* **82**, 114902 (2011).
- [43] M. Cès, D. Royer, and C. Prada, Characterization of mechanical properties of a hollow cylinder with zero group velocity Lamb modes, *J. Acoust. Soc. Am.* **132**, 180 (2012).
- [44] J. W. Hutchinson, *Stresses and Failure Modes in Thin Films and Multilayers* (Technical University of Denmark, Denmark, 1996).
- [45] H. Chai and C. D. Babcock, Two-dimensional modelling of compressive failure in delaminated laminates, *J. Compos. Mater.* **19**, 67 (1985).
- [46] N. E. Dowling, K. S. Prasad, and R. Narayanasamy, *Mechanical Behavior of Materials: Engineering Methods for Deformation, Fracture, and Fatigue* (Pearson, Essex, England, 2012).
- [47] J. Higuete, T. Valier-Brasier, T. Dehoux, and B. Audoin, Beam distortion detection and deflectometry measurements of gigahertz surface acoustic waves, *Rev. Sci. Instrum.* **82**, 114905 (2011).
- [48] J. Lemaître and J. Dufailly, Damage measurements, *Eng. Fract. Mech.* **28**, 643 (1987).
- [49] A. Maurel, V. Pagneux, F. Barra, and F. Lund, Wave propagation through a random array of pinned dislocations: Velocity change and attenuation in a generalized Granato and Lücke theory, *Phys. Rev. B* **72**, 174111 (2005).
- [50] N. Mujica, M. T. Cerda, R. Espinoza, J. Lisoni, and F. Lund, Ultrasound as a probe of dislocation density in aluminum, *Acta Mater.* **60**, 5828 (2012).

YAN, RAETZ, CHIGAREV, GUSEV, and TOURNAT

PHYS. REV. APPLIED **9**, 061001 (2018)

- [51] F. Barra, R. Espinoza-González, H. Fernández, F. Lund, A. Maurel, and V. Pagneux, The use of ultrasound to measure dislocation density, *JOM* **67**, 1856 (2015).
- [52] M. W. Barsoum, M. Radovic, T. Zhen, P. Finkel, and S. R. Kalidindi, Dynamic Elastic Hysteretic Solids and Dislocations, *Phys. Rev. Lett.* **94**, 085501 (2005).
- [53] N. Rauter, R. Lammering, and T. Kühnrich, On the detection of fatigue damage in composites by use of second harmonic guided waves, *Compos. Struct.* **152**, 247 (2016).
- [54] M. Amura and M. Meo, Prediction of residual fatigue life using nonlinear ultrasound, *Smart Mater. Struct.* **21**, 045001 (2012).
- [55] D. Farkas, M. Willemann, and B. Hyde, Atomistic Mechanisms of Fatigue in Nanocrystalline Metals, *Phys. Rev. Lett.* **94**, 165502 (2005).
- [56] M. A. Meyers, A. Mishra, and D. J. Benson, Mechanical properties of nanocrystalline materials, *Prog. Mater. Sci.* **51**, 427 (2006).

Appendix C

Examples of COMSOL code for
explanation of the details of ZGV
mode excitation & detection
simulations by finite element method
(FEM)

In this chapter of appendix, we describe some details of the utilization of the software COMSOL which is based on the finite element method and provides an IDE (Integrated Development Environment) and unified workflow for electrical, fluid and mechanical (as well as other scientific fields') applications. We present herein the screen capture of the software window as an example of the COMSOL code.

In order to simplify the calculations, we use only one physical model, i.e. the model of **Solid Mechanics**, the surface opto-thermo-acoustic source are theoretically calculated and added directly as a shear dipole stress at the central position of the defined material. The material used here is the pure Aluminium with properties given and defined by the software itself. For the theoretical part of the calculation of the applied surface shear stresses, readers could see the Chapter 4, Sec. 4.4.2, and the applied mechanical, thermal and optical properties are the same as given in Tab. 4.1 in Sec. 4.4.2.

Moreover, for avoiding the reflections from the left/right boundary, two symmetric perfect matching layers (PML), with gradient high loss, are added to the left and right ends of the model at $x = \pm 3.75$ mm, as explained in Chapter 4. The calculation duration of one input fatigue loading cycles in case as described in Chapter 4 is about 2 hours with a minimum mesh size of $1\mu\text{m}$ and a reception time of $5\mu\text{s}$. In the following examples (see Figures C.1 to C.5), because they are just for explanation of the functionality of the software, the mesh size is defined as $1\mu\text{m}$ in centre of the material ($x \in [-1, 1]\text{mm}$) and as $5\mu\text{m}$ for $x \in [1, 3.75] \cup [-3.75, -1]\text{mm}$. The connection at $x = \pm 1$ is set to be automatic for the conversion of the different mesh size. Therefore, the calculation duration is reduced to be about 15 minutes for each study (with reception time of $5\mu\text{s}$).

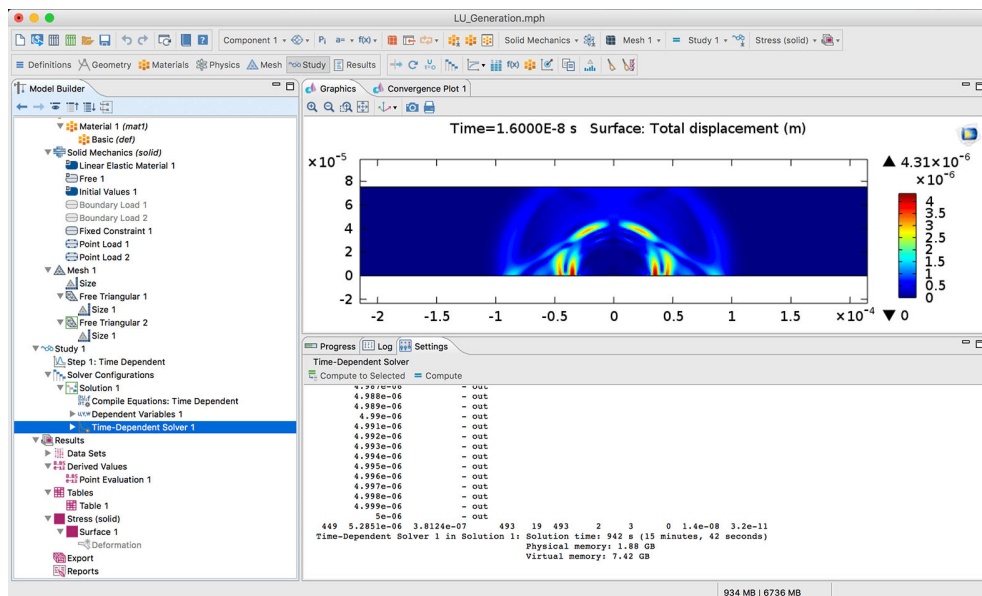


Figure C.1: Screen capture of FEM software COMSOL in case of intact sample with thickness of 75 micrometers, with illustration of the normal displacement distribution field around excitation point at time of 16 nanoseconds.

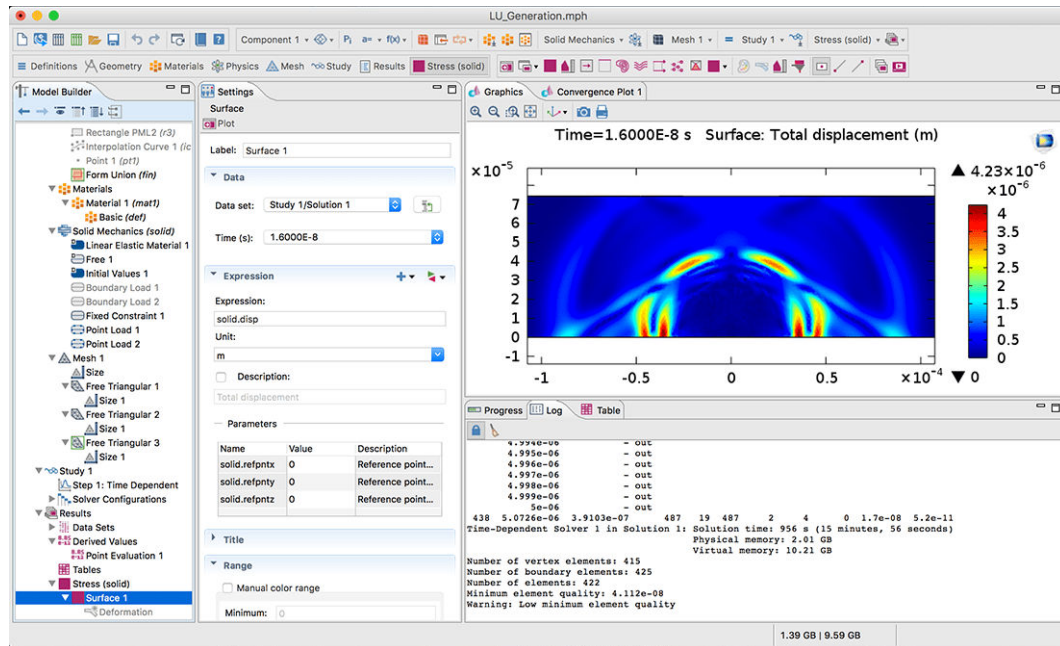


Figure C.2: Screen capture of FEM software COMSOL in case of damaged sample (maximal decrease of thickness equals to 1% at $x = 0\text{mm}$) with thickness of 75 micrometers, with illustration of the normal displacement distribution field around excitation point at time of 16 nanoseconds.

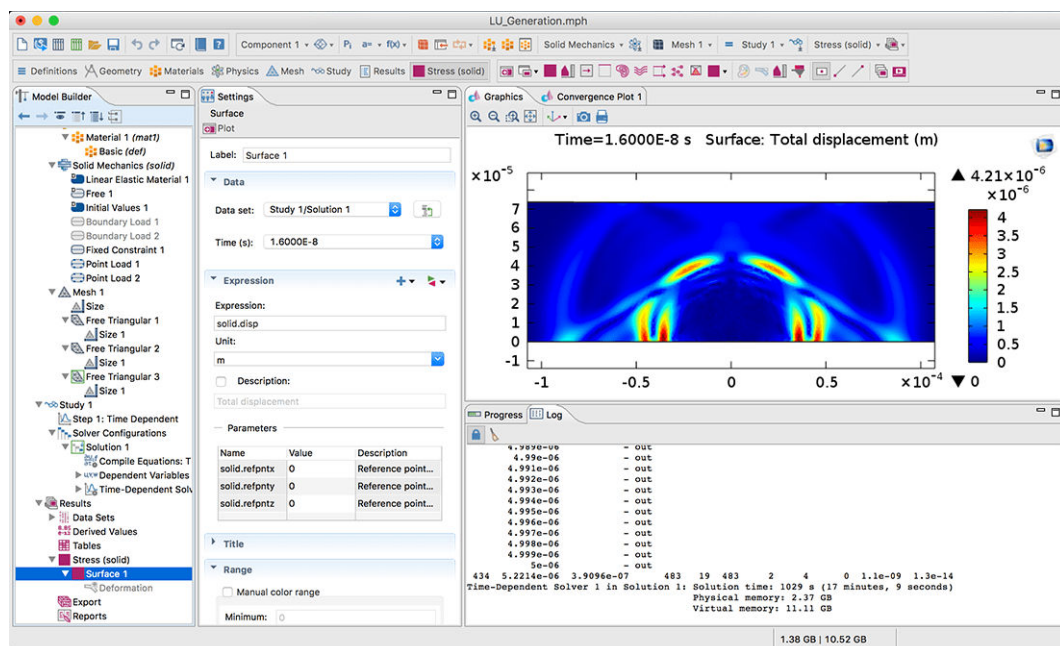
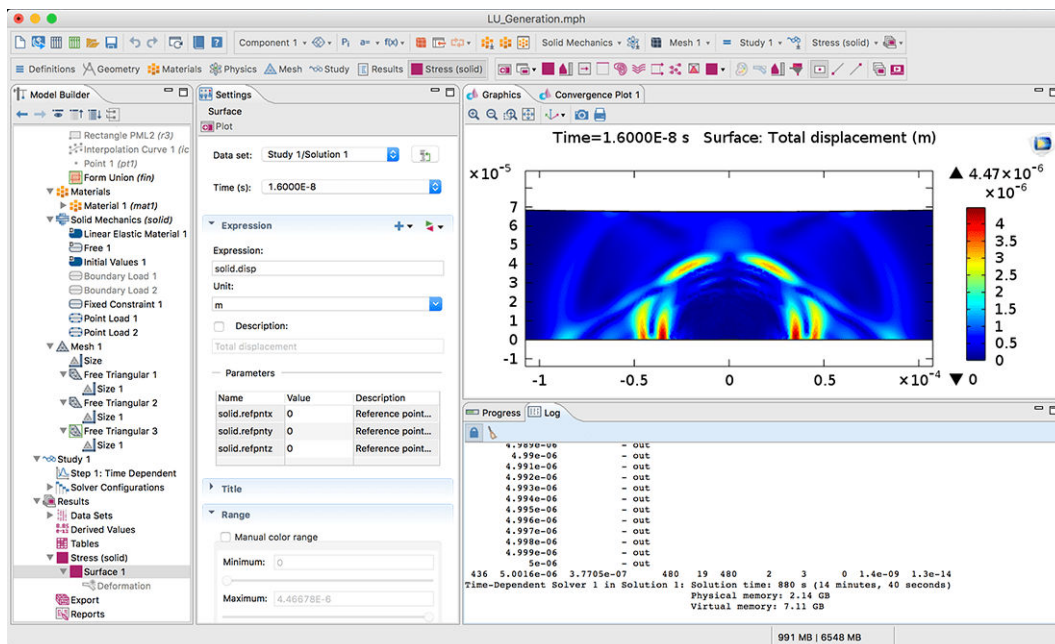
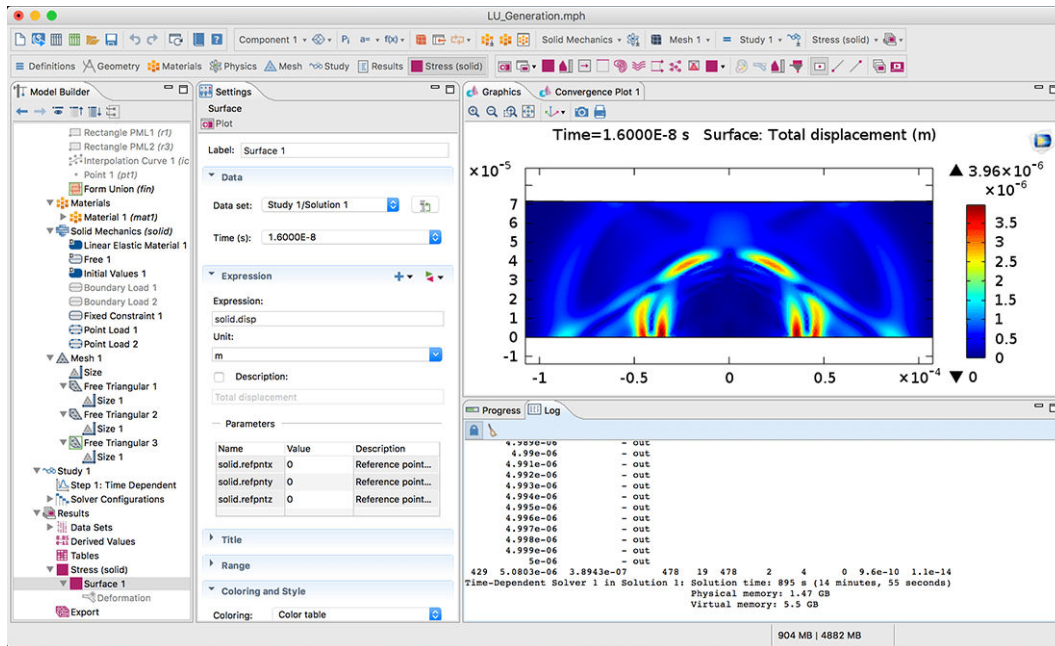


Figure C.3: Screen capture of FEM software COMSOL in case of damaged sample (maximal decrease of thickness equals to 2% at $x = 0\text{mm}$) with thickness of 75 micrometers, with illustration of the normal displacement distribution field around excitation point at time of 16 nanoseconds.



Appendix D

Matlab program for calculation of
Lamb wave dispersion curves:
frequency V.S. real wavenumber

```

1  %%% Dispersion curves by resolving the Rayleigh-Lamb equations
2  %%% Created by Guqi YAN : PhD Student at LUAM
3  %%% 21-04-2016 : First Year of PhD Student life
4  clear
5  close all
6  clc
7  format long
8  fontsize = 24;
9  %%% Input coefficients of Aluminium
10 E = 70.3e9; % Young Modulus
11 nu = 0.35; % Poisson's rqtion
12 rho = 2.7e3; % Density of Al kg/m^3
13 lambda = E*nu/(1+nu)/(1-2*nu); % First Lamé coefficient
14 mu = E/2/(1+nu); % Second Lamé coefficient
15 VL = sqrt((lambda+2*mu)/rho); % Longitudinal velocity
16 VT = sqrt(mu/rho); % Shear velocity
17 h = 100e-6; % Thickness
18 d = h/2; % Half Thickness
19 % nu = ((VL/VT)^2-2)/2/((VL/VT)^2-1); % Formula for Poisson ratio
20 NF = 2000;
21 NK = 300;
22 Fmax = 200;
23 Kmax = 500;
24 F = linspace(0,Fmax,NF);
25 F = F.*1e6;
26 K = linspace(0,Kmax,NK);
27 K = K.*1e3;
28 S = zeros(NF,length(K));
29 A = zeros(NF,length(K));
30 %%% Calculations of the RL Equation values for S and A modes
31 for i = 1:length(F)
32     f = F(i);
33     w = f*2*pi;
34     for j = 1:length(K)
35         k = K(j);
36         p = sqrt(w^2/VL^2-k^2);
37         q = sqrt(w^2/VT^2-k^2);
38         Vsym=(q^2-k^2)^2*cos(p*d)*sin(q*d)/q+4*k^2*p*sin(p*d)*cos(q*d);
39         Vasym=(q^2-k^2)^2*sin(p*d)*cos(q*d)/p+4*k^2*q*cos(p*d)*sin(q*d);
40         if i == 1
41             p = 1i*sqrt(k^2 - w^2/VL^2);
42             q = 1i*sqrt(k^2 - w^2/VT^2);
43             Vsym = 0;
44             Vasym = 0;
45         end
46         S(i,j) = Vsym;
47         A(i,j) = Vasym;
48     end
49 end
50 S = abs(S);
51 S = 20*log10(S./max(max(S)));
52 A = abs(A);
53 A = 20*log10(A./max(max(A)));
54 mm1 = find(S(3,:) == min(S(3,:),1));
55 S(1,2:mm1) = S(2,2:mm1);
56 mm2 = find(A(3,:) == min(A(3,:),1));
57 A(1,2:mm2) = A(2,2:mm2);
58 S(1,1) = min(min(S));
59 A(1,1) = min(min(A));
60 figure(1);
61 subplot(1,2,1)
62 pcolor(K./1e3,F./1e6,S)
63 shading flat
64 colorbar
65 subplot(1,2,2)
66 pcolor(K./1e3,F./1e6,A)
67 shading flat
68 colorbar
69 %%% Find out the quasi results form S and A
70 S_op = zeros(size(S));
71 A_op = zeros(size(A));
72 for i = 1:length(F)
73     for j = 1:length(K)
74         value1 = S(i,j);
75         value2 = A(i,j);
76 % Step 1: Find the quasi results for internal part of S
77         if i > 1 && i < length(F)
78             value_down = S(i-1,j);
79             value_up = S(i+1,j);
80             if value1 <= value_up && value1 <= value_down
81                 S_op(i,j) = S(i,j);
82             else
83                 S_op(i,j) = 0;
84             end
85         end
86         if i == length(F) && j > 1 && j < length(K)
87             value_left = S(i,j+1);
88             value_right = S(i,j-1);
89             value_down = S(i-1,j);
90             if value1 <= value_left && value1 <= value_right && value1 <= value_down
91                 S_op(i,j) = S(i,j);
92             else
93                 S_op(i,j) = 0;
94             end
95         end
96     end
97 end

```

```

96 % Step 2: Find the quasi results for internal part of A
97     if i > 1 && i < length(F)
98         value_down = A(i-1,j);
99         value_up   = A(i+1,j);
100         if value2 <= value_up && value2 <= value_down
101             A_op(i,j) = A(i,j);
102         else
103             A_op(i,j) = 0;
104         end
105     end
106     if i == length(F) && j > 1 && j < length(K)
107         value_left = A(i,j+1);
108         value_right = A(i,j-1);
109         value_down = A(i-1,j);
110         if value2 <= value_left && value2 <= value_right && value2 <= value_down
111             A_op(i,j) = A(i,j);
112         else
113             A_op(i,j) = 0;
114         end
115     end
116 % Finish: End of this cycle of double variables (i,j)
117     end
118 end
119 S_op(1,1) = min(min(S));
120 A_op(1,1) = min(min(A));
121 figure(2);
122 subplot(1,2,1)
123 pcolor(K,F,S_op)
124 shading flat
125 colorbar
126 colormap(gray)
127 caxis([-1 0])
128 subplot(1,2,2)
129 pcolor(K,F,A_op)
130 shading flat
131 colorbar
132 colormap(gray)
133 caxis([-1 0])
134 % Verification of the total number of calculated points for S and A
135 Vect1 = zeros(1,length(K));
136 Vect2 = zeros(1,length(K));
137 % Manque Point si necessaire
138 % Num_colon = [9,11];
139 % A_op(5,Num_colon) = 1;
140 for ii = 1:length(K)
141     Vect1(ii) = length(find(abs(S_op(:,ii))>0));
142     Vect2(ii) = length(find(abs(A_op(:,ii))>0));
143 end
144 figure(3)
145 plot(Vect1,'-r')
146 hold on
147 plot(Vect2,'-b')
148 legend('S modes', 'A modes')
149 figure(4)
150 [row1,col1] = find(abs(S_op)>0);
151 plot(K(col1),F(row1),'r.')
152 hold on
153 [row2,col2] = find(abs(A_op)>0);
154 plot(K(col2),F(row2),'b.')
155 % Optimisation of the quasi results of S and A
156 Smode = [K(col1);F(row1)];
157 Amode = [K(col2);F(row2)];
158 Smode_op = zeros(size(Smode));
159 Amode_op = zeros(size(Amode));
160 DF = F(2) - F(1);
161 % Optimisation of the quasi results of S
162 for ii = 2:length(Smode)
163     k = Smode(1,ii);
164     w = @(f)2*pi*f;
165     p = @(f)sqrt(w(f)^2/VL^2-k^2);
166     q = @(f)sqrt(w(f)^2/VT^2-k^2);
167     funcS=@(f)(q(f)^2-k^2)^2*cos(p(f)*d)*sin(q(f)*d)+4*k^2*p(f)*q(f)*sin(p(f)*d)*cos(q(f)*d);
168     funcA=@(f)(q(f)^2-k^2)^2*sin(p(f)*d)*cos(q(f)*d)+4*k^2*p(f)*q(f)*cos(p(f)*d)*sin(q(f)*d);
169     p0 = Smode(2,ii);
170     p1 = p0 + 1;
171     p2 = p0 + 2;
172     Z0 = [p0 p1 p2];
173     [RES1,FVAL1,IT1] = muller(funcS,Z0,[],[],[],'both');
174     Smode_op(2,ii) = real(RES1);
175     Smode_op(1,ii) = Smode(1,ii);
176 end
177 disp('End of optimisation for the results of S modes');
178 % Optimisation of the quasi results of A
179 for ii = 2:length(Amode)
180     k = Amode(1,ii);
181     w = @(f)2*pi*f;
182     p = @(f)sqrt(w(f)^2/VL^2-k^2);
183     q = @(f)sqrt(w(f)^2/VT^2-k^2);
184     funcS=@(f)(q(f)^2-k^2)^2*cos(p(f)*d)*sin(q(f)*d)+4*k^2*p(f)*q(f)*sin(p(f)*d)*cos(q(f)*d);
185     funcA=@(f)(q(f)^2-k^2)^2*sin(p(f)*d)*cos(q(f)*d)+4*k^2*p(f)*q(f)*cos(p(f)*d)*sin(q(f)*d);
186     p0 = Amode(2,ii);
187     p1 = p0 + 1;
188     p2 = p0 + 2;
189     Z0 = [p0 p1 p2];
190     [RES2,FVAL2,IT2] = muller(funcA,Z0,[],[],[],'both');

```

```

191     Amode_op(2,ii) = real(RES2);
192     Amode_op(1,ii) = Amode(1,ii);
193 end
194 disp('End of optimisation for the results of A modes');
195 figure(5)
196 hold off
197 plot(Smode_op(1,:),Smode_op(2:,:),'r.')
198 hold on
199 plot(Amode_op(1,:),Amode_op(2:,:),'b.')
200 %% Save the quasi results of S in vectors
201 [Value_vec1,Num_vec1] = unique(Vect1);
202 aa = Value_vec1;
203 bb = [NK,Num_vec1'];
204 cc = (bb(1:end-1) - bb(2:end)).*aa;
205 figure;
206 for ii = 1:length(Value_vec1)-1
207     Index1 = Value_vec1(end+1-ii);
208     Index2 = Num_vec1(end-ii)-1;
209     Initial_mode = bb(end-ii+1);
210     final_mode = bb(end-ii)-1;
211     if ii == 1
212         Val_Initial = 0;
213     else
214         Val_Initial = sum(cc(end-ii+2:end));
215     end
216     for jj = 1:Index1
217         K_Vect1=Smode_op(1,Val_Initial+jj:Index1:Val_Initial+cc(end+1-ii));
218         F_Vect1=Smode_op(2,Val_Initial+jj:Index1:Val_Initial+cc(end+1-ii));
219         plot(K_Vect1,F_Vect1,'.')
220         hold on
221         eval(['S',num2str(jj-1),'(Initial_mode:final_mode)=F_Vect1;'])
222     end
223 end
224 %% Save the quasi results of A in vectors
225 [Value_vec2,Num_vec2] = unique(Vect2);
226 aa = Value_vec2;
227 bb = [NK,Num_vec2'];
228 cc = (bb(1:end-1) - bb(2:end)).*aa;
229 figure;
230 for ii = 1:length(Value_vec2)-1
231     Index1 = Value_vec2(end+1-ii);
232     Index2 = Num_vec2(end-ii)-1;
233     Initial_mode = bb(end-ii+1);
234     final_mode = bb(end-ii)-1;
235     if ii == 1
236         Val_Initial = 0;
237     else
238         Val_Initial = sum(cc(end-ii+2:end));
239     end
240     for jj = 1:Index1
241         K_Vect1 = Amode_op(1, Val_Initial+jj:Index1:Val_Initial+cc(end+1-ii));
242         F_Vect1 = Amode_op(2, Val_Initial+jj:Index1:Val_Initial+cc(end+1-ii));
243         plot(K_Vect1,F_Vect1,'.')
244         hold on
245         eval(['A',num2str(jj-1),'(Initial_mode:final_mode) = F_Vect1;'])
246     end
247 end
248 %% Freq. V.S Wavenumber
249 figure;
250 for ii = 1:length(Value_vec1)-1
251     eval(['h=plot(K(1:',num2str(Num_vec1(ii)-1),')*d/pi, (1e-3)*2*d*S',num2str(ii-1),')');'])
252     hold on
253     set(h,'Linewidth',1,'Color','red','LineStyle','-');
254 end
255 for ii = 1:length(Value_vec2)-1
256     eval(['h=plot(K(1:',num2str(Num_vec2(ii)-1),')*d/pi, (1e-3)*2*d*A',num2str(ii-1),')');'])
257     hold on
258     set(h,'Linewidth',1,'Color',[0 0.447 0.741],'LineStyle','--');
259 end
260 xlim([0 2.5])
261 ylim([0 10])
262 set(gca,'xtick',0:0.5:2.5)
263 set(gca,'ytick',0:2:10)
264 ylabel('Freq. x Thickness (MHz x mm)','FontSize', fontsize,'Fontname', 'Arial')
265 xlabel('Thickness / Wavelength (kh/pi)','FontSize', fontsize,'Fontname', 'Arial')
266 set(gca,'FontSize', fontsize,'Fontname', 'Arial')
267 saveas(gcf,'DispersionFreqWaveNum', 'fig');
268 pause(0.5)
269 saveas(gcf,'DispersionFreqWaveNum', 'pdf');
270 pause(0.5)
271 %% Freq. V.S Phase Velocity
272 figure;
273 for ii = 1:length(Value_vec1)-1
274     eval(['FSmode = S' num2str(ii-1),';'])
275     KSmode = K(1:length(FSmode));
276     Vph = (FSmode*2*pi)./KSmode;
277     plot(FSmode./1e6.*(2*d*1e3),Vph./1e3,'-r')
278     hold on
279 end
280 for ii = 1:length(Value_vec1)-1
281     eval(['FSmode = A' num2str(ii-1),';'])
282     KSmode = K(1:length(FSmode));
283     Vph = (FSmode*2*pi)./KSmode;
284     plot(FSmode./1e6.*(2*d*1e3),Vph./1e3,'--b')
285     hold on

```

```

286 end
287 xlim([0 10])
288 ylim([0 15])
289 set(gca,'xtick',0:2:10)
290 set(gca,'ytick',0:5:15)
291 xlabel('Frequency x Thickness (MHz x mm)','FontSize', fontsize, 'Fontname', 'Arial')
292 ylabel('Phase Velocity','FontSize', fontsize, 'Fontname', 'Arial')
293 set(gca,'FontSize', fontsize, 'Fontname', 'Arial')
294 saveas(gcf,'DispersionVph', 'fig');
295 pause(0.5)
296 saveas(gcf,'DispersionVph', 'pdf');
297 pause(0.5)
298 %% Freq. V.S Group Phase Velocity
299 figure;
300 for ii = 1:length(Value_vec1)-1
301     eval(['FSmode = S' num2str(ii-1),';'])
302     KSmode = K(1:length(FSmode));
303     Delta_omega = (FSmode(2:end) - FSmode(1:end-1)).*(2*pi);
304     Delta_KSmode = mean(KSmode(2:end) - KSmode(1:end-1));
305     Vg = Delta_omega./Delta_KSmode;
306     % One singular point on Freq. V.S VG curve
307     if ii == 1
308         moy = Vg(44)-Vg(41);
309         moy =moy/3;
310         Vg(42) = Vg(41) + moy;
311         Vg(43) = Vg(44) - moy;
312     end
313     plot(FSmode(1:end-1)./1e6.*(2*d*1e3),Vg./1e3,'-r')
314     hold on
315 end
316 for ii = 1:length(Value_vec1)-1
317     eval(['FSmode = A' num2str(ii-1),';'])
318     KSmode = K(1:length(FSmode));
319     Delta_omega = FSmode(2:end)*2*pi - FSmode(1:end-1)*2*pi;
320     Delta_KSmode = KSmode(2:end) - KSmode(1:end-1);
321     Vg = Delta_omega./Delta_KSmode;
322     plot(FSmode(1:end-1)./1e6.*(2*d*1e3),Vg./1e3,'--b')
323     hold on
324 end
325 xlim([0 10])
326 ylim([0 6])
327 set(gca,'xtick',0:2:10)
328 set(gca,'ytick',0:1:6)
329 xlabel('Frequency x Thickness (MHz x mm)','FontSize', fontsize, 'Fontname', 'Arial')
330 ylabel('Group Velocity','FontSize', fontsize, 'Fontname', 'Arial')
331 set(gca,'FontSize', fontsize, 'Fontname', 'Arial')
332 saveas(gcf,'DispersionVg', 'fig');
333 pause(0.5)
334 saveas(gcf,'DispersionVg', 'pdf');
335 pause(0.5)
336 %% Finish: End of this programme

```


Appendix E

Details about temperature rise
influence caused on ZGV resonant
frequency in Aluminium Alloys

At first we calculate the dispersion relations (by solving the Rayleigh-Lamb equations and optimised by the Muller method) for the intact ($T = T_0$) Aluminium Alloy (AlAl-5083) as shown in Fig. E.1 and the lowest part (around ZGV point) of S_1 mode dispersion curve is then fitted by a 4th order polynomial, and then the value of the ZGV resonance frequency is extracted as the minimal value of the fitting curve (see Fig. E.2).

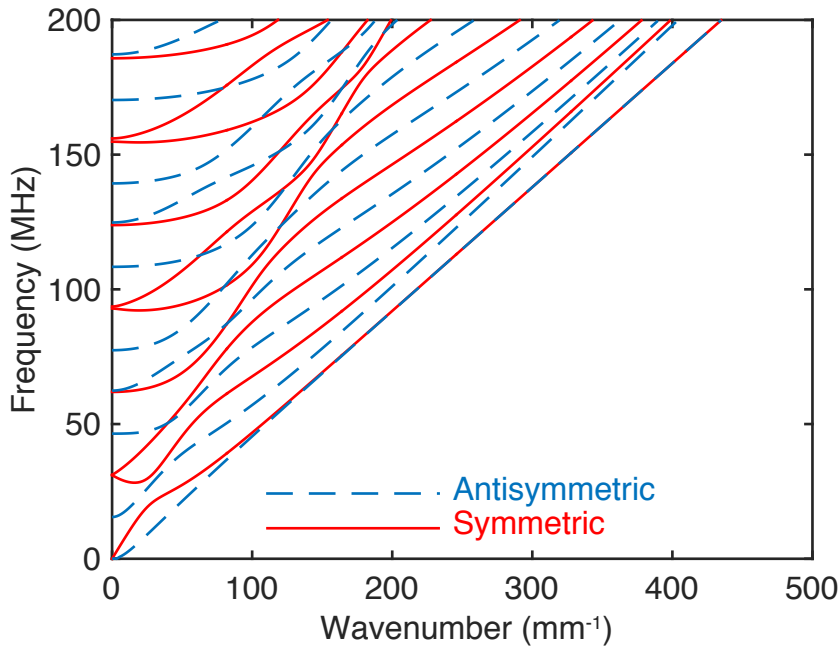


Figure E.1: Dispersion relations of Aluminium Alloy 5083 with thickness $100\mu\text{m}$.

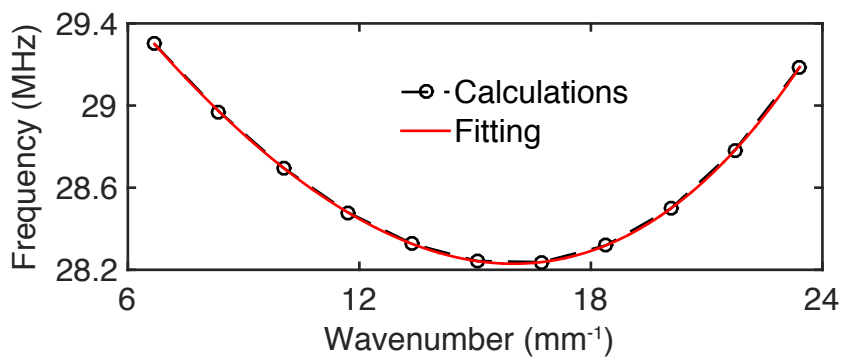


Figure E.2: S_1 mode dispersion relation: calculation and 4th order polynomial fitting.

And then, we input the values of different constants in Figures E.3 and E.4 into the Rayleigh-Lamb equations for calculations of the S_1 mode dispersion curves for different temperature rise. The extraction of the S_1 mode dispersion curves as well as the fitting curves for extraction of ZGV resonance frequency are illustrated in Fig. E.5.

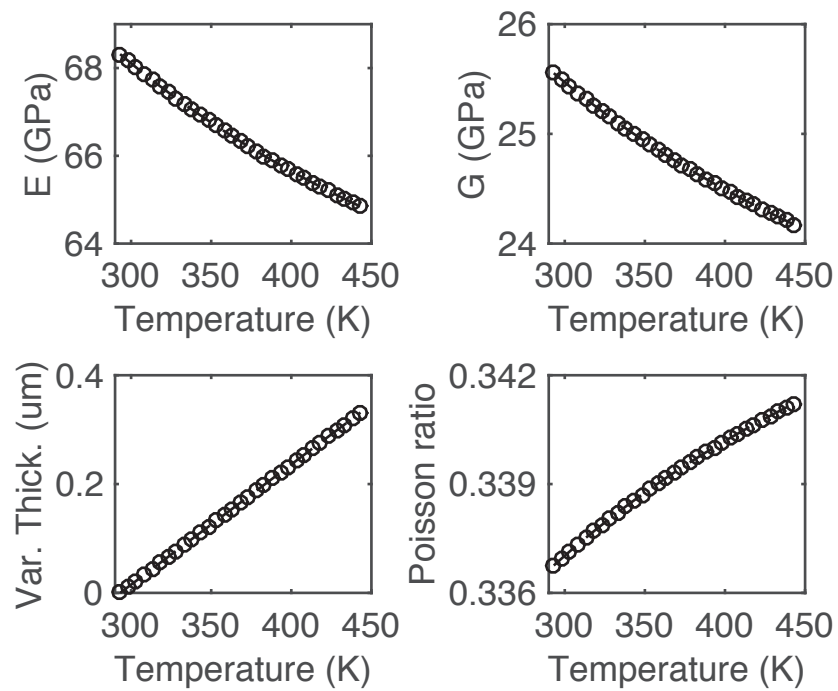


Figure E.3: Considered thermal dependant material properties.

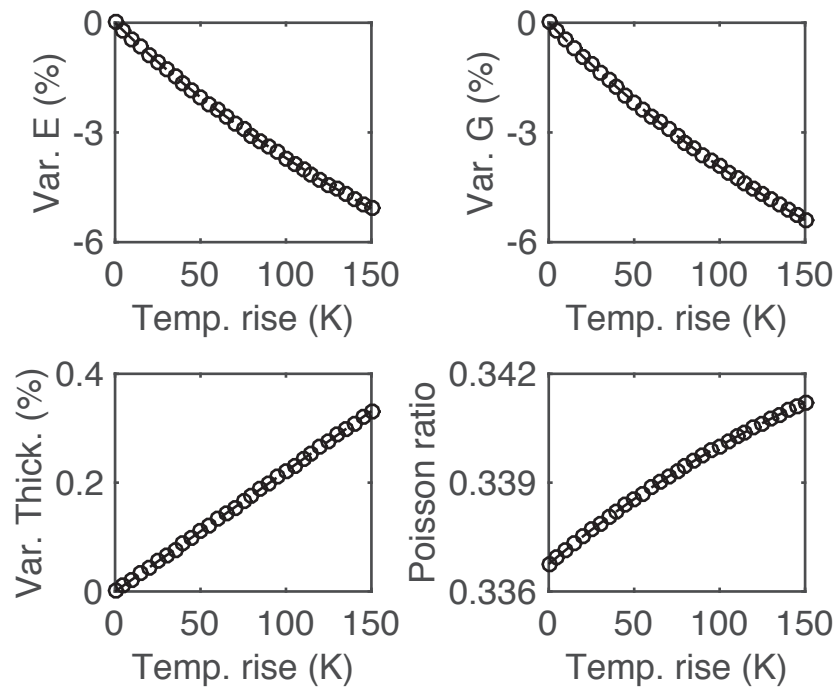


Figure E.4: Considered thermal dependant material properties variations V.S. temperature rise.

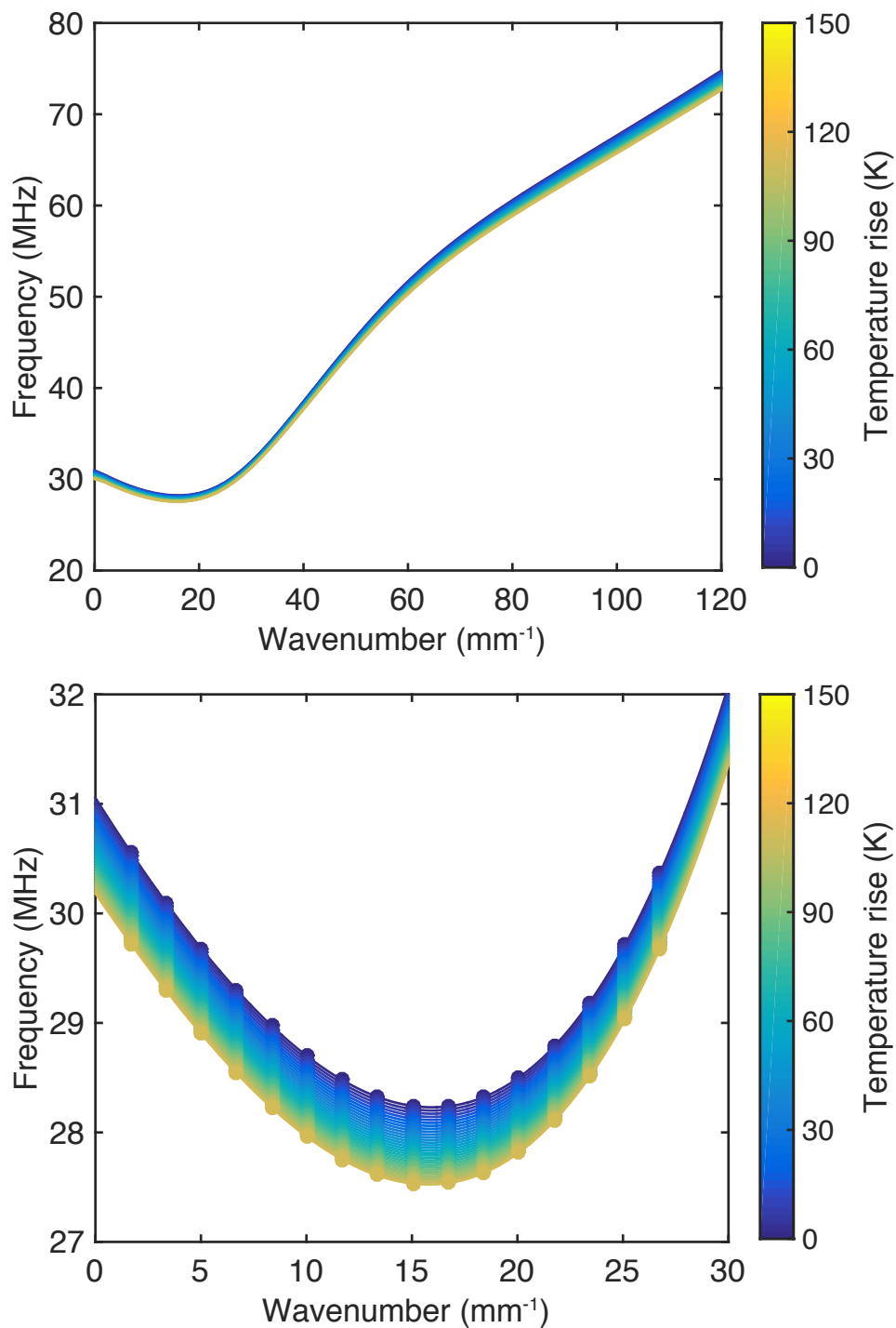


Figure E.5: S_1 mode dispersion curves for different temperature rise, above: complete dispersion curve for wavenumber until 120mm^{-1} ; below: zoomed part of sub-figure at left (coloured hollow circles) and 4th order polynomial fitting (coloured solid lines).

Finally, we inversely estimate the corresponding temperature rise values (extracted from fitting curve in Fig. E.5) from the fitting relation for different cases of $\Delta f = 0.1\%$, 0.2% , 0.5% , 1% and 2% as shown in Tab. 5.2, chapter 5, section 5.7.

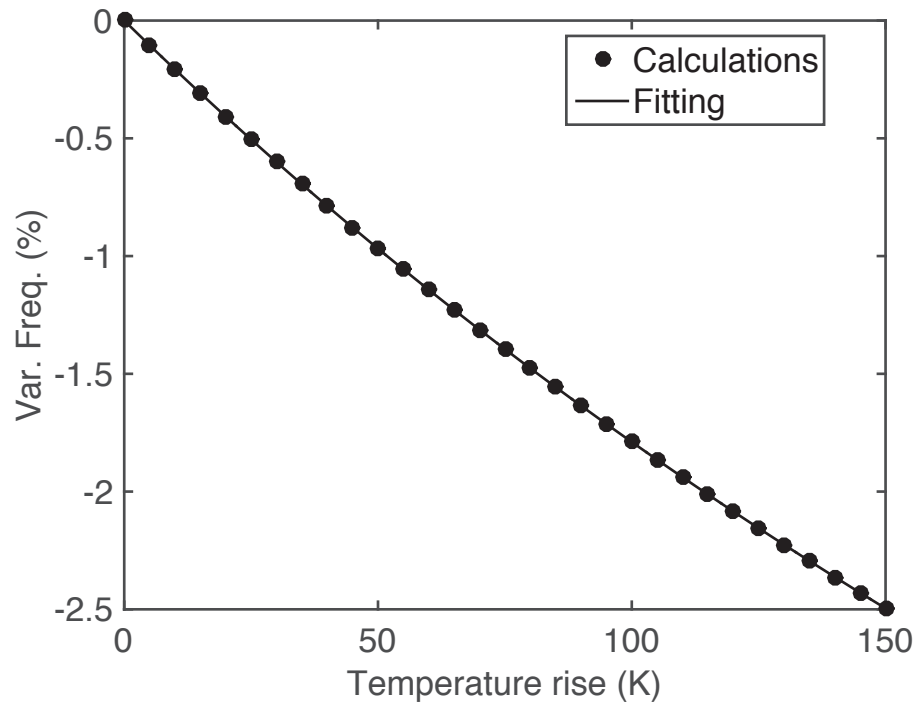


Figure E.6: Calculated ZGV frequency variation as a function of temperature rise ($\Delta f - \Delta T$) and the best fitting curve (4th order polynomial).

Titre : Ondes guidées à vitesse de groupe nulle dans laser hypersonique

Mots clés : ZGV; Ultrasons laser; Fatigue accumulée; Endommagement thermique; Nonlinéarité; ECND

Résumé : Ces dernières années, les modes à vitesse de groupe nulle (ZGV) sont révélés être un outil efficace pour sonder localement et précisément l'épaisseur d'un échantillon ou les propriétés mécaniques des matériaux isotropes ou anisotropes à l'échelle millimétrique. Ce type particulier d'ondes guidées, correspondant à des résonances locales précises de la structure inspectée, résulte de l'interférence de deux ondes de Lamb ayant une vitesse de phase opposée et coexistant à un couple de fréquence et de nombre d'ondes. La technique des ultrasons laser a démontré sa capacité à générer et à détecter efficacement de telles résonances locales aux fréquences MHz. En effet, la configuration tout optique standard, comprenant une source laser pulsée pour générer des ondes élastiques et un interféromètre pour sonder le champ de déplace-

ment associé, évite tout contact avec l'échantillon pouvant entraîner l'élargissement ou la suppression des résonances. L'utilisation de modes ZGV avec surveillance tout optique à l'échelle micrométrique pour sonder les propriétés mécaniques et les phénomènes non linéaires est assez difficile et nécessite des recherches supplémentaires. Le but de la partie théorique de la recherche doctorale sera la compréhension de la formation des modes ZGV Lamb à travers les relations de dispersion des ondes de Lamb. Le but de la partie expérimentale de la recherche doctorale sera de démontrer la génération et la détection des modes ZGV à l'échelle micrométrique par des lasers et d'appliquer cette technique pour la caractérisation non destructive des couches minces.

Title: Zero-group velocity guided waves in laser hypersonics

Keywords: ZGV; Laser ultrasonics; Cumulative fatigue; Thermal damage; Nonlinearity; NDT/E

Abstract: In recent years, zero-group velocity (ZGV) Lamb modes have proven to be an efficient tool to probe locally and very accurately the thickness of a sample or the mechanical properties of either isotropic or anisotropic materials within the millimeter range. This particular type of guided waves, corresponding to sharp local resonances of the inspected structure, results of the interference of two Lamb waves having opposite phase velocity and coexisting at a given couple of frequency and wavenumber. Laser ultrasonic technique has demonstrated its ability to efficiently generate and detect such local resonances at MHz frequencies. Indeed, the standard all-optical setup, consisting of a pulsed laser source to generate elastic waves and an interferometer to probe the associated normal displacement field, avoids any contact with the sample that could

result in the broadening or suppression of the resonances. The use of all-optically monitored ZGV modes at the micrometric scale in order to probe mechanical properties and nonlinear phenomena is quite challenging and requires additional research. The goal of the theoretical part of the PhD research will be the understanding of the formation of ZGV Lamb modes through the dispersion relations of Lamb waves. The goal of the theoretical part of the PhD research will be the understanding of the formation of ZGV Lamb modes through the dispersion relations of Lamb waves. The goal of the experimental part of the PhD research will be to demonstrate the generation and the detection of ZGV modes at the micrometric scale by lasers and to apply this technique for nondestructive characterization of thin films.